Università degli Studi di Genova

FACOLTÀ DI SCIENZE MATEMATICHE,FISICHE E NATURALI
Ph.D. degree in Physics

DISSERTATION
Defence held on 20/12/2019 in Genova

Non-equilibrium control of quantum systems and their phases

Supervisors:
Fabio Cavaliere
Niccoló Traverso Ziani

Ph. D. candidate:
Sergio Porta

Academic year 2018-2019

Contents

Introduction **v**

1 Control and engineering of quantum phases of matter **1**
1.1 Three methods to control a quantum system 2
1.2 Quantum phases of matter 10

2 Equilibrium properties of paradigmatic models **17**
2.1 Staggered potential model 18
2.2 Su-Schrieffer-Heeger model 19
2.3 Rashba spin-orbit coupled wire 23
2.4 XY model 26

3 Non-monotonic response and light-cone freezing in fermionic systems **29**
3.1 Quench from gapless to gapped states 30
3.2 Observable non-monotonic behavior 33
3.3 Klein-Gordon dynamics and light-cone freezing 37
3.4 Introducing interactions 39
3.5 Summary 42

4 Effective metal-insulator non-equilibrium phase transition **43**
4.1 Quantum quench in the SSH model 44
4.2 NEQPT robustness 52
4.3 Non-analyticities in the Ising model 55
4.4 Summary 57

5 Topological classification of dynamical quantum phase transitions **59**
5.1 Quantum quench in the XY chain 60
5.2 Loschmidt overlap 63
5.3 Dynamical topological invariant 66
5.4 Summary 69

6 Feasible model for interband pairing **71**
6.1 Equilibrium interband superconductivity 72
6.2 Laser-driven two bands semiconductor 78
6.3 Dynamics of the order parameter and phase diagram 81
6.4 Effective pairing mechanism 83
6.5 Summary 85

Conclusions **87**

Appendices **89**

A Steady state and dynamics following a quantum quench **91**
A.1 Steady state magnetization 91
A.2 Finite duration quench for the spin-orbit coupled wire 98
A.3 Klein-Gordon physics in the evolution of the Green's function 100

B Quantum quench and geometrical interpretation **103**
B.1 Quench-induced transformation in the SSH model 103
B.2 General properties 104
B.3 Effective GGE energy bands 106
B.4 Robustness 108
B.5 Other observables 110
B.6 Interacting model 111

C Observables driven-dissipative dynamics **113**
C.1 Dissipative time evolution equations for the observables 113
C.2 Solution for quadratic bands at $T = 0$ 118

Bibliography **123**

Introduction

Quantum theory is one of the major discoveries of science in the twentieth century. Initially, it has been the key to understand many unsolved and exciting problems, for instance concerning condensed matter and its microscopic structure. With the progress of scientific research, scientists became gradually aware of the importance of the quantum theory, not only to understand the microscopic domain itself, but also to explain phenomena which eventually appear in the macroscopic world. Therefore, more and more attention has been devoted to the quantum theory and its applications touched many and very different fields, from the chemical to the physical domain, resulting in crucial contributions to develop new technologies. This made it possible, for example, to create semiconductor-based electronic devices which have basically become ubiquitous in our daily life.

With the advent and the growing interest in the information technology, the peculiar characteristics of quantum mechanics are predicted to break through the limits of classical paradigms, and, hence, to give rise to exciting innovations, such as quantum computation [1–6]. Today, theory and experiments are quite far from the full understanding and realization of these predictions, even if important progress has been made towards the achievement of the so-called quantum supremacy [7], the potential ability of a quantum computing device to solve problems that classical computers practically cannot. In this respect, researchers have faced the difficulty, both from the theoretical and the experimental points of view, to control the state of a quantum system.

Quantum control, i.e. the control of quantum phenomena, is becoming one of the major concerns in condensed matter physics, even if results obtained in the recent past are mainly confined to static systems in equilibrium, due to the difficulty to experimentally manipulate out-of-equilibrium quantum systems and the absence of an efficient general theoretical framework to describe non-equilibrium dynamics [8, 9]. With the discovery of new experimental techniques, applied for example to ultra-cold atoms [10] or trapped ions [11], amazing progresses in the manipulation of non-equilibrium quantum systems have been done, and the theoretical interest has been renewed. In particular, the first question to be answered is how to efficiently bring a

quantum system out of equilibrium in a controlled way reaching a given steady state. At a later stage, it is important to study the corresponding non-equilibrium dynamics.

In this Thesis, I will address these currently open questions by inspecting several different condensed matter models, using various methods to drive the system out of equilibrium and focusing on its dynamical features as well as the properties of its equilibration towards a thermal or, more interestingly, non thermal steady state. I will discuss the possibility to manipulate various systems to give rise to peculiar dynamical behaviors and steady states with properties not attainable in thermal equilibrium, ranging from quantum phase transitions and their dynamical counterparts, to superconductivity.

This Thesis is divided in 6 Chapters.
In Chapter 1, we introduce and explain the main differences between the theoretical methods used to drive a quantum system out of equilibrium. Notably, while adiabatic manipulation mainly concerns the ground state, time dependent protocols of finite duration or periodic perturbations give us the possibility to investigate peculiar properties of highly excited states and, consequently, out-of-equilibrium and dynamical phenomena such as non-equilibrium and dynamical quantum phase transitions.
Chapter 2 is devoted to the illustration of the models we inspect in rest of whole thesis. Since during the succeeding chapters we focus only on the out-of-equilibrium features of the different models, we motivate the choice of the particular system introduced by showing its equilibrium properties and the relative possible experimental realizations.
In Chapter 3 we analyze the properties of prototypical examples of one-dimensional systems undergoing a sudden variation of the Hamiltonian parameter which controls the amplitude of the gap in the energy spectrum. In particular we inspect quantum quenches from a gapless to a gapped (or partially gapped) state. We observe an anomalous, non-monotonic, response of the steady state correlation functions as a function of the strength of the mechanism opening the gap and we give an interpretation of these results by inspecting the full dynamics of the systems, both for the integrable and non-integrable scenario. We conclude by arguing in favour of the robustness of the phenomenon in the cases of non-sudden quenches and higher dimensionality.
In Chapter 4 we further generalize the previous results by widening the parameter space inspected to drive the system between two different gapped states. When the gap is closed during the time evolution, we find, in the thermodynamic limit and for long times, non-analyticities even in simple local observables as a function of the quench parameter. In other words, we find a non-equilibrium quantum phase transition. Its appearance can be related to an effective metal-insulator transition which occurs at the level of the generalized Gibbs Ensemble [12] (describing the non-thermal steady-state of the equilibrated system). Finally, we show how these features are washed out in presence of fermion-fermion interactions or for finite system size.
In Chapter 5, we mainly focus on the dynamical properties following a quantum quench. Recently, it has been shown that when a global parameter is suddenly quenched, a non-analytic behavior of the time evolution of the dynamical free

energy can occur, giving rise to the so-called Dynamical Quantum Phase Transition (DQPT) [13]. Interestingly, we show that DQPTs can be manipulated and engineered by controlling the quench duration and protocol. Finally, introducing a dynamical topological invariant in half of the Brillouin zone, we find that DQPTs are robust only when the invariant is non-vanishing, denoting a topologically non-trivial mapping which connects the initial and final systems.
In Chapter 6 we employ a different technique to drive the system out of equilibrium. We analyze a two-band semiconductor irradiated by coherent light and subject to dissipation. By considering a pair of bands with locally the same concavity, we show that interband superconducting pairing between electrons in different bands arises under the natural assumption of the presence of phononic baths and radiative recombination processes. In light of these findings, we demonstrate how an effective model based on standard multi-band BCS theory can explain the emergence of superconductivity.

This thesis is based on the following papers co-authored by myself:

- S. Porta, F. M. Gambetta, N. Traverso Ziani, D. M. Kennes, M. Sassetti, and F. Cavaliere, "Nonmonotonic response and light-cone freezing in fermionic systems under quantum quenches from gapless to gapped or partially gapped states", Phys. Rev. B **97**, 035433 (2018) [14].

- S. Porta, N. Traverso Ziani, D. M. Kennes, F. M. Gambetta, M. Sassetti, and F. Cavaliere, "Effective metal-insulator nonequilibrium quantum phase transition in the Su-Schrieffer-Heeger model", Phys. Rev. B **98**, 214306 (2018) [15].

- S. Porta, F. Cavaliere, M. Sassetti, and N. Traverso Ziani, "Topological classification of dynamical quantum phase transitions in the xy chain", In preparation (2019) [16].

- S. Porta, L. Privitera, N. Traverso Ziani, M. Sassetti, F. Cavaliere, and B. Trauzettel, "Feasible model for photo-induced interband pairing", Phys. Rev. B **100**, 024513 (2019) [17].

Other publications not included in this thesis are:

- S. Porta, F. M. Gambetta, F. Cavaliere, N. Traverso Ziani, and M. Sassetti, "Out-of-equilibrium density dynamics of a quenched fermionic system", Phys. Rev. B **94**, 085122 (2016) [18].

- F. M. Gambetta and S. Porta, "Out-of-equilibrium density dynamics of a spinful Luttinger liquid", Il Nuovo Cimento **C 40**, 92 (2017) [19].

Note that at the beginning of every Chapter, there will be a brief introduction to assess the specific problem in a broader context and to make the Chapter self-consistent.

CHAPTER 1

Control and engineering of quantum phases of matter

In the last years, one of the major aims of condensed matter physics has been to produce new and substantial breakthrough innovations to be applied in the information technology world. Indeed, semiconductor-based devices have constantly improved their performances thanks to the ability of shrinking the components inside chips. In this process, physical components cannot however be reduced in size infinitely. Matter consists of atoms and, at the atomic level, particles behave according to the laws of quantum mechanics. With this respect, the control of quantum systems is becoming fundamental to go beyond the present technology and the engineering of powerful phases of matter, very hard to obtain in standard conditions, is one of the main goals people are trying to achieve. The realization of quantum computation devices, in this sense, strongly depends on the success of these new ideas. For example, the possible fabrication of room temperature superconductivity, favorable to the realization of scalable superconducting quantum circuits, has been deeply investigated in the last decades, at least at ambient pressure. Recent advances in laser technology have made it possible to generate pulses at terahertz frequencies, allowing coherent control to favor superconductivity at 'ultra-high' temperatures, sometimes far above the thermodynamic critical temperature [20]. Another example is the engineering and manipulation of materials with topological properties, which are predicted to be able to overcome the quantum computation greatest obstacle, that is quantum decoherence [1–6].
In this Chapter we elucidate some of the most used ways to manipulate, in a controlled fashion, a generic quantum system. Furthermore, we briefly introduce the concept of quantum phase transition (QPT) and the reason why it has been the subject of intense research activity. Finally, we generalize the idea to the non-equilibrium and dynamical cases.

1.1 Three methods to control a quantum system

We begin this chapter by considering some of the most relevant methods to control a quantum system: Adiabatic manipulation, quantum quenches, and periodic drivings.

1.1.1 Adiabatic manipulation

One of the most direct and powerful implementations of quantum state engineering is adiabiatic control [21–23]. In the adiabatic scenario, the quantum system evolves under a sufficiently slowly-varying Hamiltonian $H(t)$, thus remaining in the ground state manifold. In particular, if the system is prepared in a non-degenerate eigenstate $|n(0)\rangle$ of the Hamiltonian H at time $t = 0$, it will evolve to the corresponding instantaneous eigenstate $|n(t)\rangle$ at later times $t > 0$.
This transitionless evolution is ensured by the adiabatic theorem, which is one of the oldest and most explored tools in quantum mechanics. Performances obtained via consequences of this theorem are limited by its hypothesis. These protocols are often impractically slow to implement [24].

At least theoretically, in the absence of decoherence and losses, these protocols work well. However, real systems suffer from these effects which become crucial as time progresses, making such approaches even less optimal. The solution to this problem is to engineer a faster evolution that reaches a target state sufficiently close to the desired one in some finite control time $\tau < \infty$. These approaches have been investigated theoretically under the terms "shortcuts to adiabaticity" [25–27], "counterdiabatic driving" [28] and "optimal control" [29, 30].

A very important and interesting problem which arises in this context, especially at the optimization level, is related and have been found, for example, in the Landau-Zener transition [31, 32] and it is due to the premises of the adiabatic theorem because the time scale of the adiabatic process is set by the level spacings. With this respect, it does not hold true, in general, that an adiabatic transformation can take place for every quantum system, even for an infinitely slow process. Consider, for simplicity, a two-level quantum system: If the system starts, in the infinite past, in the lower energy eigenstate $|1\rangle$, we wish to calculate the probability of finding the system in the upper energy eigenstate $|2\rangle$ in the infinite future. To do so, we consider a time-dependent dimensionless Hamiltonian in which the energy gap between the two states varies linearly in time:

$$H(t) = \frac{1}{2}\begin{bmatrix} t/\tau_Q & 1 \\ 1 & -t/\tau_Q \end{bmatrix}, \tag{1.1}$$

where τ_Q is a constant and the Hamiltonian is written in the basis of time independent states $|1\rangle$ and $|2\rangle$. The instantaneous eigenbasis, hence, reads

$$\begin{aligned} |\uparrow(t)\rangle &= \cos[\theta(t)/2]\,|1\rangle + \sin[\theta(t)/2]\,|2\rangle \\ |\downarrow(t)\rangle &= -\sin[\theta(t)/2]\,|1\rangle + \cos[\theta(t)/2]\,|2\rangle\,, \end{aligned} \tag{1.2}$$

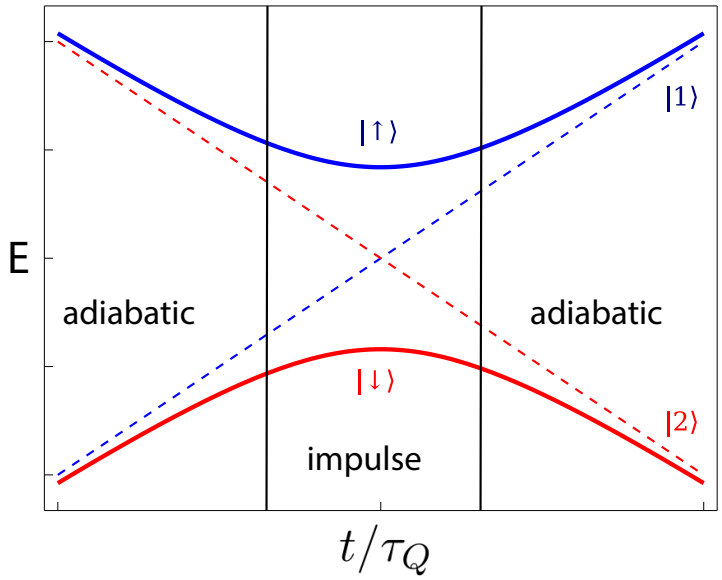

Figure 1.1: Plot of the energy levels of the Hamiltonian in Eq. (1.1). In the general case, the spectrum is gapped with an avoided crossings between levels (plain lines). Every time, during the dynamics, the gap become small enough, the system freezes out and the adiabatic evolution is lost and cannot be restored.

where $\tan\theta(t) = \tau_Q/t$. From Eqs. (1.2), we can extract the instantaneous value of the energy gap between states, given by (see Fig. 1.1)

$$E_\uparrow(t) - E_\downarrow(t) = \sqrt{1 + (t/\tau_Q)^2}. \tag{1.3}$$

The Landau-Zener formula states that the excitation probability decays exponentially with the time τ_Q. From the adiabatic theorem one knows that, as long as the inverse of the gap is small enough, the system starting its evolution from a ground state remains in the ground state. In the opposite case it undergoes the so called "impulse evolution" [33], and remains immobilized (i.e. the wave function changes only its phase factor).
Summarizing, one can adopt the Kibble-Zurek simplification of the system's dynamics: The time evolution can be either diabatic or adiabatic [33, 34]. The adiabatic part takes place when the system is away from the anti-crossing, while the impulsive part takes place in the neighborhood of an anti-crossing, where the inverse of the gap is so large that the system no longer adjusts to the changes of the Hamiltonian (see Fig. 1.1).

In this thesis, however, even if we will deal with this diabatic time evolution due to the energy level crossings, we will not particularly focus on this type of technique. Although adiabatic engineering is very powerful and widely used in the context of state preparation, we are mainly interested in a different scenario, which is the study of non-equilibrium and dynamical properties induced in systems far from their equilibrium. In this context, nevertheless, we have observed effects of the adiabatic theorem on the state reached by a one-dimensional fermionic system, brought out of

equilibrium after the manipulation of the electron-electron interaction strenght [18, 19].

1.1.2 Quantum quench

Here, quantum quenches are investigated. Such a process consists in a continuous or abrupt change in time of one or more Hamiltonian parameters, after the preparation of the system in a given state, typically its ground state. Differently from the adiabatic manipulation, which is recovered if the quench duration τ is very large, in the limit $\tau \to \infty$, and no gap closings occurs during the dynamics, this kind of quantum control allows to obtain interesting non-equilibrium features during the time evolution which may possibly leave traces in an eventual steady state. Usually, quantum quenches are studied in the context of non-dissipative systems.

More specifically, we consider a closed quantum system brought away from equilibrium by means of a change of its Hamiltonian parameters: Important questions arise in this scenario. Firstly, whether such a system will eventually achieve equilibration and, if so, what are the characteristics of the asymptotic, steady state reached after the manipulation. Regarding the last point, it is also very interesting to understand in which situation the steady state can have the form of a thermal density matrix, so that the equilibration process can be assimilated to an effective thermalization. The answer is in any sense not obvious, given the fact that the system may have a very large number of degrees of freedom. A very clean setting for the problem is the one emerging from a sudden quench of a global parameter: Initially, the system is depicted by the density matrix ρ_0 , which could be describing the ground state of an Hamiltonian. Then one or more system parameters are suddenly and globally changed and the unitary time evolution under some new Hamiltonian H is considered. Of specific interest are expectation values of observables O at later times, given by

$$\langle O(t) \rangle = \mathrm{Tr}\left\{ e^{-iHt} \rho_0 e^{iHt} O \right\}. \tag{1.4}$$

Indeed, the main point is to unveil the possibility to describe $\langle O(t) \rangle$ in Eq. (1.4) by means of an equilibrium statistical ensemble for some instant of time and, if so, for which time this description holds true. With this respect, the system time evolution is unitary. In addition, it is recurrent if the system has finite size due to the extension of the Poincaré recurrence theorem to the quantum realm [35]. It is then not so clear, by intuition, in which sense the equilibration process can take place: if we focus on observables, this means that expectation values $\langle O(t) \rangle$ of a large class of them saturates, following the transient non-equilibrium dynamics. This is specifically true for local observables, i.e. operators which are supported only on a small portion of the whole system [9].

The last statement can be proven for a special class of many-body systems, that are integrable non-interacting models, and are hence characterized by a very large set of local conserved quantities, in the sense of equilibration during intervals. One can show that the norm of the difference between $\langle O(t) \rangle$ and the time average $\mathrm{Tr}\{\omega O\}$,

where

$$\omega = \lim_{T\to\infty} \frac{1}{T} \int_0^T dt\ e^{-iHt} \rho_0 e^{iHt}, \tag{1.5}$$

is arbitrarily small after a relaxation time and remains small until a recurrence time which grows linearly with the system size [36–40]. The main arguments used to show that Eq. (1.5) holds true are the central limit theorem and the existence of the so-called Lieb-Robinson bounds, which limit the speed of information propagation in such systems. In particular, this means that information propagation outside a light-cone is exponentially suppressed and correlations can grow significantly only inside it (see Fig. 1.2). Such light-cone dynamics has been experimentally observed in optical lattice systems [41] and in cold atoms [42].

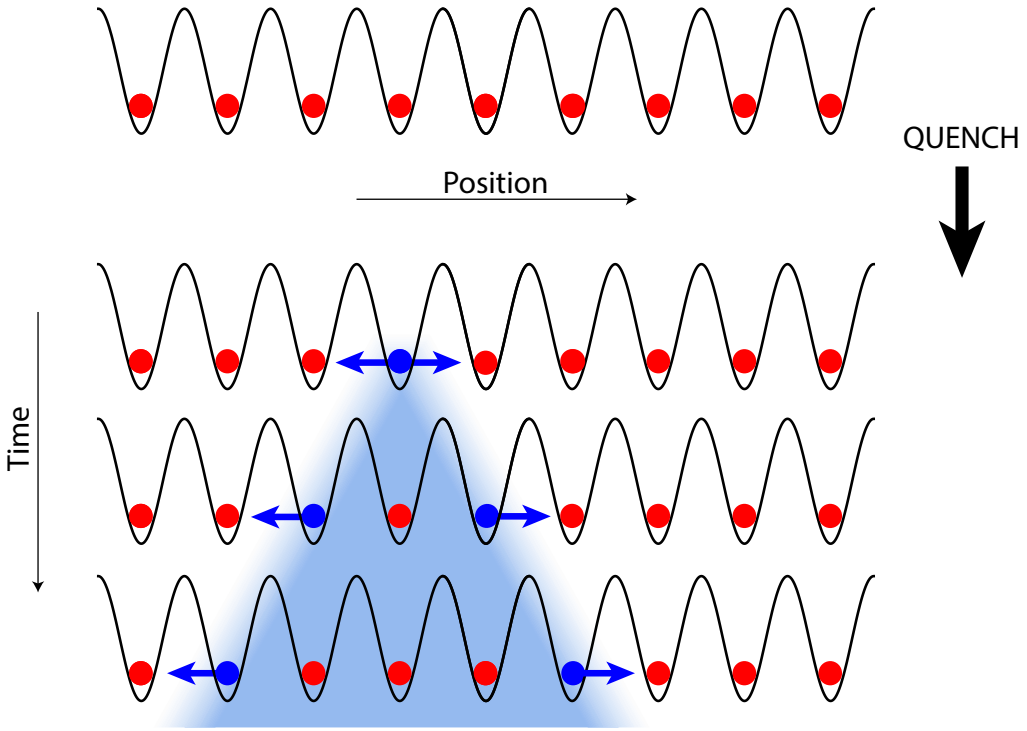

Figure 1.2: After a quench, entangled pairs of quasi-particles emerge at all sites and propagate ballistically in opposite directions, spreading information in the system. It follows that correlations build up at time t between any pair of sites separated by a distance $d = vt$, where v is the maximum relative velocity of the excitations.

Furthermore, if a quantum system is integrable, it is not expected to thermalize, since the constants of motion prevent the equilibration to a standard thermal ensemble. This behavior has been first observed by Kinoshita [43], in his quantum version of the Newton's cradle. This experiment, conducted on cold atomic gases, constitutes the first clear demonstration of the fact that a nearly integrable quantum interacting many-particle system does not thermalize for a long time (up to tens of milliseconds), until non-integrable interactions effects due to the inevitable coupling with the environment become relevant (see Figure 1.3).

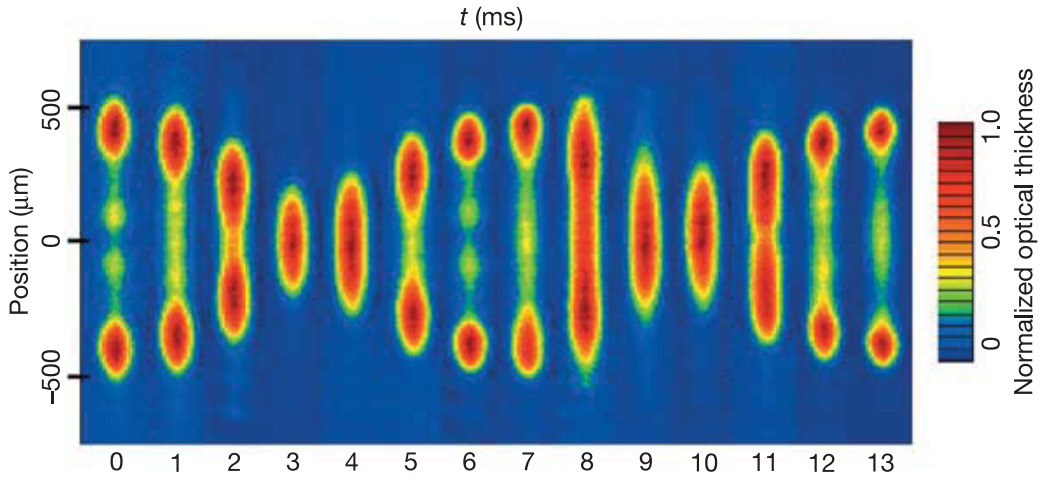

Figure 1.3: Absorption image of the quantum Newton's cradle [43]. A one-dimensional array of trapped Rb atoms is brought out of equilibrium and do not noticeably equilibrate even after thousands of collisions.

However, the system can still equilibrate to a non-thermal state obtained by the maximization of entropy, taking into account the constraints imposed by the conservation laws. Following this idea, Rigol et al. proposed the so-called generalized Gibbs Ensemble (GGE) [12], determined by the density matrix

$$\rho_{\mathrm{GGE}} = \frac{\exp\left(-\sum_\alpha \lambda_\alpha I_\alpha\right)}{Z_{\mathrm{GGE}}}. \tag{1.6}$$

Here, $Z_{\mathrm{GGE}} = \mathrm{Tr}\left\{\exp\left(-\sum_\alpha \lambda_\alpha I_\alpha\right)\right\}$ is the partition function, I_α is a suitably chosen subset of local conserved quantities and λ_α are Lagrange multipliers, fixed by the condition

$$\mathrm{Tr}\left\{\rho_0 I_\alpha\right\} = \mathrm{Tr}\left\{\rho_{\mathrm{GGE}} I_\alpha\right\} \doteq \langle I_\alpha \rangle_{\mathrm{GGE}}\,. \tag{1.7}$$

Rigol conjectured that the GGE is able to describe the asymptotic state of a generic quantum integrable model. Constructing sets of local conserved quantities is most often difficult. However, the average occupation numbers of different momentum modes become approximately additive for small subsystems, and have been proved to be a good choice to construct a working GGE in many different models [44–48].

A notable experimental detection of the veridicity of this prediction has been published in 2015 by the Schmiedmayer group [49]. In this work, they show experimentally, using a technique known as matter-wave interferometry, that a degenerate one-dimensional Bose gas of Rb atoms, after a splitting of the system into two identical halves, relaxes to a state that can be described by such a generalized statistical ensemble.

Nevertheless, the explicit construction of the GGE for general interacting integrable models remains an open problem. Moreover, there are non-integrable systems where the GGE, taking into account all known conserved quantities, fails to correctly

describe the equilibrium state [50, 51]. Indeed, when integrability is explicitly broken with a strong enough perturbation one naturally expects ergodic behavior to emerge for all observables [37, 52, 53]. The emergence of thermalization in closed systems has been conjectured by means of the so-called eigenstate thermalization hypothesis (ETH) [54, 55]: few-body operators, which are supported on a small portion of the whole system, are postulated to thermalize thanks to the interaction with all the other degrees of freedom present in the system, which act as a bath [36, 56]. In this way, all the memory of the initial state is locally lost. The range of applicability of the ETH, however, is a topic of ongoing research.
In Figure 1.4, a sketch of the different relaxation scenarios for integrable and non-integrable systems is shown.

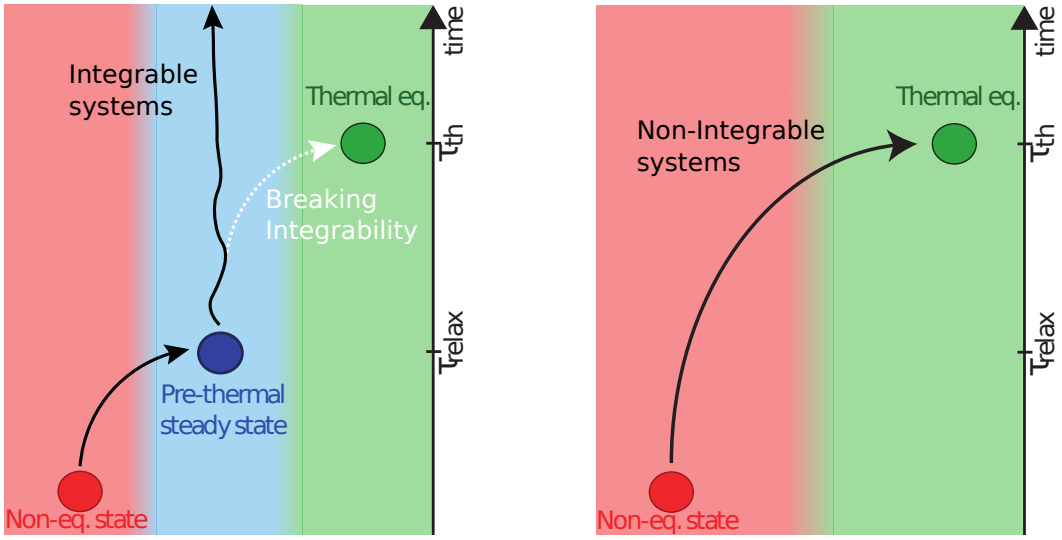

Figure 1.4: Comparison between the relaxation dynamics of the two possible classes of closed quantum systems. Integrable systems does not thermalize, but gets stuck in a non-thermal steady state that, for example, can be described by the GGE (see Eq. (1.6)). If integrability is broken due to the imperfect isolation of the system from the external background, or if the system is only nearly-integrable, thermalization takes place for long times. Non-integrable systems have only one timescale during the dynamics, and thermalization is conjectured by the ETH [55].

1.1.3 Periodic driving

Floquet engineering, the control of quantum systems using periodic driving, is an old concept in condensed matter physics and it has been introduced as a theorem yet in classical physics. It is now receiving increasing attention thanks to the huge development in laser technology and in ultrafast spectroscopy techniques from an experimental point of view, as well as growing interest in the application of quantum control in artificial matter [57]. In this section we briefly introduce the Floquet theory, which can be seen as the temporal analog of the Bloch theorem. This formalism allows for a sistematic understanding of the control of quantum systems using time-periodic external fields [58, 59]. We consider a time dependent Hamiltonian, periodic in time, such that

$$H(t+T) = H(t), \tag{1.8}$$

where $T = 2\pi/\Omega$ is the period and Ω is the driving frequency. To proceed, we expand quantities of interest into Fourier modes $e^{-im\Omega t}$, where $m = 0, 1, 2, ...$ One can show that the solution of the time-dependent Schrödinger equation can be factorized into a periodic function multiplied by a non-periodic phase factor, such that

$$|\Psi(t)\rangle = e^{-i\varepsilon t} |\Phi(t)\rangle , \text{ with } |\Phi(t+T)\rangle = |\Phi(t)\rangle . \tag{1.9}$$

The function $|\Phi(t)\rangle$ is dubbed Floquet state, while ε is the Floquet quasi-energy. One can hence fruitfully apply Fourier analysis to both the Hamiltonian and the Floquet state, to obtain

$$H(t) = \sum_m e^{-im\Omega t} H_m \tag{1.10}$$

and

$$|\Phi(t)\rangle = \sum_m e^{-im\Omega t} |\Phi_m\rangle . \tag{1.11}$$

The time-dependent Schrödinger equation is then mapped to an eigenvalue problem, given by

$$\sum_m e^{-im\Omega t} \left(H_{n-m} - m\Omega\delta_{nm}\right) |\Phi_m^\alpha\rangle = \varepsilon_\alpha |\Phi_m^\alpha\rangle , \tag{1.12}$$

where the new index α labels eigenstates. The system, hence, can be seen as a time-independent one-body system composed of many layers indexed by m, which can be considered as a lattice site index in a fictitious Floquet direction (see Figure 1.5): H_0 represents the intra-layer hopping and H_m, with $m \neq 0$, the inter-layer hopping between different layers. In addition, the frequency Ω is mapped to an effective static electric field in the Floquet direction, represented in Eq. (1.12) by the $\delta_{n,m}$ term. This equivalence can be employed to understand two important limiting cases: for small Ω we have a lattice problem in higher dimensions in a weak electric field, which can lead to the so-called Thouless pumping [60] while, in the opposite regime, the layers become isolated [61, 62].

A physical problem which arises when periodic driving is applied to condensed matter systems, is the heating resulting from the continuous injection of energy into the system itself. If we focus on stroboscopic times $t = mT$, the solution $|\Psi(t)\rangle$, given in eq.(1.9), has an identical form to that of the time evolution in time-independent

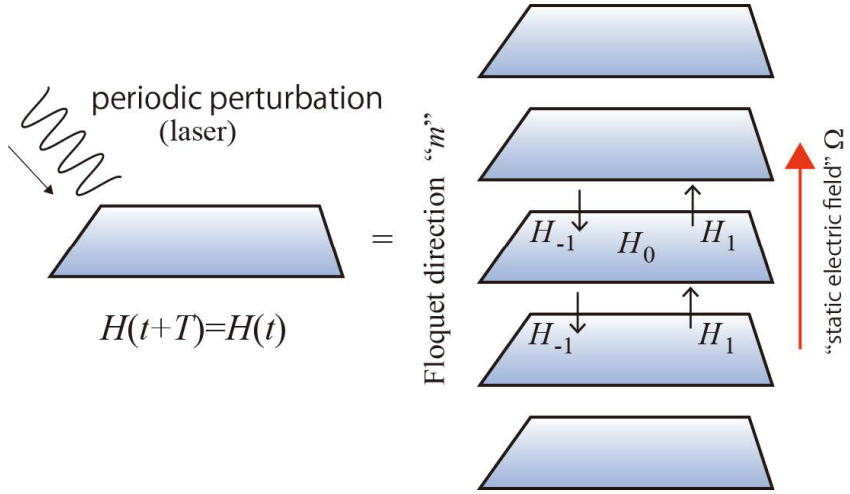

Figure 1.5: Representation of the effective time-independent model equivalent to Eq.(1.12). Figure adapted from [57].

systems where the quasi-energy ε_α plays the role of the energy eigenvalue and $|\Phi(t=0)\rangle$ is the usual eigenstate, considering t_0 as the initial time, i.e. when the perturbation is switched on. At this point, the same question of the previous section emerges: is there the possibility to reach an equilibrated state for long time, given that, in this case, an external periodic force keep on heating until the temperature goes to infinity? Since heating is expected to play a prominent role only for very long times if a good choice of the external field is done, a pre-thermalized intermediate steady state can be reached on a shorter timescale [63]. In particular, using the stroboscopic picture, this metastable state can be described, applying a perturbative expansion, as an eigenstate of the resulting effective Hamiltonian [64, 65].

Furthermore, the description of the non-thermal equilibrated state by means of a periodic ensemble has been proved, since after an initial transient period, the system is known to synchronize with the driving. For a class of integrable systems, the relevant ensemble is constructed by maximizing an appropriately defined entropy subject to constraints, which is the periodic generalization of the previously mentioned generalized Gibbs Ensemble [66], whose density matrix is given in Eq. (1.6) and is generalized as

$$\rho_{\mathrm{PGE}}(t) = \frac{\exp\left(-\sum_\alpha \lambda_\alpha I_\alpha(t)\right)}{Z_{\mathrm{PGE}}}, \tag{1.13}$$

where the Lagrange multipliers are fixed by the condition

$$\mathrm{Tr}\left\{\rho_0 I_\alpha(0)\right\} = \mathrm{Tr}\left\{\rho_{\mathrm{PGE}}(0) I_\alpha(0)\right\}. \tag{1.14}$$

The operator in Eq. (1.13), furthermore, has the following properties: It correctly gives the conserved quantity averages during the whole time evolution and it is itself manifestly periodic with time, i.e. $\rho_{\mathrm{PGE}}(t+T) = \rho_{\mathrm{PGE}}(t)$.

1.2 Quantum phases of matter

Quantum phases are quantum states of matter at zero temperature. The difference between these states and classical states of matter is that, classically, materials exhibit different phases which strictly depend on the change in some macroscopic property of the material. The emblematic example is water: The variation of temperature can produce ice in the solid state, water in the liquid state or water vapor in the gaseous state, tipically breaking and restoring symmetries like crystalline order every time the passage between different phases takes place.
Differently from that, quantum phases can vary in response to a change in a non-thermal control parameter at zero temperature, with the manipulation of external parameters such as pressure, or magnetic field, or the chemical composition. The combination of quantum mechanical effects and statistical physics has, in this respect, led to the discovery of phase transitions mediated by quantum fluctuations, an effect that arises directly from the Heisenberg uncertainty principle. Such transitions are dubbed quantum phase transitions (QPTs) [67, 68]. The point in the parameter space where the transition happens is called quantum critical point (QCP).

1.2.1 Classical vs Quantum phase transitions

In general, phase transitions are divided into two different class: First-order and continuous ones [68]. This was anticipated by Ehrenfest in his seminal work [69, 70] where he argued that whenever a non-analyticity appears in the Gibbs free energy, there is a phase transition. In the first case, the two phases connected by the transformation coexist at the critical temperature, where the transition happens, while in the second scenario the transition, as the name suggests, is continuous in the sense that the features of the system vary in a continuous manner as the critical point is crossed [67]. In this chapter, and in the whole Thesis, we concentrate on continuous transitions. Interestingly, this class can often be characterized by the so called order parameter (even if in some cases it is not easy to define): A local quantity that is zero in the disordered phase and non-vanishing in the ordered one. Furthermore, one has to observe that while the thermodynamic average of the order parameter is zero in a disordered phase, its fluctuations are non-zero. A fruitful method to investigate such a phenomenon, is to study the spatial correlations of the order parameter as a critical point is approached. In the proximity of this special point, the correlation length ξ diverges as

$$\xi \propto |\tau|^{-\nu} \tag{1.15}$$

where ν is the correlation length critical exponent and τ is the adimensionless temperature, defined as $\tau = |T - T_c|/T_c$, with T_c the critical temperature. The same can be transposed to correlations in time, to obtain

$$t_c \propto \xi^z \propto |t|^{-\nu z}, \tag{1.16}$$

where z is the dynamic critical exponent. This two quantities, namely ξ and t_c, set the characteristic length and timescale of the problem. Because of their divergence, the system is said to be scale-invariant, i.e. its features do not change if scales of length, energy, or other variables, are multiplied by a common factor. As a

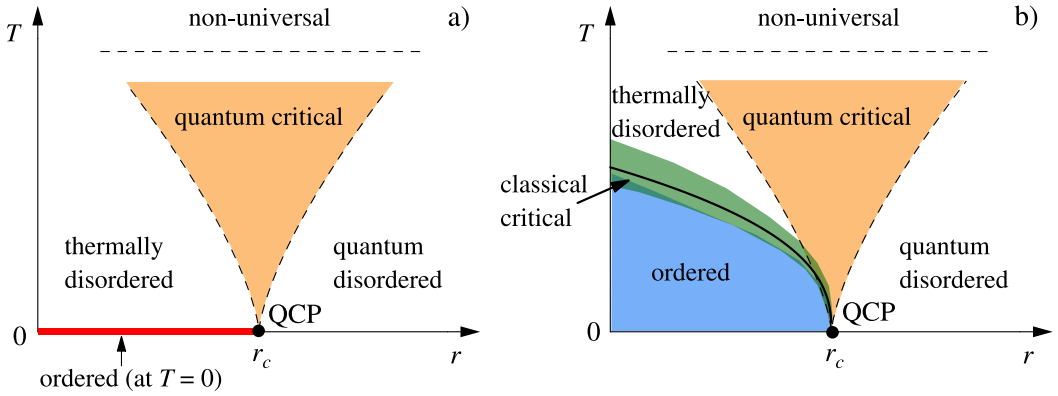

Figure 1.6: Phase diagram in the vicinity of the QCP as a function of the control parameter r and the temperature T. a) Order present only at $T = 0$. b) Order exists also at finite temperature. Figure adapted from [67].

consequence, all observables depend via power laws on the external parameters. This result is universal, i.e. it is independent of most of the microscopic details, as long as the symmetries of the order parameter are not changed, and, remarkably, this means that the critical exponents of a phase transition occurring in nature can be determined by investigating any simple model belonging to the same universality class.

Let us now turn to quantum phase transitions and to quantum mechanics. What is now discussed becomes relevant in the regime where the thermal energy is overwhelmed by the typical energy scale, whose order of magnitude is given by the inverse of τ_c in Eq.(1.16). A crossing between the classical and the quantum regimes in the fluctuations of the order parameter, consequently, can occur and can be observed in the phase diagram when the QCP is approached. In particular, if the transition takes place at zero-temperature, it is necessarily driven by a change in a non-thermal parameter r and, therefore, such behavior is strictly dominated by quantum fluctuations. As shown in Fig. 1.6, two cases can be distinguished when temperature is increased. In the first scenario, order is present only at exactly $T = 0$, and the phase transition is not experimentally detectable in a direct fashion considering the impossibility to access this extreme condition. At finite temperature, with this respect, order can be washed out by thermal fluctuations or the system can remain disordered and dominated by quantum fluctuations as happening for $r > r_c$ at $T = 0$. The region in between this two regimes is called quantum critical, and represents the crossover region where both contributions are important: Here, the main feature is the absence of quasi-particle-like excitations [67]. A different scenario is obtained if order survives also at finite temperature. The phase diagram acquires an extra ordered phase, bounded by the so-called classical critical line which ends at the QCP. Around this line, a classical description can be applied and a real and detectable phase transition is then observed. In both cases one has to note that universality is lost when temperature acquires large values.

To have a closer connection to what we will investigate in this thesis, it is possible

to formulate the problem of quantum phase transitions from the point of view of many-body eigenstates. To do so, we consider a generic Hamiltonian $H(r)$, which depends on a control parameter r. For a finite size system, the ground state energy is in general a smooth function of r, but it is worth to notice that a special case can happen. Indeed, decomposing the Hamiltonian as

$$H(r) = H_0 + rH_1, \tag{1.17}$$

a possibility is that H_0 and H_1 commute. In this particular case, eigenfunctions do not depend on r since Hamiltonians can be simultaneously diagonalized, while eigenvalues do. Therefore, a level-crossing can occur if an excited level becomes the ground state at $r = r_c$, and a non-analytic behavior of the energy is then created. This is the quantum equivalent of first-order phase transitions introduced at the beginning of this section. Taking the thermodynamic limit, we produce another, more interesting, possibility. An avoided level-crossing, in fact, can become sharper and sharper as the system size increases, leading to a different type of non-analyticity, where higher-order singularity occurs in the ground state energy. This is the continuous phase transition. The latter is more common in nature and of particular interest in the context of non-equilibrium physics, as we will show in the next section and chapters where its properties will be investigated using the quantum control methods introduced in Section 1.1.

1.2.2 Non-equilibrium quantum phase transitions

Quantum phase transitions, as mentioned, concern ground state properties of many-body systems, and hence their signatures are expected to be visible in low-energy states. However, recent theoretical efforts lead to the discovery of the existence of the fingerprints of a QPT also on higher excited states [71]. From the point of view of equilibrium physics, a positive indication follows from the existence of the so-called quantum critical region in the finite temperature phase diagram of a quantum system, where the behavior of the system is strongly affected by the existence of an underlying quantum critical point even at $T \neq 0$ (see Fig. 1.6). Similar indication is obtained from the non-equilibrium response mechanism of a system driven at a finite rate across a quantum critical point, largely known as the Kibble-Zurek mechanism [33, 72].

Another path proposed to study non-equilibrium critical phenomena is to extend equilibrium concepts and methods. The key idea is to identify a non-equilibrium quantum phase transition on the basis of non-analyticities in observables as a function of the tuning parameter in the pre-thermal regime [48, 73–75]. A pre-thermal state retains partial memory of the initial state of the system, therefore the pre-thermal value of a suitable order parameter will in general differ from its thermal equilibrium value, and it may or may not show symmetry breaking and other signatures associated with the occurrence of a phase transition [76, 77]. Non-equilibrium quantum phase transitions are expected to be related in some way to their equilibrium counterparts, as they show a similar kind of symmetry breaking and can be signalled by the same order parameter, but in general can occur in non-equilibrium critical points shifted with respect to the equilibrium ones [77]. The investigation of this kind of

phenomena, however, is still far from complete, mainly to the difficulty in setting a general theoretical framework.

1.2.3 Dynamical quantum phase transitions

Here we present a very special class of non-analytic behavior that occurs on transient time scales. The phenomenon has been termed Dynamical Quantum Phase Transition (DQPT) [78]. DQPTs are driven by progressing time as opposed to conventional phase transitions that are driven by control parameters.

To introduce this concept, we make use of a quantum quench to bring the system out of equilibrium. Following Section 1.1.2, we prepare a closed quantum system in the ground state $|\psi_0\rangle$ of an initial Hamiltonian $H_0 = H(r_0)$, where r is the tuning parameter. At a certain instant of time, say $t = 0$, a sudden quench of the parameter is performed to obtain the final Hamiltonian $H_f = H(r_f)$. If the ground state $|\psi_0\rangle$ is not an eigenstate of H_f, a non-trivial dynamics is induced into the system, and its time evolution is in general given by

$$|\psi_0(t)\rangle = e^{-iH_f t}\,|\psi_0\rangle\,. \tag{1.18}$$

We focus on the study of the Loschmidt amplitude, which gives the overlap of the time evolved state with respect to the initial state, and defined as

$$\mathcal{G}(t) = \langle\psi_0|\psi_0(t)\rangle = \langle\psi_0|e^{-iH_f t}|\psi_0\rangle\,. \tag{1.19}$$

The analysis, surprisingly, can be carried out by means of the standard techniques used in the context of thermodynamics, such as the Fisher [79] or Lee-Yang [80, 81] zeros. Indeed, by considering the transformation $it \to z$, the Loschmidt amplitude can be effectively seen as a (boundary) partition function. With this respect, it is known that for finite-size systems, partition functions are analytic functions. However, they experience a particular functional dependence on the number of degrees of freedom N in the limit of large N we have [13, 82]:

$$\mathcal{G}(t) = e^{-N g_N(t)} \tag{1.20}$$

where $g_N(t)$ is the associated rate function. We then define

$$g(t) = -\lim_{N\to\infty}\frac{1}{N}\ln\mathcal{G}(t) = -\lim_{N\to\infty} g_N(t). \tag{1.21}$$

Analogously, we define the Loschmidt echo

$$\mathcal{L}(t) = |\mathcal{G}(t)|^2 \tag{1.22}$$

and its associated rate function, given by

$$\lambda(t) = 2\mathrm{Re}\,\{g(t)\}\,. \tag{1.23}$$

This function, as sketched in Fig. 1.7, can show kinks as a function of time. The times of the kinks are called critical times t_c, in close analogy to the free energy in the equilibrium case. The appearance of the non-analyticity has been firstly

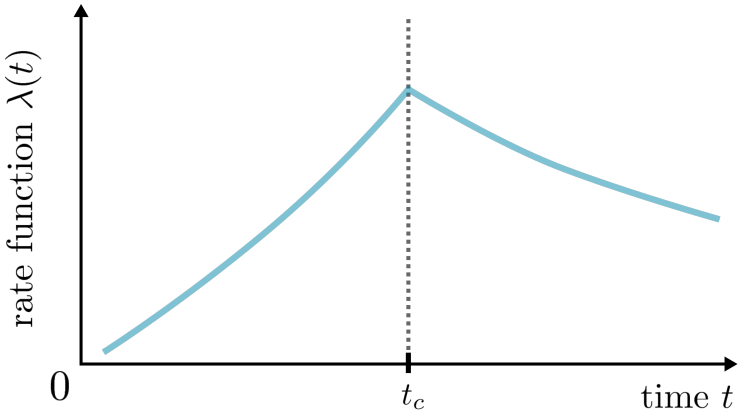

Figure 1.7: Schematic illustration of a DQPT, seen as a kink in the Loschmidt echo associated rate function λ. Figure adapted from [13].

directly connected to the quench of the control parameter across an equilibrium quantum critical point [83]. At later times, however, this behavior has been observed to hold more in general [84, 85], suggesting that DQPTs are not in one-to-one correspondence with conventional phase transitions. In the next chapters, we will deepen this concept to unveil more details of the aforementioned relations.

A more involved analogy to equilibrium quantum phase transitions, nonetheless, can be done [86]. QPTs in equilibrium represent actually an important example where the singular behavior of the ground state can influence an extended set of states within the quantum critical region at nonzero temperature. An analogous picture can also emerge for DQPTs, and can be made concrete and even measurable [87]. With this respect, the Loschmidt amplitude probe the low energy properties of the time-evolved state, since it is the projection of $|\psi_0(t)\rangle$ on the ground state. In this sense, the non-analyticities associated with DQPTs are a ground state property in close analogy to conventional QPTs occurring at zero temperature. This interpretation, then, leads to the following similarity: a phase diagram where the temperature-control parameter space $(T - r)$ is replaced by the energy density-time plane $(\epsilon - t)$, as plotted in Figure 1.8. In this picture, the DQPT occurs along the line of vanishing energy density $\epsilon = 0$ at a critical time t_c. While the non-analytic behavior can disappear for excited energy densities $\epsilon > 0$, where local observables acquire their dominant contribution, there can still be an extended region controlled by the underlying dynamical critical point, although the dynamical analog of a quantum critical region for any DQPT is not proved to exist.

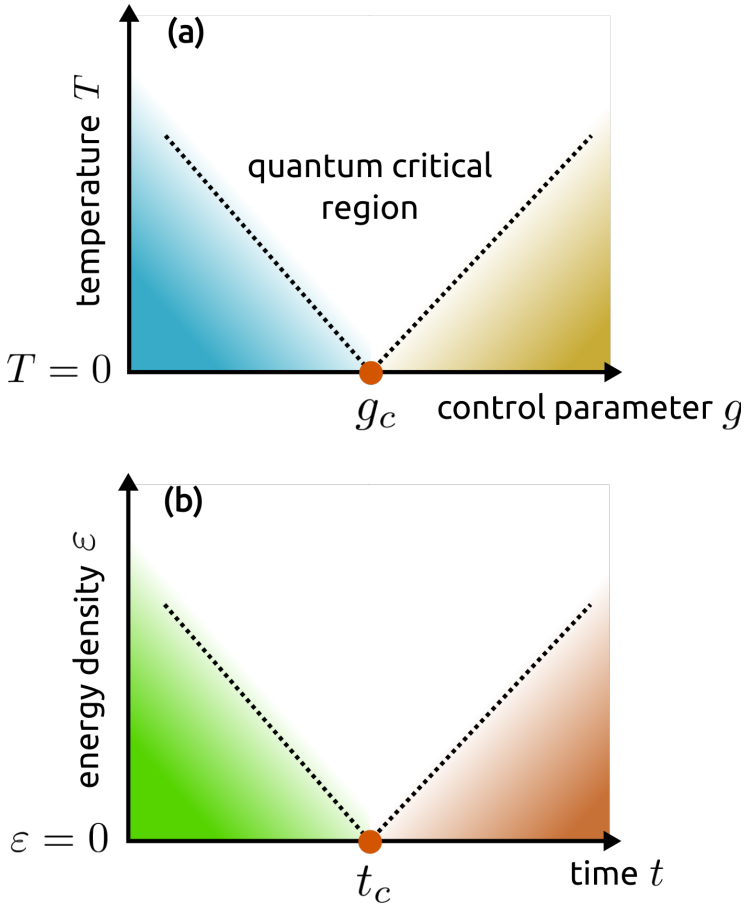

Figure 1.8: Analogy between equilibrium quantum phase transitions and dynamical quantum phase transitions, where the phase diagram is drawn as a function of the energy density in place of temperature and time in place of the control parameter. The dynamical counterpart of the quantum critical region has not proven to exist in general. Figure based on [13].

CHAPTER 2

Equilibrium properties of paradigmatic models

In this chapter, we introduce the zero temperature properties of the models we will drive far from equilibrium in the course of this Thesis by means of the techniques elucidated in Chapter 1. In particular, we will describe a one dimensional lattice of spinless fermions with a unit cell composed by two sites, where two different effects can be studied: In the Staggered potential (SP) model a staggered chemical potential is taken into account, the Su-Schrieffer-Heeger (SSH) model is represented by a staggered hopping amplitude between fermions in the same cell and in consecutive different cells. In both the cases an energy gap in the spectrum can be opened. Then, we will show the main features of a 1D quantum wire in presence of the Rashba spin-orbit coupling and an external magnetic field, while, in the last part of the chapter, we illustrate the phase diagram of the XY model.

2.1 Staggered potential model

We begin this chapter by considering a one dimensional lattice of spinless fermions at half filling, such that the number of sites is twice as large as the number of particles in the system. The model represents a metal since its energy spectrum is gapless. However, with the introduction of a staggered site potential, we can examine effects of an alternating on-site modulation of the chemical potential (see Figure 2.1). The real space Hamiltonian which describes this scenario reads

$$H_{\mathrm{SP}} = -J \sum_{j=1}^{L} \left[\left(c_j^\dagger c_{j+1} + h.c. \right) + (-1)^j \delta c_j^\dagger c_j \right], \tag{2.1}$$

where c_j are annihilation operators for spinless fermions on the site j of the lattice, we have set unit lattice spacing so that the chain length is L, and δ is the staggered potential. Moreover, J is a measure of the kinetic energy and we adopt periodic boundary conditions.

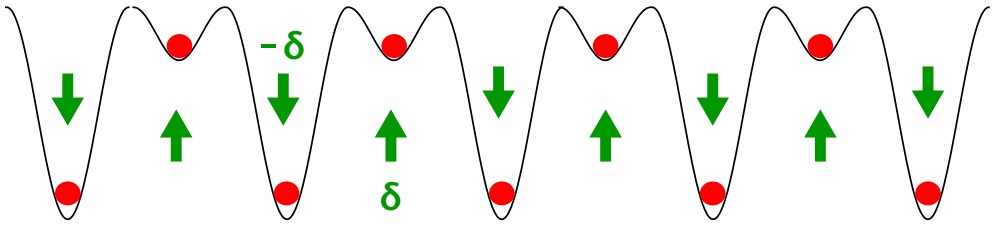

Figure 2.1: Effect of the staggered chemical potential on the fermions in the lattice, whose unit cell is chosen to be formed by two sites labelled by the indexes A and B.

Upon introducing momentum representation via the Fourier transform

$$c_j = \frac{1}{\sqrt{L}} \sum_k e^{ikj} c_k, \tag{2.2}$$

and the spinor $\Psi_k^\dagger = \left(c_k^\dagger, c_{k-\pi}^\dagger \right)$, we are able to obtain the Hamiltonian

$$H_{\mathrm{SP}} = \sum_k \Psi_k^\dagger \mathcal{H}_k \Psi_k, \tag{2.3}$$

with

$$\mathcal{H}_k = -2J \cos(k) \sigma^z + \delta \sigma^x \tag{2.4}$$

and $k \in (-\pi/2, \pi/2]$, due to the fact that the unit cell contains two lattice sites. Here, σ_i, with $i = x, y, z$ are the Pauli matrices. The diagonalization of $\mathcal{H}_k$ gives us access to the energy spectrum

$$\epsilon_{\pm,k} = \pm \sqrt{\delta^2 + 4J^2 \cos^2(k)}. \tag{2.5}$$

As shown in Figure 2.2, the system is an insulator as long as $\delta \neq 0$. The ground state is given by the state where only the valence band is filled. Note that at $\delta \ll J$, the low-energy spectrum of the band insulator is the one of free massive Dirac fermions.

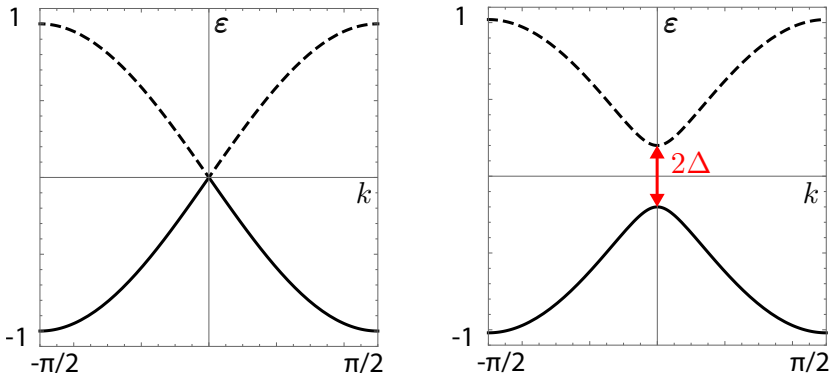

Figure 2.2: Energy spectrum of the chain of spinless fermions in the absence (left panel) and in the presence (right panel) of the staggered chemical potential δ. Fermi energy is set to zero, dashed lines represent the conduction band and solid lines the valence band. Energy is measured in units of J.

2.2 Su-Schrieffer-Heeger model

The Su-Schrieffer-Heeger (SSH) model describes electrons hopping on a one-dimensional lattice, with staggered hopping amplitudes, as shown in Figure 2.3. The chain consists of N unit cells, each unit cell hosting two sites, one on sublattice A and one on sublattice B. Interactions between the electrons are neglected, so that the dynamics of each electron is described by a single-particle Hamiltonian, of the form [88]

$$H_{\text{SSH}} = \sum_{j=1}^{N} \left[v \left(c_{j,A}^{\dagger} c_{j,B} + h.c. \right) + w \left(c_{j,B}^{\dagger} c_{j+1,A} + h.c. \right) \right], \tag{2.6}$$

where $c_{j,A}^{\dagger}$ and $c_{j,B}^{\dagger}$ are the fermionic creation operators on the unit cell m, respectively to the sublattice A or B, v represents the intra-cell and w the inter-cell hopping parameters. The SSH model describes spin-polarized electrons, and when applying it to describe a real physical system, such as polyacetylene [89], we have to always take two copies of it. We again use periodic boundary conditions.

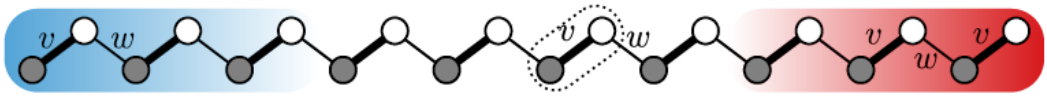

Figure 2.3: Geometry of the SSH model. Figure adapted from [88].

By means of a Pauli matrices representation, it is possible to emphasize the separation of the external degrees of freedom (unit cells) from the internal ones (sublattice indexes). The Hamiltonian, on this basis, can be recast to

$$H_{\text{SSH}} = v \sum_{j=1}^{N} c_j^{\dagger} \sigma^x c_j + w \sum_{j=1}^{N-1} c_{j+1}^{\dagger} \frac{\sigma^x + i\sigma^y}{2} c_j + h.c. \tag{2.7}$$

where the unit cell spinor on site j is defined as $c_j^{\dagger} = \left(c_{j,A}^{\dagger}, c_{j,B}^{\dagger} \right)$. Applying the Fourier transform only on the external degrees of freedom, since the model is periodic

in the Brillouin zone as

$$H_{\mathrm{SSH}}(k+2\pi) = H_{\mathrm{SSH}}(k) \tag{2.8}$$

and introducing the plane wave basis

$$c_k^\dagger = \frac{1}{\sqrt{N}} \sum_{j=1}^{N} e^{ijk} c_j^\dagger, \tag{2.9}$$

where $k = 2\pi n/N$ and $n = 1, ..., N$, we obtain the momentum space Hamiltonian

$$H_{\mathrm{SSH}}(k) = \sum_{k\in \mathrm{B.Z.}} c_k^\dagger \mathcal{H}_{\mathrm{SSH}}(k) c_k = \sum_{k\in \mathrm{B.Z.}} c_k^\dagger \begin{pmatrix} 0 & v + we^{-ik} \\ v + we^{ik} & 0 \end{pmatrix} c_k. \tag{2.10}$$

The energy spectrum of the system is read off by means of the diagonalization of the Hamiltonian $\mathcal{H}_{\mathrm{SSH}}(k)$. This gives

$$E_{\mathrm{SSH}}(k) = \left| v + we^{-ik} \right| = \sqrt{v^2 + w^2 + 2vw\cos k}. \tag{2.11}$$

In particular, as long as the hopping amplitudes are staggered, $v \neq w$, there is an energy gap of amplitude 2δ (with $\delta = |v - w|$) which, in the ground state, separates the lower filled valence band from the upper empty conduction band. Without the staggering, the SSH model describes a simple conductive chain, as mentioned in the previous section. Although the dispersion relation is useful to read off a number of physical properties of the bulk of the system, the SSH Hamiltonian becomes particularly interesting when open boundary conditions are imposed. In the fully dimerized limit, where one of the two hopping parameters is vanishing, the SSH chain falls apart to a sequence of disconnected dimers and the energy spectrum is flat.

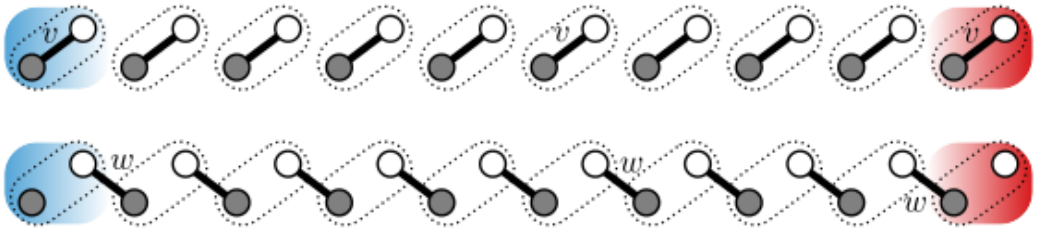

Figure 2.4: Fully dimerized limits of the SSH model, where the chain has fallen apart to disconnected dimers. In the top figure it is shown the trivial insulator, where the dimer is in the same unit cell, while in bottom figure, which shows the topological insulator, the dimer is between two contiguous unit cells. Figure adapted from [88].

The two possibilities (shown in Figure 2.4), however, emerge and are intrinsically different. In the $v = 1, w = 0$ case, which is called trivial, the dimers resides exactly in the unit cell, while in the $v = 0, w = 1$ case, which is called topological, dimers are between neighboring unit cells. In this configuration, there is one isolated site per edge that contains one zero-energy eigenstate, as there are no onsite potentials. Moving away from the very special limit of full dimerization, one observes that

the energies of the edge states remain very close to zero and the wavefunctions of the relative eigenstates are exponentially localized since the zero-energy modes are situated at the center of the bulk band gap.

The distinction between the trivial insulator and the topological insulator, however, is even more pronounced and can be analyzed in details by taking into account the so-called chiral symmetry of the SSH Hamiltonian. To do so, let us go back to the single-particle momentum space Hamiltonian introduced in Eq. (2.10). It can be rewritten as

$$\mathcal{H}_{\mathrm{SSH}}(k) = \boldsymbol{d}(k) \cdot \boldsymbol{\sigma}, \tag{2.12}$$

where the path of the endpoint of the vector $\boldsymbol{d}(k)$, as the wavenumber goes through the Brillouin zone, is a closed path restricted to the d_x, d_y plane thanks to the aforementioned symmetry. Therefore, it is possible to define an integer winding number ν around the origin, which counts the number of times $\boldsymbol{d}(k)$ intersects a curve that goes from the origin of the d_x, d_y plane to infinity and can be quantitatively defined as the following integral:

$$\nu = \frac{1}{2\pi} \int_{-\pi}^{\pi} \left[\bar{\boldsymbol{d}}(k) \times \frac{d}{dk} \bar{\boldsymbol{d}}(k) \right]_z dk \tag{2.13}$$

with $\bar{\boldsymbol{d}}(k) = \boldsymbol{d}(k)/|\boldsymbol{d}(k)|$. For the SSH model, the winding number is either 0 or 1, depending on the parameters. In the trivial case, when the intracell hopping dominates the intercell one ($v > w$), the winding number is $\nu = 0$. In the topological case ($w > v$), one obtains $\nu = 1$.

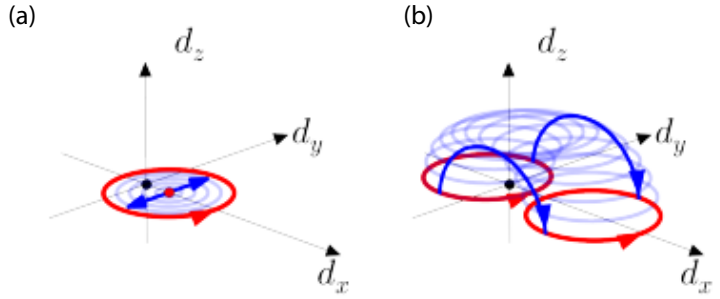

Figure 2.5: The endpoints of the vector $\boldsymbol{d}(k)$ as k goes across the Brillouin zone, for various parameter settings in the SSH model. In (a), keeping $w = 1$, we gradually decrease intracell hopping $v = 0.5$ to 0 so that the winding number changes from 0 to 1, meanwhile the bulk gap closes and reopens. In (b), keeping $v = 1$, we increase the intracell hopping w from 0.5 to 2.5, but avoid closing the bulk gap by introducing a sublattice potential. At the end of the process there is no sublattice potential, so chiral symmetry is restored and $\nu = 0$. Figure adapted from [88].

In order to have a change in the winding number ν of the SSH model, there are two possibilities: closing the bulk gap by pulling the path of $\boldsymbol{d}(k)$ through the origin in the d_x, d_y plane, or breaking the chiral symmetry by lifting $\boldsymbol{d}(k)$ out of the plane and putting it back on the plane at a different position. This is illustrated in Figure 2.5. Furthermore, the integer number characterizing an

insulating Hamiltonian is dubbed a topological invariant, or adiabatic invariant, if it cannot change under adiabatic deformations. With this respect, two insulating Hamiltonians are said to be adiabatically equivalent or adiabatically connected if there is an adiabatic deformation connecting them, that respects the important symmetries. For example, in the phase diagram of the SSH model in Figure 2.6, the two Hamiltonians corresponding to the two black points in the topological phase ($w > v$) are adiabatically connected, as one can draw a path between them which does not cross the gapless topological-trivial phase boundary ($w = v$). Interestingly, thanks to the bulk-boundary correspondence, the winding number ν, which is derived from the bulk Hamiltonian, is in one to one relation with the net number of edge states [88].

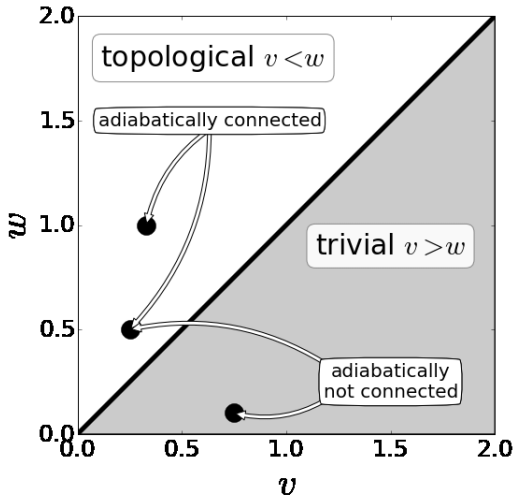

Figure 2.6: Phase diagram of the SSH model. The winding number of the bulk momentum-space Hamiltonian $H(k)$ can be $\nu = 0$ if $v > w$, or $\nu = 1$ if $v < w$. This defines the trivial (gray) and the topological phase (white). Two Hamiltonians in the same phase are said to be adiabatically connected. Figure based on [88].

2.3 Rashba spin-orbit coupled wire

The focus of this Section is on one dimensional spin-orbit coupled (SOC) systems in the presence of an external magnetic field. These systems triggered theoretical research since they allow to experimentally engineer quasi-helical liquids [90–92], which in turns approximately exhibit the so-called spin-momentum locking: fermions with opposite spin travel in opposite directions. In crystalline structures an effective magnetic field can be experienced by electrons when they move in inhomogeneous electric fields. In this scenario, the crystalline potential and all the contributions due to confinement, impurities or external electric fields could provide such a phenomenon. The effective magnetic field $\boldsymbol{B}_{\text{eff}}$, therefore, couples to the particle magnetic momentum $\boldsymbol{m}$ giving rise to the spin-orbit coupling, described by the Hamiltonian

$$H_{\text{R}} \sim \boldsymbol{m} \cdot \boldsymbol{B}_{\text{eff}}, \tag{2.14}$$

which takes its name by Rashba and his coworkers [93]. For the purposes of the present Thesis, we now focus on the 1D case. Here, the Rashba contribution to the Hamiltonian is [91, 94]

$$H_{\text{R}} = k_x \boldsymbol{\sigma} \cdot \boldsymbol{\eta}_{\text{SO}}, \tag{2.15}$$

with k_x the component of the momentum along the wire direction, x, and $\boldsymbol{\eta}_{\text{SO}}$ a vector lying in the $y-z$ plane which fully characterizes the SOC interaction. For the sake of simplicity, we assume $\boldsymbol{\eta}_{\text{SO}}$ to be along the z axis, which we also choose as the spin quantization axis. The most intriguing features of the model emerge when an external magnetic field $\mathcal{B}$ is applied in a direction orthogonal to B_{eff} , for example along the wire direction, as shown in Figure 2.7.

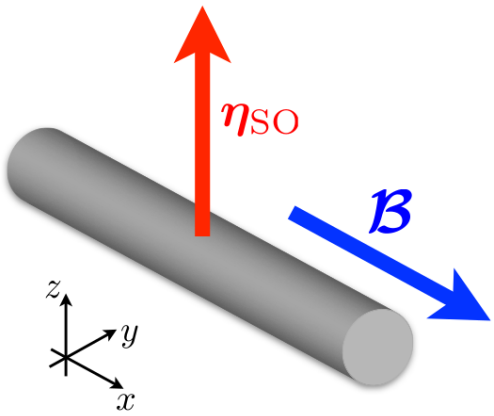

Figure 2.7: Spin-orbit coupled quantum wire with spin-orbit interaction characterized by the vector $\boldsymbol{\eta}_{\text{SO}}$ along the quantization axis z and subject to an external magnetic field parallel to the wire and orthogonal to $\boldsymbol{\eta}_{\text{SO}}$.

The single-particle Hamiltonian describing the model is thus

$$H_{\text{SOC}} = \frac{k_x^2}{2m^*} + \frac{1}{2} g \mu_B \mathcal{B} \sigma_x - \eta_{\text{SO}} k_x \sigma_z, \tag{2.16}$$

where m^* is the particle effective mass, g is the electron g-factor and μ_B is the Bohr magneton.

In order to make our discussion more general, it is useful to introduce a typical length scale of the system, ℓ , which can be for instance the length of the system, and work with a dimensionless version of the above Hamiltonian,

$$H_{\rm SOC} = k^2 + B\sigma_x - \alpha k_x \sigma_z. \tag{2.17}$$

Here, k is dimensionless, energy is measured in units of $\epsilon_0 = 1/(2m\ell^2)$ and we have introduced the parameters

$$B = \frac{g\mu_B \mathcal{B}}{2\epsilon_0}, \qquad \alpha = \frac{\eta_{\rm SO}}{\epsilon_0 \ell}. \tag{2.18}$$

The energy bands of the system are

$$\varepsilon_{\pm,k} = k^2 \pm \sqrt{\alpha^2 k^2 + B^2}, \tag{2.19}$$

and their behavior is shown in Figure 2.8 as a function of different values of the external magnetic field B.

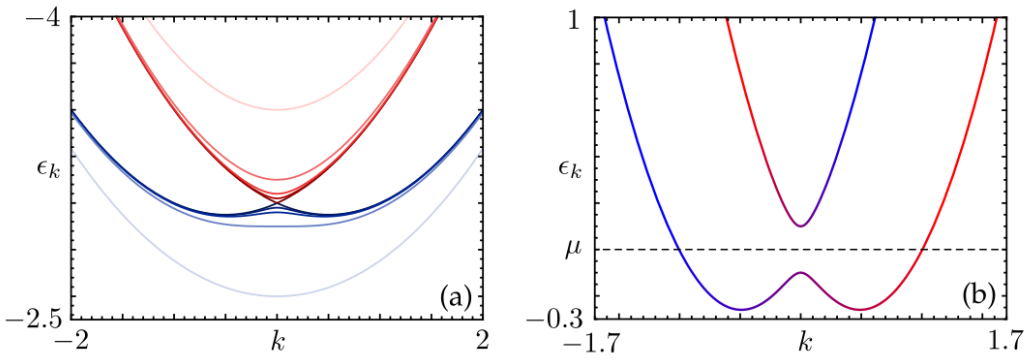

Figure 2.8: (a): Valence (blue curves) and conduction (red curves) energy bands $\varepsilon_{\pm,k}$ of the single-particle Hamiltonian of Eq. 2.19, for different values of the external magnetic field B. (b): Spin-resolved energy bands $\varepsilon_{\pm,k}$, red is associated with spin up electrons while blue to spin down ones. The chemical potential μ is set inside the Zeeman energy gap.

In particular, for $B < \alpha^2/2$ the lower band $\varepsilon_{-,k}$ has a "mexican hat" shape (with two minima at $k = \pm\sqrt{k_{\rm SO}^2 - B^2/\alpha^2}$ and one local maximum at $k = 0$), while for $B > \alpha^2/2$ it exhibits a single minimum at $k = 0$. This is due to the interplay between the SOC interaction, which shifts the two spin degenerate subbands by $k_{\rm SO} = \alpha/2$ in opposite directions (to the left for spin down fermions and to the right for spin up ones) and the magnetic field, which opens a Zeeman gap $\Delta = 2B$ in the single-particle spectrum at $k = 0$.

In the presence of finite magnetic field the two bands have no definite spin polarization, i.e. spin is no more a good quantum number. This can be clearly seen by investigating the expectation value of the spin projections along the x, y, and z directions. It can be shown that for example in the valence band these functions assume the following

form

$$\langle S_x \rangle_{-,k} = \frac{1}{2} \frac{B}{\sqrt{\alpha^2 k^2 + B^2}}, \tag{2.20a}$$

$$\langle S_y \rangle_{-,k} = 0, \tag{2.20b}$$

$$\langle S_z \rangle_{-,k} = \frac{1}{2} \frac{\alpha k}{\sqrt{\alpha^2 k^2 + B^2}}. \tag{2.20c}$$

Their behavior is shown in Figure 2.9. In particular, the spin polarization of the lower band rotates counter-clockwise from the $k > 0$ region to the $k < 0$ one. With similar steps it is possible to show that the opposite holds for the upper band, i.e. here the spin polarization rotates clockwise from $k > 0$ to $k < 0$. This can be seen also in panel (b) of Figure 2.8. It is now clear why SOC wires allow for the realization of quasi-helical liquids: For not too strong magnetic fields, if one sets the chemical potential inside the gap at $k = 0$, the system possesses only two conducting channels, one associated with right-moving electrons with (almost) spin up and the other to left-moving electrons with (almost) spin down.

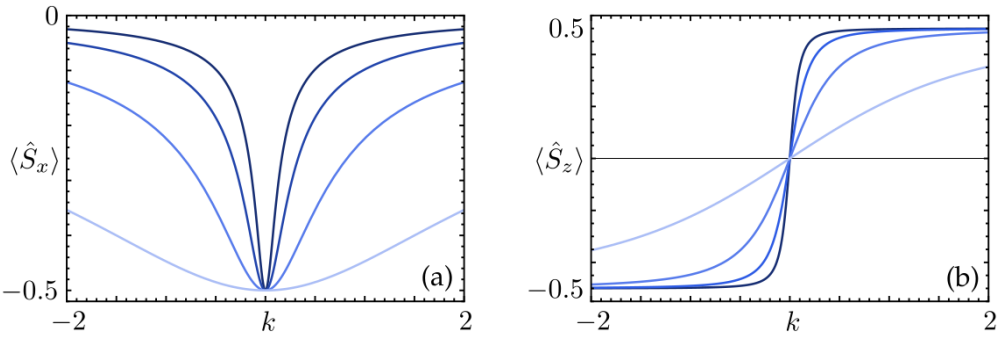

Figure 2.9: In Panel (a) is plotted $\langle S_x \rangle_{-,k}$ for different values of the magnetic field B: For darker to lighter blue $B = 0.1, B = 0.2, B = 0.5,$ and $B = 2$. In Panel (b) is reported the same as in Panel (a) but for $\langle S_z \rangle_{-,k}$.

2.4 XY model

The one-dimensional XY model in a transverse magnetic field is one of the simplest non-trivial integrable model. Because of this, it has been extensively studied and used to capture the universal behavior of low dimensional systems. This interest is justified in part by analytical tractability and in part by the possibility to implement it using optical lattices and cold Fermi gases [95–97]. It has a rich two dimensional phase diagram characterized, at zero temperature, by two QPTs: one belonging to the universality class of the XX model and the other is the phase transition of the One-Dimensional Quantum Ising model.

The Hamiltonian of the XY model can be written as [98–100]

$$H_{\mathrm{XY}} = J \sum_{j=1}^{N} \left[\left(\frac{1+\gamma}{2} \right) \sigma_j^x \sigma_{j+1}^x + \left(\frac{1-\gamma}{2} \right) \sigma_j^y \sigma_{j+1}^y - h\sigma_j^z \right], \tag{2.21}$$

where σ_j^i with $i = x, y, z$ are the Pauli matrices which describe spin operators on the j-th lattice site of the spin chain, γ is the anisotropy parameter and h is an external magnetic field. We take these parameters to be dimensionless and from now on we set the energy-scale defining parameter $J = -1$ (focusing hence on the anti-ferromagnetic case). Since the model is symmetric under both the transformations $h \to -h$ and $\gamma \to -\gamma$, we will concentrate only on the portion of the phase diagram where $\gamma \geq 0$ and $h \geq 0$. We will find two Quantum Phase Transitions (QPT). These QPTs identify two different universality classes which are located on the line $\gamma = 0$, the isotropy line, and at the critical magnetic field $h = 1$. The last transition is identified as the Ising transition, from a doubly degenerate ground state (for $h < 1$) to a single ground state system (for $h > 1$). The corresponding order parameter is the magnetization along the x-axis.

In order to get a deeper insight into the Hamiltonian in Eq. (2.21), it is possible to map the H_{XY} spins onto spinless fermions by means of a Jordan-Wigner transformation. In details

$$\sigma_j^+ = \prod_{l=1}^{j-1} \left(1 - 2\psi_l^\dagger \psi_l \right) \psi_j, \tag{2.22a}$$

$$\sigma_j^- = \prod_{l=1}^{j-1} \left(1 - 2\psi_l^\dagger \psi_l \right) \psi_j^\dagger, \tag{2.22b}$$

$$\sigma_j^z = 1 - 2\psi_j^\dagger \psi_j, \tag{2.22c}$$

where $\psi_j^\dagger$ creates a spinless fermion on the site j and $\sigma_j^\pm = (\sigma_j^x \pm i\sigma_j^y)/2$.
We observe that for non-vanishing anisotropy parameter γ, H_{XY} conserves the particle number parity even though their number is not conserved. As a consequence, it is convenient to separate the Hamiltonian into two disconnected sectors

$$H_{\mathrm{XY}} = \frac{1+\mu_N}{2} H^+ + \frac{1-\mu_N}{2} H^-, \tag{2.23}$$

where

$$\mu_N = \prod_{j=1}^{N} \left(1 - 2\psi_j^\dagger \psi_j\right) = \prod_{j=1}^{N} \sigma_j^z = \pm 1. \tag{2.24}$$

The plus sign characterizes configurations with an even number of particles and the minus sign the one with an odd number of them. Imposing periodic boundary conditions $\sigma_{j+N}^\alpha = \sigma_j^\alpha$ $(\alpha = x, y, z)$ on the spin operators implies that we have to impose anti-periodic boundary conditions for the even sector, such that

$$\psi_{j+N} = -\psi_j \qquad \text{for } \mu_N = +1, \tag{2.25}$$

and periodic boundary conditions for the odd sector, such that

$$\psi_{j+N} = \psi_j \qquad \text{for } \mu_N = -1. \tag{2.26}$$

Consequently, the two parity-defined Hamiltonians in Eq. (2.23) can be both written in the compact form

$$H^\pm = -\frac{1}{2}\sum_{j=1}^{N}\left[\psi_j^\dagger\psi_{j+1} + \psi_{j+1}^\dagger\psi_j + \gamma\psi_j^\dagger\psi_{j+1}^\dagger + \gamma\psi_{j+1}\psi_j - 2h\psi_j^\dagger\psi_j\right] - \frac{hN}{2}. \tag{2.27}$$

The model is therefore mapped into two spinless theories, described by the same Hamiltonian but with different boundary conditions and Fock spaces. In order to diagonalize the fermionic Hamiltonian, it is convenient to pass into the Fourier space. Necessarily, we have to consider the two sectors separately. However, for the aim of this thesis, we will only focus on the case of a even number of particles [1].
Performing an anti-periodic asymmetric Fourier transform, we obtain

$$H^+ = \frac{1}{2N}\sum_{q=0}^{N-1}\left(\psi_q^\dagger, \psi_{-q}\right)\begin{pmatrix} h - \cos q & -\gamma\sin q \\ -\gamma\sin q & \cos q - h \end{pmatrix}\begin{pmatrix} \psi_q \\ \psi_{-q}^\dagger \end{pmatrix} - \frac{hN}{2} \tag{2.28}$$

where $q = \frac{2\pi}{N}(n + 1/2)$ and $n = 0, ..., N-1$. The next step is to apply a Bogoliubov rotation to each of the momenta involved, i.e.

$$\begin{pmatrix} \psi_q \\ \psi_{-q}^\dagger \end{pmatrix} = \begin{pmatrix} \cos\theta_q & \sin\theta_q \\ -\sin\theta_q & \cos\theta_q \end{pmatrix}\begin{pmatrix} \chi_q \\ \chi_{-q}^\dagger \end{pmatrix}, \tag{2.29}$$

where the Bogoliubov angle is found to be $\tan\theta_q = \dfrac{\gamma\sin q}{h - \cos q}$. With this definition, the Hamiltonian can be written in terms of fermionic Bogoliubov quasi-particles,

$$H^+ = \frac{1}{N}\sum_{q=0}^{N-1}\varepsilon(q)\left(\chi_q^\dagger\chi_q - \frac{N}{2}\right) \tag{2.30}$$

and describes free fermions with an energy spectrum given by

$$\varepsilon(q) = \sqrt{(h - \cos q)^2 + \gamma^2\sin^2 q}. \tag{2.31}$$

[1] For a complete derivation, see [101].

We are at this point able to locate the two different QPTs previously mentioned, since they are identified as the points in the (γ, h) plane where the minimum of the dispersion relation in Eq. (2.31) is zero. Indeed, these gapless points are characterized by a scale-invariant behavior [101].

As a last remark, we emphasize that since the energy spectrum is always positive, the ground state of the Hamiltonian within the even number of particles sector is defined by

$$\chi_q \left|GS\right\rangle_+ = 0, \qquad \forall q, \tag{2.32}$$

i.e. is the state devoid of Bogoliubov quasi-particles. From the point of view of physical fermions, it can be shown that the ground state takes the form

$$\left|GS\right\rangle_+ = \prod_q \left[\cos\theta_q + \frac{1}{N}\sin\theta_q \psi_q^\dagger \psi_{-q}^\dagger\right] \left|0\right\rangle \tag{2.33}$$

where $\left|0\right\rangle$ represents the vacuum state.

CHAPTER 3

Non-monotonic response and light-cone freezing in fermionic systems

In this Chapter, we present our original findings published in [14].
The details of the calculations, not shown here, are reported in Appendix A.

Nonequilibrium quantum physics is at the heart of most relevant applications of solid-state physics, such as transistors and lasers [102–104]. More fundamentally, one of the main difficulties in studying many-body nonequilibrium quantum physics is represented by the unavoidable interactions that any quantum system has with its surroundings. This coupling is difficult to control and causes an effectively nonunitary evolution, even on short time scales [105]. The recent advent of cold atom physics [106, 107] has allowed not only the access of quantum systems characterized by weak coupling to the environment, but also the engineering of Hamiltonians which show nonergodic behavior [43, 108], the so-called integrable systems [109]. Moreover, in the context of cold atom physics, it is possible to manipulate the parameters of the Hamiltonian in a time-dependent and controllable fashion. The combination of these three ingredients resulted in a renewed interest in the physics of quantum quenches. To characterize the peculiar out of equilibrium steady states that such quenched systems sometimes exhibit, the novel and powerful tool of the Generalized Gibbs Ensembre (GGE) has been theoretically put forward and successfully applied in several different contexts such as interaction quenches in Luttinger liquids [18, 19, 110] and magnetic field quenches in the one-dimensional (1D) Ising model [111, 112]. These are prominent examples in this direction. Furthermore, at the level of free fermions, quantum quenches between gapped phases characterized by different Chern numbers have also been studied [113]. However, not much attention has been devoted to the study of quantum quenches between gapless and gapped states. Indeed, the characterization of the main features of gapless-to-gapped quantum quenches is still lacking. In this chapter we consider paradigmatic examples of gapless 1D systems which get partially or completely gapped by a change in the parameters of the Hamiltonian. Namely, a spin-orbit coupled (SOC) quantum wire

in the presence of an applied magnetic field and a chain of spinless 1D fermions. For the latter, the gapping quench mechanism is either induced by a staggered potential (SP) or by the sudden switch-on of fermion-fermion interactions.

3.1 Quench from gapless to gapped states

In this section we show in detail the quench protocol for the different models under study. In particular, following the notations introduced in Chapter 2, we consider first a sudden variation of the Hamiltonian parameter Δ tuning the amplitude of the gap in the energy spectrum. This is done for both lattice and continuum models, to show the generality of our results. The starting point, is the gapless ground state where a crossing of the energy levels of the Hamiltonian $H(t<0)$ takes place: The time-dependent Hamiltonian H can then be written as

$$H(t) = \sum_k \Psi_k^\dagger [\mathcal{H}_k + \theta(t)\Delta\sigma^x]\Psi_k, \tag{3.1}$$

where $\mathcal{H}_k$ is a family of 2×2 matrices indexed by the (quasi-) momentum k. Here, σ^x is the first Pauli matrix in the usual representation, Δ is the strength of the gap opening mechanism and $\theta(t)$ is the Heaviside function. Finally, $\Psi_k^\dagger = (d_{a,k}^\dagger, d_{b,k}^\dagger)$ is a two-component momentum resolved Fermi spinor.
In the case of the SOC wire, the indexes a, b represent the spin projection along the quantization axis and Δ is proportional to the applied magnetic field. In the case of the SP model, the former labels left- and right-movers while Δ is proportional to the strength of the staggered potential.

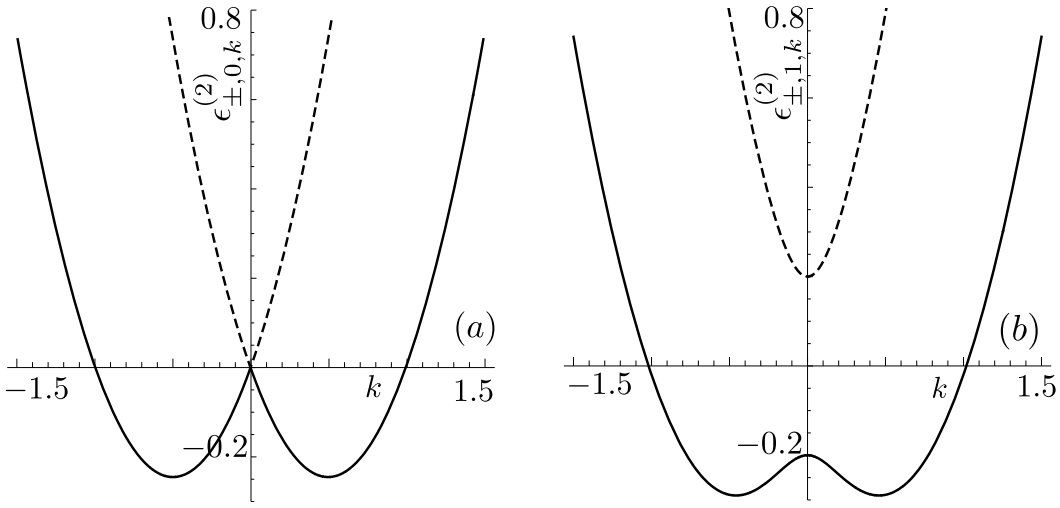

Figure 3.1: (a) Dispersion relation of the continuum theory for the SOC quantum wire in the absence of applied magnetic fields, for $\alpha = 1$. (b) Dispersion relation for the SOC quantum wire with $\alpha = 1$ and $B = 0.2$.

To clarify the notation, we introduce the index $i = 1, 2, 3, 4$, which represents respectively the 4 non-interacting models.
For the SOC quantum wire on the lattice we have

$$\mathcal{H}_k^{(1)} = 2[1-\cos(k)]\sigma^0 + \alpha\sin(k)\sigma^z \tag{3.2}$$

with $\sigma^0 = I_{2\times 2}$ and the gap opening time-dependent mechanism is given by the magnetic field $\Delta^{(1)} = B$, which represents its component along the x-direction perpendicular to the wire. Here, the lattice constant has been set to 1 and α represents the spin-orbit coupling. The corresponding low-energy continuous theory is obtained by replacing $\mathcal{H}_k^{(1)}$ with

$$\mathcal{H}_k^{(2)} = k^2\sigma^0 + \alpha k\sigma^z, \tag{3.3}$$

with gap opening parameter $\Delta^{(2)} = B$. This approximation has been obtained by expanding around the momentum point where the bands cross, namely $k = 0$.

We also discuss the SP model, with

$$\mathcal{H}_k^{(3)} = -2J\cos(k)\sigma^z \tag{3.4}$$

and $\Delta^{(3)}$ the strength of the staggered potential. In this case, k is restricted to positive values only, because of the spinor representation of the Hamiltonian due to the introduction of a two-site unit cell into the lattice. To obtain a low-energy theory for the SP model we expand around $k = \pi/2$, obtaining a Dirac cone with velocity $2J$ with a gap opening term $\Delta^{(4)} = \Delta^{(3)}$. The Hamiltonian density is, in this case,

$$\mathcal{H}_k^{(4)} = -2Jk\sigma^z. \tag{3.5}$$

From the dispersion relation point of view, the main differences between the two models are related to the gap shape, since while for the SP model the instantaneous energy spectrum is fully gapped for $t > 0$, for the SOC wire it is partially-gapped. The avoided-crossing, indeed, appears only around $k = 0$, leaving substantially unaffected the Brillouin zone edges. These features are shown in Figure 3.1 for the continuum models.

As mentioned, we assume that, before the quench, the chemical potential is set to zero and the system is in its zero-temperature equilibrium ground state. We define $|\Phi_0^{(i)}(0)\rangle$ as the system ground state at $t = 0$ of the corresponding pre-quench Hamiltonian. We introduce the unitary transformation $U_{0,k}^{(i)}$ resulting in a conduction/valence band representation of the diagonalized pre-quench Hamiltonian satisfying

$$U_{0,k}^{(i)}\mathcal{H}_k^{(i)}U_{0,k}^{(i)\dagger} = \begin{bmatrix} \epsilon_{+,0,k}^{(i)} & 0 \\ 0 & \epsilon_{-,0,k}^{(i)} \end{bmatrix}, \tag{3.6}$$

with $\epsilon_{-,0,k}^{(i)} \leq \epsilon_{+,0,k}^{(i)}$, $\forall k$. This transformation is particularly useful to write in a simple form the ground state, which reads

$$|\Phi_0^{(i)}(0)\rangle = \prod_{k_1^{(i)}}^{k_2^{(i)}} \left(U_{0,k}^{(i)\dagger}\Psi_k^{(i)\dagger}\right)_2 |0^{(i)}\rangle, \tag{3.7}$$

Here, $|0^{(i)}\rangle$ is the vacuum of the $i-$th Hamiltonian, $k_{1/2}^{(i)}$ are fixed by the condition that only states with negative and zero energy are occupied, and the subscript 2

means that the second component of the spinor has to be considered: Only states in the valence band will be filled. Note that the choice of the occupation of the zero energy modes is of no importance for the following. All results, indeed, will be evaluated in the thermodynamic limit.
The values of the $k_{1/2}^{(i)}$ can be calculated exactly, to find:

	$i=1$	$i=2$	$i=3$	$i=4$
$k_1^{(i)}$	$-2\arctan(\alpha/2)$	$-\alpha$	0	0
$k_2^{(i)}$	$2\arctan(\alpha/2)$	α	π	π

Note that in order to mimic the finite energy range, we have set the summation range between 0 and π also in the low-energy expansion of the SP model, using therefore a box-like cutoff in the momentum space.

In order to get the time evolution of the system for $t > 0$, we introduce a second unitary operator $U_{1,k}^{(i)}$ related to the post-quench Hamiltonian, analogously to the pre-quench case, given by

$$U_{1,k}^{(i)}[\mathcal{H}_k^{(i)} + \Delta^{(i)}\sigma^x]U_{1,k}^{(i)\dagger} = \begin{bmatrix} \epsilon_{+,1,k}^{(i)} & 0 \\ 0 & \epsilon_{-,1,k}^{(i)} \end{bmatrix}, \tag{3.8}$$

with $\epsilon_{-,1,k}^{(i)} \leq \epsilon_{+,1,k}^{(i)}$, $\forall k$. In the Heisenberg representation, the time evolution of the systems is thus encoded in the Fermi spinor

$$\Psi_k^{(i)}(t) = U_{1,k}^{(i)\dagger} \begin{bmatrix} e^{-i\epsilon_{+,1,k}^{(i)}t} & 0 \\ 0 & e^{-i\epsilon_{-,1,k}^{(i)}t} \end{bmatrix} U_{1,k}^{(i)}\Psi_k^{(i)}(0) \ . \tag{3.9}$$

We are now able to prove that, long after the quench, each of the four systems under investigation reaches a steady state which is locally described by a GGE (see Chapter 1.1). The latter is constructed by considering the set of the occupation numbers $n_{k,j=1,2}^{(i)}$ of the energy levels of the post-quench Hamiltonians, given by

$$n_{k,j=1,2}^{(i)} = \left(\Psi_k^{(i)\dagger}U_{1,k}^{(i)\dagger}\right)_j \left(U_{1,k}^{(i)}\Psi_k^{(i)}\right)_j . \tag{3.10}$$

Here, the subscript j on the right-hand side means that the j-th component of the spinor must be considered. The GGE density matrices are given by

$$\rho^{(i)} = \frac{e^{-\sum_{k,j}\lambda_{k,j}n_{k,j}^{(i)}}}{\mathrm{Tr}\left\{e^{-\sum_{k,j}\lambda_{k,j}n_{k,j}^{(i)}}\right\}}. \tag{3.11}$$

The Lagrange multipliers $\lambda_{k,j}$ are fixed by the condition

$$\langle\Phi_0^{(i)}(0)|n_{k,j}^{(i)}|\Phi_0^{(i)}(0)\rangle = \mathrm{Tr}\left\{n_{k,j}^{(i)}\rho^{(i)}\right\} \doteq \langle n_{k,j}^{(i)}\rangle_{\mathrm{GGE}} , \tag{3.12}$$

which also defines the average by means of the generalized Gibbs Ensemble.

3.2 Observable non-monotonic behavior

We are now able to calculate the observables of interest in the different models introduced. In particular, in this section, we focus on their expectation value in the long time and thermodynamic limit, where they equilibrate to a non-thermal steady state described by the GGE. With this respect, we choose the most direct manifestation in the system of the parameter we are manipulating. We consider, therefore, the following quantity

$$M^{(i)} = \sum_k \langle \Psi_k^{(i)\dagger} \sigma^x \Psi_k^{(i)} \rangle_{GGE} / n^{(i)}, \tag{3.13}$$

with $n^{(i)}$ the total number of particles in the $i-$th system, which represents the magnetization along the direction of the applied magnetic field in the case of the SOC wire, while, for the SP model, it gives the amount of staggered magnetization, a concept borrowed from the anti-ferromagnetic scenario. All quantities can be evaluated analytically, and the resulting expressions can be found in the Appendix A.3.

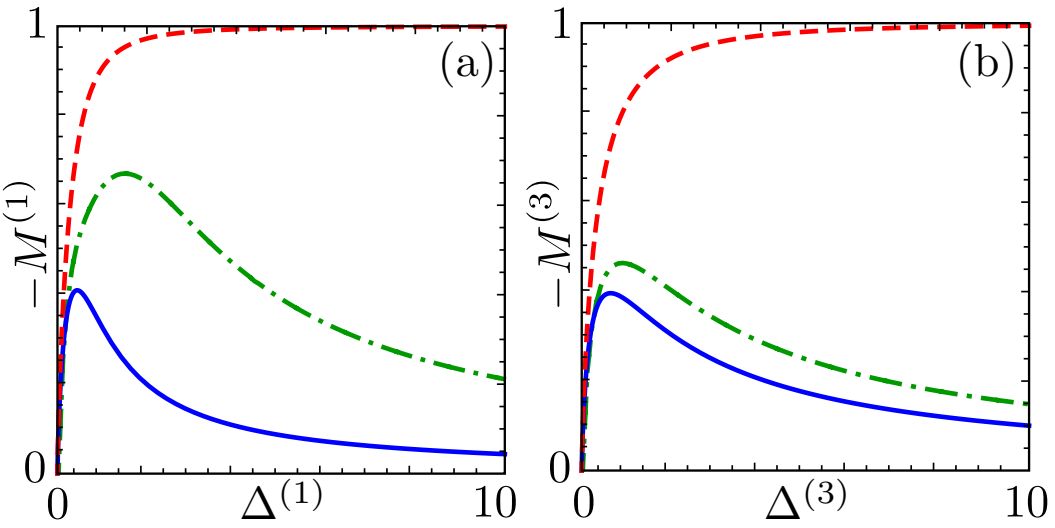

Figure 3.2: (*a*) $M^{(1)}$ for the lattice SOC wire as a function of $\Delta^{(1)}$ with $\alpha = 1$; (*b*) $M^{(3)}$ for the lattice SP model as a function of $\Delta^{(3)}$ and $J = 1$. In both panels, the blue solid lines represent the quenched long-time limit, the red dashed lines show the equilibrium magnetization of the post-quench Hamiltonian and the green dash-dotted lines represent the results evaluated with an effective thermal model (see text).

Interestingly, all these quantities exhibit a maximum for a finite value of Δ and tend to the gapless value for $\Delta \to \infty$, meaning that the stronger is the quench intensity, the less observables are affected by the quench itself, and in the limit of infinite intensity, magnetization does not feel the switching-on of the external field at all. The results are shown by blue solid lines in Figures 3.2 and 3.3, as $\Delta^{(i)}$ is increased. In all cases, $M^{(i)}$ is non-monotonous, increasing up to a maximum before

dropping to the pre-quench value. A qualitative interpretation of the phenomenon is the following: For infinitesimal $\Delta^{(i)}$ we do not expect any difference between a sudden quench and an adiabatic switching on of the gap opening mechanism. Thus, since in the latter case the magnetization equals the one associated with the equilibrium regime of the post-quench Hamiltonian, the systems begin to magnetize. On the other hand, for $\Delta^{(i)}$ strongly dominating the kinetic energy, $M^{(i)}$ is conserved and hence it remains at the value characterizing the pre-quench ground state. A maximum for finite $\Delta^{(i)}$ is thus expected.

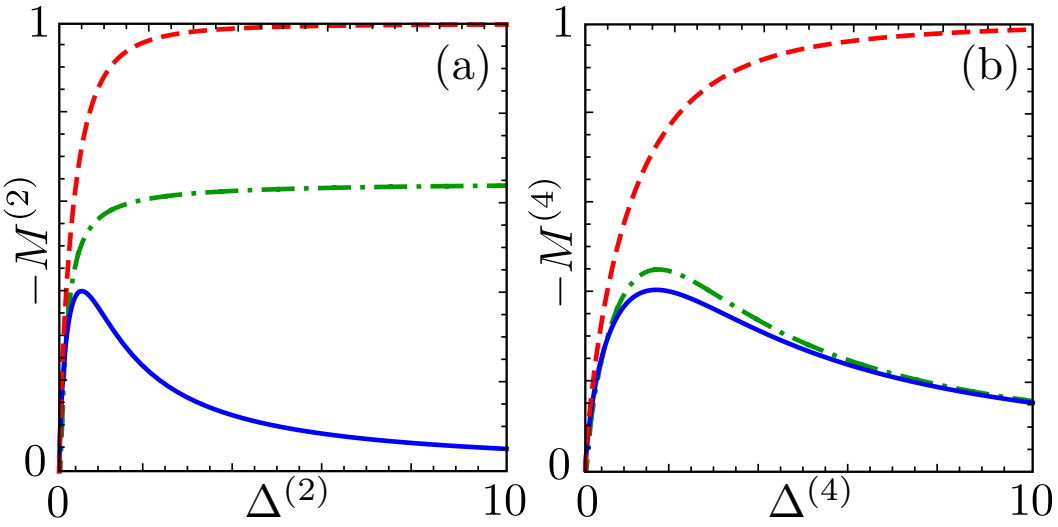

Figure 3.3: (*a*) $M^{(2)}$ for the continuum SOC wire as a function of $\Delta^{(2)}$ with $\alpha = 1$; (*b*) $M^{(4)}$ for the continuum SP model as a function of $\Delta^{(4)}$ and $J = 1$. In both panels, the blue solid lines represent the quenched long-time limit, the red dashed lines show the equilibrium magnetization of the post-quench Hamiltonian and the green dash-dotted lines represent the results evaluated with an effective thermal model (see text).

These results are in sharp contrast to the equilibrium zero-temperature scenario: Here, see red dashed lines in Figures 3.2 and 3.3, $M^{(i)}$ is monotonous and increases to its saturation value for $\Delta^{(i)} \to \infty$ when the average is taken with respect to the ground state of the post-quench Hamiltonian, as one could expect.

A better and more involved physical comparison is shown by the green dash-dotted lines in Figures 3.2 and 3.3. Since the quench necessarily inject energy into the system, it has been conjectured that the key features of observables in the pre-thermal steady state can be captured by an effective temperature description [111]. This temperature, which we denote as T_{eff}, is obtained by evaluating the energy of the initial state after the quench, and comparing it to a thermal ensemble average in equilibrium at T_{eff}. In particular, to do so, we have to numerically solve the equation

$$\langle \Phi_0^{(i)}(0)|H_{pq}^{(i)}|\Phi_0^{(i)}(0)\rangle = \frac{\mathrm{Tr}\left\{e^{-\beta_{\text{eff}}(\Delta^{(i)})[H_{pq}^{(i)}-\mu(\Delta^{(i)})n^{(i)}]}H_{pq}^{(i)}\right\}}{\mathrm{Tr}\left\{e^{-\beta_{\text{eff}}(\Delta^{(i)})[H_{pq}^{(i)}-\mu(\Delta^{(i)})n^{(i)}]}\right\}}, \tag{3.14}$$

for the inverse effective temperature $\beta_{\text{eff}}(\Delta^{(i)})$. Here, $H^{(i)}_{pq} = H^{(i)}(t > 0)$ is the post-quench Hamiltonian and $\mu(\Delta^{(i)})$ is the Lagrange multiplier associated to particle number conservation. The evaluation of the r.h.s. of Eq. (3.14) returns

$$\frac{n^{(i)}}{2\pi} \int_{-\bar{k}^{(i)}}^{\bar{k}^{(i)}} \left[\epsilon^{(i)}_{+,1,k} f^{(i)}_{+,k}(\beta_{\text{eff}}) + \epsilon^{(i)}_{-,1,k} f^{(i)}_{-,k}(\beta_{\text{eff}}) \right] dk, \tag{3.15}$$

where

$$f^{(i)}_{\pm,k}(\beta_{\text{eff}}) = \frac{1}{1 + e^{\beta_{\text{eff}}(\Delta^{(i)})[\epsilon^{(i)}_{\pm,0,k} - \mu(\Delta^{(i)})]}} \tag{3.16}$$

is the Fermi distribution and and $\bar{k}^{(i)} = \begin{cases} \pi & \text{if } i = 1,3 \\ \infty & \text{if } i = 2,4 \end{cases}$.

While for the SP model there is a good qualitative agreement, for the continuum version of the SOC wire the disagreement is dramatic as the effective-temperature magnetization saturates to a nonzero value and is monotonic. The mechanism behind the nonmonotonous behavior of $M^{(i)}$, hence, cannot be an effective heating induced by the manipulation of the external field.

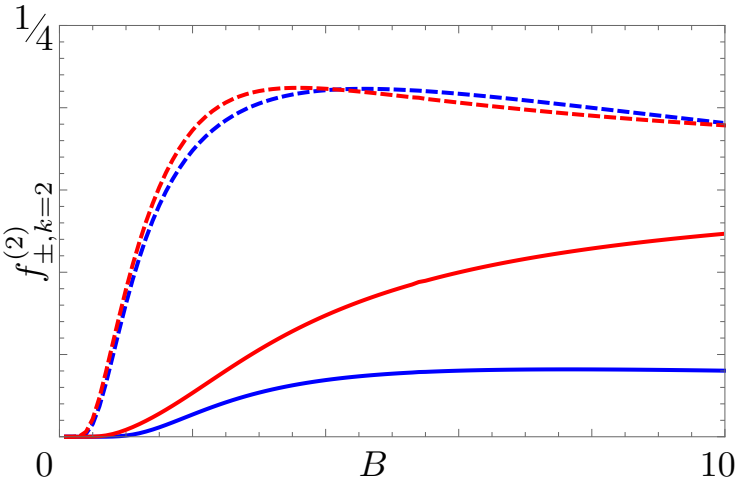

Figure 3.4: Thermal occupation numbers of conduction (dashed lines) and valence (solid lines) bands as a function of the magnetic field B, with $\alpha = 1$ and $k = 2$. The red curves represent the lattice SOC wire, while the blue curves the continuum SOC wire.

This unexpected behavior can be related to the thermal occupation numbers of valence and conduction bands, by a careful observation of their features as a function of the external magnetic field for the particularly interesting case of the SOC wire, shown in Figure 3.4. Assuming high values of the magnetic field the conduction and valence bands become quasi-spin polarized in the x-direction. We observe, in the continuum model, that the valence band is always much more populated compared to the conduction one. Also states with large momentum k, which are never involved during the quench, contribute to the magnetization. This leads to

a non-zero magnetization for large B. On the contrary, in the lattice model, k is constrained in the interval $[-\pi, \pi)$. Therefore, once the valence band is full, the only available states are the ones in conduction band: Increasing B results in an increasing of the number of occupied states in the conduction band, and then in a vanishing magnetization when $f_{+,k} \simeq f_{-,k}$.

3.2.1 Robustness in higher dimensions and for finite time quenches

To further support the idea that this mechanism is robust and represents a generic feature, we have checked that the results showed are valid even with respect to the rapidity of the quench. We have studied the continuum SOC wire model when the magnetic field linearly ramps from 0 to a finite value. The results are plotted in Figure 3.5 (a): For longer ramps, the asymptotic value of $M^{(2)}$ for large $\Delta^{(2)}$ increases, but the non-monotonous behaviour of the magnetization persists.

The results are robust even in higher dimensions. We have considered the paradigmatic case of a quench of a magnetic field applied to a Rashba-coupled two-dimensional electron gas [114], whose Hamiltonian reads

$$H_{2D}(t) = \sum_{k_x,k_y} \Psi^\dagger_{k_x,k_y}[(k_x^2 + k_y^2)I_{2\times 2} + \alpha(\sigma^x k_y - \sigma^y k_x) + \theta(t)B\sigma^z]\Psi_{k_x,k_y}. \quad (3.17)$$

Here, k_x and k_y are the two components of the momentum vector $\boldsymbol{k}$, while $\Psi^\dagger_{k_x,k_y}$ is the two-component fermionic spinor for spin up and down electrons. Also in this case, the long-time magnetization shows a non-monotonous behaviour as a function of the magnetic field, increasing to a maximum before eventually turning to the pre-quench value for large quenches, as shown in Figure 3.5 (b).

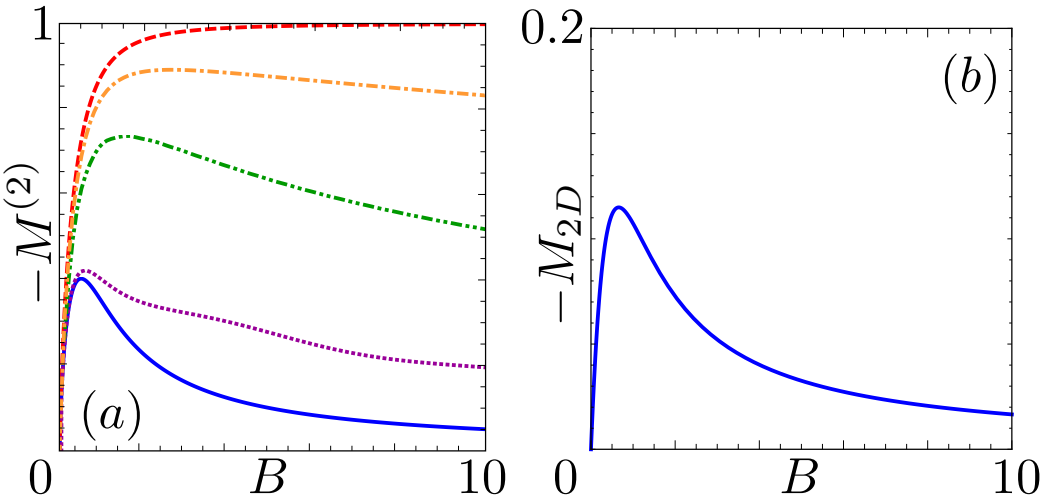

Figure 3.5: (a)Plot of $M^{(2)}$ for the lattice SOC wire as a function of $\Delta^{(1)} = B$ and $\alpha = 1$ for different quench protocols with increasingly long switch-on times τ: $\tau = 0$, sudden quench (blue, solid), $\tau = 1$ (purple, dot), $\tau = 10$ (green, dash-dot-dot), $\tau = 100$ (yellow, dash-dot), $\tau = \infty$ -corresponding to the equilibrium magnetization of the post-quench Hamiltonian red - (red, dash). (b) Plot of M_{2D} for the 2D Rashba-coupled electron gas as a function of B and $\alpha = 1$.

3.3 Klein-Gordon dynamics and light-cone freezing

To get a deeper understanding of the non-monotonic behavior of the observables, we now focus on the time-evolution which bring the system to the previously described non-thermal steady state. We consider the continuum models and introduce the Green's function

$$\mathcal{G}^{(i)}(x,t) = \langle \Phi_0^{(i)}(0)|\Psi^{(i)\dagger}(x,t)\sigma^x\Psi^{(i)}(0,t)|\Phi_0^{(i)}(0)\rangle, \tag{3.18}$$

which is the direct generalization of the magnetization, since $\mathcal{G}^{(i)}(0,t) = M^{(i)}(t)$. Starting from the Heisenberg equation of motion for the Fermi spinor $\Psi_k^{(i)}(t)$, it is possible to show that, in the case of a sudden quench, $\mathcal{G}^{(i)}(x,t)$ satisfies, for $t > 0$, an inhomogeneous KG equation

$$\left(\partial_x^2 - \frac{1}{4u_i^2}\partial_t^2\right)\mathcal{G}^{(i)}(x,t) = \lambda_i^2\mathcal{G}^{(i)}(x,t) + \lambda_i\phi_i(x)\,, \tag{3.19}$$

where $\lambda_i = \Delta^{(i)}/u_i$ (with $u_2 = \alpha$, $u_4 = J$) and the source term is

$$\phi_i(x) = i\partial_x\langle \Phi_0^{(i)}(0)|\Psi^{(i)\dagger}(x,0)\mathcal{M}^{(i)}\Psi^{(i)}(0,0)|\Phi_0^{(i)}(0)\rangle\,, \tag{3.20}$$

with $\mathcal{M}^{(2)} = \sigma^z$ and $\mathcal{M}^{(4)} = \sigma^y$ (see Appendix A.3 for the detailed derivation). Equation (3.19) is solved with the pre-quench boundary-value condition $\mathcal{G}^{(i)}(x,0) = 0$ and supports a steady-state solution for $t \to \infty$: It can indeed be explicitly checked that

$$\lim_{t\to\infty}\mathcal{G}^{(i)}(0,t) = M^{(i)}. \tag{3.21}$$

Therefore, analyzing the time evolution of $\mathcal{G}^{(i)}(x,t)$ can shed light on the dynamics leading to the non-monotonous magnetization. This is shown in Fig. 3.6 for the SOC wire model, in the case of (a) small quench $\Delta^{(2)} = 0.3$ and (b) large quench $\Delta^{(2)} = 2$.

For a small quench, $\mathcal{G}^{(2)}(x,t)$ exhibits the typical light-cone behavior discussed in Chapter 1 and the information of the quench is therefore able to propagate throughout the system. This leaves a finite "trail" in $x = 0$, which eventually results in a finite value of $M^{(2)}$ at large times. On the other hand, the response of $\mathcal{G}^{(2)}(x,t)$ to the "shock" induced by a large quench is dramatically different. Indeed, in this regime, $\mathcal{G}^{(2)}(x,t)$ is characterized by weakly damped and almost stationary oscillations both in space and in time, which strongly hinder the propagation of the information through the system and lead to both a slowdown and an overall suppression of the light cone. The Green's function $\mathcal{G}^{(2)}(x,t)$ oscillates around its pre-quench initial one and reaches in the long-time limit a value very close to the latter. This phenomenon can thus be interpreted as an effective freezing of the light cone. The same qualitative behavior is observed also for the continuum SP model (not shown). We thus attribute the emergence of the non-monotonous behavior of $M^{(i)}$ as a function of $\Delta^{(i)}$ to the competition between the propagating and freezing regimes.

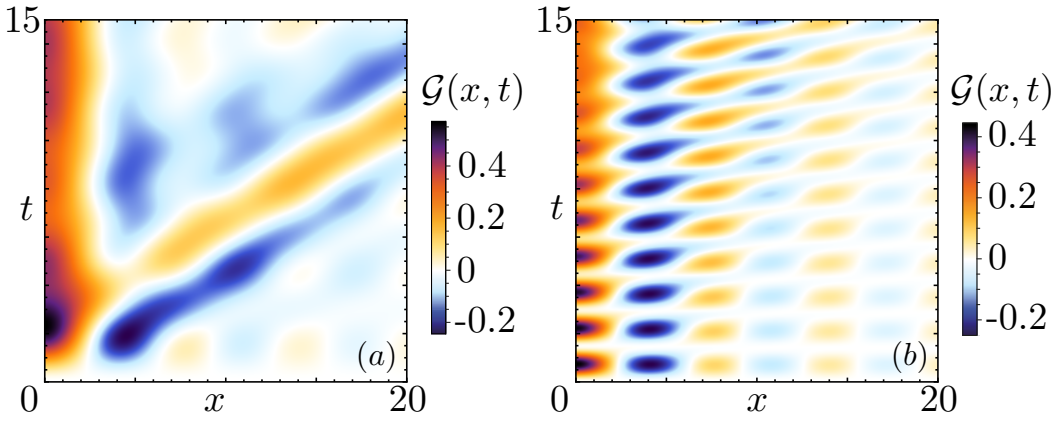

Figure 3.6: (a) Light-cone propagation regime: Density plot of $-\mathcal{G}^{(2)}(x,t)$ as a function of x and t for $\Delta^{(2)} = 0.3$ and $\alpha = 1$; (b) Light-cone freezing regime: Same as in (a) but for $\Delta^{(2)} = 2$ and $\alpha = 1$.
The Green's functions are both evaluated in the thermodynamic limit.

The identification of a freezing regime for large quenches constitutes a crucial result and - as we shall show in the last part of this chapter - is a quite universal and robust feature of gap-opening sudden quench models. It represents a new concept in the physics of quantum quenches: Even though the gap is not able to dynamically introduce a length scale in the correlation functions, it dramatically influences the light-cone propagation, eventually affecting the long time behavior of observables.

With the aim of proving the generality of the features of this phenomenon, and, in particular, to show that it is not in any case an effect due to the thermodynamic limit, we have performed simulations in a finite-size system with a small number of electrons. Figure 3.7 (a) shows the case of the quench of a small magnetic field, which represents the propagation regime. The light cone moves through the system bouncing, as expected, at its boundaries. The case of large magnetic fields, as in the infinite system, is dramatically different. Here, as it can be seen in panel (b), the light cone is frozen and does not propagate. This behavior has to be expected every time the quench-induced length scale becomes shorter than the size of the system. Thus, for a given system size, one can always expect, in general terms, a freezing regime for large enough quenching fields.

In order to get a picture of the effect, it is worth to notice that, in a simple mechanical interpretation [115], the KG equation given in Eq. (3.19) represents the transverse vibrations of a string driven by a force $\propto \lambda_i$, embedded into an elastic medium of elastic constant $\propto \lambda_i^2$. When the medium is slack, vibrations can propagate almost without disturbance, while in a stiff medium the wave propagation is strongly suppressed. The turning point turns out to be for $\lambda_i \sim 1$, which corresponds to the location of the maximum of $M^{(i)}$ shown in Figures 3.2 and 3.3. Therefore, when the gap becomes comparable to the average kinetic energy scale, the freezing of the light cone begins to occur. Thanks to Wick's theorem, a similar behaviour characterizes all higher order correlators. This issue is relevant, since some of those correlators

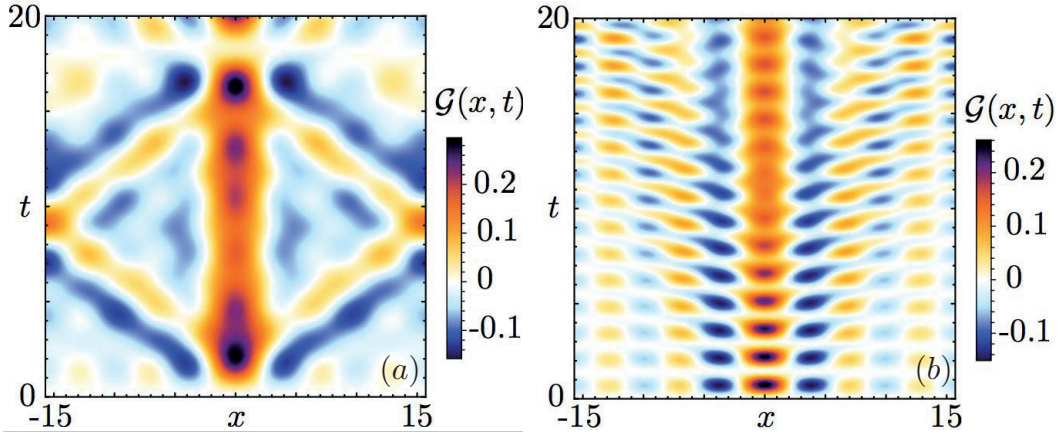

Figure 3.7: (a) Light-cone propagation regime: Density plot of $-\mathcal{G}^{(2)}(x,t)$ as a function of x and t for $\Delta^{(2)} = 0.3$ and $\alpha = 1$; (b) Light-cone freezing regime: Same as in (a) but for $\Delta^{(2)} = 2$ and $\alpha = 1$.
The Green's function are both evaluated in a finite size system with 15 particles.

are either easier to numerically evaluate in the interacting systems we will analyze, or experimentally more accessible.

3.4 Introducing interactions

We now turn back to the lattice model described by $\mathcal{H}_k^{(3)}$ in Eq. (3.4) where, instead of switching on a staggered potential, a sudden quench of the nearest-neighbour interaction U and/or of the next-to-nearest neighbour interaction V is performed. In this way, we are able to test the generality of our findings in presence of fermionic interactions. In particular, the real space lattice Hamiltonian is defined by

$$H = -J \sum_j \left[\left(c_j^\dagger c_{j+1} + h.c. \right) + U(t) n_j n_{j+1} + V(t) n_j n_{j+2} \right], \tag{3.22}$$

where c_j are annihilation operators of spinless fermions on the site j of the lattice and $n_j = c_j^\dagger c_j$ is the density. For $V = 0$ the system is Bethe-Ansatz solvable [116], and thus integrable, while for $V \neq 0$ no solution via the Bethe-Ansatz is known and, moreover, is believed to be nonexistent. We consider quenches out of the initial ground state for $U = V = 0$ and perform the time evolution with respect to a finite U and possibly V. In the integrable scenario, with $V = 0$, it is known that for $U/J < 2$ the system remains gapless after the quench, while for $U/J > 2$ a gap in the energy spectrum opens at the Fermi energy (see [116] for more details and a precise classification of phases by means of a phase diagram).

In contrast to the examples studied above, this interacting Hamiltonian cannot be diagonalized analytically and we resort to numerical means. To this extent, we employ the density matrix renormalization group (DMRG) [117, 118], a numerical variational technique devised to obtain the low-energy physics of quantum many-body one-dimensional systems with high accuracy. As a variational method, DMRG

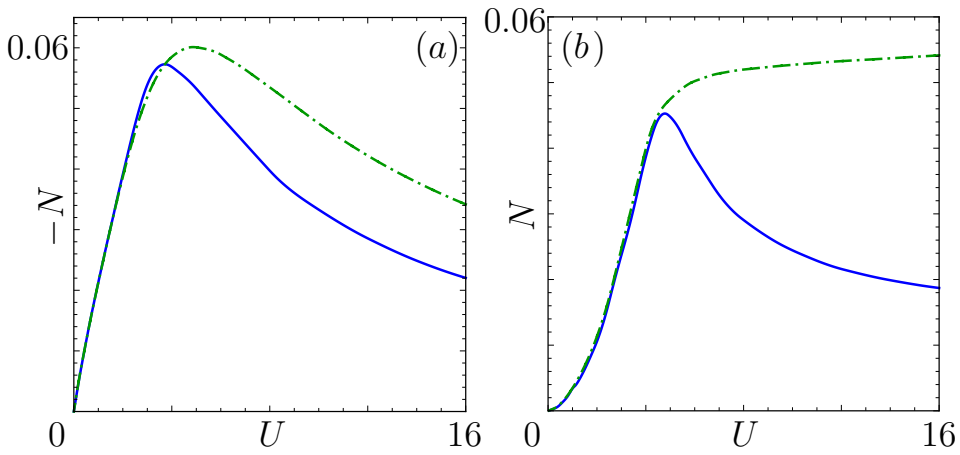

Figure 3.8: (a) Integrable interacting scenario: Plot of N for an interaction-quenched fermion chain, as a function of U with $V = 0$ and $J = 1$; (b) Non-integrable interacting scenario: Plot of N for an interaction-quenched fermion chain, as a function of U with $V = U$ and $J = 1$. In both panels, the blue solid lines represent the quenched long-time limit, while the green dash-dotted lines show the results evaluated with an effective thermal model (see text).

is an efficient algorithm that attempts to find the lowest-energy matrix product state wave-function of a Hamiltonian. In practice, the accuracy of DMRG simulations is controlled by the so-called bond dimension χ. By increasing χ, and with it the numerical effort, we achieve converged results, which are "numerically exact". In every simulation we choose χ such that no changes of the results can be observed on the scales of the respective plots if it is further increased.

To obtain numerical results we need to

1. prepare the ground state of the noninteracting ($U = 0 = V$) system,
2. perform the time evolution with respect to finite U and possibly V,
3. calculate the finite temperature canonical ensemble (as a reference), with respect to finite U and possibly V,

Note that the third point is independent of the former two. All of these are routinely coded in the limit of infinite lattice size $n \to \infty$ [119, 120], using the language of matrix product states (MPS) [118]. Within the DMRG, we have access to finite times only, as the results are obtained by explicit forward time evolution. To push the simulations to larger time scales we employ the ideas of Ref. [121], using extrapolation to obtain the long time limit behavior. Of course, like in any finite time simulation, we cannot exclude that the results achieved are not truly steady and that on some very large time scale another relaxation mechanism sets in. However, we can access time scales on which typical observables appear approximately relaxed on the scale of their respective plots. Either way the results reported here are then, at least, valid on an extensively long time scale, which would be relevant to experiments.

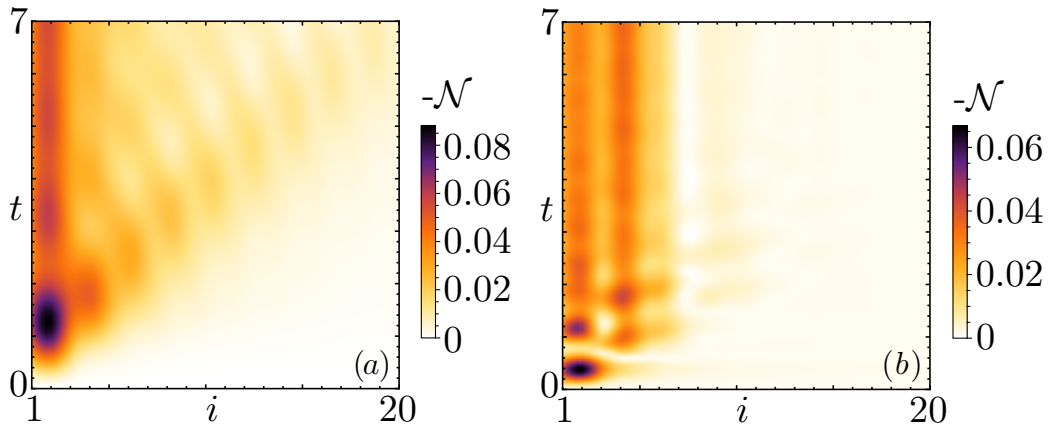

Figure 3.9: (a) Light-cone propagation regime: Density plot of $-\mathcal{N}(i,t)$ as a function of i and t for $U=2$, $V=0$ and $J=1$; (b) Light-cone freezing regime: Same as in (a) but for $U=16$, $V=0$ and $J=1$.

After the technical analysis of the numerical methods, we can focus on the observable features. Since the model is invariant under rotations in the spinor space, we analyze the long-time stationary limit N of the correlation function $\mathcal{N}(1,t)$, defined by

$$\mathcal{N}(i,t) = \langle (n_0(t) - 1/2)(n_i(t) - 1/2)\rangle_0 - \langle (n_0(0) - 1/2)(n_i(0) - 1/2)\rangle_0, \qquad (3.23)$$

where $n_i(t)$ is the time-resolved occupation number of the i-th site and $\langle\cdot\rangle_0$ represents the average with respect to the pre-quench ground state. Results are shown in Figure 3.8 (a) for the integrable case $V=0$ (blue solid line). The quantity N, explicitly defined as

$$N = \lim_{t\to\infty} \mathcal{N}(1,t), \qquad (3.24)$$

follows the same qualitative behaviour of the magnetization in the non-interacting models, rising for small quenches up to a maximum value. As the gap size increases over the crossover point, N begins to decrease and tends to the pre-quench value for very large U. Even when integrability is lost, as is the case of Figure 3.8 (b) ($V=U$, solid line), the qualitative picture remains, on the accessible time-scales, the same. In both cases, a description in terms of an effective temperature (green dash-dotted lines) fails to reproduce the results.

Also in this model a competition between a propagation and a freezing regime for the light cone occurs. To show this fact, we consider the correlation function $\mathcal{N}(i,t)$, whose density plot as a function of the site index and time is shown in Figure. 3.9. For small quenches with $U \leq 2J$ one clearly observes a propagation of the quench information spreading through the system. On the other hand, large quenches with $U > 2J$ display a sharp freezing of the light cone. We have proved that, remarkably, the freezing of the light cone is a generic feature of systems subject to quenches opening large gaps in the spectrum.

3.5 Summary

In summary, a non-monotonic behavior of observables characterizes a wide range of gapless-to-(partially) gapped quantum quenches, both for sudden and non-sudden protocols, integrable and non-integrable models and not only in one spatial dimension. It is the hallmark of a peculiar phenomenon, namely the freezing of the light cone which conveys the quench information through the system. This freezing results in a state described by a GGE which differs from effective thermal states, in some cases even dramatically, thus providing an experimentally accessible way to test the GGE physics. In non-interacting models, the freezing of the light cone is captured by a KG equation, which provides an intuitive interpretation of the behaviour of the system in terms of a simple continuum mechanical model. As a limit for the universality of the physics described, we point out that we do not expect to observe the effects when the gap is opened by merging of crossings, as relevant, for example, for Weyl semimetals [122], or for the models discussed in Refs. [123, 124]. A static fermion-fermion interaction, which could be taken into account by means of bosonization [125] or DMRG [117, 118] for instance, is expected to renormalize the gap to larger values [94], so we expect the phenomenon to persist with a shifted and renormalized maximum [126].

CHAPTER 4

Effective metal-insulator non-equilibrium phase transition

In this chapter, we present our original findings published in [15].
The details of the calculations, not shown here, are reported in Appendix B.

Recently, technological advances in the experimental control of ultracold gases [43, 107] and trapped ions [127] allowed to probe the time evolution of isolated quantum systems. Since, in such systems, the time evolution is unitary, no information about the initial state is lost. However, most often, this information spreads over the whole system, so that, at long times, it is challenging to recollect it. The origin of this behavior lies in the Eigenstate Thermalization Hypothesis (ETH) [54, 55], that, qualitatively speaking, states that, in the thermodynamic limit, the expectation value of local observables over any eigenstate with finite energy density can be well approximated by the average over a properly defined thermal density matrix. In this sense, most isolated systems thermalize. A violation of ETH is provided by many-body systems that have an extensive amount of local or quasi-local conserved quantities. In this case, in fact, the local information stored in the initial wavefunction is preserved locally by the time evolution. Consequently, systems exhibiting such a behavior can have interesting applications in the field of quantum information [128]. A first class of systems with quasi-local conserved quantities are many-body localized systems [129, 130]. In this case, the quasi-local integrals of motion arise due to real space localization and are robust with respect to weak perturbations. In these systems, there is no simple guideline for building a sensitive effective density matrix for the local observables. A second class of such systems is given by the so-called integrable models [109]. In this case, while the violation of ETH is not stable with respect to generic perturbations [131], it is indeed possible to build a statistical ensemble capturing the long time expectation value of the local observables. Such an ensemble is called generalized Gibbs Ensemble (GGE). Conceptually speaking it is obtained by maximizing the entropy while taking into account the constraints posed by the local conserved quantities. From the formal point of view, the GGE density matrix could be an exceptionally useful tool, since concepts such as non-equilibrium phase transitions, introduced in Chapter 1, in integrable systems could be made

universal, in this framework, in the very same way transitions in equilibrium are described within the canonical ensemble. However, GGE density matrices are in general difficult to obtain and no systematic link between them and non-equilibrium phase transitions has been performed.

In this chapter, we begin to address this issue in two paradigmatic cases: The Su-Schrieffer-Heeger (SSH) model 2.2, that represents a starting point for the study of topological phases of matter and the appearance of fractional charges in one dimension, and the transverse field one-dimensional quantum Ising (QI) model, whose simplicity has opened the way to countless insights in the theory of quantum quenches [39, 78]. Moreover, the QI model can be mapped onto the Kitaev chain and hence encodes the physics of the so called Majorana bound states [132].

4.1 Quantum quench in the SSH model

First, we consider the steady state of a quenched Su-Schrieffer-Heeger (SSH) model. Quenches from an initial Hamiltonian with a hopping imbalance δ_0 to a final one with δ_1 are considered (see Chapter 2). As we will show in the following, of particular interest are the quenches which pass trough the gapless regime.

The momentum space Hamiltonian for the quenched SSH model, on a finite ring with $\mathcal{N}$ unit cells and lattice constant set to one, is given by (see Chapter 2)

$$H(t) = \sum_k \Psi_k^\dagger \left\{ \sigma_x \left[w + w\cos(k) + \delta(t) \right] + w\sigma_y \sin(k) \right\} \Psi_k \ . \tag{4.1}$$

Here, $\Psi_k^\dagger = (c_{k,A}^\dagger, c_{k,B}^\dagger)$ is a Fermi spinor, A and B the two sublattice labels and $k = 2\pi j/\mathcal{N}$ with $|j| \leq \mathcal{N}$. Furthermore, σ_i are Pauli matrices and w is the hopping energy. The hopping imbalance term $\delta(t)$, which in equilibrium determines the gap, encodes the quench details: For now, we consider a sudden change $\delta(t) = \delta_0\theta(-t) + \delta_1\theta(t)$, with $\theta(t)$ the Heaviside step function.

The SSH Hamiltonians for $t < 0 (\mu = 0)$ and $t \geq 0 (\mu = 1)$ are diagonalized as

$$H_\mu = \sum_k \epsilon_{\mu,k} \left[d_{\mu,c,k}^\dagger d_{\mu,c,k} - d_{\mu,v,k}^\dagger d_{\mu,v,k} \right] . \tag{4.2}$$

Here $d_{\mu,\nu,k}$ are fermionic operators with $\nu = c, v$, which correspond respectively to the conduction and valence bands, and

$$\epsilon_{\mu,k} = \sqrt{\delta_\mu^2 + 2(w^2 + w\delta_\mu)[1 + \cos(k)]} \tag{4.3}$$

represents the energy spectrum. In the initial state ($t < 0$), the system is prepared in the ground state $|G_0\rangle$ of H_0. Since we are considering half-filling, the states occupied before the quench corresponds to the completely filled valence band, i.e. only states with negative energy are occupied.

In the thermodynamic limit, the quantum average of local observables

$$\mathcal{O}(t) = \langle G_0 | O(t) | G_0 \rangle \tag{4.4}$$

approaches a steady value $\bar{\mathcal{O}} = \mathcal{O}(t \to \infty)$ with a typical $\propto t^{-1}$ power-law decay. Since the system is integrable, this steady value can also be obtained as the trace

$$\bar{\mathcal{O}} = \mathrm{Tr}\{O(0)\rho_G\} \tag{4.5}$$

over the GGE density matrix constructed via the conserved charges $N_{\nu,k} = d^\dagger_{1,\nu,k} d_{1,\nu,k}$ as

$$\rho_G = \frac{e^{-\sum_{\nu,k} \lambda_{\nu,k} N_{\nu,k}}}{Z_G}, \tag{4.6}$$

with

$$Z_G = \mathrm{Tr}\left\{ e^{-\sum_{\nu,k} \lambda_{\nu,k} N_{\nu,k}} \right\}, \tag{4.7}$$

where $\lambda_{\nu,k} = \log(n_{\bar{\nu},k}/n_{\nu,k})$, with $n_{\nu,k} = \langle G_0 | N_{\nu,k} | G_0 \rangle$ and $\bar{\nu} = v/c$ if $\nu = c/v$.

A physically interesting way of building the Lagrange multipliers $\lambda_{\nu,k}$ giving the GGE density matrix, in the case of sudden quench from the ground state, is by the transformation

$$\mathcal{U}^1_{0,k} = e^{i\vec{\mathcal{D}}_k \cdot \vec{\sigma}}, \tag{4.8}$$

connecting post-quench Fermi operators $d_{1,\nu,k}$ to the pre-quench ones $d_{0,\nu,k}$, with $\vec{\sigma}$ the vector of Pauli matrices. Explicitly, the norm

$$|\vec{\mathcal{D}}_k| = \arctan\left\{ \frac{\sqrt{4 - (1 - \Delta_k)^2}}{1 - \Delta_k} \right\} \tag{4.9}$$

plays a central role in defining the behavior of the quench. In fact, the function Δ_k is such that (cf B.22, B.23)

$$n_{c/v,k} = \frac{1 \pm \Delta_k}{2}, \quad \lambda_{c/v,k} = \pm \log\left(\frac{1 - \Delta_k}{1 + \Delta_k} \right), \tag{4.10}$$

and thus directly controls the GGE.

At this point, we can focus on the functional form of the occupation numbers, or, equivalently, of Δ_k, in the Brillouin zone (BZ) (see Figure 4.1). One finds $|\Delta_k| \leq 1$ with $0 \leq |\vec{\mathcal{D}}_k| \leq \pi/2$. Furthermore, $|\Delta_k| = 1$ only holds true for $k = 0, \pm\pi$. In particular one has

$$\Delta_0 = -\mathrm{sign}(\delta_0 + 2w)\ \mathrm{sign}(\delta_1 + 2w), \tag{4.11}$$

and

$$\Delta_{\pm\pi} = -\mathrm{sign}(\delta_0)\ \mathrm{sign}(\delta_1), \tag{4.12}$$

with $\mathrm{sign}(x) = |x|/x$ the sign function. This means that when $\Delta_k = -1$, one finds $\mathcal{U}^1_{0,k} = \sigma_0$ and the quench does not affect the populations, while for $\Delta_k = 1$ the transformation $\mathcal{U}^1_{0,k} = i\sigma_y$ induces a swap of the c, v states. The value of Δ_k at $k = 0, \pm\pi$, hence, is constant and insensitive to variations of the quench parameters provided they remain within one of the nine regions bounded by the 4 lines $\delta_\mu = 0, -2w$ with $\mu = 0, 1$, shown in the phase diagram in Figure 4.3 and which correspond to the equilibrium quantum critical points. Their footprint, as we are

going to comprehensively characterize in the last part of this chapter, remain then visible also in non-equilibrium features that show up both in the quench induced transformation and in the observables behavior in the long time limit, once the equilibration process has taken place.

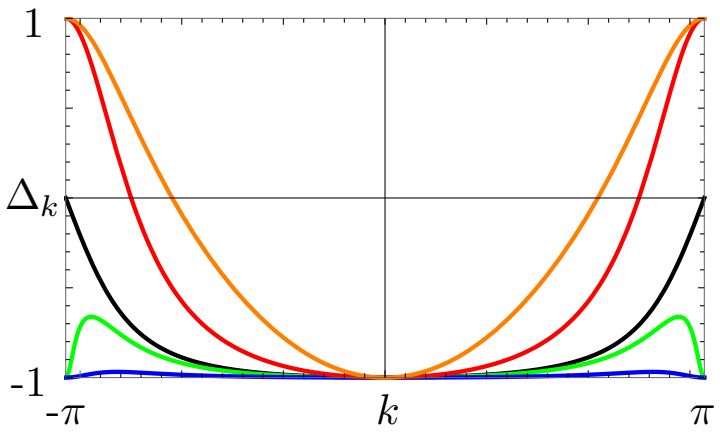

Figure 4.1: Plot of the function Δ_k in the Brillouin zone. Here we have considered a quench from an initial gap $\delta_0 = w$ to $\delta_1 = 0.5w$ (blue line), $\delta_1 = 0.1w$ (green line), $\delta_1 = 0$ (black line), $\delta_1 = -0.5w$ (red line) and $\delta_1 = -w$ (orange line).

On the other hand, indeed, crossing one of the boundaries results in a sharp, non-analytical feature in Δ_k. Thus, the center and edges of the Brillouin zone act for the quench as fixed points, whose character is determined by the quench parameters. A detailed study of Δ_k (see Appendix B) allows us to identify four non-contiguous regions out of the nine defined in Figure 4.3: Here, when $\Delta_0\Delta_\pi < 0$, a non-trivial inversion of population, characterized by $n_{\nu,0}n_{\bar{\nu},\pm\pi} = 0$, occurs. This inversion of population also gives rise to a DQPT, which we observe in the time evolution of the Loschmidt echo of the system. This feature, however, does not seem to have consequences into the dynamics of observable quantities.

4.1.1 Population inversion and DQPTs

In this Section, we focus on the population inversion that can happen for a class of quantum quench protocols, in particular when the manipulation brings the system from one phase to another, crossing at least one equilibrium critical point. Furthermore, we unveil the relation between the populations and the dynamics of the system.

In order to gain a deeper understanding of the aforementioned relation, it is useful to parameterize the Hamiltonian in Eq. (4.1) by means of a vector $\vec{d}_k$, such that

$$H(t) = \sum_k \Psi_k^\dagger h_k(t) \Psi_k, \qquad h_k(t) = \vec{d}_k \cdot \vec{\sigma} \tag{4.13}$$

with

$$\vec{d}_k(t) = \begin{cases} \vec{d}_k^{\,0} & \text{for } t < 0 \\ \vec{d}_k^{\,1} & \text{for } t \geq 0 \end{cases} . \tag{4.14}$$

The Loschmidt amplitude, introduced in Eq. (1.19) and which we recall to be

$$\mathcal{G}(t) = \langle \psi_0 | \psi_0(t) \rangle = \langle \psi_0 | e^{-iH(t>0)t} | \psi_0 \rangle \,, \tag{4.15}$$

gives the overlap of the time evolved state with the initial pre-quench state, which reads

$$|\psi_0\rangle = \prod_{k=-\pi}^{\pi} d^{\dagger}_{0,v,k} |0\rangle. \tag{4.16}$$

Following a sudden quench, it can be expressed in the compact form [133]

$$\mathcal{G}(t) = \prod_{k \in BZ} \left[\cos(t\epsilon_{+,1,k}) + i\hat{d}^0_k \cdot \hat{d}^1_k \sin(t\epsilon_{+,1,k}) \right], \tag{4.17}$$

where $\hat{d}^i_k = \vec{d}^i_k / |\vec{d}^i_k|$ denotes the unit vector in the direction of $\vec{d}^i_k$ and $|\vec{d}^i_k| = \epsilon_{+,1,k}$. Furthermore, it can be shown that

$$\hat{d}^0_k \cdot \hat{d}^1_k = n_{c,k} - n_{v,k} = \Delta_k, \tag{4.18}$$

so that the relation between the Loschmidt amplitude and the conserved quantities used to construct the GGE, or, equivalently, the function Δ_k, becomes clear.

With this respect, we study the associated rate function in the thermodynamic limit, which reads

$$g(t) = -\lim_{N\to\infty} \frac{1}{N} \ln \mathcal{G}(t) = -\frac{1}{2\pi} \int_{-\pi}^{\pi} \ln \left[\cos(t\epsilon_{+,1,k}) + i\hat{d}^0_k \cdot \hat{d}^1_k \sin(t\epsilon_{+,1,k}) \right] dk. \tag{4.19}$$

Within the model here under consideration, this function shows a non-analytic behavior if and only if there exists at least one point in the BZ where conduction and valence bands are equally filled, so that $\Delta_k = 0$ and, at the same time, $\hat{d}^0_k$ is perpendicular to $\hat{d}^1_k$.

As anticipated in the previous section, this condition is satisfied only when a swap of the c, v states is induced by the quench. Consequently, a quantum critical point has to be crossed during the quench protocol. This behavior can be observed in Figure 4.2, where the functional form of the occupation numbers as well as the kinks in the Loschmidt amplitude rate function are shown. The latters, when present, show up at specific times: every time the cosine in Eq. (4.19) vanishes, the function $g(t)$ is non-analytic. In particular, as shown in 4.2 (b), one finds that the sequence of critical times, which are the dynamical counterparts of the quantum critical points, is given by

$$t_n = \frac{(2n+1)\pi}{2\epsilon_{+,1,\bar{k}}} \tag{4.20}$$

where $\bar{k}$ is given by the solution of the equation $\Delta_k = 0$. Note that, in the model under study, at least one equilibrium quantum critical point has to be crossed, and the starting or ending precisely on the gapless state is not sufficient to obtain a non-trivial population inversion as well as a DQPT.

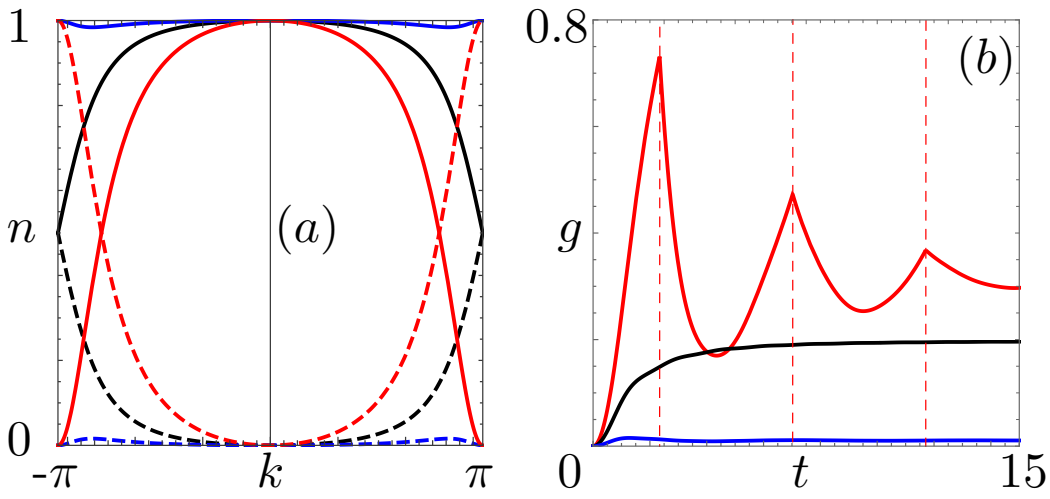

Figure 4.2: (a) Plot of the conduction (dashed lines) and valence (solid lines) bands occupation numbers given in Eq. (4.10) after the quench in the Brillouin zone. (b) Plot of the Loschmidt amplitude associated rate function $g(t)$ in the thermodynamic limit: kinks appear if an equilibrium quantum critical point is crossed in the quench protocol. Red dashed lines represent the critical time sequence t_n, for the first three terms.
In both panels, we consider a sudden quench from $\delta_0 = w$ to $\delta_1 = 0.5w$ (blue line), $\delta_1 = 0$ (black line) and $\delta_1 = -0.5w$ (red line).

4.1.2 Metal-insulator transition

Having investigated the dynamical properties in the previous section, we get back to the quench induced transformation given in Eq. (4.8). As mentioned, this transformation is directly linked to the GGE, since, in the sudden case f, one has

$$n_{\nu,k}^{-1} = 1 + e^{\xi_{\nu,k}\beta^*}, \tag{4.21}$$

where $\xi_{\nu,k} = w\lambda_{\nu,k}$ and $\beta^* = w^{-1}$ is an arbitrary, non-zero, inverse temperature. In other words, one can reinterpret the GGE density matrix as the Grancanonical ensemble of free fermions with Hamiltonian

$$\bar{H} = \sum_{\nu,k} \xi_{\nu,k} d_{1,\nu,k}^\dagger d_{1,\nu,k}, \tag{4.22}$$

inverse temperature β^*, and zero chemical potential. Combining the above analysis and Eq. (4.10) one can conclude that when a non-trivial inversion of population of the bands $\epsilon_{\nu,k}$ of the post-quench Hamiltonian is present, the effective bands $\xi_{\nu,k}$ cross zero energy and thus have a metallic character, while no crossing occurs in all other cases and the bands $\xi_{\nu,k}$ have an insulating character. When the quench parameters cross one of the boundary lines described above, thus an effective metal-insulator transition (MIT) in $\bar{H}$ occurs. The structure of the effective energy bands is shown in the nine different tiles of Fig. 4.3. We stress here that the MIT is an effective one showing up in the GGE, i.e. in the non-equilibrium steady state following a quantum quench: How this reflects in physically relevant (local) observables is a

priori unclear, but in our case we will show explicitly in the following that its imprint is quite pronounced.

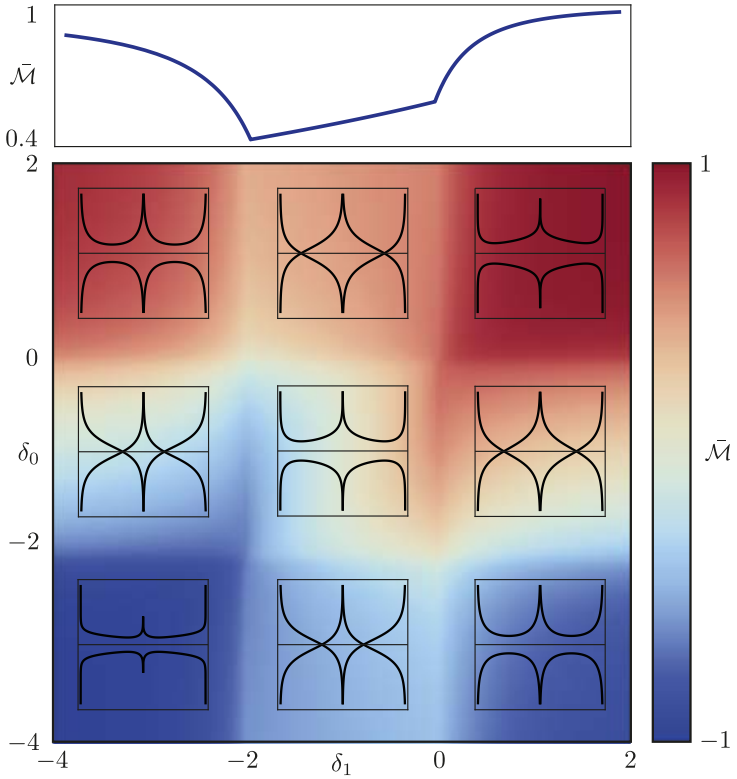

Figure 4.3: Bottom: Density plot of $\bar{\mathcal{M}}$ as a function of δ_0, δ_1 for a sudden quench and the corresponding typical effective band structure $\xi_{\nu,k}$ (see text). Top: plot of $\bar{\mathcal{M}}$ as a function of δ_1 for $\delta_0 = 2w$. Here, δ_μ is in units w.

We now analyze how the effective MIT influences observables of interest. We start by the average level of dimerization $\bar{\mathcal{M}}$, given by the expectation value of

$$\mathcal{M} = \Psi_x^\dagger \sigma_x \Psi_x, \tag{4.23}$$

with $\Psi_x = \sum_k e^{ikx}\Psi_k/\sqrt{L}$. Note that translational invariance implies that its expectation value is independent of the position. The main panel of Fig. 4.3 shows a density plot of $\bar{\mathcal{M}}$ as a function of δ_μ. Crossing any of the transition lines $\delta_\mu = 0, -2w$, a kink in $\bar{\mathcal{M}}$ is encountered. The top panel shows results for $\delta_0 = 2w > 0$: the discontinuity in $\partial_{\delta_1}\bar{\mathcal{M}}$ at $\delta_1 = 0, -2w$ is evident. These kinks represent a signature of the occurrence of the effective MIT. Their origin is the non-analytic dependencies of the populations at $k = 0, \pm\pi$ combined with the fact that, in the thermodynamic limit, the density of states of such points diverges as the curvature of $\epsilon_{1,k}$ vanishes at these points. Several other quantities show a similar behavior. Given the presence of the effective MIT in the GGE, we inspect the fluctuations of the space-averaged effective "current" $J_0 = \sum_{\nu,k} (\partial_k \xi_{\nu,k}) N_{\nu,k}$. Such fluctuations are defined using the phase velocity associated to the effective bands [134]. In the steady limit one has $\bar{\sigma}_0 = \langle J_0^2 \rangle$ (see Appendix B.5.2). This

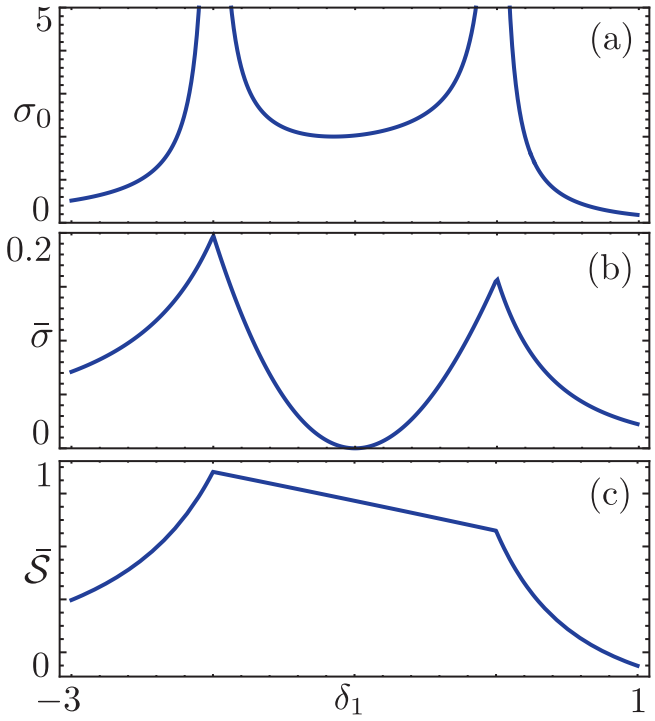

Figure 4.4: (a) Plot of $\bar{\sigma}_0$ (units w^2); (b) Plot of $\bar{\sigma}$ (units w^2) ; (c) Plot of $\mathcal{S}$ as a function of δ_1 (units w) for $\delta_0 = 2w$.

quantity is shown in Fig. 4.4(a) for $\delta_0 > 0$. For $\delta_1 = 0$ (and $\delta_1 = -2w$) it diverges $\propto |\delta_1|^{-1}$ (and $\propto |\delta_1 + 2|^{-1}$). Furthermore, fluctuations are larger in the effective metallic phase, while they tend to vanish in the insulating one, as one would expect [134]. Although $\bar{\sigma}_0$ is not a directly accessible quantity, signatures of the effective MIT are present also in the steady state fluctuations $\bar{\sigma} = \langle J^2 \rangle$ of the space-averaged physical current $J = \sum_k (\partial_k \epsilon_{\nu,k}) N_{\nu,k}$, shown in Fig. 4.4(b). In contrast to the current fluctuations in the effective picture though, here no marked differences in the magnitudes are found in the different phases. However, kinks occur at the boundaries between the phases. As a third example, Fig. 4.4(c) shows the thermodynamic entropy (see Appendix B.5.2) $\bar{\mathcal{S}}$ of the system for $\delta_0 > 0$: It is largest in the metallic phase and displays kinks for $\delta_1 = 0, -2w$. This quantity is particularly interesting, since it is intrinsic to thermodynamics.

4.1.3 Physical interpretation of the non-analyticities

We want to give a physical interpretation of the non-analyticities we observe in the observables evaluated within the GGE picture. Since the equilibrium state of the SSH model has two quantum critical points (QCPs) for $\delta = 0$ and $\delta = -2w$, we want to show that the non-analiticities are not only due to the presence of the quantum phase transition in the equilibrium model, but also to the time evolution induced by the quench in the system.

To do so, we study both the behavior of the eigenvectors and the eigenvalues of the Hamiltonian which describes the system: together they should give us a complete characterization of the problem.

We start by considering the overlap of the time evolution of the initial state with the ground state of the post-quench Hamiltonian H_1 (a sort of modified Loschmidt Echo):

$$\mathcal{L}_{\rm gs}(t) = |\langle\psi_1|\psi_0(t)\rangle|^2 = |\langle\psi_1|e^{-iH_1 t}|\psi_0\rangle|^2 \tag{4.24}$$

and the overlap with the state with the maximum energy of the post-quench Hamiltonian H_1, where only the conduction band is filled

$$\mathcal{L}_{\rm me}(t) = |\langle\bar{\psi}_1|\psi_0(t)\rangle|^2 = |\langle\bar{\psi}_1|e^{-iH_1 t}|\psi_0\rangle|^2 \tag{4.25}$$

with

$$|\psi_1\rangle = \prod_{k=-\pi}^{\pi} d^\dagger_{1,v,k}|0\rangle, \tag{4.26}$$

$$|\bar{\psi}_1\rangle = \prod_{k=-\pi}^{\pi} d^\dagger_{1,c,k}|0\rangle \tag{4.27}$$

and $|0\rangle$ represents the vacuum state. Both $\mathcal{L}_{\rm gs}$ and $\mathcal{L}_{\rm me}$ are time-independent functions.

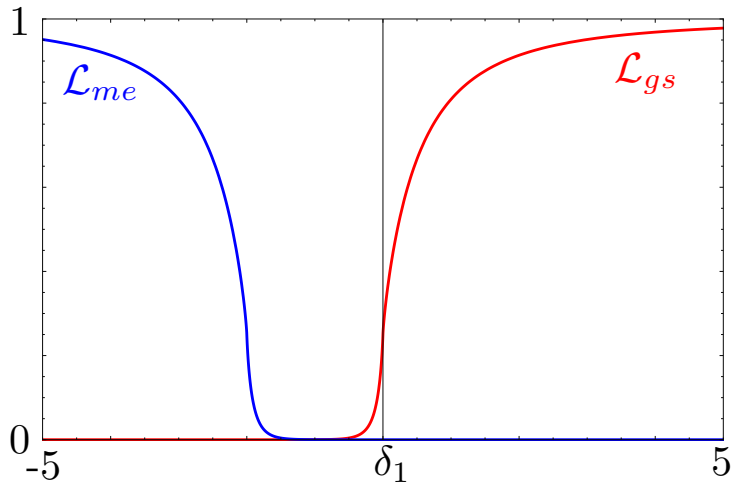

Figure 4.5: Plot of $\mathcal{L}_{\rm me}$ (blue line) and of $\mathcal{L}_{\rm gs}$ (red line) as a function of δ_1(units w) for $\delta_0 \to \infty$ in the thermodynamic limit.

In fig. 4.5 are shown these two quantities as a function of δ_1 for $\delta_0 \to \infty$. The quantity $\mathcal{L} = \mathcal{L}_{\rm me} + \mathcal{L}_{\rm gs}$ goes to one in the two insulating phases, while vanishes in the metallic one. Moreover it is non-analytic in the QCPs, where the post-quench Hamiltonian is gapless. In this sense, only when the effective Hamiltonian $\bar{H}$ in Eq. (4.22) has at least one crossing point, it is possible to have a spectral transfer between the bands.

Note that, interestingly, even if we are performing a sudden quench, the non-equilibrium stationary state is very similar to the post-quench Hamiltonian ground state (if $\delta_1 > 0$) or to the post-quench Hamiltonian maximum energy state (if $\delta_1 < -2w$).

We can now study the behavior of the average of H_1 on the GGE density matrix $\langle H_1 \rangle_0$, i.e. the average of the post-quench Hamiltonian performed over the pre-quench ground state, with respect to the energy of the post-quench Hamiltonian ground state $\langle H_1 \rangle_1$ or to the post-quench Hamiltonian maximum energy state $-\langle H_1 \rangle_1$.

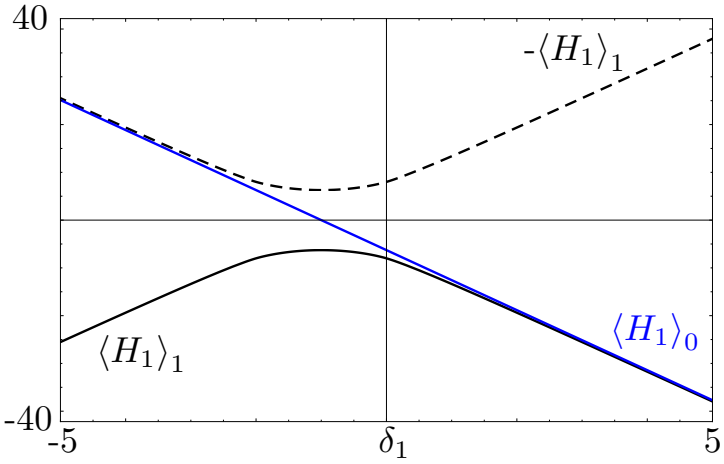

Figure 4.6: Plot of $\langle H_1 \rangle_0$ (blue line), $\langle H_1 \rangle_1$ (black solid line), and $-\langle H_1 \rangle_1$ (black dashed line) as a function of δ_1(units w) for $\delta_0 \to \infty$ in the thermodynamic limit.

In this sense (see Fig. 4.6), we compare $\langle H_1 \rangle_0$ with the quantity $W = \langle H_1 \rangle_1 (\mathcal{L}_{\rm gs} - \mathcal{L}_{\rm me})$, which weighs the two energies with the respective probability $\mathcal{L}$ of being in that state. In addition to the previous findings, this tells us that only excited states very close in energy to the ground state (if $\delta_1 > 0$) or to the post-quench Hamiltonian maximum energy state (if $\delta_1 < -2w$) are involved when we quench in the insulating phase. On the contrary, when δ_1 is in the metallic phase, both $\mathcal{L}_{\rm gs}$ and $\mathcal{L}_{\rm me}$ are vanishing, so the main contribution has to be given by the other excited states we are not considering. In particular, since $\langle H_1 \rangle_0 \propto \delta_1$, in this parameter region the state of the system after the quench seems to be a superposition of states near $E \simeq 0$, where the density of state $D(E)$ is very peaked.

4.2 NEQPT robustness

As shown above, signatures of the effective MIT occur in a vast array of quantities. It is important, however, to establish how robust the results are. We will consider $\bar{\mathcal{M}}$ as an example but the conclusions apply to all quantities discussed above. We begin by discussing deviations from the thermodynamic limit. With a finite number of lattice sites, averages do not converge to a steady value for long time but oscillate with a finite recursion time: the GGE hypothesis fails altogether. Figure 4.8(a)

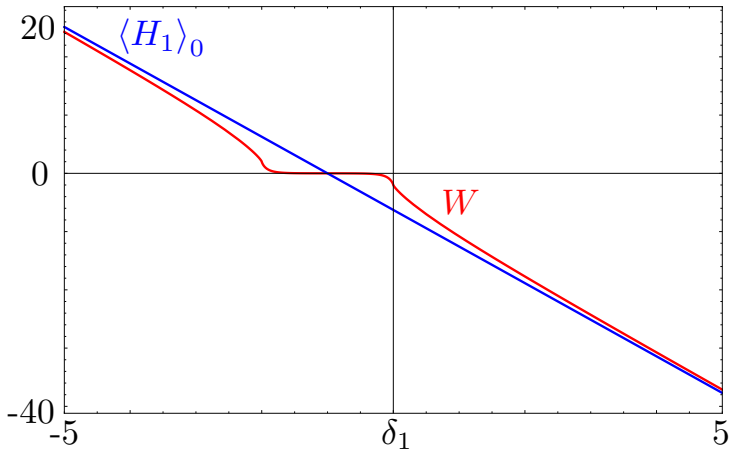

Figure 4.7: Plot of $\langle H_1 \rangle_0$ (blue line) and of W (red line) as a function of δ_1(units w) for $\delta_0 \to \infty$ in the thermodynamic limit.

shows the quantum and time average over a period of $\mathcal{M}(t)$ near $\delta_1 = 0$. Dashed and dotted curves, calculated with a finite number of lattice sites, show that kinks are smoothed out as the number of sites decreases. This confirms the thermodynamic limit as a crucial ingredient for the non-analyticities to arise in the GGE predictions. Interestingly, though, even for $\mathcal{N}$ as small as 20 one can still observe a distinct imprint of the non-analyticities found for $N \to \infty$ in the time-averaged $\bar{\mathcal{M}}$.

Furthermore, the features are robust in the case of a thermal preparation of the initial state[1]. Figure 4.8(b) shows $\bar{\mathcal{M}}$ obtained for an initial state at different temperatures T: although the curves are quantitatively different, with a global suppression of the dimerization, non-analyticities are always present. The origin of the robustness is that, for an initial temperature T, one has $n_{c,k} - n_{v,k} = f_{T,k}\Delta_k$ with $f_{T,k} = \sinh(\epsilon_{0,k}/k_B T)/[1 + \cosh(\epsilon_{0,k}/k_B T)] > 0$ (cf B.29). This result means that the effective MIT occurs in the same parameter regions as in the $T = 0$ case. Note that the robustness of the non-analyticity with respect to temperature is particularly intriguing since it is not present in the equilibrium QPT characterizing the model.

We then consider the case of a quantum quench of finite time duration τ, where the quench protocol is described by a linear ramp. Typical results are shown in Fig. 4.8(c). The non-analytic behavior persists, although results again differ quantitatively. This is due to the robustness of the effective MIT, that can be demonstrated by showing that the fixed points of the quench transformation only differ by an additional phase shift with respect to the case of sudden quench (see Appendix B).

Finally, we address the effects of static inter-particle interactions. We consider here a very similar model which - in the absence of interactions - displays the same qualitative behavior as the one discussed so far, but it is easier to simulate using density matrix renormalization group (DMRG) techniques. The Hamiltonian is

[1] No contact with an external thermostat is assumed during or after the quench.

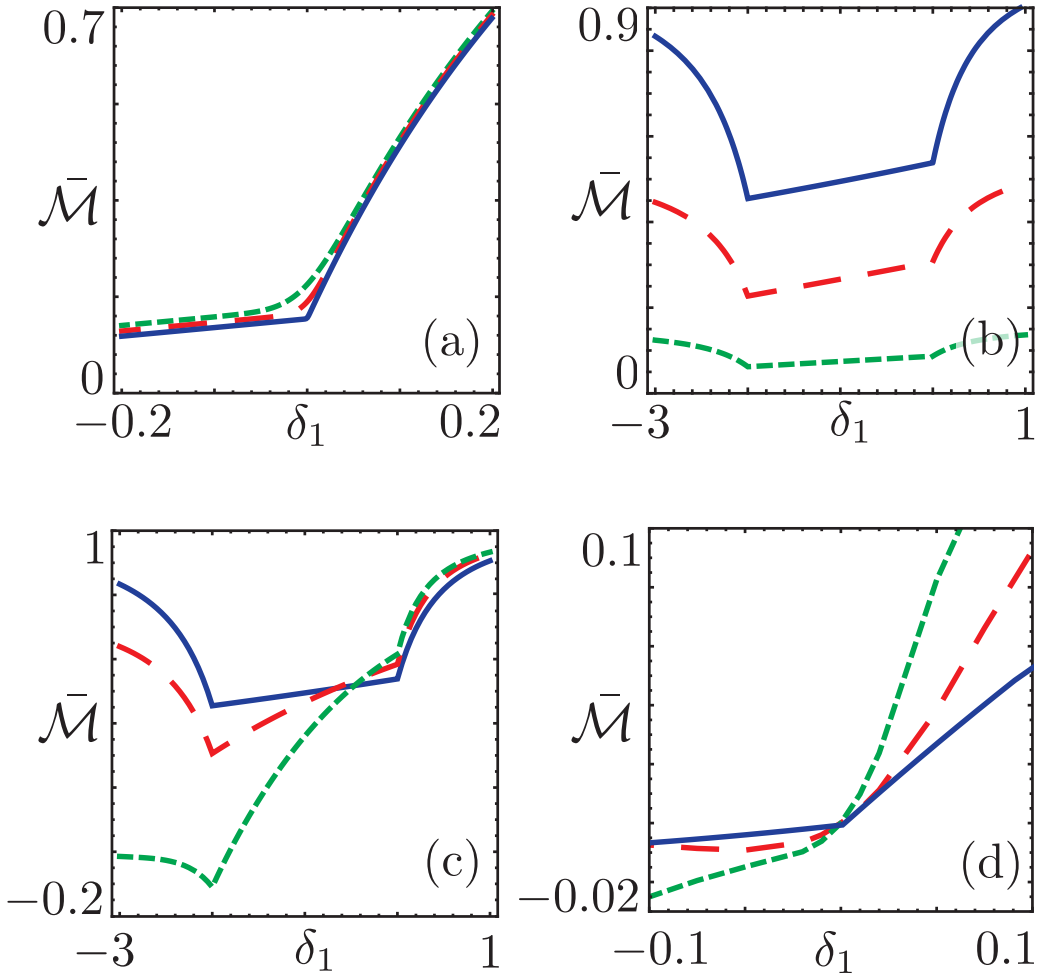

Figure 4.8: Plot of $\bar{\mathcal{M}}$ as a function of δ_1 (in units of w) for different (a) number of lattice sites: solid the thermodynamic limit, dashed $\mathcal{N} = 80$, dotted $\mathcal{N} = 20$. The last two curves are averaged over a period - see text; (b) temperature of the initial state: solid $T = 0$, dashed $T = 5$, dotted $T = 20$; (c) duration of the quench ramp: solid $\tau = 0$, dashed $\tau = 2$, dotted $\tau = 10$; (d) Strength of the fermion-fermion interaction - see text: solid $U = 0$, dashed $U = 1$, dotted $U = 2$, $T = 0$. Here, $\delta_0 = 5w$ in panels (a-c) and $\delta_0 = w$ in panel (d), T is in units of wk_B^{-1} with k_B the Boltzmann constant, τ is in units of $\hbar w^{-1}$ and U is in units of w.

given by

$$H(t) = \sum_{i}^{N} w c_i^\dagger c_{i+1} + \text{h.c.} + \delta(t)(-1)^i n_i + U n_i n_{i+1} \tag{4.28}$$

and we consider the expectation value $\bar{\mathcal{M}} = \langle n_0 - 1/2 \rangle$ as an observable. Here, c_i annihilates a spinless fermion on lattice site i. The model thus describes spinless fermions on a one-dimensional chain with staggered field $\delta(t)$ and nearest-neighbor interaction U. At time $t = 0$ the staggered field is subject to the quench $\delta(t) = \delta_0\theta(-t) + \delta_1\theta(t)$, abruptly changing its value from δ_0 to δ_1. This model can be simulated with relative ease using standard DMRG techniques based on matrix product states [117, 118, 121]. The time scales which can be reached are bound within this approach by the entanglement growth of the system and, thus, the steady state behavior has to be read off at large but finite times. For $U = 0$ strong oscillations in the dynamics after the quench render such an extrapolation difficult, but for this particular parameter value exact methods can be employed to extract the asymptotic behavior. At finite U these oscillations are strongly damped out allowing for a straightforward extrapolation to long times (see Appendix B.6). The inclusion of the interaction term makes the model non-integrable, which in turn is believed to destroy the GGE picture. Fig. 4.8(d) shows results for different values of the interaction strength: non-analyticities are washed out, as would be expected.

4.3 Non-analyticities in the Ising model

In this section, we consider the transverse field QI model, that is, the XY model with vanishing anisotropy parameter. We consider sudden quantum quenches, so that $h(t) = h_0\theta(-t) + h_1\theta(t)$, and we impose the system to be in the ground state $|0_I\rangle$ for $t < 0$, and to evolve unitarily for $t > 0$. Note that the state $|0_I\rangle$ is uniquely defined, even in the thermodynamic limit, since we consider $h_0 > 1$.
In the even parity sector, relevant for the case inspected since we perform a quantum quench from the ground state at $h_0 > 1$, the diagonal forms of the pre/post quench Hamiltonians $H_I^{(i)}$ ($i = 0/1$ respectively) read

$$H_I^{(i)} = \sum_{k=-N}^{N-1} \xi_k^{(i)} \left(b_k^{(i)\dagger} b_k^{(i)} - \frac{1}{2} \right), \tag{4.29}$$

with

$$\xi_k^{(i)} = \sqrt{[h_i - \cos(p_k)]^2 + \sin^2(p_k)}. \tag{4.30}$$

Here, $p_k = 2\pi k/\mathcal{N}$ and $b_k^{(i)}$ are fermionic operators. The fermionic occupation numbers $N_k^{(I)} = b_k^{(1)\dagger} b_k^{(1)}$ and their averages $n_k^{(I)} = \langle 0_I | N_k^{(I)} | 0_I \rangle$ allow to define, in the thermodynamic limit and for times $t \to \infty$, the post quench thermodynamic entropy

$$\bar{\mathcal{S}}_I = -\sum_k n_k^{(I)} \ln(n_k^{(I)}) + (1 - n_k^{(I)}) \ln(1 - n_k^{(I)}) \tag{4.31}$$

and the GGE density matrix of the system. The latter quantity reads as

$$\rho_G^{(I)} = \frac{e^{-\sum_k \varepsilon_k^{(I)} N_k^{(I)}}}{Z_G^{(I)}}, Z_G^{(I)} = \mathrm{Tr}\left\{e^{-\sum_k \varepsilon_k^{(I)} N_k^{(I)}}\right\}, \tag{4.32}$$

with $\varepsilon_k^{(I)}$ implicitly given by

$$n_k^{(I)} = \frac{1}{e^{\varepsilon_k^{(I)}} + 1}. \tag{4.33}$$

Again, we can interpret the GGE density matrix as a Grancanonical density matrix, at temperature set to unity and at zero chemical potential, for fermions with effective Hamiltonian

$$\bar{H}^{(I)} = \sum_k \varepsilon_k^{(I)} b_k^{(1)\dagger} b_k^{(1)}. \tag{4.34}$$

As in the case of the SSH model, the entropy shows kinks as a function of the quench parameter, in correspondence to the gapless points of the dispersion relation, signalling the equilibrium QPT between the paramagnetic and the ferromagnetic phase. Correspondingly the effective Hamiltonian $\bar{H}^{(I)}$ undergoes a metal insulator transition. The analogy to the behavior characterizing the SSH model is hence complete. Examples are given in Fig. 4.9. In panel (a), the entropy $\bar{\mathcal{S}}_I$ is plotted as a function of h_1, for $h_0 = 10$. $\bar{\mathcal{S}}_I$ is shown to have non-analyticities in correspondence to the equilibrium QPTs occurring at $h_1 = \pm 1$. In panel (b), the effective energies $\varepsilon_k^{(I)}$ are plotted, as a function of k, for $h_0 = 2$ and $h_1 = 5$ (red solid line), $h_1 = 1$ (green dashed line), and $h_1 = 0$ (blue dashed line). As in the case of the SSH model, these effective bands undergo an effective MIT in correspondence to the equilibrium QPT. In fact, for $h_1 > 1$ the dispersion does not cross the chemical potential (zero in this case), while for $h_1 < 1$ it does.

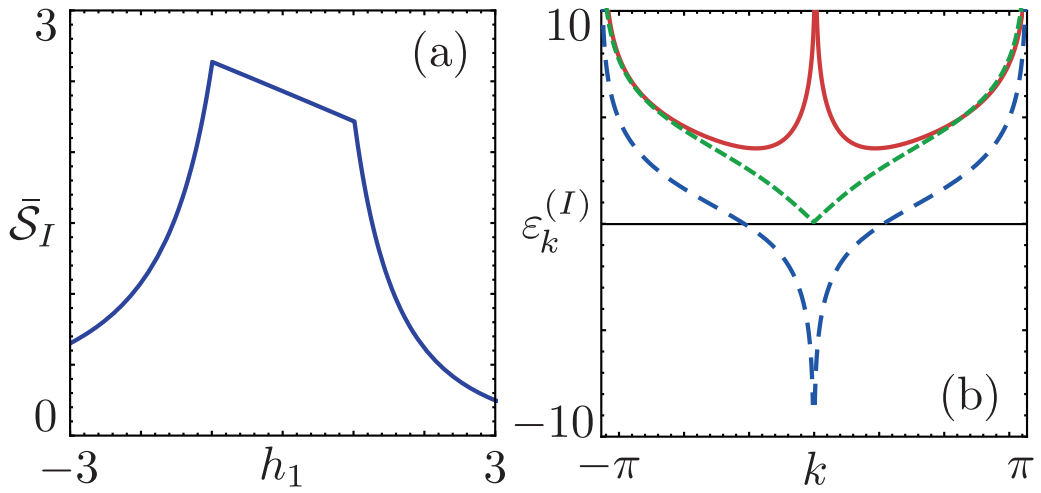

Figure 4.9: (a) Plot of $\bar{\mathcal{S}}_I$ as a function of h_1, for $h_0 = 0$; (b) Plot of $\varepsilon_k^{(I)}$, as a function of k, for $h_0 = 2$ and $h_1 = 5$ (red solid line), $h_1 = 1$ (green dashed line), and $h_1 = 0$ (blue dashed line). The thin black line corresponds to the chemical potential.

4.4 Summary

We have observed that, in the paradigmatic cases of the SSH model and of the transverse field QI model, the non-equilibrium QPTs appear in connection to both an equilibrium QPT and an effective MIT in the GGE density matrix of the system. By direct inspection in the case of the SSH model, we have also shown that the non-equilibrium QPT is indeed robust with respect to those perturbations that do not spoil the validity of the GGE, and hence the presence of the effective MIT. The phenomenology we describe appears general and should hold true also for higher dimensional systems. An interesting extension to our work includes the discussion of terms that break integrability only weakly. The results we report should carry over to the prethermal state reached in these situations.

CHAPTER 5

Topological classification of dynamical quantum phase transitions

In this Chapter, we present our original findings published in [16].

It has been shown that periodic drivings can lead, for example, to topological phases (that are promising for spintronics and quantum computation purposes) [135, 136], can enhance superconductivity [20], and can result in new phases such as discrete time crystals [137–139]. From the fundamental side, on top of the possibility of engineering new phases and access solid state counterparts of quantum optics, the advances in the control of trapped ions [43], ultracold gases [127], nitrogen vacancy centres in diamonds [140], and, in condensed matter environments, of pump probe experiments [141], enable the inspection of the dynamics of isolated quantum systems and hence a better understanding of thermalization. In this context, depending on the nature of the system under inspection, many scenarios can take place. In the thermodynamic limit, most systems follow the eigenstate thermalization hypothesis [55, 135], that is, the expectation values of local observables are thermal. However, notable exceptions of both fundamental and technological interest exist. Anderson [142] and Many body Localized [143] phases as well as integrable systems [12] are characterized by extensive sets of local or quasi-local conserved quantities. In these cases, if quantum information is stored in the initial state, such information is still available locally at later times and hence the system does not thermalize. In localized systems, the lack of thermalization is robust with respect to the parameters of the model, but the statistical ensemble describing the long time behavior of the system cannot be constructed a priori. In integrable systems, the lack of thermalization is a fine tuned property but the long time mean value of local observables can be described by the GGE. If integrability is only weakly broken, the GGE describes a long lived pre-thermal plateau [144]. The usual (gedanken) experiment that is performed in order to access the main thermalization properties of a system is the following: The system is prepared in the ground state of a Hamiltonian $H(g)$, where the dependence on a parameter g is made explicit. At some time t_0, the parameter g varies, suddenly or according to some specific finite duration protocol, to a new constant value g'. If the variation in the parameter is

abrupt, the experiment is called sudden quantum quench, otherwise it is called finite duration quantum quench. Aside from the issues related to thermalization, that are mostly inspected by means of the long time behaviour of the systems, quantum quenches are also interesting at finite times. In translational invariant systems, two point correlators are characterized by a light-cone structure, as we have shown in Chapter 3. This intriguing phenomenon is related to the fact that information can only propagate at finite velocity. More recently, it was discovered that some systems undergoing a quantum quench can show non-analytical behaviours as a function of time, in quantities related to the Loschmit echo [83]. Such non-analiticities, dubbed Dynamical Quantum Phase Transitions (DQPTs) [78] bear a similarity with thermal phase transitions and represent an attempt to characterize far-from-equilibrium phases. At first, the presence of DQPTs following a quantum quench appeared to be linked to the fact that the pre-quench and the post quench parameters of the Hamiltonian represented points in parameter space that could only be connected by lines crossing a quantum critical line. It was however shown that this is not necessarily the case: sudden quantum quenches in the quantum XY chain can be characterized by DQPTs even when they take place between points in the parameter space belonging to the same quantum phase. Conversely, quantum quenches between phases separated by quantum critical lines can be characterized by the absence of DQPTs.

5.1 Quantum quench in the XY chain

In this chapter, we extend the study of the XY chain, introduced in Chapter 2, to finite duration quantum quenches, which have been proven in several instances to be drastically different from their sudden counterpart [145]. We find that the number $\mathcal{N}$ of (inequivalent) quantum DQPTs can indeed be manipulated by the duration of the quantum quench. Moreover, we show that, surprisingly, the parity of $\mathcal{N}$ does not depend on the quench duration and is related to a topological invariant. To be more specific, we consider the XY chain in a transverse magnetic field with periodic boundary conditions [101]. Its Hamiltonian can be written as

$$H(t) = \sum_{j=1}^{N} \left[\left(\frac{1+\gamma(t)}{2} \right) \sigma_j^x \sigma_{j+1}^x + \left(\frac{1-\gamma(t)}{2} \right) \sigma_j^y \sigma_{j+1}^y - h(t) \sigma_j^z \right], \tag{5.1}$$

where σ_j^i with $i = x, y, z$ are the Pauli matrices which describe spin operators on the j-th lattice site of the spin chain, N is the number of sites, γ is the anisotropy parameter and h is the external magnetic field. By means of a Jordan-Wigner transformation, this model can be mapped onto a chain of free fermions with superconductive correlations (see Chapter 2). We will for simplicity concentrate on the case of an even number of fermions, since the results are not qualitatively affected by this choice.

In the static case, the model is characterized by a rich phase diagram, as shown in Fig. 5.1, where two different Equilibrium Quantum Phase transitions (EQPTs) are present: one of them belongs to the universality class of the XX model (the quantum critical segment is $\gamma = 0$, $|h| < 1$) and the other is the phase transition of the 1D Quantum Ising model (the critical lines are given by $|h| = 1$). The EQPTs

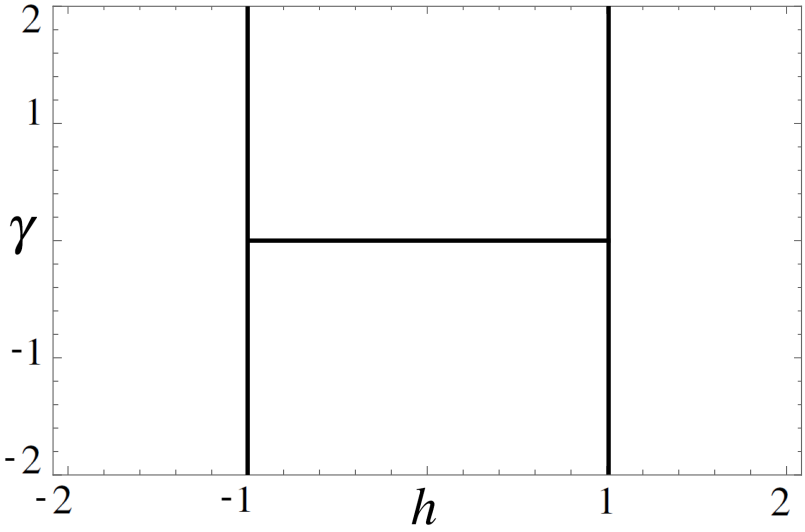

Figure 5.1: Phase diagram of the XY model as a function of the anisotropy γ and the external magnetic field h. The black lines represent the critical lines.

are visible in the spectrum $\epsilon_q(\gamma, h)$ as gap closings in the thermodynamic limit. In fact, one finds $\epsilon_q(\gamma, h) = \sqrt{(h - \cos q)^2 + \gamma^2 \sin^2 q}$, with $q = \frac{\pi}{N}(2n + 1)$ labelling the quasi-momentum of the fermions.
Explicitly, the diagonalized Hamiltonian in terms of fermionic quasi-particles reads, in the momentum representation,

$$H = \frac{1}{2} \sum_{q=0}^{\pi} \Phi_q^\dagger \begin{pmatrix} \epsilon_q(\gamma, h) & 0 \\ 0 & -\epsilon_q(\gamma, h) \end{pmatrix} \Phi_q, \tag{5.2}$$

where $\Phi_q^\dagger = \left(\chi_q^\dagger, \chi_{-q}\right)$ and χ_q is the quasi-particle fermionic operator.
Sudden quantum quenches of the form $(\gamma(t), h(t) = (\gamma_0\Theta(-t) + \gamma_1\Theta(t), h_0\Theta(-t) + h_1\Theta(t))$, where $\Theta(t)$ is the Heaviside step function, have been considered in connection to DQPTs. A DQPT is a non-analytic behavior, as a function of time, of the quantity

$$\mathcal{F}(t) = -\lim_{N\to\infty} \frac{1}{N} \ln \mathcal{G}(t). \tag{5.3}$$

Here, $\mathcal{G}(t) = \langle 0|0(t)\rangle$ is the Loshmidt overlap between the ground state $|0\rangle$ of the Hamiltonian for $t < 0$ and the time evolved state $|0(t)\rangle$ at time t. The quantity $F(t)$ bears similarities with the free energy, and hence its non-analiticities are to some extent analogous to phase transitions. As mentioned, the XY chain has the peculiarity that DQPTs can appear even for sudden quantum quenches in which the initial and the final values for h and γ can be connected in parameter space without passing a quantum critical point. At the same time, when the quantum quench takes place between points in parameter space that cannot be connected without going through an equilibrium critical point, it can happen that DQPTs are absent [84]. To better understand this intriguing phenomenon and in order to deepen the characterization of DQPTs, we inspect, in this Chapter, the fate of DQPTs when the quantum quench is not sudden.

5.1.1 Solution of the non-sudden quantum quench

We consider a time-dependent Hamiltonian of the form

$$H(t) = H(\gamma(t), h(t)), \tag{5.4}$$

where the quench protocol is encoded in the explicit time evolution of the model parameters, given by

$$\gamma(t) = \gamma_0 + (\gamma_1 - \gamma_0)Q_\gamma(t), \tag{5.5}$$

$$h(t) = h_0 + (h_1 - h_0)Q_h(t). \tag{5.6}$$

The function $Q_l(t)$, with $l = \gamma, h$, is determined by the quench duration τ and its functional dependence on time, which is left generic at this stage. In general, it is defined as

$$Q_l(t) = \begin{cases} 0 & t \leq 0 \\ \tilde{Q}_l(t) & 0 < t < \tau \\ 1 & t \geq \tau \end{cases} . \tag{5.7}$$

The time evolution of the fermionic operators diagonalizing the initial Hamiltonian $H(\gamma_0, h_0)$ can be formally obtained by means of the ansatz

$$\Phi_q^0(t) = \begin{bmatrix} \chi_q^0(t) \\ \chi_{-q}^{0\dagger}(t) \end{bmatrix} = \begin{bmatrix} f_{q,1}(t) & g_{q,1}(t) \\ f_{q,2}(t) & g_{q,2}(t) \end{bmatrix} \begin{bmatrix} \chi_q^0 \\ \chi_{-q}^{0\dagger} \end{bmatrix} = M_q(t)\Phi_q^0, \tag{5.8}$$

where the time dependence is transferred to the coefficients $f_{q,m}(t)$ and $g_{q,m}(t)$, with $m = 1, 2$. The initial conditions are given by $f_{q,1}(0) = g_{q,2}(0) = 1$ and $f_{q,2}(0) = g_{q,1}(0) = 0$. To ensure the validity of the anticommutation relations during the dynamics, the coefficients have to satisfy the condition $|f_{q,m}(t)|^2 + |g_{q,m}(t)|^2 = 1$, $\forall t$. The Heisenberg equation for the fermionic operators gives two coupled systems of differential equations for the time-dependent quantities, namely

$$\frac{dF_q(t)}{dt} = \frac{d}{dt}\begin{bmatrix} f_{q,1}(t) \\ f_{q,2}(t) \end{bmatrix} = \frac{1}{2i}\begin{bmatrix} a_q(t) & b_q(t) \\ b_q(t) & -a_q(t) \end{bmatrix}\begin{bmatrix} f_{q,1}(t) \\ f_{q,2}(t) \end{bmatrix} = \mathcal{M}_q(t)F_q, \tag{5.9}$$

$$\frac{dG_q(t)}{dt} = \frac{d}{dt}\begin{bmatrix} g_{q,1}(t) \\ g_{q,2}(t) \end{bmatrix} = \frac{1}{2i}\begin{bmatrix} a_q(t) & b_q(t) \\ b_q(t) & -a_q(t) \end{bmatrix}\begin{bmatrix} g_{q,1}(t) \\ g_{q,2}(t) \end{bmatrix} = \mathcal{M}_q(t)G_q. \tag{5.10}$$

where

$$a_q(t) = [h(t) - \cos q]\cos 2\theta_q(\gamma_0, h_0) + \gamma(t)\sin q \sin 2\theta_q(\gamma_0, h_0), \tag{5.11}$$

$$b_q(t) = [h(t) - \cos q]\sin 2\theta_q((\gamma_0, h_0)) - \gamma(t)\sin q \cos 2\theta_q(\gamma_0, h_0). \tag{5.12}$$

Here, $\theta_q(\gamma, h)$ is defined via $\tan 2\theta_q(\gamma, \theta) = \gamma \sin q/(h - \cos q)$.
We note that, in general, the system cannot be solved analytically during the quench, while it is easy to obtain the post-quench solution provided the correct matching conditions for $F_q(t)$ and $G_q(t)$ in $t = \tau$, obtained using numerical methods, are used. In the post-quench regime, the coefficients $a_q(t \geq \tau) = a_q(\tau)$ and $b_q(t \geq \tau) = b_q(\tau)$ are constant. In this case, we obtain

$$\begin{aligned} f_{q,1}(t \geq \tau) =& f_{q,1}(\tau)\cos[\epsilon_q(\gamma_1, h_1)(t - \tau)/2] + \\ & - i\,[f_{q,1}(\tau)\cos 2\Theta_q - f_{q,2}(\tau)\sin 2\Theta_q]\sin[\epsilon_q(\gamma_1, h_1)(t - \tau)/2], \end{aligned} \tag{5.13}$$

$$\begin{aligned} f_{q,2}(t \geq \tau) =& f_{q,2}(\tau)\cos[\epsilon_q(\gamma_1,h_1)(t-\tau)/2]+ \\ &+ i\left[f_{q,2}(\tau)\cos 2\Theta_q + f_{q,1}(\tau)\sin 2\Theta_q\right]\sin[\epsilon_q(\gamma_1,\theta_1)(t-\tau)/2], \end{aligned} \tag{5.14}$$

where $\Theta_q = \theta_q(\gamma_1,h_1) - \theta_q(\gamma_0,h_0)$. The solution for $G_q(t)$ can be obtained from F_q since $f_{q,1}(t) = g^*_{q,2}(t)$ and $f_{q,2}(t) = -g^*_{q,1}(t)$.
We are now able to evaluate the expectation values of the occupation numbers related to the fermionic operators $\chi^1_q, \chi^{1\dagger}_{-q}$ which diagonalize the final Hamiltonian $H(\gamma_1,h_1)$, over the initial state $|0\rangle$. Such occupation numbers are conserved quantities in the post-quench regime. We obtain

$$\begin{aligned} N^{\mathrm{GGE}}_q =& \langle 0|\chi^{1\dagger}_q\chi^1_q|0\rangle = \langle 0|\chi^{1\dagger}_{-q}\chi^1_{-q}|0\rangle = \\ =& |f_{q,1}(\tau)|^2\sin^2\Theta_q + |f_{q,2}(\tau)|^2\cos^2\Theta_q + 2\mathrm{Re}\left[f_{q,1}(\tau)f^*_{q,2}(\tau)\right]\cos\Theta_q\sin\Theta_q, \end{aligned} \tag{5.15}$$

where $|0\rangle$, as mentioned in Chapter 2, represents the ground state of the initial Hamiltonian $H(\gamma_0,h_0)$ and is defined as the vacuum of quasi-particles, i.e. $\chi^0_q(t<0)\,|0\rangle = 0$, for every q.

5.2 Loschmidt overlap

In this section we evaluate the Loschmidt overlap $\mathcal{G}(t)$ following a non sudden quantum quench. Thanks to the solution to the full dynamics of the fermionic operators previously outlined, it can be shown [145] that

$$\mathcal{F}(t) = -\frac{1}{\pi}\int_0^\pi dq \ln|f_{q,1}(t)|, \tag{5.16}$$

where in the post-quench regime Eq. 5.16 can be simplified by means of Eqs. 5.13 to obtain

$$\begin{aligned} \mathcal{F}(t \geq \tau) = -\frac{1}{\pi}\int_0^\pi dq \ln\Big| & f_{q,1}(\tau)\cos[\epsilon^1_q(t-\tau)/2] \\ & -i\left[f_{q,1}(\tau)\cos 2\Theta_q - f_{q,2}(\tau)\sin 2\Theta_q\right]\sin[\epsilon^1_q(t-\tau)/2]\Big|. \end{aligned} \tag{5.17}$$

We are therefore able to evaluate analytically the zeros of the log-function argument by rewriting it in the following form:

$$f_{q,1}(t \geq \tau) = \cos\left[\epsilon^1_q(t-\tau)/2 - \varphi_q\right], \tag{5.18}$$

where

$$\varphi_q = \arctan\left[-i(f_{q,1}(\tau)\cos 2\Theta_q - f_{q,2}(\tau)\sin 2\Theta_q)\right]. \tag{5.19}$$

Since φ_q is a complex function, we find the momenta q^*_i such that its imaginary part is vanishing. Hence, the times $t^*_{i,n}$ where the dynamical free energy shows a non-analytic behavior are given by:

$$t^*_{i,n} = \tau + \left[(2n+1)\pi + 2\varphi_{q^*_i}\right]/\epsilon^1_{q^*_i}. \tag{5.20}$$

Interestingly, the number of q_i^*, can vary as a function of the initial and final phases as well as the quench duration and protocol. Furthermore, every zero gives rise to a new non-equilibrium time scale in the dynamics. The typical result is shown in Fig. 5.2.

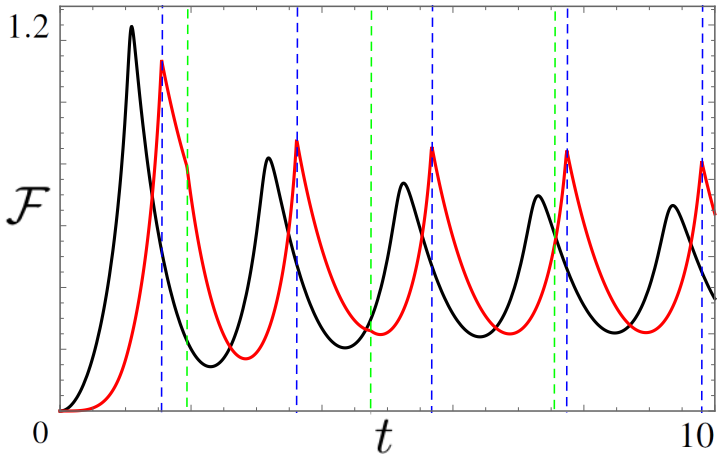

Figure 5.2: Appearance of DQPTs by manipulating the quench duration. The black solid line represents $\mathcal{F}(t)$ for a sudden quench, where no kinks can be observed. Performing a ramp of duration $\tau = 1$, the function $\mathcal{F}(t)$ (red solid line) acquire a non-analytical behavior and two inequivalent DQPTs build up, shown here as blue and green dashed lines. Quench parameters: $(h_0, \gamma_0) = (2, 2) \to (h_1, \gamma_1) = (-2, 2)$.

The quantity $\mathrm{Im}(\varphi_q)$, that sets the existence and the number of inequivalent DQPTs $\mathcal{N}$, strongly depends on the quench protocol. However, it can be inferred from the general discussion that will be presented in the following, that the sign of the quantities $\mathrm{Im}(\varphi_{0^+})$ and $\mathrm{Im}(\varphi_{\pi^-})$ only depends on the initial and the final values of the parameters. Moreover, at these two special points of the Brillouin zone, φ_q can be expressed as a simple function of the occupation numbers of the post-quench fermionic excitations as

$$\varphi_{0/\pi} = -i \operatorname{arctanh}[1 - 2N_{0/\pi}^{GGE,s}], \tag{5.21}$$

where $N_{0/\pi}^{GGE,s}$ correspond to a sudden quench and, therefore, does not depend on the quench protocol.
With this respect, we are now able to evaluate the sign of the function φ_q at the edges of the region we are inspecting. In particular, from Eq. (5.21), we deduce that every time the occupation numbers $N_{0/\pi}^{GGE,s}$ jump from 0 to 1 or viceversa, the sign of $\mathrm{Im}(\varphi_{\pi^-/0^+})$ changes accordingly. This relation is apparent in Fig. 5.3, where some prototypical examples of both these functions are plotted.

However, the peculiar behavior of the occupation numbers and, consequently, of the sign of the imaginary part of φ_q, is strictly related to the XY model phase diagram, illustrated in Chapter 2 and in particular in Fig. 5.1. Indeed, there is a well-defined correspondence between the phases connected by the quench, or rather the critical lines involved, and the value of the occupation numbers $N_q^{GGE,s}$ in $q = 0, \pi$.
The value of $N_0^{GGE,s}$, actually, is vanishing if the quench starts and finish in the

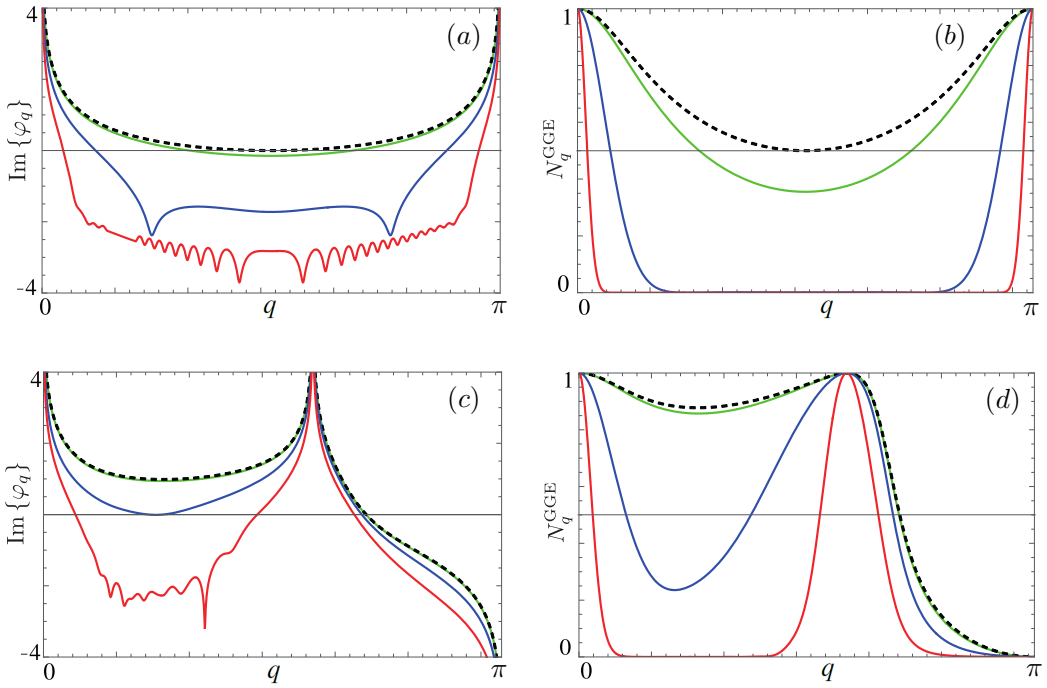

Figure 5.3: Plot of $\mathrm{Im}\{\varphi_q\}$ (left panels, (a) and (c)) and N_q^{GGE} (right panels, (b) and (d)) as a function of the momentum q for different values of the quench duration: $\tau = 0$ (black dashed), $\tau = 1$ (green), $\tau = 10$ (blue) and $\tau = 100$ (red). Quench parameters: Top figures (a) and (b) $(h_0, \gamma_0) = (2, 2) \to (h_1, \gamma_1) = (-2, 2)$; Bottom figures (c) and (d) $(h_0, \gamma_0) = (2, -2) \to (h_1, \gamma_1) = (-0.5, 0.2)$.

same phase, while it jumps to 1 when the $h = 1$ critical line separates the initial and final phases connected by the quench. On the other hand, but analogously, $N_\pi^{GGE,s}$ have the same jump when the $h = -1$ critical line is involved. The mentioned feature can be analytically observed by inspecting Eq. (5.15) in the particular cases outlined. The number $\mathcal{N}$ of zeros of $\mathrm{Im}(\varphi_q)$ can hence be argued. Nevertheless, the argument is not straightforward since a third independent non-analytical behavior of the occupation numbers as a function of the quench parameters can occur. Going back to the model phase diagram, we note that the horizontal critical segment $\gamma = 0$ has not yet been considered. Such equilibrium critical line may give rise, in particular circumstances, to an additional infinity in $\mathrm{Im}(\varphi_{\bar{q}})$, with

$$\bar{q} = \arccos\left(\frac{h_0\gamma_1 - h_1\gamma_0}{\gamma_1 - \gamma_0}\right), \tag{5.22}$$

i.e. if $\bar{q} \in \mathbb{R}$. However, given the continuity of the occupation numbers N_q^{GGE} and the relation

$$\mathrm{Im}(\varphi_q) \sim -\mathrm{arctanh}[1 - 2N_q^{GGE}] \tag{5.23}$$

in the proximity of $q = 0, \pi, \bar{q}$, we observe that $\mathrm{Im}(\varphi_q)$ does not change sign in the proximity of these non-analytical points. We can conclude, therefore, that the number of its zeros $\mathcal{N}$, irrespective of what happens in $q = \bar{q}$, is even(odd) if $\mathrm{Sgn}[\mathrm{Im}(\varphi_0)] \cdot \mathrm{Sgn}[\mathrm{Im}(\varphi_0)]$ is even (odd). If we transpose the argument on the occupation numbers, we obtain that, analogously, the number of zeros of $\mathrm{Im}(\varphi_q)$ is

even if $N_0^{GGE,s} = N_\pi^{GGE,s}$ and odd if $N_0^{GGE,s} \neq N_\pi^{GGE,s}$.

Note that, importantly, the usual paradigm stating that the DQPTs occur whenever the occupation number of the quasi-particle states crosses 1/2 is here violated, as also observed for non-sudden quantum quenches in the Ising model [145]. Even more significant is the fact that despite the number of zeros in $\mathrm{Im}(\varphi_q)$ can vary as the quantum quench duration is changed, as already discussed for a generalized XY-like spin model [146], the parity of such number only depends on the initial and final parameters. With respect to DQPTs, the quantum quenches in the XY chain in a transverse field can hence be classified on the basis of the parity of DQPTs they induce. This is the main result we have achieved. In the next section we exhibit a topological invariant that allows us to put this $\mathbb{Z}_2$ classification on a more formal basis. Note that this classification allows us to make a distinction between quantum quenches that can show or not DQPTs depending on the quantum quench duration and those that are bounded to show DQPTs. According to the initial and final parameters one can hence have 'robust' (odd parity) or non-robust (even parity) DQPTs.

5.3 Dynamical topological invariant

Following Chen's work [147], we first introduce a Dynamical Topological Invariant for the case of a sudden quantum quench. We then generalize it to the finite-duration quench case and draw a connection to the parity of the DQPTs in the XY chain in a transverse magnetic field.
We start by considering the most general gapped 1D two band Hamiltonian with discrete translational symmetry. In the momentum representation, the Hamiltonian can be represented as the sum of two level systems, and, k by k, it reads

$$h(k,g) = d_i(k,g)\mathbb{I} + \vec{d}(k,g)\cdot\vec{\sigma}. \tag{5.24}$$

Here, k is an index for the quasi-momentum, g represents a set of parameters appearing in the Hamiltonian, $\mathbb{I}$ is the 2×2 identity matrix, $\vec{d}(k,g)$ is a three-vector and $\vec{\sigma}$ is the vector containing the Pauli matrices. The related density matrix diagonal elements are given by

$$\rho_\pm(k,g) = |\psi_\pm(k,g)\rangle\langle\psi_\pm(k,g)| = \frac{1}{2}\left[1 \pm \hat{d}(k,g)\cdot\vec{\sigma}\right], \tag{5.25}$$

where $|\psi_\pm(k,g)\rangle$ are the Hamiltonian eigenvectors, with $|\psi_-(k,g)\rangle$ lower (or equal) in energy, and $\hat{d}(k,g) = \vec{d}(k,g)/|\vec{d}(k,g)|$.
We now consider a sudden quench transforming the initial Hamiltonian $h(k,g_0)$ into $h(k,g_1)$, and we study the non-equilibrium properties of the system if it is prepared in the ground state of $h_0(k,g_0)$. By means of the Liouville-Von Neumann equation, we obtain the time evolution of the density matrix. Explicitly we have

$$\rho(k,g_1,t) = \frac{1}{2}\left[1 - \tilde{d}(k,g_0,g_1,t)\cdot\vec{\sigma}\right], \tag{5.26}$$

where

$$\begin{aligned}\tilde{d}(k,g_0,g_1,t) =& \hat{d}(k,g_0)\cos\left[2|\vec{d}(k,g_1)|t\right] + \hat{d}(k,g_1)\left[\hat{d}(k,g_0)\cdot\hat{d}(k,g_1)\right]\sin^2\left[|\vec{d}(k,g_1)|t\right] \\ &+ \hat{d}(k,g_0)\times\hat{d}(k,g_1)\sin\left[2|\vec{d}(k,g_1)|t\right].\end{aligned} \tag{5.27}$$

Note that $\tilde{d}(k,g_0,g_1,t)$ is a periodic function both of time, with periodicity $\pi/|\vec{d}(g_1,k)|$, and momentum, with periodicity 2π. This means that the topology of the Brillouin zone, as well as of time, is S^1 so that the momentum-time manifold has, in general, a topology T^2. However, it can happen for some points k_m in the BZ (called here fixed points), that the vector $\tilde{d}(k,g_0,g_1,t)$ does not evolve in time. This translates to a momentum-time manifold that becomes a set of spheres S^2, the number of which equals the number of fixed points. These two scenarios are sketched in Fig. 5.4. It is hence possible to define the Chern numbers

$$C^m_{\rm dyn} = \frac{1}{4\pi}\int_{k_m}^{k_{m+1}} dk \int_0^{\pi} dt' \left(\tilde{d}(k,g_0,g_1,t)\times\partial_{t'}\tilde{d}(k,g_0,g_1,t)\right)\cdot\partial_k\tilde{d}(k,g_0,g_1,t), \tag{5.28}$$

where the time has been rescaled to $t' = t/|\vec{d}(k,g_1)|$.

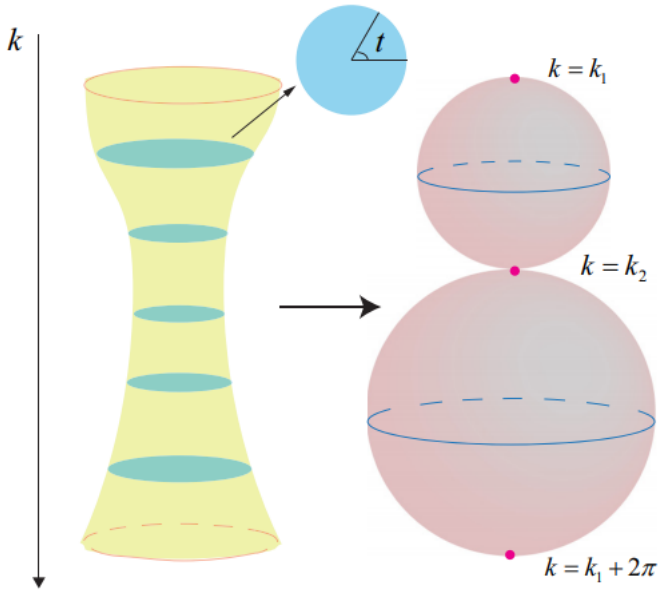

Figure 5.4: Scheme of the momentum-time manifold. In the left figure, for any fixed momentum k, the cross section can be viewed as a circle S^1 where the azimuthal angle represents the time t. After gluing $k = 0$ and $k = 2\pi$, the topology of the momentum-time manifold becomes T^2. If there are two fixed points $k = k_1$ and $k = k_2$, the corresponding circle contracts to a point, then the momentum-time manifold can be reduced to a series of spheres S^2. Figure based on [147].

The number $C^m_{\rm dyn}$ indicates if the mapping from the corresponding momentum-time sub-manifold to the Bloch vector is trivial ($C^m_{\rm dyn} = 0$) or not ($C^m_{\rm dyn} = \pm 1$).

Going back to the sudden quantum quenches in the XY model, after recasting the Hamiltonian into the form of Eq.(5.24), one finds

$$C^m_{\rm dyn} = \frac{\cos(2\Theta_{k_m}) - \cos(2\Theta_{k_{m+1}})}{2}. \tag{5.29}$$

Moreover, $k = 0$ and $k = \pi$ are always fixed points and, at every fixed point, $\cos(2\Theta_{k_j}) = \pm 1$.
Of particular interest is the quantity

$$C_{\rm dyn} = \sum_{k_m \in [0,\pi]} C^m_{\rm dyn} = \frac{1}{2}\left(\cos 2\Theta_0 - \cos 2\Theta_\pi\right) = N^{GGE,s}_\pi - N^{GGE,s}_0. \tag{5.30}$$

In fact one finds $C_{\rm dyn} = 0$ if the population of the quasiparticles in $k = 0$ is equal to the population at $k = \pi$, while we have $C_{\rm dyn} = \pm 1$ if the populations are different. This fact draws an interesting link between the robustness of the DQPTs with respect to the duration of the quench and the topological number associated to the sudden quenches.
However, with respect to the topological indexes, the scenario in the case of non sudden quantum quenches is in principle rather different. In Eq.(5.27), instead of the unit vector $\hat{d}(k, g_0)$, the evolution for $t > \tau$ is regulated by the unit vector $\hat{d}'(k, g_0, \tau)$ describing the quantum state at time τ. Since however the unit vector $\hat{d}'(k, g_0, \tau)$ cannot, in general, be found analytically, universal statements becomes a priori unlikely. The fixed points can be obtained by studying the transformation which connects the two diagonalizing basis of the initial (H_0) and final (H_1) Hamiltonians, namely

$$\Phi^1_q = \begin{bmatrix} \chi^1_q \\ \chi^{1\dagger}_{-q} \end{bmatrix} = \begin{bmatrix} \cos\Theta_q & -\sin\Theta_q \\ \sin\Theta_q & \cos\Theta_q \end{bmatrix} \begin{bmatrix} \chi^0_q \\ \chi^{0\dagger}_{-q} \end{bmatrix} = \mathcal{B}_q \Phi^0_q \,. \tag{5.31}$$

The transformation matrix $\mathcal{B}_q$, evaluated in the fixed point $q = k_m$, is the identity matrix if the corresponding critical line is crossed an even number of times, while it is $i\sigma^y$ otherwise. Crucially, as previously discussed, $k = 0$ and $k = \pi$ are fixed points even in the case of finite duration quantum quenches. This behaviour is due to the fact that one has

$$\partial_t \hat{d}(0/\pi, t) = 2\left[0, 0, a_{0/\pi}(t)\right] \times \hat{d}(0/\pi, t), \tag{5.32}$$

with initial condition given by $\hat{d}(k, 0) = [0, 0, a_{0/\pi}(0)]$. Hence, explicitly, $\hat{d}(k, t) = \hat{d}(k, 0)$ for $0 < t < \tau$, so that this points are not affected by the quench protocol or its duration. The time evolution, once the final Hamiltonian has been reached, is hence given by Eq. 5.27, as in the sudden quench case. The sum of the dynamical topological invariants $C_{\rm dyn}$ in half of the BZ is then independent of the quench duration, even if the single $C^m_{\rm dyn}$ are not. In particular, whenever $C_{\rm dyn} = 0$, DQPTs are not robust and can be cancelled out (created) increasing the quench duration if in the sudden quench regime they are present (absent). When $C_{\rm dyn} = \pm 1$, on the other hand, by varying the quench duration it is not possible to find a quench protocol where DQPTs disappear. So, the number of points in the momentum space which give rise to non-analyticities (see Eq. 5.20) can vary as a function of the quench duration and protocol, but its parity is determined solely by the initial and final Hamiltonian and coincides with $C_{\rm dyn}$.

5.4 Summary

The results presented demonstrate that, within a model as simple as the XY chain in a transverse field, the effect of the time duration of quantum quenches can be dramatic. In fact, the number and the very existence of DQPTs strongly depend on the quench duration. However, surprisingly, the parity of the DQPTs is fixed once the initial and final parameters are fixed. We have associated this behaviour to a new topological invariant that essentially counts the parity of the number of k-states that evolve trivially in time after the quantum quench.

CHAPTER 6

Feasible model for interband pairing

In this Chapter, we present our original findings published in [17].
The details of the calculations, not shown here, are reported in Appendix C.

The realization of normal [148–151] and superconducting [152, 153] topological states of matter and materials with strong spin-orbit coupling [92, 154] has been recently achieved, and may lead to substantial advances in spintronics [155], superconducting spintronics [156], and topological quantum computation [157]. Most of these accomplishments strongly rely on the ability to precisely control the atomic structure of matter or on the ability to perform nanostructuring [152, 153]. Static external perturbations, such as pressure [158] and magnetic fields [159], are also routinely used to qualitatively alter the properties of quantum materials.
A complementary way of engineering quantum states on demand is to perturb solid state quantum systems in a time-dependent fashion, such as manipulating system parameters in the context of quantum quenches. In particular, intense short electromagnetic pulses and periodic (Floquet) drivings have been proven to be extremely powerful tools . Short electromagnetic pulses, which in the pump-probe setups allow for the study of ultra-fast dynamics [160], can, for example, induce phase transitions [161] and drive higher harmonic generation [162]. Periodic drivings allow to induce topological band structures and boundary states [135], and to create new phases of matter, such as time-crystals [163].
An important sub-field of time-dependent quantum engineering in solids deals with the control of the superconducting order parameter. The importance of non-constant perturbations on the superconducting order parameter has been known for a long time [164–166]. Recently, however, the technological progress in the generation of intense sub-picosecond laser pulses, determined a renewed interest in the field [20]. Striking signatures of transient out of equilibrium superconductivity have been observed in cuprates and doped fullerenes: the ultimate aim is to engineer room temperature superconductivity, although serious limitations like heating still need to be overcome. All these observations have been associated to the action of the laser on lattice degrees of freedom, in particular optical phonons, e.g to light-enhanced

electron-phonon coupling. In the context of doped fullerenes, a possible electronic mechanism for intralevel pairing has been conjectured [167].

A novel scheme for generating interband superconducting pairing in periodically driven semiconductors has been proposed in Refs. [168, 169]. In this case, however, the laser couples to the electronic degrees of freedom, and the crucial interplay of driving and dissipation leads to a steady state characterized by superconducting correlations.
The original proposals for such a state relied on particular fermionic dissipative baths able to exchange particles with the two bands of the semiconductor involved in the interband pairing or on effective simplified master equations. Moreover, a finite value of the order parameter in the steady state required the concurrent tuning of band dispersion and electronic interactions.
In this chapter, we develop a more realistic model for steady state interband superconductivity. We consider a two-band semiconductor resonantly driven by a laser, and we include two physically relevant intraband relaxation processes, namely acoustic phonons and radiative recombination. The steady state reached by the system, for which we provide a phase diagram, can develop interband superconducting correlations. Here, we present our original findings published in [17].

6.1 Equilibrium interband superconductivity

In this first section, we briefly address the problem of the pairing between electrons and its implications in the case of multiple bands. Starting from the standard Bardeen-Cooper-Schrieffer (BCS) theory in a one-band scenario, we generalize the results and we introduce a simple model [170] which shows unconventional pairing between electrons in a wide range of the parameters. Furthermore, this equilibrium model will allow us to better interpret our non-equilibrium results (see Section 6.4).

6.1.1 One-band systems

The great achievement of the BCS theory was to recognize that the ground state of a super- conductor is a coherent superposition of pairs of electrons, and that the lowest energy configuration would generally pair electrons of opposite momenta [171, 172]. With this assumption, we can learn a great deal about the possible symmetries of the electron pairs, without worrying about what physically binds them together. In a lattice system with time reversal symmetry, such as a nonmagnetic metal in zero field, Kramer's theorem [173] guarantees that there is always a degenerate doublet of single-particle states connected by time reversal $\mathcal{T}$, such that

$$|\boldsymbol{k},\sigma\rangle \qquad \text{and} \qquad \mathcal{T}\,|\boldsymbol{k},\sigma\rangle = |-\boldsymbol{k},-\sigma\rangle\,. \tag{6.1}$$

In this context, it is straightforward to argue within BCS theory that pairing time-reversed states will necessarily give the lowest energy: Suppose instead that we paired the two electrons $|\boldsymbol{k}+\boldsymbol{q}/2,\sigma\rangle$ and $|-\boldsymbol{k}+\boldsymbol{q}/2,-\sigma\rangle$ for some $\boldsymbol{q}$. This would correspond to a pair with total momentum $\boldsymbol{q}$, i.e. an excess of kinetic energy compared to our first choice.

Proceed, we can suppose that the pair wave-function of the system is represented by the so-called "anomalous amplitude", defined as

$$b_{\boldsymbol{k}} = \langle c_{-\boldsymbol{k},\uparrow} c_{\boldsymbol{k},\downarrow} \rangle_{\mathrm{BCS}} \,. \tag{6.2}$$

Here, the average is taken over the BCS ensemble [171], that is, self-consistently over an effective particle non-conserving Hamiltonian. Suppose now that in addition our system is centrosymmetric, i.e. parity $\mathcal{P}$ is a good quantum number. Then

$$|\boldsymbol{k},\sigma\rangle \qquad \text{and} \qquad \mathcal{P}\,|\boldsymbol{k},\sigma\rangle = |-\boldsymbol{k},\sigma\rangle \,. \tag{6.3}$$

are also degenerate. We may then define a more general order parameter pairing any of the four states

$$|\boldsymbol{k},\uparrow\rangle \,, \quad |-\boldsymbol{k},\uparrow\rangle \,, \quad |\boldsymbol{k},\downarrow\rangle \,, \quad |-\boldsymbol{k},\downarrow\rangle \tag{6.4}$$

as

$$b_{\boldsymbol{k},\sigma,\sigma'} = \langle c_{-\boldsymbol{k},\sigma} c_{\boldsymbol{k},\sigma'} \rangle_{\mathrm{BCS}} \tag{6.5}$$

which is a 2×2 matrix in spin space. The Pauli principle imposes that the 2-particle wave-function must be anti-symmetric under exchange of all particle indices, i.e.

$$b_{-\boldsymbol{k},\sigma',\sigma} = -b_{\boldsymbol{k},\sigma,\sigma'}. \tag{6.6}$$

Eventually, this argument leads to the following classification, which covers all the possible cases (we here neglect the peculiar cases in which odd-frequency pairing is developed):

1) $b_{\boldsymbol{k}}$ is even under the transformation $\boldsymbol{k} \to -\boldsymbol{k}$, therefore it has to be odd under spin exchange (singlet, $S = 0$):

$$b_{\boldsymbol{k},\sigma,\sigma'} = b_{-\boldsymbol{k},\sigma,\sigma'} = -b_{\boldsymbol{k},\sigma',\sigma}. \tag{6.7}$$

2) $b_{\boldsymbol{k}}$ is odd under the transformation $\boldsymbol{k} \to -\boldsymbol{k}$, therefore it has to be even under spin exchange (triplet, $S = 1$):

$$b_{\boldsymbol{k},\sigma,\sigma'} = -b_{-\boldsymbol{k},\sigma,\sigma'} = b_{\boldsymbol{k},\sigma',\sigma}. \tag{6.8}$$

Note that the first step in each chain of equalities is the statement of definite parity, the second one is the application of the Pauli's principle.

6.1.2 Orbital symmetry

At this point, it is fruitful to use one further important result from BCS theory: Electrons pair over a narrow shell of energies near the Fermi surface, creating an instability of the Fermi sea. In this case the matrix $b_{\boldsymbol{k}}$ in Eq. (6.5) is non-zero only on the vicinity of the Fermi surface. We can expand any function on a surface in terms of some set of surface harmonics chosen to be orthonormal to one another on the given surface [174]. In the simplest, spherical symmetric case, we know how to expand $b_{\boldsymbol{k}}$ in terms of the spherical harmonics $Y_{lm}(\theta,\phi)$, where θ is the polar and

ϕ the azimuthal angles of the unit vector $\hat{k}$ normalized on the sphere of radius k_F, which corresponds to the Fermi wave-vector, to obtain

$$b_{\hat{k}} = b_0 + \sum_{m=-1}^{1} b_{1m} Y_{1m} + \sum_{m=-2}^{2} b_{2m} Y_{2m} + ... \tag{6.9}$$

We also know that for the considered centrosymmetric system the order parameter $b_{\hat{k}}$ should have definite parity, i.e. only even or odd l-terms can be nonzero. It is furthermore quite likely that given a set of b_{lm} in the ground state, only one will be important. Indeed, treated independently, each one may be shown within BCS theory to correspond to a critical temperature which varies like [171]

$$T_c^l \simeq \omega_D e^{1/N_0 V_l}, \tag{6.10}$$

where N_0 is the density of states at the Fermi level and V_l is component of the pairing interaction, expanded similarly, in the l-th angular momentum channel:

$$V_{\boldsymbol{k},\boldsymbol{k}'} = V_0 + V_1 Y_{1m}(\hat{k}) Y_{1m}(\hat{k})^* + ... \tag{6.11}$$

The exponential dependence of T_c^l on the interaction V_l means that unless two channels are nearly degenerate, one will necessarily win and dominate over nearly the entire temperature range. We can therefore speak of a s-, p-, d-, ... wave orbital symmetry of the order parameter, meaning the function $b_{\hat{k}}$ is proportional to $Y_l(\hat{k})$ with $l = 0, 1, 2, ...$. The parity constraints on the b_{lm}, hence, mean that

1) a spin singlet order parameter has orbital symmetry s, d, ...

2) a spin triplet order parameter has orbital symmetry p, f, ...

6.1.3 Multi-band systems

The preceding section shows that for the situation we considered, where we labelled states only by $|\boldsymbol{k}, \sigma\rangle$ since the only degrees of freedom involved are orbital symmetry and spin, spin singlet pair states must be even parity and spin triplet pair states, conversely, odd parity, to satisfy the Pauli's principle. This conclusion did not make use of any particular property of the electronic bands, since we have focused on the one-band scenario.

It is interesting to focus on the case where an additional degree of freedom is taken into account: In particular we add the quantum number ν relative to the band index. For the sake of simplicity, in this section we will deal with a two-band system, since it will be the only relevant one in the following discussion.
The electrons pair is then described by a wave-function which has to fulfill

$$b_{\boldsymbol{k},\sigma,\nu,\sigma',\nu'} = -b_{-\boldsymbol{k},\sigma',\nu',\sigma,\nu} \ . \tag{6.12}$$

All the admitted possibilities are, this time, four:

1) $b_{\boldsymbol{k}}$ is even under the transformation $\boldsymbol{k} \to -\boldsymbol{k}$, therefore it can be:

a) odd under spin exchange (singlet, $S = 0$) and even under band exchange

$$b_{\boldsymbol{k},\sigma,\nu,\sigma',\nu'} = b_{-\boldsymbol{k},\sigma,\nu,\sigma',\nu'} = -b_{\boldsymbol{k},\sigma',\nu,\sigma,\nu'} = b_{\boldsymbol{k},\sigma,\nu',\sigma',\nu} \tag{6.13}$$

b) even under spin exchange (triplet, $S = 1$) and odd under band exchange

$$b_{\boldsymbol{k},\sigma,\nu,\sigma',\nu'} = b_{-\boldsymbol{k},\sigma,\nu,\sigma',\nu'} = b_{\boldsymbol{k},\sigma',\nu,\sigma,\nu'} = -b_{\boldsymbol{k},\sigma,\nu',\sigma',\nu} \tag{6.14}$$

2) $b_{\boldsymbol{k}}$ is odd under the transformation $\boldsymbol{k} \to -\boldsymbol{k}$, therefore it can be:

a) odd under spin exchange (singlet, $S = 0$) and odd under band exchange

$$b_{\boldsymbol{k},\sigma,\nu,\sigma',\nu'} = -b_{-\boldsymbol{k},\sigma,\nu,\sigma',\nu'} = -b_{\boldsymbol{k},\sigma',\nu,\sigma,\nu'} = -b_{\boldsymbol{k},\sigma,\nu',\sigma',\nu} \tag{6.15}$$

b) even under spin exchange (triplet, $S = 1$) and even under band exchange

$$b_{\boldsymbol{k},\sigma,\nu,\sigma',\nu'} = -b_{-\boldsymbol{k},\sigma,\nu,\sigma',\nu'} = b_{\boldsymbol{k},\sigma',\nu,\sigma,\nu'} = b_{\boldsymbol{k},\sigma,\nu',\sigma',\nu} \tag{6.16}$$

Note that the first step in each chain of equalities is the statement of definite parity, the second one is the application of the spin exchange and the third one of the band index exchange. Furthermore, the new, "exotic" possibilities 1b) and 2a) involve pairing electrons in different bands.
It is important to observe that all we have done so far is to enumerate the possible symmetry classes of the presumed BCS pair amplitude. Of the various possibilities thus identified, one will be chosen by the system as the temperature is lowered. Which one dominate is determined by the interaction $V_{\boldsymbol{k},\boldsymbol{k}'}$, which depends on many aspects of the system.

6.1.4 Interband pairing in a simple model

Now that the problem of how electrons in different bands can pair is set, we address qualitatively the issue of its stability, by studying the two-band simplified model with interband pairing proposed in Ref. [170] and given by the Hamiltonian

$$H = \sum_{\boldsymbol{k},\alpha,\sigma} \epsilon_\alpha(\boldsymbol{k}) c^{\alpha\dagger}_{\boldsymbol{k},\sigma} c^{\alpha}_{k,\sigma} + V \sum_{\boldsymbol{k},\alpha\neq\beta} \left(c^{\alpha\dagger}_{\boldsymbol{k},\uparrow} c^{\beta\dagger}_{-\boldsymbol{k},\downarrow} + h.c. \right), \tag{6.17}$$

where $\alpha, \beta = 1, 2$ label two bands that are not hybridized, σ is the spin projection and

$$\epsilon_\alpha(\boldsymbol{k}) = -\frac{k^2}{2m_\alpha} + C \tag{6.18}$$

which gives parabolic bands that are degenerate at $k = 0$ with energy C and with a chemical potential set to zero. The interaction V is the product of an attractive potential V_0 between electrons in the two different bands and a mean-field parameter Δ determined by minimizing the total energy. For simplicity, we have considered the pair wavefunction with s-wave symmetry. Using the Bogoliubov-de Gennes representation, is it possible to diagonalize the Hamiltonian to obtain the following four energy eigenvalues

$$E(\boldsymbol{k}) = \pm \left[\frac{\epsilon_1 - \epsilon_2}{2} \pm \sqrt{\left(\frac{\epsilon_1 + \epsilon_2}{2} \right)^2 + V^2} \right]. \tag{6.19}$$

In the nontrivial case of V different from zero, the bands $\pm E_A$ and $\pm E_B$ result from the hybridization of the ϵ_1 and ϵ_2 bands due to V. It is interesting to observe that an internal gap opens at the crossing of bands E_A with $-E_B$ above the chemical potential and between E_B and $-E_A$ below the chemical potential, as indicated with circles in Fig. 6.1, where results for $V = 0.5$ are displayed. Interestingly, the two Fermi surfaces existent in the non-interacting regime get closer, i.e. $k'_{F1} > k_{F1}$ and $k'_{F2} < k_{F2}$ and, for sufficiently strong V, merge and then disappear.

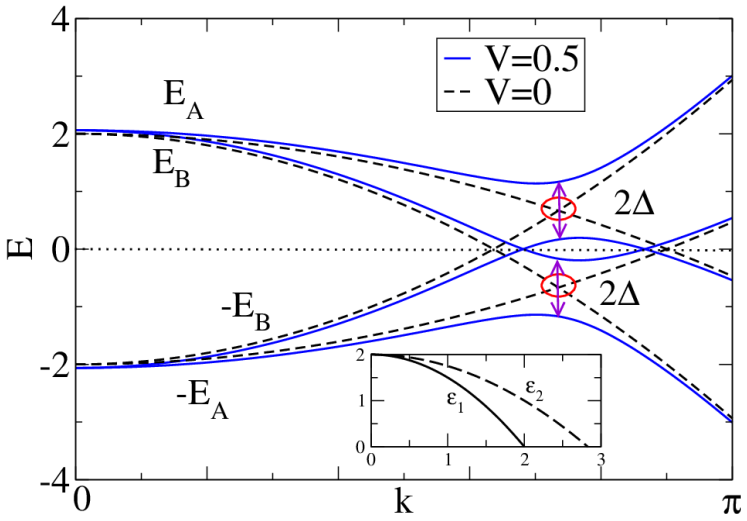

Figure 6.1: Mean-field band dispersion for the model defined by Eq. (6.17), for the indicated values of V defined in the text as a function of the momentum k in the Brillouin zone. The case shown is for $m_1 = 1$, $m_2 = 2$, and $C = 2$. Inset: noninteracting band dispersion for the same parameters. Figure based on [170].

To have a deeper understanding of the physical meaning of these features, we focus now on the band-resolved fermions occupation numbers, defined as

$$n_\alpha(\boldsymbol{k}) = \sum_\sigma c^{\alpha\dagger}_{\boldsymbol{k},\sigma} c^{\alpha}_{\boldsymbol{k},\sigma}, \tag{6.20}$$

and on the total electronic occupation of the system, given by

$$n(\boldsymbol{k}) = \sum_\alpha n_\alpha(\boldsymbol{k}). \tag{6.21}$$

These quantities behavior is shown in Figure 6.2 as a function of the momentum in the Brillouin zone, in the weak (top panel) and strong (bottom panel) attraction regimes. In the first case, jumps indicate the existence of the two Fermi surfaces, which are here present even in the paired state. Thus, electrons in the region in between the two Fermi surfaces behave like normal unpaired electrons. As the interaction V increases further, the number of unpaired electrons is reduced, until a full gap opens in the system. Its physics, now, resembles BCS theory, except for the fact that Cooper pairs are constituted by electrons from different orbitals. All the particles around the two non-interacting Fermi surfaces, at this point, participate in the pairing.
Summarizing, three scenarios arise and strongly depend, as one could expect, on the

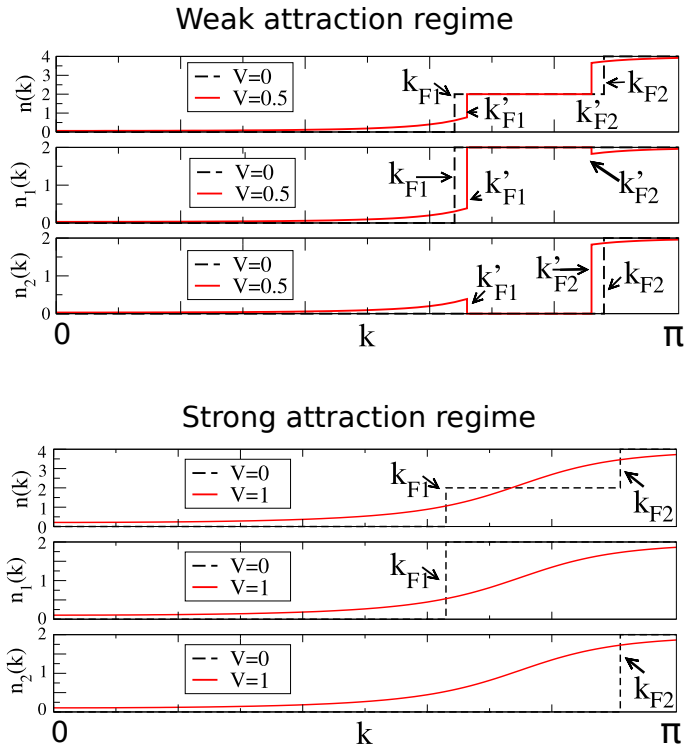

Figure 6.2: Mean-field state population as a function of momentum along the diagonal $k_x = k_y$ for (a) the whole system, (b) band 1, and (c) band 2 for the indicated values of the pairing potential V, and $m_1 = 1$, $m_2 = 2$, and $C = 2$.
Top panel: The case $V = 0.5$ illustrates the "weak" pairing attraction regime. Bottom panel: The case $V = 1$ illustrates the "strong" pairing attraction regime. Figure adapted from [170].

attractive interaction strength: When $V \simeq 0$, no electrons pair and a normal regime where the ground state is not superconducting persists; increasing V, an exotic intermediate "breached" regime appears, where gaps open at the original Fermi surfaces while new Fermi surfaces defining regions containing unpaired electrons are created; finally, a superconducting regime resembling BCS states, at large attractive coupling, is found.

A study of the stability issue, however, proves that the purely interband-paired state only becomes stable when the attraction is sufficiently strong that no unpaired particles are left, so that the breached regime is not physically relevant. This means that, although the pairs would be formed by electrons in different orbitals, the physics is analogous to the one described by the BCS one-band theory.

6.2 Laser-driven two bands semiconductor

Here we start to analyze a d-dimensional semiconductor with only two non-degenerate bands close to the Fermi energy, namely, the valence ($\alpha = 1$) and conduction ($\alpha = 2$) bands. These are coupled by means of a laser, whose frequency is tuned at resonance around a single point in the Brillouin zone (BZ), where the band distance is E_g. Our main goal is to understand if a superconducting pairing, whose amplitude is computed self-consistently by taking electron-electron interactions into account, is allowed and can develop in the system in a stable non-equilibrium steady state. The system is described by the Hamiltonian $H_{\rm sys} = H_0 + H_{\rm int}$, where ($\hbar = 1$, lattice constant $a = 1$)

$$H_0 = \sum_{\boldsymbol{k},\alpha} E_\alpha(\boldsymbol{k}) c^{\alpha\dagger}_{\boldsymbol{k}} c^{\alpha}_{\boldsymbol{k}} + \Omega(t) \sum_{\boldsymbol{k},\alpha,\beta} c^{\alpha\dagger}_{\boldsymbol{k}} \sigma^{x}_{\alpha\beta} c^{\beta}_{\boldsymbol{k}} \,, \tag{6.22}$$

$$H_{\rm int} = \frac{i}{2}\Delta \sum_{\boldsymbol{k},\alpha,\beta} c^{\alpha\dagger}_{\boldsymbol{k}} \sigma^{y}_{\alpha\beta} c^{\beta\dagger}_{-\boldsymbol{k}} - \frac{i}{2}\Delta^* \sum_{\boldsymbol{k},\alpha,\beta} c^{\alpha}_{\boldsymbol{k}} \sigma^{y}_{\alpha} c^{\beta}_{-\boldsymbol{k}} \,. \tag{6.23}$$

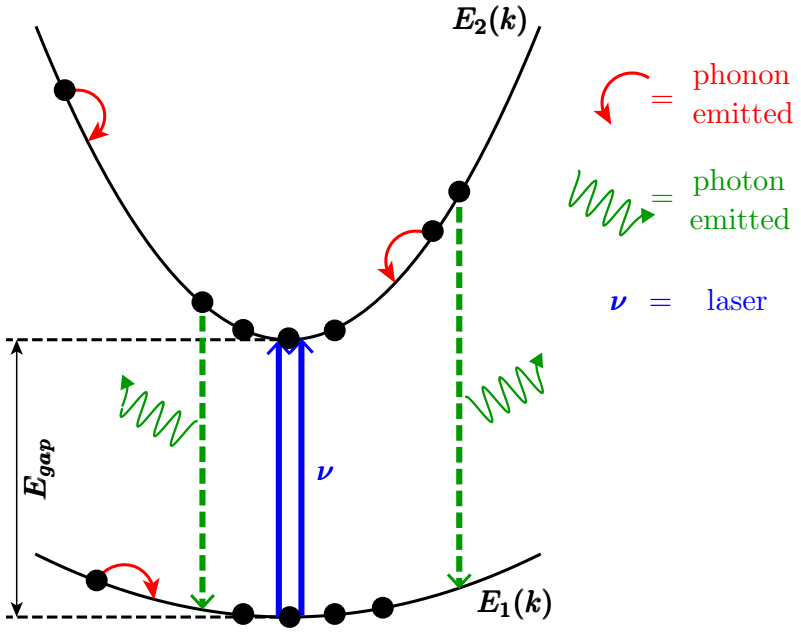

Figure 6.3: Sketch of a restricted momentum region of the two bands in presence of a laser (blue double arrow) tuned to a frequency ν equal to the amplitude of the band distance E_g at $\boldsymbol{k} = 0$. Emission of intraband acoustic phonons (red curved arrows) and radiative recombination (green dashed arrows) accompanied by photon emissions (green waved arrows) are indicated.

Here $c^{\alpha}_{\boldsymbol{k}}$ is the fermionic annihilation operator in the α-band with momentum $\boldsymbol{k}$, $E_\alpha(\boldsymbol{k})$ is the α-band dispersion relation, $\Omega(t) = \Omega\cos(\nu t)$ is set by the laser frequency ν and the Rabi frequency Ω. Moreover, the complex order parameter Δ quantifies the Cooper pairing between electrons in different bands and is defined as

$$\Delta^* = \frac{V}{N} \sum_{\boldsymbol{k}} \langle c^{2\dagger}_{\boldsymbol{k}} c^{1\dagger}_{-\boldsymbol{k}} \rangle \,, \tag{6.24}$$

where V parametrizes the strength of electron-electron interactions and N is the number of electrons in the system. Since the relevant part of the dynamics takes place in a small region of the k-space around the resonance point that we conventionally fix to be $\boldsymbol{k} = 0$, we could assume $V(\boldsymbol{k})$ to be k-independent. It is worth to notice that, differently from Δ, the parameter V does not have to be computed self-consistently, since it parameterizes the bare, repulsive, electron-electron interaction. Moreover, again due to the fact that the physics takes place in a small region in k-space, we expand the dispersion relation up to second order (We imagine the two bands to be separated outside the region in momentum space that we consider. They can, for instance, bend down.). For simplicity we postulate spherical symmetry,

$$E_\alpha(\boldsymbol{k}) = A_\alpha \boldsymbol{k}^2 + (-1)^\alpha E_g/2. \tag{6.25}$$

For technical reasons that will be explained below, we consider the scenario where the conduction and valence bands have same effective mass sign, i.e. $A_1, A_2 > 0$, in the BZ window where the laser is resonant. Furthermore, in order to get a realistic picture of the system (see Fig. 6.3), we study the effect of two relevant bosonic baths, namely the phonons and the radiative field.

As far as phonons are concerned, we consider the acoustic branch, described by the Hamiltonian

$$H^{\text{ph}}_{\text{bath}} = \sum_{\boldsymbol{q}} v|\boldsymbol{q}| a^\dagger_{\boldsymbol{q}} a_{\boldsymbol{q}} \tag{6.26}$$

where $a^\dagger_{\boldsymbol{q}}$ creates a phonon with momentum $\boldsymbol{q}$ and v is the (constant and isotropic) velocity. The electron-phonon coupling is modelled by the Fröhlich Hamiltonian [175]

$$H^{\text{ph}}_{\text{sys-bath}} = \sum_{\boldsymbol{k},\boldsymbol{q},\alpha} t_{\boldsymbol{k},\boldsymbol{q}} (c^{\alpha\dagger}_{\boldsymbol{k}+\boldsymbol{q}} c^{\alpha}_{\boldsymbol{k}} a^\dagger_{-\boldsymbol{q}} + h.c.) \ , \tag{6.27}$$

where $t_{\boldsymbol{k},\boldsymbol{q}}$ represents the momentum dependent coupling strength. We assume that phonons can induce transitions only within the same band, since interband transitions due to phonons are typically suppressed [176, 177] due to symmetry reasons [178]. Note that, in principle, we can consider additional optical branches without significantly affecting our results, as long as the coupling between the laser and the optical phonons is negligible.
We also take into account the possibility of interband radiative recombination processes [176], where a conduction band electron relaxes to the valence band and emits a photon. In this case, as opposed to the phononic bath, the emission is associated to a pseudospin-flip to obey the angular momentum selection rules and can then only take place between different bands. The corresponding contribution to the Hamiltonian can be written similarly to Eqs. (6.26) and (6.27):

$$H^{\text{rr}}_{\text{bath}} = \sum_{\boldsymbol{q}} c|\boldsymbol{q}| b^\dagger_{\boldsymbol{q}} b_{\boldsymbol{q}}, \tag{6.28}$$

$$H^{\text{rr}}_{\text{sys-bath}} = \sum_{\boldsymbol{k}} w(c^{1\dagger}_{\boldsymbol{k}} c^{2}_{\boldsymbol{k}} b^\dagger_{\boldsymbol{0}} + h.c.), \tag{6.29}$$

where $b^\dagger_{\boldsymbol{0}}$ creates a photon with energy $\omega_0(\boldsymbol{k}) = E_2(\boldsymbol{k}) - E_1(\boldsymbol{k})$, w is the coupling intensity and we focus on vertical transitions since the photon momentum is in general negligible with respect to the typical momentum discretization.

6.2.1 Derivation of the Lindblad master equation

To study the dynamics of the system, we focus on the time evolution of the reduced density matrix $\rho_{\rm sys} = {\rm Tr}_{\rm bath}\{\rho_{\rm tot}\}$, where $\rho_{\rm tot}$ is the combined density matrix of system and reservoirs. By means of a rotating wave approximation (RWA), that is justified by the fact that the laser is tuned resonantly with the energy gap, we eliminate the explicit time dependence of $H_{\rm sys}$ and we obtain a Lindblad type master equation of the form [179]

$$\frac{d}{dt}\rho_{\rm sys} = -i[H_{\rm sys}, \rho_{\rm sys}] + \mathcal{L}_{\rm sys}\rho_{\rm sys}, \tag{6.30}$$

where

$$\begin{aligned}\mathcal{L}_{\rm sys}\rho_{\rm sys} = \sum_{\boldsymbol{k},\boldsymbol{q},\boldsymbol{k}',\boldsymbol{q}'}\sum_{\alpha,\beta}\Big[&\left(\mathcal{S}^{\alpha\dagger}_{\boldsymbol{k},\boldsymbol{q}}\rho_{\rm sys}\mathcal{S}^{\beta}_{\boldsymbol{k}',\boldsymbol{q}'} - \rho_{\rm sys}\mathcal{S}^{\beta}_{\boldsymbol{k}',\boldsymbol{q}'}\mathcal{S}^{\alpha\dagger}_{\boldsymbol{k},\boldsymbol{q}}\right) W^{\beta(1)}_{\boldsymbol{q},\boldsymbol{k}',\boldsymbol{q}'} + \\ &+ \left(\mathcal{S}^{\alpha}_{\boldsymbol{k},\boldsymbol{q}}\rho_{\rm sys}\mathcal{S}^{\beta\dagger}_{\boldsymbol{k}',\boldsymbol{q}'} - \rho_{\rm sys}\mathcal{S}^{\beta\dagger}_{\boldsymbol{k}',\boldsymbol{q}'}\mathcal{S}^{\alpha}_{\boldsymbol{k},\boldsymbol{q}}\right) W^{\beta(2)}_{\boldsymbol{q},\boldsymbol{k}',\boldsymbol{q}'} + h.c.\Big],\end{aligned} \tag{6.31}$$

$$\begin{aligned}W^{\alpha\beta(1)}_{\boldsymbol{q},\boldsymbol{k}',\boldsymbol{q}'} &= \int_0^\infty e^{-i\left[E_\alpha(\boldsymbol{k}') - E_\beta(\boldsymbol{k}'+\boldsymbol{q}')\right]\tau}\,{\rm Tr}_{\rm bath}\left\{\mathcal{F}_{\boldsymbol{k}',\boldsymbol{q}}(t-\tau)\mathcal{F}^\dagger_{\boldsymbol{k}',\boldsymbol{q}'}(t)\rho_{\rm bath}(0)\right\}d\tau \\ &\simeq \Gamma^{\alpha\beta}_{\boldsymbol{k}',\boldsymbol{q}}\left[1+n_B\right]\delta(\boldsymbol{q}-\boldsymbol{q}'),\end{aligned} \tag{6.32}$$

$$\begin{aligned}W^{\alpha\beta(2)}_{\boldsymbol{q},\boldsymbol{k}',\boldsymbol{q}'} &= \int_0^\infty e^{i\left[E_\alpha(\boldsymbol{k}') - E_\beta(\boldsymbol{k}'+\boldsymbol{q}')\right]\tau}\,{\rm Tr}_{\rm bath}\left\{\mathcal{F}^\dagger_{\boldsymbol{k}',\boldsymbol{q}}(t-\tau)\mathcal{F}_{\boldsymbol{k}',\boldsymbol{q}'}(t)\rho_{\rm bath}(0)\right\}d\tau \\ &\simeq \Gamma^{\alpha\beta}_{\boldsymbol{k}',\boldsymbol{q}}\; n_B\;\delta(\boldsymbol{q}-\boldsymbol{q}'),\end{aligned} \tag{6.33}$$

with

$$\Gamma^{\alpha\beta}_{\boldsymbol{k}',\boldsymbol{q}} = \pi|t_{\boldsymbol{k}',\boldsymbol{q}}|^2\;\delta\left[E_\beta(\boldsymbol{k}') - E_\beta(\boldsymbol{k}'+\boldsymbol{q}) - v|\boldsymbol{q}|\right]\delta_{\alpha,\beta} = \Gamma^{\rm ph}\delta_{\alpha,\beta} \tag{6.34}$$

for the phononic bath and

$$\Gamma^{\alpha\beta}_{\boldsymbol{k}',\boldsymbol{q}} = \pi|w|^2\delta_{\alpha,\bar{\beta}} = \Gamma^{\rm rr}\delta_{\alpha,\bar{\beta}} \tag{6.35}$$

for the photons, where $\bar{\beta} = 1$ (2) if $\alpha = 2$ (1). The Bose distribution n_B is a function of the dispersion relation of phonons (6.26) or photons (6.28) respectively, with the chemical potential set to zero. Here we have neglected the principal value of the integral in Eq. (6.32) and Eq. (6.33), since it only slightly renormalizes the band structure [103, 169].

The time evolution of the expectation value of a generic observable $O_{\boldsymbol{p}}$ that only depends on the system degrees of freedom, can be derived from the density matrix equation (6.30) by multiplying it by $O_{\boldsymbol{p}}$ and performing the trace operation. Using the cyclic property of the trace one obtains:

$$\begin{aligned}\frac{d}{dt}\langle O_{\boldsymbol{p}}\rangle = -i\langle[O_{\boldsymbol{p}}, H_{\rm sys}]\rangle + \sum_{\boldsymbol{k},\boldsymbol{k}',\boldsymbol{q}}\sum_{\alpha,\beta}\Gamma^{\alpha\beta}_{\boldsymbol{k}',\boldsymbol{q}}\Big\{&[1+n_B]\langle\mathcal{S}^{\beta}_{\boldsymbol{k}',\boldsymbol{q}}\left[O_{\boldsymbol{p}},\mathcal{S}^{\alpha\dagger}_{\boldsymbol{k},\boldsymbol{q}}\right] + \left[\mathcal{S}^{\alpha}_{\boldsymbol{k},\boldsymbol{q}}, O_{\boldsymbol{p}}\right]\mathcal{S}^{\beta\dagger}_{\boldsymbol{k}',\boldsymbol{q}}\rangle + \\ &+ n_B\langle\mathcal{S}^{\beta\dagger}_{\boldsymbol{k}',\boldsymbol{q}}\left[O_{\boldsymbol{p}},\mathcal{S}^{\alpha}_{\boldsymbol{k},\boldsymbol{q}}\right] + \left[\mathcal{S}^{\alpha\dagger}_{\boldsymbol{k},\boldsymbol{q}}, O_{\boldsymbol{p}}\right]\mathcal{S}^{\beta}_{\boldsymbol{k}',\boldsymbol{q}}\rangle\Big\}.\end{aligned} \tag{6.36}$$

Hereafter, we set $E_g = 1$ as a common energy scale. The validity range δ_k of the RWA is inferred by solving the full dynamics in the absence of superconducting pairing: We compare the exact dynamics with the RWA, extrapolating δ_k. Within the full model δ_k is the natural cut-off. However, varying δ_k does not qualitatively change our results.

6.3 Dynamics of the order parameter and phase diagram

We numerically solve the dynamics for some relevant observables, i.e. the populations of valence $n_k^{11} = \langle c_k^{1\dagger} c_k^1 \rangle$ and conduction $n_k^{22} = \langle c_k^{2\dagger} c_k^2 \rangle$ bands, and the ordinary $n_k^{21} = \langle c_k^{2\dagger} c_k^1 \rangle$ as well as the anomalous $s_k^{21} = \langle c_k^{2\dagger} c_k^{1\dagger} \rangle$ interband correlations. Their complete time evolution, encoded in a set of non-linear coupled differential equations, is shown in Appendix C.1.5 and has been evaluated numerically performing a 4^{th} order adaptive Runge-Kutta method. For clarity, we focus only on the zero temperature regime for the rates, since finite temperature corrections (for $k_B T \ll E_g$) do not affect qualitatively our results and interpretation. Moreover, we initialize the dynamics with the respective equilibrium state of the system and the baths, where only the valence band is populated. We also assume the initial interband anomalous correlations to be non-zero even though very small, in order to avoid the unstable fixed point solution of the dissipative mean field equations $s_k^{21} = 0$ [168].

Our main result is that, in a rather generic parameter range, the anomalous interband correlator s_k^{21} reaches a non-zero steady state for any non-zero, but arbitrarily small, initial value. Consequently, a finite interband pairing Δ can develop in the system. A phase diagram is shown in Fig. 6.4, where the steady state value of the order parameter is plotted as a function of laser intensity and interaction strength for fixed values of the dissipation rates. Throughout this section, we assume the momentum dependence of $t_{\boldsymbol{k},\boldsymbol{q}}$, introduced in Eq. (6.27), such that the corresponding scattering rates Γ^{ph}, derived in Eq. (6.34)), are approximately constant over the momentum region around the resonance [180].

Thresholds in both electron-electron interactions and laser intensity are present. Moreover, in the parameter range we could access, both stronger interactions and laser intensity generally imply a larger induced superconducting pairing.
It is worth to notice the different roles played by the phononic and the photonic baths. While the phononic bath is crucial in establishing the superconducting steady-state, the radiative recombination does not qualitatively influence the phase diagram, as long as $\Gamma^{\mathrm{rr}} = \pi |w|^2 < \Omega$. Increasing the phononic rate Γ^{ph}, however, qualitatively modifies the value of the superconducting order parameter Δ achieved in the stationary state. It moves in fact, the threshold on the interaction strength to larger values. If Γ^{ph} is raised up even further, superconducting correlations will eventually be washed out. The dependence of the phase diagram on the other parameters involved is weaker.
In order to better understand the physics it is worth to notice that the time evolution of the anomalous interband correlator s_k^{21}, and hence the superconducting pairing, is strongly dependent on the quantity $\tilde{n}_k = n_k^{22} + n_{-k}^{11} - 1$ [168, 169]. Whenever $\tilde{n}_k$

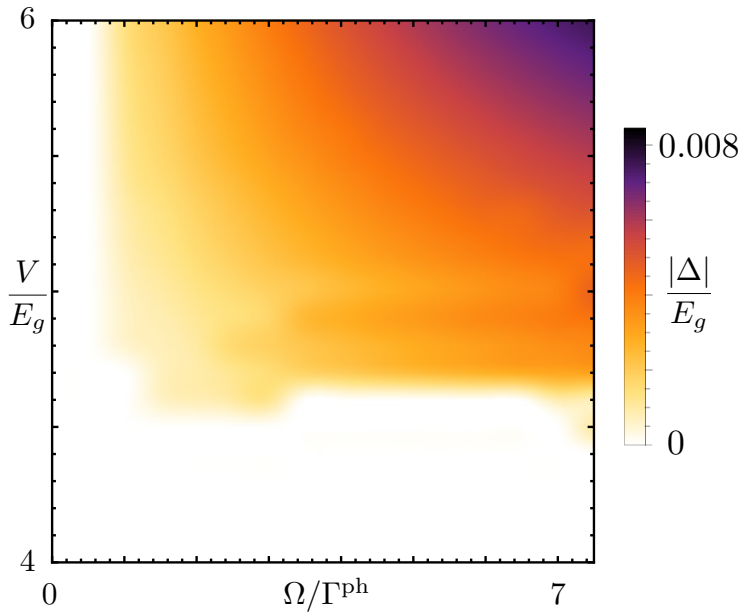

Figure 6.4: Phase diagram of the system, representing the absolute value of the complex order parameter $|\Delta|$ as a function of the laser intensity Ω and the repulsive interaction strength V. Here, $\Gamma^{\mathrm{ph}} = 0.02E_g$ is the phonon rate, $\Gamma^{\mathrm{rr}} = \Gamma^{\mathrm{ph}}/10$ is the radiative recombination rate and $A_1 = 7E_g$, $A_2 = 24E_g$ and we consider a momentum cutoff such that $|k| \leq \delta_k = 0.2$.

is close to zero, s_k^{21} behaves accordingly C.2.2. Heuristically, the condition $\tilde{n}_k = 0$ implies zero probability of forming a Cooper pair of electrons (or holes) between momenta k and $-k$. However $\tilde{n}_k \neq 0$ is only a necessary condition for obtaining $\Delta \neq 0$. The condition $\tilde{n}_k \neq 0$ cannot be realized by means of photonic dissipation alone, since there is no significant momentum transfer in the electron sector as a result of such processes. On the other hand, phonon scattering tends to place the electrons at the bottom of the bands, due to the fact that the bands have the same concavity at the resonance point. Hence, it is phonon scattering that generates the condition $\tilde{n}_k \neq 0$ necessary for the development of the superconducting correlations.

The behavior of the populations is shown in Fig. 6.6. We find in fact $\tilde{n}_k \simeq 1$ for the momenta around the minima of the quadratic bands while $\tilde{n}_k \simeq -1$ on the edge of the region where the rotating wave applies. Note that the transition between these two regions is not sharp, but smoothed out: In the next section we comment how this feature becomes crucial in the explanation of the Cooper pairs creation. Qualitatively speaking, the smoothing signals the (superconducting) pairing between the two bands, in analogy with the destruction of the Fermi surface in BCS superconductors.

In order to understand the role played by the radiative recombination, we show in Fig. 6.5 the real time evolution of the modulus of the complex order parameter $|\Delta|$. The role played by this relaxation mechanism is evident here: the larger the

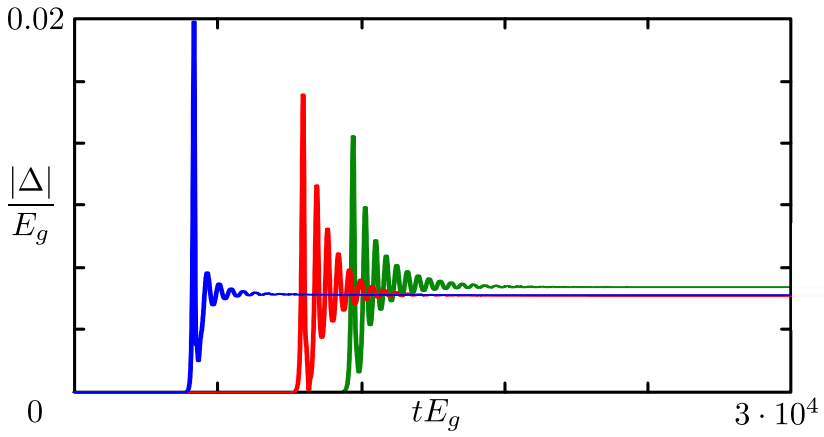

Figure 6.5: Time evolution of the absolute value of the complex order parameter $|\Delta|$, for different values of the radiative recombination rate: $\Gamma^{\rm rr} = \Gamma^{\rm ph}/20$ (green line), $\Gamma^{\rm rr} = \Gamma^{\rm ph}/10$ (red line), and $\Gamma^{\rm rr} = \Gamma^{\rm ph}/2$ (blue line). We choose $\Omega/\Gamma^{\rm ph} = 25$, where $\Gamma^{\rm ph}$ is the phonon rate, and $\Omega = 0.25E_g$, $A_1 = 7E_g$, $A_2 = 24E_g$, $V = 4E_g$. The momentum cutoff is $|k| \leq \delta_k = 0.2$ and the number of k points $N_k = 200$.

photonic relaxation rate, the shorter the time needed to reach the steady state. This behavior can be understood by noticing that photonic relaxation adds a qualitatively new (interband) dissipation channel. So, while the steady state populations are not substantially affected by the photonic relaxation, the time needed to establish them changes (see Fig. 6.5).

6.4 Effective pairing mechanism

As shown in Fig. 6.6, in the superconducting steady state the bands are qualitatively empty at the edges of the momentum region considered and filled in the center, around the minima. We can mimic this situation by employing an equilibrium system, with two bands with positive concavity and coincident minima. Indeed, the action of the laser is to effectively shift the lower band up to the upper one, balancing the gap energy difference between different bands electrons. An attractive interaction of the form

$$-U(n_k^{11} - 1/2)(n_{-k}^{22} - 1/2), \tag{6.37}$$

with $U > 0$ favours the situation where, if the state k in band 1 is occupied (empty), the corresponding state $-k$ in band 2 is occupied (empty). The chemical potential then determines whether the ground state is given by the couple of empty or filled states. If we apply the mean field approximation to the above-mentioned attractive interaction term, we obtain exactly the model studied in Section 6.1.4, which reads:

$$H = \sum_{k,\alpha} \epsilon_\alpha(k) c_k^{\alpha\dagger} c_k^\alpha - \tilde{\Delta} \sum_{k,\alpha\neq\beta} \left(c_k^{\alpha\dagger} c_{-k}^{\beta\dagger} + h.c. \right), \tag{6.38}$$

where $\alpha, \beta = 1, 2$ labels the two bands, $\epsilon_\alpha(k) = A_\alpha k^2 - C$ and $\tilde{\Delta} = U\Delta$. We fix $C \simeq 0.2E_g$ to obtain a Fermi energy compatible with the steady state reached by

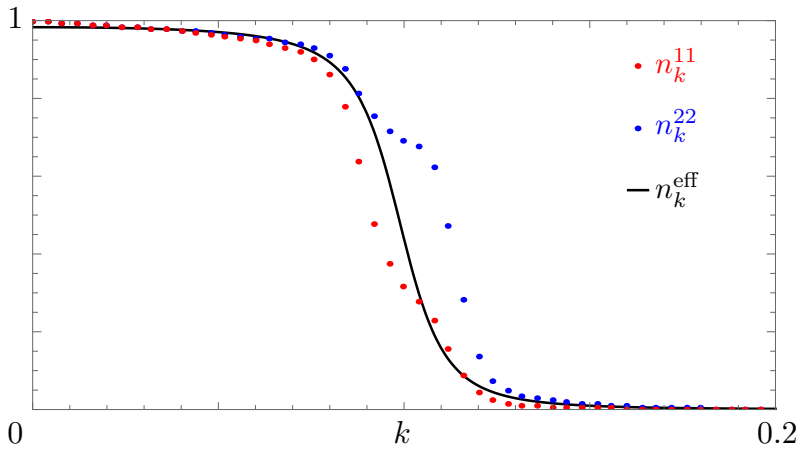

Figure 6.6: Steady state population of valence (blue dots) and conduction (red dots) bands as a function of the momentum k. We choose $\Omega/\Gamma^{\text{ph}} = 25$, where Γ^{ph} is the phonon rate, $\Gamma^{\text{rr}} = \Gamma^{\text{ph}}/10$ is the radiative recombination rate, $\Omega = 0.25E_g$, $A_1 = 7E_g$, $A_2 = 24E_g$. We also consider a momentum cutoff such that $|k| \leq \delta_k = 0.2$. The black solid line represents the population of the two bands in the effective system [170] where attractive interaction of strenght $U = -0.05$ are present.

our model as long as $U = 0$ (parameters in Fig. 6.6).

Using a Bogoliubov-de Gennes representation, we are able to diagonalize the Hamiltonian and evaluate the expectation value of the population. In this picture, we observe a very similar qualitative behavior of the populations in the two bands with respect to the nonequilibrium steady state populations (see black solid line in Fig. 6.6). Therefore, the steady state can be effectively seen as an equilibrium two band system where the laser shifts the valence band up to the conduction band and an attractive interaction creates Cooper pairs. This simple effective model is intended to clarify the reason why the condition $\tilde{n}_k \neq 0$ is essential but not sufficient for the superconducting pairing. In fact, a simpler model with two bands and two different chemical potentials would lead to $\tilde{n_k} \neq 0$, but would not imply coupling between the bands and consequently the smearing of the populations as well as superconductivity.

A full qualitative interpretation of the rather involved results can hence be given: The laser excites electrons from the valence to the conduction band, at any k in the resonance region. The phonons let the electrons in each band get as close as possible to the bottom of the bands. Interactions between the two bands drive the system into a correlated state. A possible mean field effective model describing the steady state reached is provided by the simple Bogoliubov-de Gennes Hamiltonian for interband superconductors, given in Eq. (6.38).

6.5 Summary

We have shown that a non-equilibrium steady state characterized by a finite superconducting order parameter related to an anomalous interband pairing can be achieved in a semiconductor by coupling the bands with laser light. Specifically, we have considered quadratic bands with the same sign of the effective mass. We have shown that an acoustic phononic bath, which is responsible of intraband transitions only, can induce an electronic distribution in the valence and conduction bands which favours the development of such an unusual pairing. Remarkably, this picture is not destroyed even if an interband relaxation with the same order of magnitude as the intraband one is switched on. Indeed, interband relaxation can speed up the formation of the superconducting order parameter. Furthermore, the stationary state with $|\Delta| = 0$ can be achieved only for sufficiently large repulsive density- density electronic interaction ($V \geq 2E_g$) and for an initial configuration where $|\Delta|$ can be vanishing compatibly with the numerical precision. The Rabi frequency Ω, on the other hand, has to be strong enough ($\Omega > \Gamma_{\mathrm{ph}}$), since the laser has to be able to drive a sufficient number of electrons in the conduction band. Only in this case, the two populations can be forced to satisfy the favourable condition $\tilde{n_k} \neq 0$. The result is stable against changing the velocity of the acoustic phonons, the amplitude of the bands and the k-space discretization step. Moreover, the phonon coupling Γ_{ph}, as well as the radiative recombination strength Γ_{rr}, have been chosen to represent a realistic scenario: Phonon transitions in prototypical semiconductors such as Silicon or Germanium have tipically a lifetime $\tau_{\mathrm{ph}} = 0.1ps$, which correspond to a rate $\Gamma_{\mathrm{ph}} \sim 0.01E_g$ [180], while radiative recombination rates are strongly dependent on the electron concentration [181]. However, their action does not qualitatively affect the steady state reached by the system. Finally, we argue that our results corroborate the original proposal of Goldstein et al. [168], by putting it in a more realistic framework. This fact, together with the interpretation of the non-equilibrium pairing based on equilibrium multiband BCS theory, should facilitate the experimental detection of this novel route to light- induced insulator/superconductor transition.

Conclusions

The main focus of this Thesis has been the study of integrable and non-integrable quantum systems out-of-equilibrium. In particular, we have investigated both the dynamics and the non-equilibrium steady state reached by a variety of systems, introduced in Chapter 2, following different protocols to drive each system far from its standard equilibrium configuration. We have put our attention in particular onto the so-called quantum quench, consisting in a change in time of one of the system parameters and, on the other hand, onto the so-called Floquet engineering, where an external periodic driving is imposed to the system. Both methods are experimentally accessible in the context of quantum gases, optical lattices and, mainly for the latter type of quantum control, in condensed matter systems.
The mentioned techniques made us possible to explore and engineer very peculiar phases of matter, going through non-equilibrium and dynamical phase transitions, which are the far-from-equilibrium counterparts of the zero-temperature equilibrium quantum phase transitions (QPTs) and have been extensively discussed in Chapter 1.

In Chapter 3, we have focused on the effects resulting from the quench of a gap-opening mechanism, from a gapless to a gapped (or partially-gapped) state. A non-monotonic behavior of observables characterizes a wide range of quantum quenches, both for sudden and non-sudden protocols, integrable (Staggered potential and spin-orbit coupled wire) and non-integrable (a chain of fermions in presence of nearest and next-to-nearest neighbors interactions) models and not only in one spatial dimension. Indeed, this is the result of a peculiar phenomenon, namely the freezing of the light cone which spreads information through the system. Interestingly, in non-interacting models, the freezing of the light cone is captured by a Klein-Gordon equation, which provides an intuitive interpretation of the behavior of the system in terms of a simple continuum mechanical model.

By enlarging the parameters space investigated, we have been able to deepen the study of this type of quantum quenches. In the subsequent Chapter 4, indeed, we have observed that, in the paradigmatic cases of the Su-Schrieffer-Heeger model and of the transverse field quantum Ising model, non-equilibrium QPTs appear in connection to both an equilibrium QPT and an effective metal-insulator transition in

the GGE density matrix of the system. We have also shown that the non-equilibrium QPT is robust with respect to perturbations that do not spoil the validity of the GGE.

Understanding the properties of far-from-equilibrium quantum systems is becoming a major challenge in both fundamental and applied physics. The effort in providing a classification, in terms of local or topological order parameters, of far-from-equilibrium phases is hence intense. In Chapter 5, the concept Dynamical Quantum Phase Transition (DQPT) has been investigated. A DQPT is naively defined as a zero of the Loschmit-Echo as a function of time and represents a natural non-equilibrium counterpart of a thermal phase transition. Here, we have studied the DQPTs characterizing the quantum XY chain subject to a quantum quench of finite duration. We have shown that the number of DQPTs with different periods can vary as the duration of the quantum quench is varied. However, the parity of such number only depends on the pre-quench and post-quench Hamiltonians and is related to a topological invariant.

In the last part, namely Chapter 6, we have shown that a non-equilibrium steady state characterized by finite superconducting correlations between electrons in different bands can be achieved in a semiconductor by coupling the bands with a laser light. In particular, this is possible only if the effect of an acoustic phonon bath is taken into account, since it is responsible of the creation of a peculiar electronic non-equilibrium distribution which favors the creation of a state characterized by a non-vanishing interband order parameter. Finally, we have given a physical interpretation of the effective pairing mechanism by means of the standard BCS multi-band theory using realistic parameters for a possible experimental realization in condensed matter systems.

Appendices

APPENDIX A

Steady state and dynamics following a quantum quench

A.1 Steady state magnetization

A.1.1 Diagonalization of a generic 2×2 Hermitian matrix

In order to set the conventions, we begin this Section by briefly summarizing the diagonalization procedure for a generic 2×2 Hermitian matrix,

$$\mathcal{H} = \begin{bmatrix} h_{11} & h_{12} \\ h_{12}^* & h_{22} \end{bmatrix}, \tag{A.1}$$

with h_{11}, $h_{12} \in \mathbb{R}$ and $h_{12} \in \mathbb{C}$. We first focus on the case $h_{12} \neq 0$. Then, the eigenvalues of $\mathcal{H}$ are

$$\epsilon_\pm = \frac{1}{2}\left(h_{11} + h_{22}\right) \pm D, \tag{A.2}$$

where $D = \sqrt{(h_{11} - h_{22})^2 + 4|h_{12}|^2}/2$. The Hamiltonian of Eq. (A.1) can be diagonalized by means of the unitary matrix U,

$$UHU^\dagger = \begin{bmatrix} \epsilon_+ & 0 \\ 0 & \epsilon_- \end{bmatrix}, \qquad \text{with} \qquad U = \begin{bmatrix} A_- & -A_- \frac{\epsilon_- - h_{22}}{h_{12}^*} \\ -A_+ \frac{\epsilon_+ - h_{11}}{h_{12}} & A_+ \end{bmatrix} \quad \text{and} \quad \varepsilon_+ > \varepsilon_-, \tag{A.3}$$

where we have introduced the coefficients

$$A_+ = \frac{|h_{12}|}{\sqrt{(\epsilon_+ - h_{11})^2 + |h_{12}|^2}} \qquad \text{and} \qquad A_- = \frac{|h_{12}|}{\sqrt{(\epsilon_- - h_{22})^2 + |h_{12}|^2}}. \tag{A.4}$$

On the other hand, in the case $h_{12} = 0$, the unitary matrix U that transforms $\mathcal{H}$ in the diagonal form of Eq. (A.3), i.e. with $\epsilon_+ > \epsilon_-$, is

$$U = \begin{cases} I_{2\times 2}\theta(h_{11} - h_{22}) + i\sigma^y \theta(h_{22} - h_{11}), & \text{if } h_{11} \neq h_{22}, \\ \frac{1}{\sqrt{2}}\left(I + i\sigma^y\right), & \text{if } h_{11} = h_{22}, \end{cases} \tag{A.5}$$

with $I_{2\times 2}$ the 2×2 identity matrix and σ^y the y Pauli matrix in the usual representation.

A.1.2 Some general formulas on the calculation of M in 1D systems

As stated in the main text, the Hamiltonian of both the SOC wire and the SP model can be written as

$$H^{(i)}(t) = \sum_k \Psi_k^{(i)\dagger}[\mathcal{H}_k^{(i)} + \theta(t)\Delta^{(i)}\sigma^x]\Psi_k^{(i)}. \tag{A.6}$$

Here, $\Psi_k^{(i)\dagger} = \left(d_{a,k}^{(i)\dagger}, d_{b,k}^{(i)\dagger}\right)$ is a two-component momentum resolved Fermi spinor. In the case of the SOC wire ($i = \{1, 2\}$), the indexes a and b represent the positive and negative spin projections along the quantization axis, respectively, while in the case of the SP model ($i = \{3, 4\}$) they are associated with the left-/right-movers. The pre-quench single-mode Hamiltonian $\mathcal{H}_k^{(i)}$ can always be written in a diagonal form with eigenvalues $\epsilon_{\pm,0,k}^{(i)}$ such that $\epsilon_{-,0,k}^{(i)} \leq \epsilon_{+,0,k}^{(i)}$, $\forall k$, by means of a unitary matrix [see Eqs. (A.3) and (A.5)]. In particular, for all the cases considered in this paper the latter takes the form

$$U_{0,k}^{(i)} = \begin{bmatrix} a_{0,k}^{(i)} & b_{0,k}^{(i)} \\ -b_{0,k}^{(i)*} & a_{0,k}^{(i)} \end{bmatrix}, \tag{A.7}$$

where the coefficients $a_{0,k}^{(i)} \in \mathbb{R}$ and $b_{0,k}^{(i)} \in \mathbb{C}$ are determined by Eqs. (A.3) and (A.5). Moreover, $U_{0,k}^{(i)}\mathcal{H}_k^{(i)}U_{0,k}^{(i)\dagger} = \mathrm{diag}\left\{\epsilon_{+,0,k}^{(i)}, \epsilon_{-,0,k}^{(i)}\right\}$. For $t < 0$ the diagonalized Hamiltonian reads

$$H^{(i)}(t<0) = \sum_k \left[\epsilon_{-,0,k}^{(i)} d_{v,0,k}^{(i)\dagger} d_{v,0,k}^{(i)} + \epsilon_{+,0,k}^{(i)} d_{c,0,k}^{(i)\dagger} d_{c,0,k}^{(i)}\right], \tag{A.8}$$

where the conduction and valence band operators, $d_{c,0,k}^{(i)}$ and $d_{v,0,k}^{(i)}$, are defined by

$$\Phi_{0,k}^{(i)} = U_{0,k}^{(i)}\Psi_k^{(i)} = \begin{bmatrix} d_{c,0,k}^{(i)} \\ d_{v,0,k}^{(i)} \end{bmatrix}. \tag{A.9}$$

In all cases considered we set the chemical potential to zero and assume the $i-$th system to be in its pre-quench zero-temperature equilibrium ground state, $|\Phi_0^{(i)}(0)\rangle$. Therefore, for $t < 0$, the bands are filled up to the linear crossing and $|\Phi_0^{(i)}(0)\rangle$ is defined as

$$|\Phi_0^{(i)}\rangle = \prod_{k_1^{(i)}}^{k_2^{(i)}} \left(\Phi_{0,k}^{(i)\dagger}\right)_2 |0^{(i)}\rangle = \prod_{k_1^{(i)}}^{k_2^{(i)}} \left(U_{0,k}^{(i)\dagger}\Psi_k^{(i)\dagger}\right)_2 |0^{(i)}\rangle, \tag{A.10}$$

with $|0^{(i)}\rangle$ the vacuum of the $i-$th system and $k_{1,2}^{(i)}$ determined by imposing that only negative energy states are filled. Here, the subscript 2 means that the second component of the spinor has to be considered.

We now turn to the regime with $t > 0$. The post-quench single-mode Hamiltonian $\mathcal{H}_k^{(i)} + \Delta^{(i)}\sigma^x$ is diagonalized by the unitary matrix

$$U_{1,k}^{(i)} = \begin{bmatrix} a_{1,k}^{(i)} & b_{1,k}^{(i)} \\ -b_{1,k}^{(i)*} & a_{1,k}^{(i)} \end{bmatrix}, \tag{A.11}$$

with $a^{(i)}_{1,k} \in \mathbb{R}$ and $b^{(i)}_{1,k} \in \mathbb{C}$ determined again by Eqs. (A.3) and (A.5), and $U^{(i)}_{1,k}[\mathcal{H}^{(i)}_k + \Delta^{(i)}\sigma^x]U^{(i)\dagger}_{1,k} = \mathrm{diag}\{\epsilon^{(i)}_{+,1,k}, \epsilon^{(i)}_{-,1,k}\}$. The total Hamiltonian thus becomes

$$H^{(i)}(t>0) = \sum_k \left[\epsilon^{(i)}_{-,1,k} d^{(i)\dagger}_{v,1,k} d^{(i)}_{v,1,k} + \epsilon^{(i)}_{+,1,k} d^{(i)\dagger}_{c,1,k} d^{(i)}_{c,1,k}\right], \tag{A.12}$$

where $\epsilon^{(i)}_{-,1,k} \leq \epsilon^{(i)}_{+,1,k}$, $\forall k$, with the new conduction and valence band fermionic operators, $d^{(i)}_{c,1,k}$ and $d^{(i)}_{v,1,k}$, given by

$$\Phi^{(i)}_{1,k} = U^{(i)}_{1,k}\Psi^{(i)}_k = \begin{bmatrix} d^{(i)}_{c,1,k} \\ d^{(i)}_{v,1,k} \end{bmatrix}. \tag{A.13}$$

We now evaluate the magnetization of system along the direction of the applied magnetic field in the SOC wire or the staggered magnetization in the SP model within the framework of the GGE. To do this, it is sufficient to know the average over the pre-quench ground state $|\Phi^{(i)}_0\rangle$, denoted by $\langle\cdot\rangle_0$, of the occupation numbers $n^{(i)}_{k,j}$ of the energy levels of the corresponding post-quench Hamiltonian, given by

$$n^{(i)}_{k,j=1,2} = \left(\Psi^{(i)\dagger}_k U^{(i)\dagger}_{1,k}\right)_j \left(U^{(i)}_{1,k}\Psi^{(i)}_k\right)_j. \tag{A.14}$$

Since all the $n^{(i)}_{k,j}$ commute with the post-quench Hamiltonian, they are conserved for $t>0$ and, therefore, $\langle n^{(i)}_{k,j}\rangle_0 = \langle n^{(i)}_{k,j}\rangle_{GGE}$. We obtain

$$\langle n^{(i)}_{k,1}\rangle_0 = \langle n^{(i)}_{k,1}\rangle_{GGE} = \left|-a^{(i)}_{1,k}b^{(i)}_{0,k} + a^{(i)}_{0,k}b^{(i)}_{1,k}\right|^2 \langle d^{(i)\dagger}_{v,0,k} d^{(i)}_{v,0,k}\rangle_0, \tag{A.15a}$$

$$\langle n^{(i)}_{k,2}\rangle_0 = \langle n^{(i)}_{k,2}\rangle_{GGE} = \left|a^{(i)}_{1,k}a^{(i)}_{0,k} + b^{(i)}_{0,k}b^{(i)*}_{1,k}\right|^2 \langle d^{(i)\dagger}_{v,0,k} d^{(i)}_{v,0,k}\rangle_0, \tag{A.15b}$$

where the averages $\langle d^{(i)\dagger}_{v,0,k} d^{(i)}_{v,0,k}\rangle_0$ can be easily evaluated from Eq. (A.10). Using Eq. (A.13) and the fact that $\langle d^{(i)\dagger}_{c,1,k} d^{(i)}_{v,1,k}\rangle_{GGE} = \langle d^{(i)\dagger}_{v,1,k} d^{(i)}_{c,1,k}\rangle_{GGE} = 0$, one gets the steady state magnetization (SOC wire) or the staggered magnetization (SP)

$$M^{(i)} = \frac{1}{n^{(i)}} \sum_k \langle \Psi^{(i)\dagger}_k \sigma^x \Psi^{(i)}_k\rangle_{GGE} \tag{A.16}$$

$$= \frac{1}{\left|k^{(i)}_1\right| + \left|k^{(i)}_2\right|} \int_{k^{(i)}_1}^{k^{(i)}_2} dk \left(a^{(i)}_{1,k}b^{(i)}_{1,k} + a^{(i)}_{1,k}b^{(i)*}_{1,k}\right)\left(\langle n^{(i)}_{k,1}\rangle_{GGE} - \langle n^{(i)}_{k,2}\rangle_{GGE}\right), \tag{A.17}$$

where $n^{(i)} = L(|k^{(i)}_1| + |k^{(i)}_2|)/(2\pi)$ is the total number of particles in the $i-$th system and L is its length. Furthermore, in the last step, the thermodynamic limit has been performed.

A.1.3 Spin-orbit coupled quantum wire

We now explicitly apply the general discussion of Sec. A.1.2 to the quench of the external magnetic field in a SOC wire. We start by introducing the real space

lattice Hamiltonian, imposing periodic boundary conditions:

$$H = \sum_{j=1}^{L} \left\{ \Psi_j^\dagger \left[2I_{2\times 2} + B\theta(t)\sigma^x \right] \Psi_j + \Psi_j^\dagger \left[\frac{i\alpha}{2}\sigma^z - I_{2\times 2} \right] \Psi_{j+1} + h.c. \right\}, \tag{A.18}$$

where L is the total length of the system and we set the lattice spacing to 1. In this case the pre-quench single-mode Hamiltonians $\mathcal{H}_k^{(i)}$, with $i = \{1, 2\}$, are

$$\mathcal{H}_k^{(1)} = 2[1 - \cos(k)] I_{2\times 2} + \alpha \sin(k)\sigma^z, \qquad \text{with } k \in [-\pi, \pi), \tag{A.19a}$$

$$\mathcal{H}_k^{(2)} = k^2 I_{2\times 2} + \alpha k \sigma^z, \tag{A.19b}$$

for the lattice and the low-energy continuous models, respectively. Note that, because of the translational invariance, $\Psi_j = \sum_k e^{ikj}\ \Psi_k/\sqrt{L}$. Although the pre-quench single-mode Hamiltonian $\mathcal{H}_k^{(i)}$ is already diagonal, it can be more conveniently rewritten in terms of conduction and valence band Fermi operators using Eq. (A.7). In this case the coefficients of the unitary matrix $U_{0,k}^{(i)}$ are

$$a_{0,k}^{(i)} = [1 - \delta_{k,0}]\theta(k) + \frac{\delta_{k,0}}{\sqrt{2}} \qquad b_{0,k}^{(i)} = [1 - \delta_{k,0}]\theta(-k) + \frac{\delta_{k,0}}{\sqrt{2}}, \tag{A.20}$$

while the conduction and valence energy bands are

$$\epsilon_{\pm,0,k}^{(1)} = 2[1 - \cos(k)] \pm \alpha |\sin(k)|, \tag{A.21a}$$

$$\epsilon_{\pm,0,k}^{(2)} = k^2 \pm \alpha |k|. \tag{A.21b}$$

From $\epsilon_{-,0,k}^{(i)} = 0$ it follows that $k_{1/2}^{(1)} = \mp 2 \arctan[\alpha/2]$ and $k_{1/2}^{(2)} = \mp\alpha$.

In the post-quench regime $t > 0$, the unitary matrix $U_{1,k}^{(i)}$ which diagonalizes the single-mode Hamitonian $\mathcal{H}_k^{(1)} + B\sigma^x$ has coefficients

$$a_{1,k}^{(1)} = \frac{B}{\sqrt{\left[D_k^{(1)} - \alpha \sin(k)\right]^2 + B^2}}, \qquad b_{1,k}^{(1)} = \frac{D_k^{(1)} - \alpha \sin(k)}{\sqrt{\left[D_k^{(1)} - \alpha \sin(k)\right]^2 + B^2}}, \tag{A.22a}$$

$$a_{1,k}^{(2)} = \frac{B}{\sqrt{\left[D_k^{(2)} - \alpha k\right]^2 + B^2}}, \qquad b_{1,k}^{(2)} = \frac{D_k^{(2)} - \alpha k}{\sqrt{\left[D_k^{(2)} - \alpha k\right]^2 + B^2}}, \tag{A.22b}$$

where $D_k^{(1)} = \sqrt{\alpha^2 \sin^2(k) + B^2}$ and $D_k^{(2)} = \sqrt{\alpha^2 k^2 + B^2}$, while the post-quench conduction and valence bands are

$$\epsilon_{\pm,1,k}^{(1)} = 2[1 - \cos(k)] \pm D_k^{(1)}, \tag{A.23a}$$

$$\epsilon_{\pm,1,k}^{(2)} = k^2 \pm D_k^{(2)}. \tag{A.23b}$$

From Eq. (A.17) one immediately obtains the steady state magnetization along the direction of the applied magnetic field in the thermodynamic limit,

$$M^{(i)} = \frac{1}{\left|k_1^{(1)}\right| + \left|k_2^{(1)}\right|} \left(\int_{k_1^{(i)}}^{0} - \int_{0}^{k_2^{(i)}} \right) dk\, 2 a_{1,k}^{(i)} b_{1,k}^{(i)} \left[\left(a_{1,k}^{(i)}\right)^2 - \left(b_{1,k}^{(i)}\right)^2 \right]. \tag{A.24}$$

For the lattice model, using Eq. (A.22a), we have

$$M^{(1)} = \frac{1}{\left|k_1^{(1)}\right| + \left|k_2^{(1)}\right|} \frac{B}{2\sqrt{\alpha^2 + B^2}} \log\left(\frac{Z_+}{Z_-}\right), \tag{A.25}$$

with

$$Z_\pm = (\sqrt{\alpha^2 + B^2} \mp \alpha)^2 \left[\sqrt{\alpha^2 + B^2} \pm \alpha \frac{4 - \alpha^2}{4 + \alpha^2}\right]^2. \tag{A.26}$$

On the other hand, for the low-energy continuous model one gets from Eq. (A.22b)

$$M^{(2)} = -\frac{B}{4\alpha^2} \log\left[1 + 2\frac{\alpha^4}{B^2} + \frac{\alpha^8}{B^4}\right]. \tag{A.27}$$

A.1.4 Staggered Potential model

In this Section we apply the discussion of Sec. A.1.2 to the quench of the staggered potential in the SP model. The real space lattice Hamiltonian reads

$$H = -J \sum_{j=1}^{L} \left[\left(c_j^\dagger c_{j+1} + h.c.\right) + (-1)^j \delta(t) c_j^\dagger c_j\right], \tag{A.28}$$

where c_j are annihilation operators for spinless fermions on the site j of the lattice, L is the length of the system and we set the lattice spacing to 1. Introducing the spinor $\Psi_k^\dagger = \left(c_k^\dagger, c_{k-\pi}^\dagger\right)$, with $c_j = \sum_k e^{ikj} c_k/\sqrt{L}$, we obtain the pre-quench single mode Hamiltonians $\mathcal{H}_k^{(i)}$, with $i = \{3, 4\}$,

$$\mathcal{H}_k^{(3)} = -2J\cos(k)\sigma^z, \tag{A.29a}$$

$$\mathcal{H}_k^{(4)} = -2J(k - \pi/2)\sigma^z, \tag{A.29b}$$

with $k \in [0, \pi)$, for the lattice and the low-energy continuous models, respectively. Also in this model the pre-quench single-mode Hamiltonians are diagonal, and again we can conveniently introduce conduction and valence band Fermi operators using Eq. (A.7). The coefficients of the unitary matrix $U_{0,k}^{(i)}$ are:

$$a_{0,k}^{(i)} = [1 - \delta_{k,\pi/2}]\theta\left(\frac{\pi}{2} - k\right) + \frac{\delta_{k,\pi/2}}{\sqrt{2}} \qquad b_{0,k}^{(i)} = [1 - \delta_{k,\pi/2}]\theta\left(k - \frac{\pi}{2}\right) + \frac{\delta_{k,\pi/2}}{\sqrt{2}}, \tag{A.30}$$

while the pre-quench conductance and valence bands are

$$\epsilon_{\pm,0,k}^{(3)} = \pm 2J|\cos(k)|, \tag{A.31a}$$

$$\epsilon_{\pm,0,k}^{(4)} = \pm 2J|k - \pi/2|. \tag{A.31b}$$

One obtains $k_1^{(3)} = k_1^{(4)} = 0$ and $k_2^{(3)} = k_2^{(4)} = \pi$. Note that we are considering a continuum model with the same number of particles of the lattice one and energy bands filled up to the crossing point.

In the post-quench regime the single-mode Hamiltonian $\mathcal{H}_k^{(i)} + \delta\sigma^x$ is diagonalized by the unitary matrix $U_{1,k}^{(i)}$, whose coefficients are

$$a_{1,k}^{(3)} = \frac{\delta}{\sqrt{(\epsilon_{+,1,k}^{(3)} + 2J\cos(k))^2 + \delta^2}}, \qquad b_{1,k}^{(3)} = \frac{\epsilon_{+,1,k}^{(3)} + 2J\cos(k)}{\sqrt{(\epsilon_{+,1,k}^{(3)} + 2J\cos(k))^2 + \delta^2}}, \tag{A.32a}$$

$$a_{1,k}^{(4)} = \frac{\delta}{\sqrt{\left[\epsilon_{+,1,k}^{(4)} + 2J(k-\pi/2)\right]^2 + \delta^2}}, \quad b_{1,k}^{(4)} = \frac{\epsilon_{+,1,k}^{(4)} + 2J(k-\pi/2)}{\sqrt{\left[\epsilon_{+,1,k}^{(4)} + 2J(k-\pi/2)\right]^2 + \delta^2}}, \tag{A.32b}$$

where the new energy bands are

$$\epsilon_{\pm,1,k}^{(3)} = \pm\sqrt{\delta^2 + 4J^2\cos^2(k)}, \tag{A.33a}$$

$$\epsilon_{\pm,1,k}^{(4)} = \pm\sqrt{\delta^2 + 4J^2(k-\pi/2)^2}. \tag{A.33b}$$

Using Eqs. (A.17), (A.30) and (A.32) one finds that the steady state staggered magnetization after the quench evaluates to

$$M^{(i)} = \frac{1}{\pi}\left(\int_{\pi/2}^{\pi} - \int_0^{\pi/2}\right) dk\, 2a_{1,k}^{(i)} b_{1,k}^{(i)} \left[\left(a_{1,k}^{(i)}\right)^2 - \left(b_{1,k}^{(i)}\right)^2\right]. \tag{A.34}$$

For the lattice model, using Eq. (A.32a), we obtain

$$M^{(3)} = -\frac{2\delta}{\pi\sqrt{\delta^2 + 4J^2}} \operatorname{arctanh}\left(\frac{2J}{\sqrt{\delta^2 + 4J^2}}\right). \tag{A.35}$$

On the other hand, from Eq. (A.32b), one gets for the low-energy continuous model

$$M^{(4)} = -\frac{\delta}{2J\pi} \ln\left[1 + \left(\frac{\pi J}{\delta}\right)^2\right]. \tag{A.36}$$

A.1.5 2D Rashba-coupled electron gas

In this Section we consider the quench of magnetic field in a 2D Rashba-coupled electron gas. The Hamiltonian of the system is $H_{2D}(t) = \sum_{k_x,k_y} \Psi_{k_x,k_y}^\dagger [\mathcal{H}_{k_x,k_y} + \theta(t) B\sigma^z] \Psi_{k_x,k_y}$, with

$$\mathcal{H}_{k_x,k_y} = (k_x^2 + k_y^2) I_{2\times 2} + \alpha(\sigma^x k_y - \sigma^y k_x). \tag{A.37}$$

Here, k_x and k_y are the two components of the momentum vector $\vec{k}$, while $\Psi_{k_x,k_y}^\dagger = \left(d_{a,k_x,k_y}^\dagger, d_{b,k_x,k_y}^\dagger\right)$, with d_{a,k_x,k_y} (d_{b,k_x,k_y}) fermionic annihilation operators for spin up (down) electrons. Following the same steps outlined in the previous Sections, we begin with the pre-quench case. For $t < 0$ the single-mode Hamiltonian is diagonalized by the unitary matrix

$$U_{0,k_x,k_y} = \begin{bmatrix} a_{0,k_x,k_y} & b_{0,k_x,k_y} \\ -b_{0,k_x,k_y}^* & a_{0,k_x,k_y} \end{bmatrix}, \tag{A.38}$$

with

$$a_{0,k_x,k_y} = \frac{1}{\sqrt{2}} \qquad b_{0,k_x,k_y} = \frac{1}{\sqrt{2}} \frac{k_x + ik_y}{k}, \tag{A.39}$$

where $k = |\vec{k}| = \sqrt{k_x^2 + k_y^2}$. The pre-quench conduction and valence fermionic operators are thus given by

$$\Phi_{0,k_x,k_y} = U_{0,k_x,k_y} \Psi_{k_x,k_y} = \begin{bmatrix} d_{c,0,k_x,k_y} \\ d_{v,0,k_x,k_y} \end{bmatrix}, \tag{A.40}$$

with associated energy levels

$$\epsilon_{\pm,0,k_x,k_y} = k^2 \pm \alpha k. \tag{A.41}$$

When the energy bands are filled up to the linear crossing (i.e. the chemical potential is set to zero) the pre-quench equilibrium ground state $|\Phi_0^{(2D)}(0)\rangle$ is

$$|\Phi_0^{(2D)}\rangle = \prod_{k \leq \alpha} \left(\Phi^\dagger_{0,k_x,k_y} \right)_2 |0_{2D}\rangle = \prod_{k \leq \alpha} \left(U^\dagger_{0,k_x,k_y} \Psi^\dagger_{k_x,k_y} \right)_2 |0_{2D}\rangle, \tag{A.42}$$

with $|0_{2D}\rangle$ the vacuum of the system. As usual, the subscript 2 means that the second component of the spinor has to be considered.

We now turn to the post-quench regime. For $t > 0$ the unitary matrix diagonalizing the single-mode Hamiltonian $\mathcal{H}_{k_x,k_y} + B\sigma^z$ is

$$U_{1,k_x,k_y} = \begin{bmatrix} a_{1,k_x,k_y} & b_{1,k_x,k_y} \\ -b^*_{1,k_x,k_y} & a_{1,k_x,k_y} \end{bmatrix}, \tag{A.43}$$

with

$$a_{1,k_x,k_y} = \frac{\alpha k}{\sqrt{(D_{k_x,k_y} - B)^2 + \alpha^2 k^2}}, \qquad b_{1,k_x,k_y} = \frac{D_{k_x,k_y} - B}{\sqrt{(D_{k_x,k_y} - B)^2 + \alpha^2 k^2}} \frac{k_x + ik_y}{k}, \tag{A.44}$$

where we have introduced the coefficient $D_{k_x,k_y} = \sqrt{B^2 + \alpha^2 k^2}$. The post-quench conductance and valence band Fermi operators are

$$\Phi_{1,k_x,k_y} = U_{1,k_x,k_y} \Psi_{k_x,k_y} = \begin{bmatrix} d_{c,1,k_x,k_y} \\ d_{v,1,k_x,k_y} \end{bmatrix}, \tag{A.45}$$

with associated energy levels

$$\varepsilon_{\pm,1,k_x,k_y} = (k_x^2 + k_y^2) \pm D_{k_x,k_y}. \tag{A.46}$$

In order to get the steady state magnetization along the applied magnetic field within the GGE picture, we evaluate the averages of the conserved occupation numbers of the post-quench energy levels,

$$n_{k_x,k_y,j=1,2} = \left(\Psi^\dagger_{k_x,k_y} U^\dagger_{1,k_x,k_y} \right)_j \left(U_{1,k_x,k_y} \Psi_{k_x,k_y} \right)_j, \tag{A.47}$$

over the pre-quench ground state $|\Phi_0^{(2D)}(0)\rangle$, obtaining

$$\langle n_{k_x,k_y,1}\rangle_0 = \langle n_{k_x,k_y,1}\rangle_{GGE} = \left|-a_{1,k_x,k_y}b_{0,k_x,k_y} + a_{0,k_x,k_y}b_{1,k_x,k_y}\right|^2 \langle d^\dagger_{v,0,k_x,k_y} d_{v,0,k_x,k_y}\rangle_0, \tag{A.48a}$$

$$\langle n_{k_x,k_y,2}\rangle_0 = \langle n_{k_x,k_y,2}\rangle_{GGE} = \left|a_{1,k_x,k_y}a_{0,k_x,k_y} + b_{0,k_x,k_y}b^*_{1,k_x,k_y}\right|^2 \langle d^\dagger_{v,0,k_x,k_y} d_{v,0,k_x,k_y}\rangle_0. \tag{A.48b}$$

Since $\langle d^\dagger_{c,1,k_x,k_y} d_{v,1,k_x,k_y}\rangle_{GGE} = \langle d^\dagger_{v,1,k_x,k_y} d_{c,1,k_x,k_y}\rangle_{GGE} = 0$, the steady state magnetization after the quench evaluates to

$$\begin{aligned} M_{2D} &= \frac{1}{N_{2D}} \sum_{k_x,k_y} \langle \Psi^\dagger_{k_x,k_y} \sigma^z \Psi_{k_x,k_y}\rangle_{GGE} \\ &= \frac{1}{N_{2D}} \sum_{k_x,k_y} \left(a^2_{1,k_x,k_y} - |b_{1,k_x,k_y}|^2\right) \left(\langle n_{k_x,k_y,1}\rangle_{GGE} - \langle n_{k_x,k_y,2}\rangle_{GGE}\right) \\ &= -\frac{B}{\alpha^2}\left[1 - \frac{B}{\alpha^2}\mathrm{arccot}\left(\frac{B}{\alpha^2}\right)\right], \end{aligned} \tag{A.49}$$

where in the last step the thermodynamic limit has been performed and we used that $N_{2D} = L_x L_y/(2\pi)^2$, with L_x and L_y the length of the system in the x and y directions respectively.

A.2 Finite duration quench for the spin-orbit coupled wire

In this Section we outline the evaluation of the steady state magnetization of the SOC wire in the presence of a quench with finite duration. In particular, we consider a quench protocol in which the magnetic field is switched on with a linear ramp of duration τ. The Hamiltonian of the systems is

$$H = \sum_k \Psi^{(2)\dagger}_k \left[\mathcal{H}^{(2)}_k + Q(t) B \sigma^x\right] \Psi^{(2)}_k, \tag{A.50}$$

with

$$Q(t) = \begin{cases} 0 & \text{for } t < 0 \\ t/\tau & \text{for } 0 \le t \le \tau \\ 1 & \text{for } t > \tau \end{cases}. \tag{A.51}$$

During and after the quench, the Heisenberg equations of motion for the Fermi spinor components are

$$\partial_t d^{(2)}_{\sigma,k}(t) = -i\left[(k^2 + \sigma\alpha k) d^{(2)}_{\sigma,k}(t) + Q(t) B d^{(2)}_{-\sigma,k}(t)\right], \tag{A.52}$$

where $\sigma = \{a, b\} = \{+, -\}$. To solve this coupled system of differential equations, we take the following ansatz [182]

$$\begin{bmatrix} d^{(2)}_{a,k}(t) \\ d^{(2)}_{b,k}(t) \end{bmatrix} = \begin{bmatrix} f_{a,k}(t) & g_{a,k}(t) \\ f_{b,k}(t) & g_{b,k}(t) \end{bmatrix} \begin{bmatrix} d^{(2)}_{a,k} \\ d^{(2)}_{b,k} \end{bmatrix} = V_k(t) \begin{bmatrix} d^{(2)}_{a,k} \\ d^{(2)}_{b,k} \end{bmatrix}, \tag{A.53}$$

where $d^{(2)}_{\sigma,k}$ is the Fermi operator in the Schrödinger picture at $t = 0$. Therefore, all the time dependence is encoded in the functions $f_{\sigma,k}(t)$ and $g_{\sigma,k}(t)$, with initial conditions given by $f_{a,k}(0) = g_{b,k}(0) = 1$ and $f_{b,k}(0) = g_{a,k}(0) = 0$. Since anti-commutation relations between the operators $d^{(2)}_{\sigma,k}(t)$ have to be satisfied during the whole time evolution,we have that $|f_{\sigma,k}(t)|^2 + |g_{\sigma,k}(t)|^2 = 1,\ \forall t$. By substituting the ansatz of Eq. (A.53) in Eq. (A.52), we obtain two decoupled systems for $f_{\sigma,k}(t)$ and $g_{\sigma,k}(t)$, respectively,

$$i\partial_t \begin{bmatrix} f_{a,k}(t) \\ f_{b,k}(t) \end{bmatrix} = \begin{bmatrix} k^2 + \alpha k & Q(t)B \\ Q(t)B & k^2 - \alpha k \end{bmatrix} \begin{bmatrix} f_{a,k}(t) \\ f_{b,k}(t) \end{bmatrix}, \tag{A.54}$$

$$i\partial_t \begin{bmatrix} g_{a,k}(t) \\ g_{b,k}(t) \end{bmatrix} = \begin{bmatrix} k^2 + \alpha k & Q(t)B \\ Q(t)B & k^2 - \alpha k \end{bmatrix} \begin{bmatrix} g_{a,k}(t) \\ g_{b,k}(t) \end{bmatrix}. \tag{A.55}$$

The latter systems can be solved with same method, given that the appropriate initial conditions are used. In particular, introducing the notation $\nu = \{f, g\}$, we define the functions [18]

$$S_{\nu,k}(t) = \nu_{a,k}(t) + \nu_{b,k}(t), \qquad D_{\nu,k}(t) = \nu_{a,k}(t) - \nu_{b,k}(t). \tag{A.56}$$

Using Eq. (A.54), one obtains that the following differential equations hold

$$\begin{cases} i\partial_t S_{\nu,k}(t) = \left[k^2 + Q(t)B\right] S_{\nu,k}(t) + \alpha k D_{\nu,k}(t) \\ i\partial_t D_{\nu,k}(t) = \left[k^2 - Q(t)B\right] D_{\nu,k}(t) + \alpha k S_{\nu,k}(t) \end{cases}, \tag{A.57}$$

From the above system we derive the second-order differential equation

$$\partial_t^2 D_{\nu,k}(t) + 2ik^2 \partial_t D_{\nu,k}(t) + \left[B^2 Q^2(t) - k^4 + \alpha^2 k^2 - iB\partial_t Q(t)\right] D_{\nu,k}(t) = 0, \tag{A.58}$$

which can be analytically solved in every region defined by the quench protocol in Eq. (A.51) using the appropriate matching conditions on the boundaries of each them. Moreover, once we get $D_{\nu,k}(t)$, the function $S_{\nu,k}(t)$ is automatically determined by the second equation in Eq. (A.57).

The magnetization along the applied magnetic field can be evaluated within the GGE, with a straightforward generalization of procedure described in Sec. A.1.2. In particular, the quantities conserved after the quench (i.e. for $t > \tau$) are $\langle n^{(2)}_{k,j}(\tau)\rangle_0 = \langle n^{(2)}_{k,j}(\tau)\rangle_{GGE}$, with

$$n^{(2)}_{k,j}(\tau) = \left(\Phi^{(2)\dagger}_{0,k} U^{(2)}_{0,k} V^{\dagger}_k(\tau) U^{(2)\dagger}_{1,k}\right)_j \left(U^{(2)}_{1,k} V_k(\tau) U^{(2)\dagger}_{0,k} \Phi^{(2)}_{0,k}\right)_j \tag{A.59}$$

the occupation numbers of the post-quench energy levels and the unitary matrix $V_k(t)$ introduced in Eq. (A.53). From the knowledge of $\langle n^{(2)}_{k,j}(\tau)\rangle_{GGE}$ and thanks to the fact that $\langle d^{(i)\dagger}_{c,1,k}(\tau) d^{(i)}_{v,1,k}(\tau)\rangle_{GGE} = \langle d^{(i)\dagger}_{v,1,k}(\tau) d^{(i)}_{c,1,k}(\tau)\rangle_{GGE} = 0$, one can evaluate the steady state magnetization

$$M^{(2)} = \frac{1}{n^{(2)}} \sum_k \langle \Psi^{(2)\dagger}_k \sigma^x \Psi^{(2)}_k \rangle_{GGE} = \frac{1}{n^{(2)}} \sum_k \langle \Phi^{(2)\dagger}_{1,k}(\tau) U^{(2)}_{1,k} V_k(\tau) \sigma^x V^{\dagger}_k(\tau) U^{(2)\dagger}_{1,k} \Phi^{(2)}_{1,k}(\tau)\rangle_{GGE}. \tag{A.60}$$

As one can clearly see, the non-monotonic behavior persists also in this case, for quench protocols with different time duration τ.

A.3 Klein-Gordon physics in the evolution of the Green's function

In this Section we focus on the low-energy continuous theories for the SOC wire and the SP model and derive KG equation [see Eq. (3.19) of the main text] satisfied by the general Green's function

$$\mathcal{G}^{(i)}(x,t) = \langle \Psi^{(i)\dagger}(x,t)\sigma^x \Psi^{(i)}(0,t)\rangle_0 \tag{A.61}$$

after a sudden quench of the gap opening mechanism. Here,

$$\Psi^{(i)\dagger}(x,t) = \left(\psi_a^{(i)\dagger}(x,t), \psi_b^{(i)\dagger}(x,t)\right) \tag{A.62}$$

is the space-resolved Fermi spinor in the Heisenberg picture, while the average is evaluated on the pre-quench equilibrium ground state $|\Phi_0^{(i)}\rangle$.

A.3.1 Spin-orbit coupled wire

We start by deriving the equation of motion of the Fermi field operator $\Psi^{(2)}(x,t)$ for the SOC wire. By rewriting the Hamiltonian of Eq. (A.6) in real space as a function of $\Psi^{(2)}(x)$ one gets the Heisenberg equations of motion for the Fermi spinor components,

$$\partial_t \psi_\sigma^{(2)}(x,t) = \left(i\partial_x^2 - \sigma\alpha\partial_x\right)\psi_\sigma^{(2)}(x,t) - iB\psi_{-\sigma}^{(2)}(x,t), \tag{A.63}$$

with $\sigma,\sigma' = \{a,b\} = \{+,-\}$. From the above equation, we can derive the equations of motion for the spin resolved Green's functions,

$$G_{\sigma\sigma'}^{(i)}(x,t) = \langle \psi_\sigma^{(i)\dagger}(x,t)\psi_{\sigma'}^{(i)}(0,t)\rangle_0. \tag{A.64}$$

As a result, we obtain the following closed set of differential equations

$$\partial_t G_{++}^{(2)}(x,t) = -iB\left[G_{+-}^{(2)}(x,t) - G_{-+}^{(2)}(x,t)\right], \tag{A.65a}$$

$$\partial_t G_{+-}^{(2)}(x,t) = -iB\left[G_{++}^{(2)}(x,t) - G_{--}^{(2)}(x,t)\right] + 2\alpha\partial_x G_{+-}^{(2)}(x,t), \tag{A.65b}$$

$$\partial_t G_{-+}^{(2)}(x,t) = +iB\left[G_{++}^{(2)}(x,t) - G_{--}^{(2)}(x,t)\right] - 2\alpha\partial_x G_{-+}^{(2)}(x,t), \tag{A.65c}$$

$$\partial_t G_{--}^{(2)}(x,t) = +iB\left[G_{+-}^{(2)}(x,t) - G_{-+}^{(2)}(x,t)\right]. \tag{A.65d}$$

Note that the Green's function of Eq. (A.61) can be written as $\mathcal{G}^{(2)}(x,t) = G_{+-}^{(2)}(x,t) + G_{-+}^{(2)}(x,t)$. From Eqs. (A.65), we thus obtain

$$\begin{aligned}\partial_t^2 \mathcal{G}^{(2)}(x,t) =& 2\alpha\partial_x\partial_t\left[G_{+-}^{(2)}(x,t) - G_{-+}^{(2)}(x,t)\right] \\ =& 4\alpha^2\partial_x^2\mathcal{G}^{(2)}(x,t) - 4i\alpha B\partial_x\left[G_{++}^{(2)}(x,t) - G_{--}^{(2)}(x,t)\right].\end{aligned} \tag{A.66}$$

It is now convenient to introduce the function $S(x,t) = G_{++}^{(2)}(x,t) - G_{--}^{(2)}(x,t)$, whose time derivative reads

$$\partial_t S(x,t) = -2iB\left[G_{+-}^{(2)}(x,t) - G_{-+}^{(2)}(x,t)\right]. \tag{A.67}$$

By integrating the above equation, one obtains

$$S(x,t) = S(x,0) - 2iB\int_0^t \left[G^{(2)}_{+-}(x,t') - G^{(2)}_{-+}(x,t')\right] dt'. \tag{A.68}$$

Then, by taking the space derivative of $S(x,t)$ and noting that

$$\partial_x \left[G^{(2)}_{+-}(x,t') - G^{(2)}_{-+}(x,t')\right] = (2\alpha)^{-1}\partial_t \mathcal{G}^{(2)}(x,t) \tag{A.69}$$

[see Eqs. (A.65b) and (A.65c)], it follows that

$$\partial_x S(x,t) = \partial_x S(x,0) - i\frac{B}{\alpha}\mathcal{G}^{(2)}(x,t). \tag{A.70}$$

Finally, turning back to Eq. (A.66), we obtain the desired result

$$\left(\partial_x^2 - \frac{1}{4\alpha^2}\partial_t^2\right)\mathcal{G}^{(2)}(x,t) = \frac{B^2}{\alpha^2}\mathcal{G}^{(2)}(x,t) + \frac{B}{\alpha}\phi_2(x), \tag{A.71}$$

where the source term $\phi_2(x)$ is defined as

$$\phi_2(x) = i\partial_x S(x,0) = i\partial_x \langle \Psi^{(2)\dagger}(x,0)\sigma^z \Psi^{(2)}(0,0)\rangle_0. \tag{A.72}$$

In particular, $\phi_2(x)$ can be analytically evaluated to obtain

$$\phi_2(x) = 2\left[\frac{1-\cos(\alpha x)}{x^2} - \frac{\alpha \sin(\alpha x)}{x}\right]. \tag{A.73}$$

A.3.2 Staggered potential model

We now focus on the SP model. In principle, the KG equation satisfied by the Green's function $\mathcal{G}^{(4)}(x,t)$ can be obtained following the same steps of the SOC wire case. However, in order to show an alternative method to derive it, we demonstrate that $\mathcal{G}^{(4)}(x,t)$ satisfies the analogous of Eq. (A.71) by a direct calculation. We begin by explicitly evaluating $\mathcal{G}^{(4)}(x,t) = \langle \Psi^{(4)\dagger}(x,t)\sigma^x \Psi^{(4)}(0,t)\rangle$. The time evolution of the Fermi spinor $\Psi^{(4)}(x,t) = \sum_k \Psi^{(4)}_k(t)e^{ikx}/\sqrt{L^{(4)}}$ in the Heisenberg picture can be obtained from Eq. (2) of the main text,

$$\Psi^{(4)}_k(t) = U^{(4)\dagger}_{1,k}\mathrm{diag}\{e^{-i\epsilon^{(4)}_{+,1,k}t}, e^{-i\epsilon^{(4)}_{-,1,k}t}\}U^{(4)}_{1,k}U^{(4)\dagger}_{0,k}\Phi^{(4)}_{0,k}(0), \tag{A.74}$$

with the coefficients of the matrices $U^{(4)}_{0,k}$ and $U^{(4)}_{1,k}$ given in Eqs. (A.30) and (A.32b), respectively. Here, $\Psi^{(i)\dagger}_k(t) = \left(d^{(i)\dagger}_{a,k}(t), d^{(i)\dagger}_{b,k}(t)\right)$ is the momentum resolved Fermi spinor and $L^{(4)}$ is the length of the system. The Green's function $G^{(4)}(x,t)$ can thus be rewritten as

$$\mathcal{G}^{(4)}(x,t) = \frac{1}{L^{(4)}}\sum_k e^{-ikx}\langle d^{(4)\dagger}_{b,k}(t)d^{(4)}_{a,k}(t) + h.c.\rangle_0, \tag{A.75}$$

where the average is evaluated on the ground state of the pre-quench Hamiltonian $\mathcal{H}^{(4)}_k$, defined in Eq. (A.10). Using Eqs. (A.30), (A.32b) and (A.74), we obtain

$$\begin{aligned}\langle d^{(4)\dagger}_{b,k}(t)d^{(4)}_{a,k}(t)\rangle_0 =& \frac{1}{8}\langle d^{(4)\dagger}_{v,1,k}d^{(4)}_{v,1,k}\rangle_0 \cdot \\ &\cdot\left[-4\beta_k \mathrm{Im}\{\beta_k\} - ie^{-2it\epsilon^{(4)}_{+,1,k}}\left(1+\beta_k^2\right) - ie^{-2it\epsilon^{(4)}_{-,1,k}}\beta_k^2\left(1+\beta_k^{*2}\right)\right],\end{aligned} \tag{A.76}$$

where $\beta_k = \sqrt{2}b^{(4)}_{1,k}$. Substituting in Eq. (A.75) and performing the thermodynamic limit, one has

$$\mathcal{G}^{(4)}(x,t) = -\frac{1}{\pi}\int_0^\pi e^{-ikx}\frac{Jk\delta}{J^2k^2+\delta^2}\left[1-\cos\left(2t\epsilon^{(4)}_{+,1,k}\right)\right]dk. \tag{A.77}$$

Finally, after evaluating the second-order time and space derivatives of $G^{(4)}(x,t)$,

$$\partial_t^2\mathcal{G}^{(4)}(x,t) = -\frac{4}{\pi}\int_0^\pi e^{-ikx}Jk\delta\cos\left(2t\epsilon^{(4)}_{+,1,k}\right)dk, \tag{A.78a}$$

$$\partial_x^2\mathcal{G}^{(4)}(x,t) = \frac{1}{\pi}\int_0^\pi e^{-ikx}\frac{Jk^3\delta}{J^2k^2+\delta^2}\left[1-\cos\left(2t\epsilon^{(4)}_{+,1,k}\right)\right]dk, \tag{A.78b}$$

and performing some algebraic manipulations, one can directly verify that the following KG equation is satisfied

$$\left(\partial_x^2 - \frac{1}{4J^2}\partial_t^2\right)\mathcal{G}^{(4)}(x,t) = \frac{\delta^2}{J^2}\mathcal{G}^{(4)}(x,t) + \frac{\delta}{J}\phi_4(x), \tag{A.79}$$

where the source term $\phi_4(x)$ is

$$\phi_4(x) = 2\frac{\cos(\pi x)+\pi x\sin(\pi x)-1}{\pi x^2} = i\partial_x\langle\Psi^{(4)\dagger}(x,0)\sigma^y\Psi^{(4)}(0,0)\rangle_0. \tag{A.80}$$

APPENDIX B

Quantum quench and geometrical interpretation

B.1 Quench-induced transformation in the SSH model

We start this section by giving, as stated in the main text, the Hamiltonian of the Su-Schrieffer-Heeger (SSH) model (see Section 2.2)

$$H(t) = \sum_k \Psi_k^\dagger \left\{ \sigma_x \left[w + w\cos k + \delta(t) \right] + w\sigma_y \sin k \right\} \Psi_k, \tag{B.1}$$

where $\Psi_k^\dagger = \left(c_{k,A}^\dagger, c_{k,B}^\dagger \right)$ is a two-component momentum resolved Fermi spinor, A and B represent the two sublattices of the unit cell and the hopping between the same and different cells is staggered. This difference is encoded in the quantity $\delta(t)$, which measures the amplitude of the gap in the spectrum of the system. In the context of sudden quantum quenches, $\delta(t)$ abruptly changes its value, namely

$$\delta(t) = \delta_0 \theta(-t) + \delta_1 \theta(t). \tag{B.2}$$

Here, we conveniently use the indexes 0 or 1 for the pre- or post-quench quantities, respectively, and the symbol θ denotes the Heaviside step function. The Hamiltonian, accordingly, can be written as

$$H(t) = H_0 \theta(-t) + H_1 \theta(t). \tag{B.3}$$

It is useful, at this point, to diagonalize both the pre- and post-quench Hamiltonians, by means of a unitary transformation, to obtain ($\mu = 0, 1$)

$$H_\mu = \sum_k \epsilon_{\mu,k} \left(d_{\mu,c,k}^\dagger d_{\mu,c,k} - d_{\mu,v,k}^\dagger d_{\mu,v,k} \right), \tag{B.4}$$

where the subscripts c and v are associated with the conduction and valence bands respectively, and

$$\epsilon_{\mu,k} = \sqrt{\delta_\mu^2 + 2(w^2 + w\delta_\mu)(1 + \cos k)} \tag{B.5}$$

is the energy spectrum. The transformation, which relates the lattice and the diagonal bases, is defined as:

$$\Phi_{\mu,k} = \begin{pmatrix} d_{\mu,c,k} \\ d_{\mu,v,k} \end{pmatrix} = U_{\mu,k}\Psi_k, \tag{B.6}$$

where

$$U_{\mu,k} = \begin{pmatrix} A_{\mu,k} & B_{\mu,k} \\ -B^*_{\mu,k} & A_{\mu,k} \end{pmatrix} \tag{B.7}$$

and

$$A_{\mu,k} = \frac{1}{\sqrt{2}}\,, \qquad B_{\mu,k} = \frac{1}{\sqrt{2}}\frac{w\left(1+e^{-ik}\right)+\delta_\mu}{\epsilon_{\mu,k}}\,. \tag{B.8}$$

One can easily compose these transformations to get the unitary matrix which connects the two diagonal pre- and post-quench bases. It has the following form:

$$\Phi_{1,k} = U_{1,k}U^\dagger_{0,k}\Phi_{0,k} = \mathcal{U}^1_{0,k}\Phi_{0,k}. \tag{B.9}$$

B.2 General properties

To get more insight about the quench-induced transformation, it is instructive to rewrite $\mathcal{U}^0_{1,k}$ in the following form,

$$\mathcal{U}^0_{1,k} = \exp\left(i\vec{\mathcal{D}}_k\cdot\vec{\sigma}\right) \tag{B.10}$$

where $\vec{\sigma}$ is the vector of Pauli matrices and $\vec{\mathcal{D}}_k = |\vec{\mathcal{D}}_k|\ \vec{n}_k$. By exploiting the properties of Pauli matrices one obtains (from here on we set $w = 1$ for simplicity)

$$|\vec{\mathcal{D}}_k| = \arctan\left[\frac{\sqrt{4-(1-\Delta_k)^2}}{1-\Delta_k}\right], \tag{B.11}$$

$$\vec{n}_k = \frac{1}{\sqrt{4-(1-\Delta_k)^2}}\begin{pmatrix} -\sin k\left(\dfrac{1}{\epsilon_{1,k}}+\dfrac{1}{\epsilon_{0,k}}\right) \\ \dfrac{1+\delta_1+\cos k}{\epsilon_{1,k}} - \dfrac{1+\delta_0+\cos k}{\epsilon_{0,k}} \\ \dfrac{\delta_0-\delta_1}{\epsilon_{0,k}\epsilon_{1,k}}\sin k \end{pmatrix}, \tag{B.12}$$

$$\Delta_k = -\frac{1+(1+\delta_0)(1+\delta_1)+(2+\delta_0+\delta_1)\cos k}{\epsilon_{0,k}\epsilon_{1,k}}. \tag{B.13}$$

The function Δ_k introduced above emerges naturally from the transformation, i.e. from the sudden quench: note that, indeed, $|\vec{\mathcal{D}}_k|$ only depends on the momentum via Δ_k. The following general properties hold:

1. Δ_k is a periodic and analytic function *of the momentum* k, with $\Delta_k = \Delta_{-k}$ due to time-reversal symmetry;

2. $-1 \leq \Delta_k \leq 1$, which in turns implies $0 \leq |\vec{\mathcal{D}}_k| \leq \pi/2$.

Moreover, the unit vector $\vec{n}_k$ shows a clear symmetry with respect to the parameter k, such that for $k \to -k$ the vector $\vec{\mathcal{D}}_k$ gets mirrored about the y-axis. In view of the properties outlined above let us study Δ_k over half of the BZ, namely on $\mathcal{I} = [0, \pi]$, where one finds that the equation $|\Delta_k| = 1$ has solutions only if $k = 0, \pi$. More specifically, denoting $s(x) = x/|x|$ the sign function, one finds

$$\Delta_0 = -s(\delta_0 + 2)s(\delta_1 + 2) \; ; \; \Delta_\pi = -s(\delta_0)s(\delta_1). \tag{B.14}$$

Clearly, as a function of the quench parameters, Δ_k is *not* analytic but exhibits *jumps* when the critical lines $\delta_\mu = 0$ and $\delta_\mu = -2$ are crossed, while for all other values of k, Δ_k is instead a continous and analytic function of the quench parameters. Note that at $\delta_\mu = 0, -2$ the equilibrium SSH model presents two quantum critical points (QCPs) associated to a quantum phase transition (QPT). This defines nine regions in the (δ_0, δ_1)-plane: within each region the values of Δ_0 and Δ_π are constant and independent of the quench. One finds

$$\Delta_k = -1 \implies \mathcal{U}^0_{1,k} = \begin{pmatrix} 1 & 0 \\ 0 & 1 \end{pmatrix}, \tag{B.15}$$

$$\Delta_k = 1 \implies \mathcal{U}^0_{1,k} = \begin{pmatrix} 0 & 1 \\ -1 & 0 \end{pmatrix}. \tag{B.16}$$

When $\Delta_k = -1$ the c, v states are unchanged, while for $\Delta_k = 1$ the c, v states are essentially swapped. In addition, $\Delta_k = 1 \implies \vec{n}_k = (0, -1, 0)$. Therefore, the transformation $\mathcal{U}^0_{1,k}$ has two fixed points, namely $\vec{D}_k = (0, 0, 0)$ (henceforth called I) where it reduces to the identity and $\vec{D}_k = (0, -\pi/2, 0)$ (henceforth called R), where bands are swapped.

B.2.1 Occupation numbers and GGE weights

In this section we introduce the Generalized Gibbs Ensemble (GGE) which, in the thermodynamic limit, reproduces the long time limit of the expectation value of the system observables. We start by presenting the GGE density matrix, obtained by maximizing the entropy while keeping into account the conservation of the occupation number operators $N_{\alpha,k} = d^\dagger_{1,\alpha,k} d_{1,\alpha,k}$,

$$\rho_G = \frac{e^{-\sum_{\alpha,k} \lambda_{\alpha,k} N_{\alpha,k}}}{\mathrm{Tr}\left\{ e^{-\sum_{\alpha,k} \lambda_{\alpha,k} N_{\alpha,k}} \right\}}, \tag{B.17}$$

where $\alpha = c, v$ and $\lambda_{\alpha,k}$ are the corresponding Lagrange multipliers, obtained by imposing

$$\mathrm{Tr}\left\{ N_{\alpha,k} \rho_G \right\} = \langle G_0 | N_{\alpha,k} | G_0 \rangle = n_{\alpha,k}, \tag{B.18}$$

with $|G_0\rangle$ the pre-quench ground state. One has

$$\langle G_0 | N_{c,k} | G_0 \rangle = |A_{0,k} B_{1,k} - A_{1,k} B_{0,k}|^2, \tag{B.19}$$

$$\langle G_0 | N_{v,k} | G_0 \rangle = \left| A_{0,k} A_{1,k} + B^*_{1,k} B_{0,k} \right|^2, \tag{B.20}$$

and

$$\lambda_{c,k} = \ln\left(\frac{n_{v,k}}{n_{c,k}}\right) = -\lambda_{v,k}. \tag{B.21}$$

Interestingly, by recalling Eq. (B.19), we observe that

$$\Delta_k = n_{c,k} - n_{v,k}, \tag{B.22}$$

and

$$\lambda_{c,k} = \ln\left(\frac{1-\Delta_k}{1+\Delta_k}\right). \tag{B.23}$$

Equation (B.22) is particularly interesting since it links the imbalance between c and v states to the function Δ_k, which, in turn, is directly connected with the presence of the quench. With $|G_0\rangle$ as the pre-quench state, $\Delta_k = 1$ implies a complete inversion of population. Three different scenarios can occur, according to the quench parameters:

- If $\Delta_0 = -1$ and $\Delta_\pi = -1$, the function Δ_k must have at least one maximum in each half of the BZ. It is easy to prove that in this situation $\Delta_k < 0$ always. As a result, no inversion of population occurs;
- If $\Delta_0 = \mp 1$ and $\Delta_\pi = \pm 1$, the function Δ_k must have at least one zero in each half of the BZ. Indeed, there is exactly one zero per half, located at

  $$k^* = -\arccos\left(\frac{2+\delta_0+\delta_1+\delta_0\delta_1}{2+\delta_0+\delta_1}\right). \tag{B.24}$$

  In this situation a non-trivial inversion of population occurs for $-\pi \leq k < -k^*$ and $k^* < k \leq \pi$;
- If $\Delta_0 = 1$ and $\Delta_\pi = 1$, the function Δ_k must have at least one minimum in each half of the BZ and one can prove that $\Delta_k > 0$ always. As a result, a complete inversion of population in the whole BZ occurs. Formally, this last case can be analyzed by simply swapping the role of the c and v states throughout the entire BZ, thus we label this a "trivial" inversion of population.

B.3 Effective GGE energy bands

Upon defining $\varepsilon_{\alpha,k} = w\lambda_{\alpha,k}$ and introducing a fictitious effective inverse temperature $\beta^* = w^{-1}$ we can re-write

$$n_{\alpha,k} = \frac{1}{1+e^{\beta^*\varepsilon_{\alpha,k}}}. \tag{B.25}$$

Thus, the occupation numbers $n_{\alpha,k}$ correspond to a thermal distribution of free fermions with effective energy bands $\varepsilon_{\alpha,k}$ and zero chemical potential. By exploiting this analogy, from the above discussion and Eq. (B.23), we can conclude that:

- If $\Delta_0\Delta_\pi = 1$, the two effective bands never touch nor cross the chemical potential and thus describe an effective insulating configuration;
- If $\Delta_0\Delta_\pi = -1$, the two effective bands cross precisely at chemical potential, exactly once per half of the BZ, and thus describe an effective metallic configuration.

Therefore, each of the nine regions in the quench parameters space is associated, in the GGE, to an effective metallic or insulating “phase", and transitions occur whenever one of the δ_i crosses the critical lines.

B.3.1 A geometrical interpretation

We can provide a geometrical interpretation of what discussed above. As k sweeps the BZ, the vector $\vec{\mathcal{D}}_k$ describes a closed curve γ in the three-dimensional space, pinned to either or both the fixed points I, R. To be specific and without loss of generality, here we consider the case $\delta_0 > 0$ only.

- For $\delta_1 > 0$, one has $\Delta_0 = \Delta_\pi = -1$. Thus, γ passes twice through the point I;
- For $-2 < \delta_1 < 0$, one has $\Delta_0 = -\Delta_\pi = -1$. As a consequence, γ passes through both I and R;
- For $\delta_1 < -2$ and γ passes through both I and R;

In the first and last cases the GGE has an insulating character and the curve γ describes a butterfly shape pinned either at the origin ($\delta_1 > 0$) or at $(0, -\pi/2, 0)$ ($\delta_1 < -2$). On the other hand, for $-2 < \delta_1 < 0$ the GGE is metallic and γ describes a closed loop pinned at I and R. A variation of the quench parameters which does not result in a crossing of the critical lines does not alter the qualitative features of the curve γ. The scenario is summarized in Fig. B.1.

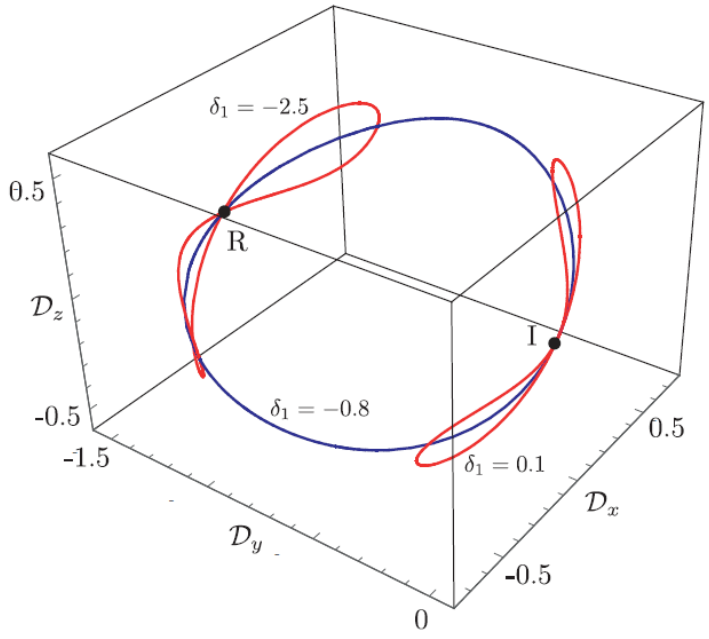

Figure B.1: Three different curves γ described by the vector $\vec{\mathcal{D}}_k$ with k spanning the BZ. Here we set $\delta_0 = 5w$ and three possible representations of the different regimes are shown for $\delta_1 = 0.1w$ and $\delta_1 = -2.5w$, which describe the insulating effective phase (red curves), and for $\delta_1 = -0.8w$, which describe the metallic effective phase (blu curve).

B.4 Robustness

In this section we give some details about the robustness of the effective metal-insulator transition with respect to a thermal initial state and a finite-duration quench.

B.4.1 Thermal initial state

We start by observing that, given a generic occupation of the pre-quench states $n^{(0)}_{\alpha,k}$, using the quench transformation one can promptly obtain

$$n_{c,k} - n_{v,k} = [n^{(0)}_{v,k} - n^{(0)}_{c,k}]\Delta_k \,. \tag{B.26}$$

This relationship is very powerful: Let us apply it to the case of a system prepared at a generic temperature $T = (k_B\ \beta)^{-1}$, with occupation numbers

$$n^{(0)}_{c,k} = \frac{1}{1+e^{\beta\epsilon_{0,k}}} \qquad \text{and} \qquad n^{(0)}_{v,k} = \frac{1}{1+e^{-\beta\epsilon_{0,k}}} \,. \tag{B.27}$$

One then easily obtains

$$n_{c,k} - n_{v,k} = f_{T,k}\Delta_k \,, \tag{B.28}$$

with

$$f_{T,k} = \frac{\sinh(\beta\epsilon_{0,k})}{1+\cosh(\beta\epsilon_{0,k})} > 0. \tag{B.29}$$

Equipped with Eq. (B.28) one obtains the GGE multipliers

$$\lambda_{c,k} = \ln\left(\frac{1-f_{T,k}\Delta_k}{1+f_{T,k}\Delta_k}\right) \qquad \text{and} \qquad \lambda_{v,k} = -\lambda_{c,k} \,. \tag{B.30}$$

The key observation is that for any temperature T the qualitative features of $n_{c,k} - n_{v,k}$ (governing the inversion of population) and of the new GGE multipliers (dictating the effective metal-insulator transitions) remain unchanged since $f_{T,k}$ has no zeroes and thus can neither destroy the insulating phase, nor distort the metallic one. Thus, all the conclusions obtained in the $T = 0$ case still hold, including the presence of non-analyticities in the steady state of quantities, still hold.

B.4.2 Finite-duration quenches

Turning to the study of the effects of a quench with finite duration, we introduce a new quench protocol encoded in the time dependence of the quench parameter $\delta(t)$, defined in Eq. (B.1). Here we consider a linear ramp, namely

$$\delta(t) = \begin{cases} \delta_0 & t \le 0 \\ \delta_0 + (\delta_1 - \delta_0)t/\tau & 0 < t \le \tau \\ \delta_1 & t > \tau \end{cases} , \tag{B.31}$$

where τ is the quench duration. By means of the Heisenberg equation of motion and taking the following ansatz,

$$\begin{aligned}\begin{pmatrix} c_{k,A}(t) \\ c_{k,B}(t) \end{pmatrix} &= \begin{pmatrix} f_{k,A}(t) & g_{k,A}(t) \\ f_{k,B}(t) & g_{k,B}(t) \end{pmatrix} \begin{pmatrix} c_{k,A} \\ c_{k,B} \end{pmatrix} \\ &= V_k(t) \begin{pmatrix} c_{k,A} \\ c_{k,B} \end{pmatrix},\end{aligned} \tag{B.32}$$

where $c_{k,A}$ and $c_{k,B}$ are the Fermi operator in the Schrödinger picture at $t = 0$, we can evaluate the time evolution of the whole Fermi spinor $\Psi_k^\dagger = \left(c_{k,A}^\dagger, c_{k,B}^\dagger\right)$, given the initial conditions $f_{k,A}(t=0) = g_{k,B}(t=0) = 1$ and $f_{k,B}(t=0) = g_{k,A}(t=0) = 0$. We obtain that the coefficients of the matrix $V_k(t)$ satisfy the following systems of differential equations:

$$\begin{aligned}\begin{pmatrix} f_{k,A}(t) \\ f_{k,B}(t) \end{pmatrix} &= \begin{pmatrix} 0 & m_k(t) \\ m_k^*(t) & 0 \end{pmatrix} \begin{pmatrix} f_{k,A} \\ f_{k,B} \end{pmatrix}, \\ \begin{pmatrix} g_{k,A}(t) \\ g_{k,B}(t) \end{pmatrix} &= \begin{pmatrix} 0 & m_k(t) \\ m_k^*(t) & 0 \end{pmatrix} \begin{pmatrix} g_{k,A} \\ g_{k,B} \end{pmatrix},\end{aligned} \tag{B.33}$$

where

$$m_k(t) = 1 + e^{-ik} + \delta(t). \tag{B.34}$$

Therefore, we are able to write the transformation which connects the pre- and post-quench diagonal bases,

$$\Phi_{1,k} = U_{1,k} V_k(\tau) U_{0,k}^\dagger \Phi_{0,k} = \mathcal{V}_{1,k}^0(\tau) \Phi_{0,k}. \tag{B.35}$$

which represents the generalization to the finite duration quench of Eq. (B.9). Equation (B.35) allows us to evaluate the GGE conserved quantities

$$\begin{aligned}n_{c,k} = &|A_{0,k} \left[B_{1,k} g_{k,B}(\tau) + A_{1,k} g_{k,A}(\tau)\right] \\ &- B_{0,k} \left[B_{1,k} f_{k,B}(\tau) + A_{1,k} f_{k,A}(\tau)\right]|^2 = 1 - n_{v,k}.\end{aligned} \tag{B.36}$$

As done above, we focus now on the points $k = 0, \pi$, where the analysis becomes transparent. At these points $m_k(t)$ is real and the coefficients of the matrix $V_k(t)$ fulfill the following differential equation

$$\partial_t^2 V_k - \frac{\delta_1 - \delta_0}{\tau \mu_k(t)} \partial_t V_k + \mu_k(t)^2 V_k = 0, \tag{B.37}$$

where $\mu_0(t) = 2 + \delta(t)$ and $\mu_\pi(t) = \delta(t)$. Solving this equation and assuming for simplicity $\delta_0 > 0$, we obtain for $k = \pi$

$$\mathcal{V}_{1,\pi}^0(\tau) = \frac{1 + s(\delta_1)}{2} \begin{pmatrix} e^{-i\eta\tau} & 0 \\ 0 & e^{i\eta\tau} \end{pmatrix} - \frac{1 - s(\delta_1)}{2} \begin{pmatrix} 0 & e^{i\eta\tau} \\ -e^{-i\eta\tau} & 0 \end{pmatrix}, \tag{B.38}$$

where $\eta = \dfrac{\delta_0 + \delta_1}{2}$. Analogous results are achieved for $k = 0$, where the sign function is shifted to the second critical point, i.e. it becomes $s(\delta_1 + 2)$. In qualitative

agreement with the sudden case, to which the above equation reduces for $\eta \to 0$, for $\delta_1 > 0$ the c, v bands remain essentially the same with the exception of an η-dependent phase shift while for $\delta_1 < 0$, in addition to the c, v the η-dependent phase shift, the c, v bands swap their role. Crucially, however, the phase shift is irrelevant in the evaluation of Δ_k at $k = 0, \pi$. As a consequence, the same qualitative conclusions concerning a non-trivial inversion of population and an effective metal-insulator transition can be drawn.

B.5 Other observables

In this section we provide some details about the steady state value of the quantities discussed in the main text.

B.5.1 Dimerization

The dimerization operator is defined as

$$\mathcal{M}(x) = \sum_{k,k'} e^{i(k'-k)x} \Psi_k^\dagger \sigma_x \Psi_{k'}. \tag{B.39}$$

Exploiting Eqns. (B.6-B.8) and the definition of the GGE one finally obtains

$$\begin{aligned} \bar{\mathcal{M}} &= \langle G_0 | M(x) | G_0 \rangle \\ &= \frac{1}{\pi} \int_{-\pi}^{\pi} A_{1,k} \mathrm{Re}\{B_{1,k}\} \left(n_{c,k} - n_{v,k}\right) dk. \end{aligned} \tag{B.40}$$

B.5.2 Entropy

We consider the entropy associated to the GGE, defined as

$$S = \mathrm{Tr}\left\{\rho_G \ln(\rho_G)\right\}. \tag{B.41}$$

The quantity S has to be interpreted as the extensive part of the entanglement entropy of long enough subsystems. Its evaluation can be performed by standard means by noticing the formal analogy to a system of free fermions unveiled in Sec. B.2.1. We obtain:

$$S = -\sum_{\alpha,k} n_{\alpha,k} \ln\left(n_{\alpha,k}\right). \tag{B.42}$$

Current fluctuations

Here we consider the fluctuations of the spatially-averaged current, related to the DC conductance, both in the real and in the effective GGE bands. We start by defining the current operator as the derivative of the energy spectrum with respect to the momentum k. In the thermodynamic limit,

$$J_{(0)} = \sum_\alpha J_\alpha^{(0)} = \frac{1}{2\pi} \sum_\alpha \int_{-\pi}^{\pi} j_{\alpha,k}^{(0)} N_{\alpha,k} dk \tag{B.43}$$

with $j_{\alpha,k} = \pm\partial_k \epsilon_{1,k}$ ($\pm$ for c, v) and $j^0_{\alpha,k} = \partial\varepsilon_{\alpha,k}$ for the real (J) and GGE effective bands (J_0) respectively. The DC fluctuations $\bar{\sigma}_{(0)} = \langle G_0|J^2_{(0)}|G_0\rangle$ are thus given by

$$\bar{\sigma}_{(0)} = \frac{1}{(2\pi)^2}\sum_\alpha \int_{-\pi}^{\pi} \left(j^{(0)}_{\alpha,k}\right)^2 n_{\alpha,k}\left(1 - n_{\alpha,k}\right) dk \tag{B.44}$$

and, given the relation between the GGE conserved quantities and the effective bands in Eq. (B.22), we obtain

$$\bar{\sigma}_{(0)} = \frac{1}{(2\pi)^2}\int_0^{\pi} \left(j^{(0)}_{c,k}\right)^2 \frac{dk}{1 + \cosh(\lambda_{c,k})}. \tag{B.45}$$

B.6 Interacting model

To include interactions we concentrate on a model that is easier to simulate than the SSH model considered in the rest of the text. The Hamiltonian we want to consider is given by spinless fermions on a chain where we allow for a staggered field, nearest neighbor hopping as well as interactions

$$H(t) = \sum_{i=1}^{N} w c_i^\dagger c_{i+1} + \text{H.c.} + \delta(t)(-1)^i n_i + U n_i n_{i+1}. \tag{B.46}$$

Here $c_i^{(\dagger)}$ annihilates (creates) a spinless fermion on lattice site i. The quench is performed at time $t = 0$, at which the staggered field is is abruptly changed from δ_0 to δ_1. This model exhibits the same qualitative behavior of the SSH model in the absence of interactions. To simulate the dynamics we use an implementation of the density matrix renormalization group directly set up in the thermodynamic limit $N \to \infty$. Here we use an iterative algorithm to prepare the ground state of $H(t < 0)$ and then propagate the wave function in real time with respect to $H(t > 0)$ employing a fourth order Suzuki-Trotter decomposition. The decomposition time steps are chosen small enough to yield converged results. We dynamically increase the so-called bond-dimension, the parameter describing the numerical accuracy, as the simulation time progress, which allows us to achieve numerically exact results. By this procedure the truncation error in the wavefunction is kept below a 10^{-7} threshold. As simulation time progresses the entanglement in the system rises and with it the bond dimension as well as the numerical effort needed. Entanglement growth in simulation time is typically linear leading to an exponential increase in bond dimension. Therefore, at a certain time t the numerical resources are exhausted and no further progress in simulation time can be made. Luckily, at finite U the dynamics for the observable $\bar{\mathcal{M}} = \langle n_0 - 1/2\rangle$ of interest become strongly damped facilitating an extrapolation to long times, compare Fig. B.2. For $U = 0$, where the strong oscillations make an extrapolation more difficult, we check convergence by comparison with exact results obtained from the GGE directly.

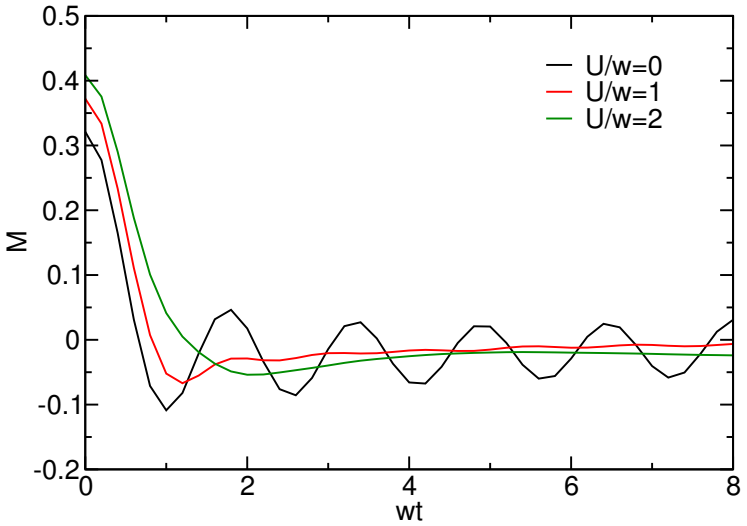

Figure B.2: Time evolution of M for different values of the interaction strength U, for $\delta_0 = w$ and $\delta_1 = -0.01w$. Increasing the interaction strength strongly suppresses the transient oscillations.

APPENDIX C

Observables driven-dissipative dynamics

C.1 Dissipative time evolution equations for the observables

In this section, we obtain the time evolution equations for the relevant observables of the system. Since the first term of the right hand side of Eq. (6.36) is the same as the one studied in [168], we give only the explicit evaluation of the dissipative term of the Lindblad equation.

C.1.1 Population of the valence band

Here we focus on the derivation of the dynamics of the occupation number of the valence band, $n_{\boldsymbol{p}}^{11} = c_{\boldsymbol{p}}^{1\dagger} c_{\boldsymbol{p}}^{1}$. We start by exploiting the commutators in eq. (6.36) corresponding to this specific case,

$$\left[\mathcal{S}_{\boldsymbol{k},\boldsymbol{q}}^{\alpha}, n_{\boldsymbol{p}}^{11}\right] = \left[c_{\boldsymbol{k}}^{\alpha\dagger} c_{\boldsymbol{k}+\boldsymbol{q}}^{\alpha}, c_{\boldsymbol{p}}^{1\dagger} c_{\boldsymbol{p}}^{1}\right] = \delta_{\alpha,1}\left[\delta(\boldsymbol{k}+\boldsymbol{q}-\boldsymbol{p}) c_{\boldsymbol{p}-\boldsymbol{q}}^{1\dagger} c_{\boldsymbol{p}}^{1} - \delta(\boldsymbol{k}-\boldsymbol{p}) c_{\boldsymbol{p}}^{1\dagger} c_{\boldsymbol{p}+\boldsymbol{q}}^{1}\right] = -\left[n_{\boldsymbol{p}}^{11}, \mathcal{S}_{\boldsymbol{k},\boldsymbol{q}}^{\alpha}\right], \tag{C.1}$$

$$\left[n_{\boldsymbol{p}}^{11}, \mathcal{S}_{\boldsymbol{k},\boldsymbol{q}}^{\alpha\dagger}\right] = \left[c_{\boldsymbol{p}}^{1\dagger} c_{\boldsymbol{p}}^{1}, c_{\boldsymbol{k}+\boldsymbol{q}}^{\alpha\dagger} c_{\boldsymbol{k}}^{\alpha}\right] = \delta_{\alpha,1}\left[\delta(\boldsymbol{k}+\boldsymbol{q}-\boldsymbol{p}) c_{\boldsymbol{p}}^{1\dagger} c_{\boldsymbol{p}-\boldsymbol{q}}^{1} - \delta(\boldsymbol{k}-\boldsymbol{p}) c_{\boldsymbol{p}+\boldsymbol{q}}^{1\dagger} c_{\boldsymbol{p}}^{1}\right] = -\left[\mathcal{S}_{\boldsymbol{k},\boldsymbol{q}}^{\alpha\dagger}, n_{\boldsymbol{p}}^{11}\right]. \tag{C.2}$$

Using Wick's theorem, we can simplify the terms obtained after the evaluation of the commutators. Here we show the ones multiplied in Eq. (6.36) by $(1+n_B)$, i. e. the first line:

$$\langle c_{\boldsymbol{k}'}^{\beta\dagger} c_{\boldsymbol{k}'+\boldsymbol{q}}^{\beta} c_{\boldsymbol{p}}^{1\dagger} c_{\boldsymbol{p}-\boldsymbol{q}}^{1}\rangle = \delta_{\beta,2}\delta(\boldsymbol{k}'+\boldsymbol{p}) \langle s_{-\boldsymbol{p}}^{21}\rangle \langle s_{-\boldsymbol{p}+\boldsymbol{q}}^{21\dagger}\rangle + \delta(\boldsymbol{k}'-\boldsymbol{p}+\boldsymbol{q}) \left[\delta_{\beta,1} \langle n_{\boldsymbol{p}-\boldsymbol{q}}^{11}\rangle \langle 1-n_{\boldsymbol{p}}^{11}\rangle - \delta_{\beta,2} \langle n_{\boldsymbol{p}-\boldsymbol{q}}^{21}\rangle \langle n_{\boldsymbol{p}}^{12}\rangle\right] \tag{C.3}$$

$$\langle c_{\boldsymbol{k}'}^{\beta\dagger} c_{\boldsymbol{k}'+\boldsymbol{q}}^{\beta} c_{\boldsymbol{p}+\boldsymbol{q}}^{1\dagger} c_{\boldsymbol{p}}^{1}\rangle = \delta_{\beta,2}\delta(\boldsymbol{k}'+\boldsymbol{p}+\boldsymbol{q}) \langle s_{-\boldsymbol{p}-\boldsymbol{q}}^{21}\rangle \langle s_{-\boldsymbol{p}}^{21\dagger}\rangle + \delta(\boldsymbol{k}'-\boldsymbol{p}) \left[\delta_{\beta,1} \langle n_{\boldsymbol{p}}^{11}\rangle \langle 1-n_{\boldsymbol{p}+\boldsymbol{q}}^{11}\rangle - \delta_{\beta,2} \langle n_{\boldsymbol{p}}^{21}\rangle \langle n_{\boldsymbol{p}+\boldsymbol{q}}^{12}\rangle\right] \tag{C.4}$$

$$\langle c_{\boldsymbol{p}-\boldsymbol{q}}^{1\dagger} c_{\boldsymbol{p}}^{1} c_{\boldsymbol{k}'+\boldsymbol{q}}^{\beta\dagger} c_{\boldsymbol{k}'}^{\beta}\rangle = \langle c_{\boldsymbol{k}'}^{\beta\dagger} c_{\boldsymbol{k}'+\boldsymbol{q}}^{\beta} c_{\boldsymbol{p}}^{1\dagger} c_{\boldsymbol{p}-\boldsymbol{q}}^{1}\rangle^{*} \tag{C.5}$$

$$\langle c_{\boldsymbol{p}}^{1\dagger} c_{\boldsymbol{p}+\boldsymbol{q}}^{1} c_{\boldsymbol{k}'+\boldsymbol{q}}^{\beta\dagger} c_{\boldsymbol{k}'}^{\beta}\rangle = \langle c_{\boldsymbol{k}'}^{\beta\dagger} c_{\boldsymbol{k}'+\boldsymbol{q}}^{\beta} c_{\boldsymbol{p}+\boldsymbol{q}}^{1\dagger} c_{\boldsymbol{p}}^{1}\rangle^{*} \tag{C.6}$$

while now we show the ones multiplied in Eq. (6.36) by n_B, i. e. the second line:

$$\langle c^{\beta\dagger}_{\boldsymbol{k}'+\boldsymbol{q}} c^{\beta}_{\boldsymbol{k}'} c^{1\dagger}_{\boldsymbol{p}-\boldsymbol{q}} c^{1}_{\boldsymbol{p}}\rangle = \delta_{\beta,2}\delta(\boldsymbol{k}'+\boldsymbol{p})\,\langle s^{21}_{-\boldsymbol{p}+\boldsymbol{q}}\rangle\,\langle s^{21\dagger}_{-\boldsymbol{p}}\rangle + \delta(\boldsymbol{k}'-\boldsymbol{p}+\boldsymbol{q})\left[\delta_{\beta,1}\,\langle n^{11}_{\boldsymbol{p}}\rangle\,\langle 1-n^{11}_{\boldsymbol{p}-\boldsymbol{q}}\rangle - \delta_{\beta,2}\,\langle n^{21}_{\boldsymbol{p}}\rangle\,\langle n^{12}_{\boldsymbol{p}-\boldsymbol{q}}\rangle\right] \tag{C.7}$$

$$\langle c^{\beta\dagger}_{\boldsymbol{k}'+\boldsymbol{q}} c^{\beta}_{\boldsymbol{k}'} c^{1\dagger}_{\boldsymbol{p}} c^{1}_{\boldsymbol{p}+\boldsymbol{q}}\rangle = \delta_{\beta,2}\delta(\boldsymbol{k}'+\boldsymbol{p}+\boldsymbol{q})\,\langle s^{21}_{-\boldsymbol{p}}\rangle\,\langle s^{21\dagger}_{-\boldsymbol{p}-\boldsymbol{q}}\rangle + \delta(\boldsymbol{k}'-\boldsymbol{p})\left[\delta_{\beta,1}\,\langle n^{11}_{\boldsymbol{p}+\boldsymbol{q}}\rangle\,\langle 1-n^{11}_{\boldsymbol{p}}\rangle - \delta_{\beta,2}\,\langle n^{21}_{\boldsymbol{p}+\boldsymbol{q}}\rangle\,\langle n^{12}_{\boldsymbol{p}}\rangle\right] \tag{C.8}$$

$$\langle c^{1\dagger}_{\boldsymbol{p}} c^{1}_{\boldsymbol{p}-\boldsymbol{q}} c^{\beta\dagger}_{\boldsymbol{k}'} c^{\beta}_{\boldsymbol{k}'+\boldsymbol{q}}\rangle = \langle c^{\beta\dagger}_{\boldsymbol{k}'+\boldsymbol{q}} c^{\beta}_{\boldsymbol{k}'} c^{1\dagger}_{\boldsymbol{p}-\boldsymbol{q}} c^{1}_{\boldsymbol{p}}\rangle^* \tag{C.9}$$

$$\langle c^{1\dagger}_{\boldsymbol{p}+\boldsymbol{q}} c^{1}_{\boldsymbol{p}} c^{\beta\dagger}_{\boldsymbol{k}'} c^{\beta}_{\boldsymbol{k}'+\boldsymbol{q}}\rangle = \langle c^{\beta\dagger}_{\boldsymbol{k}'+\boldsymbol{q}} c^{\beta}_{\boldsymbol{k}'} c^{1\dagger}_{\boldsymbol{p}} c^{1}_{\boldsymbol{p}+\boldsymbol{q}}\rangle^* \tag{C.10}$$

Hence, the dissipative part of the time evolution of $\langle n^{11}_{\boldsymbol{p}}\rangle$ due to the acoustic phonons is given by

$$\begin{aligned}\frac{d}{dt}\langle n^{11}_{\boldsymbol{p}}\rangle^{\mathrm{ph}} =& 2\sum_{\boldsymbol{q}}\Big\{ n_B\left[\Gamma^{1}_{\boldsymbol{p}-\boldsymbol{q},\boldsymbol{q}}\,\langle n^{11}_{\boldsymbol{p}}\rangle\,\langle 1-n^{11}_{\boldsymbol{p}-\boldsymbol{q}}\rangle - \Gamma^{2}_{\boldsymbol{p}-\boldsymbol{q},\boldsymbol{q}}\mathrm{Re}\left\{\langle n^{21}_{\boldsymbol{p}}\rangle\,\langle n^{12}_{\boldsymbol{p}-\boldsymbol{q}}\rangle\right\} - \Gamma^{2}_{-\boldsymbol{p},\boldsymbol{q}}\mathrm{Re}\left\{\langle s^{21}_{-\boldsymbol{p}+\boldsymbol{q}}\rangle\,\langle s^{21\dagger}_{-\boldsymbol{p}}\rangle\right\}\right] + \\ &- [1+n_B]\left[\Gamma^{1}_{\boldsymbol{p},\boldsymbol{q}}\,\langle n^{11}_{\boldsymbol{p}}\rangle\,\langle 1-n^{11}_{\boldsymbol{p}+\boldsymbol{q}}\rangle - \Gamma^{2}_{\boldsymbol{p},\boldsymbol{q}}\mathrm{Re}\left\{\langle n^{21}_{\boldsymbol{p}}\rangle\,\langle n^{12}_{\boldsymbol{p}+\boldsymbol{q}}\rangle\right\} - \Gamma^{2}_{-\boldsymbol{p}-\boldsymbol{q},\boldsymbol{q}}\mathrm{Re}\left\{\langle s^{21}_{-\boldsymbol{p}-\boldsymbol{q}}\rangle\,\langle s^{21\dagger}_{-\boldsymbol{p}}\rangle\right\}\right] + \\ &[1+n_B]\left[\Gamma^{1}_{\boldsymbol{p}-\boldsymbol{q},\boldsymbol{q}}\,\langle n^{11}_{\boldsymbol{p}-\boldsymbol{q}}\rangle\,\langle 1-n^{11}_{\boldsymbol{p}}\rangle - \Gamma^{2}_{\boldsymbol{p}-\boldsymbol{q},\boldsymbol{q}}\mathrm{Re}\left\{\langle n^{21}_{\boldsymbol{p}-\boldsymbol{q}}\rangle\,\langle n^{12}_{\boldsymbol{p}}\rangle\right\} - \Gamma^{2}_{-\boldsymbol{p},\boldsymbol{q}}\mathrm{Re}\left\{\langle s^{21}_{-\boldsymbol{p}}\rangle\,\langle s^{21\dagger}_{-\boldsymbol{p}+\boldsymbol{q}}\rangle\right\}\right] + \\ &- n_B\left[\Gamma^{1}_{\boldsymbol{p},\boldsymbol{q}}\,\langle n^{11}_{\boldsymbol{p}+\boldsymbol{q}}\rangle\,\langle 1-n^{11}_{\boldsymbol{p}}\rangle - \Gamma^{2}_{\boldsymbol{p},\boldsymbol{q}}\mathrm{Re}\left\{\langle n^{21}_{\boldsymbol{p}+\boldsymbol{q}}\rangle\,\langle n^{12}_{\boldsymbol{p}}\rangle\right\} - \Gamma^{2}_{-\boldsymbol{p}-\boldsymbol{q},\boldsymbol{q}}\mathrm{Re}\left\{\langle s^{21}_{-\boldsymbol{p}}\rangle\,\langle s^{21\dagger}_{-\boldsymbol{p}-\boldsymbol{q}}\rangle\right\}\right]\Big\}.\end{aligned} \tag{C.11}$$

Analogously, the dissipative part due to the radiative recombination reads ($\Gamma^{\mathrm{rr}} = \pi|w|^2$)

$$\frac{d}{dt}\langle n^{11}_{\boldsymbol{p}}\rangle^{\mathrm{rr}} = \Gamma^{\mathrm{rr}}\langle n^{22}_{\boldsymbol{p}}\rangle\langle 1-n^{11}_{\boldsymbol{p}}\rangle. \tag{C.12}$$

C.1.2 Population of the conduction band

The derivation is completely analogous to the previous case. For the phonons, we have to simply exchange the band index $1 \to 2$. Therefore, we get:

$$\begin{aligned}\frac{d}{dt}\langle n^{22}_{\boldsymbol{p}}\rangle^{\mathrm{ph}} =& 2\sum_{\boldsymbol{q}}\Big\{ n_B\left[\Gamma^{2}_{\boldsymbol{p}-\boldsymbol{q},\boldsymbol{q}}\,\langle n^{22}_{\boldsymbol{p}}\rangle\,\langle 1-n^{22}_{\boldsymbol{p}-\boldsymbol{q}}\rangle - \Gamma^{1}_{\boldsymbol{p}-\boldsymbol{q},\boldsymbol{q}}\mathrm{Re}\left\{\langle n^{12}_{\boldsymbol{p}}\rangle\,\langle n^{21}_{\boldsymbol{p}-\boldsymbol{q}}\rangle\right\} - \Gamma^{1}_{-\boldsymbol{p},\boldsymbol{q}}\mathrm{Re}\left\{\langle s^{12}_{-\boldsymbol{p}+\boldsymbol{q}}\rangle\,\langle s^{12\dagger}_{-\boldsymbol{p}}\rangle\right\}\right] + \\ &- [1+n_B]\left[\Gamma^{2}_{\boldsymbol{p},\boldsymbol{q}}\,\langle n^{22}_{\boldsymbol{p}}\rangle\,\langle 1-n^{22}_{\boldsymbol{p}+\boldsymbol{q}}\rangle - \Gamma^{1}_{\boldsymbol{p},\boldsymbol{q}}\mathrm{Re}\left\{\langle n^{12}_{\boldsymbol{p}}\rangle\,\langle n^{21}_{\boldsymbol{p}+\boldsymbol{q}}\rangle\right\} - \Gamma^{1}_{-\boldsymbol{p}-\boldsymbol{q},\boldsymbol{q}}\mathrm{Re}\left\{\langle s^{12}_{-\boldsymbol{p}-\boldsymbol{q}}\rangle\,\langle s^{12\dagger}_{-\boldsymbol{p}}\rangle\right\}\right] + \\ &[1+n_B]\left[\Gamma^{2}_{\boldsymbol{p}-\boldsymbol{q},\boldsymbol{q}}\,\langle n^{22}_{\boldsymbol{p}-\boldsymbol{q}}\rangle\,\langle 1-n^{22}_{\boldsymbol{p}}\rangle - \Gamma^{1}_{\boldsymbol{p}-\boldsymbol{q},\boldsymbol{q}}\mathrm{Re}\left\{\langle n^{12}_{\boldsymbol{p}-\boldsymbol{q}}\rangle\,\langle n^{21}_{\boldsymbol{p}}\rangle\right\} - \Gamma^{1}_{-\boldsymbol{p},\boldsymbol{q}}\mathrm{Re}\left\{\langle s^{12}_{-\boldsymbol{p}}\rangle\,\langle s^{12\dagger}_{-\boldsymbol{p}+\boldsymbol{q}}\rangle\right\}\right] + \\ &- n_B\left[\Gamma^{2}_{\boldsymbol{p},\boldsymbol{q}}\,\langle n^{22}_{\boldsymbol{p}+\boldsymbol{q}}\rangle\,\langle 1-n^{22}_{\boldsymbol{p}}\rangle - \Gamma^{1}_{\boldsymbol{p},\boldsymbol{q}}\mathrm{Re}\left\{\langle n^{12}_{\boldsymbol{p}+\boldsymbol{q}}\rangle\,\langle n^{21}_{\boldsymbol{p}}\rangle\right\} - \Gamma^{1}_{-\boldsymbol{p}-\boldsymbol{q},\boldsymbol{q}}\mathrm{Re}\left\{\langle s^{12}_{-\boldsymbol{p}}\rangle\,\langle s^{12\dagger}_{-\boldsymbol{p}-\boldsymbol{q}}\rangle\right\}\right]\Big\}\end{aligned} \tag{C.13}$$

while, for the radiative recombination, we obtain ($\Gamma^{\mathrm{rr}} = \pi|w|^2$)

$$\frac{d}{dt}\langle n^{22}_{\boldsymbol{p}}\rangle^{\mathrm{rr}} = -\Gamma^{\mathrm{rr}}\langle n^{22}_{\boldsymbol{p}}\rangle\langle 1-n^{11}_{\boldsymbol{p}}\rangle. \tag{C.14}$$

C.1.3 Standard interband correlations

Next, we focus on the time evolution of the standard interband correlations, namely $n^{21}_{\boldsymbol{p}} = c^{2\dagger}_{\boldsymbol{p}} c^{1}_{\boldsymbol{p}}$. The commutators, in this case, read

$$\left[\mathcal{S}^{\alpha}_{\boldsymbol{k},\boldsymbol{q}}, n^{21}_{\boldsymbol{p}}\right] = \left[c^{\alpha\dagger}_{\boldsymbol{k}} c^{\alpha}_{\boldsymbol{k}+\boldsymbol{q}}, c^{2\dagger}_{\boldsymbol{p}} c^{1}_{\boldsymbol{p}}\right] = \delta_{\alpha,2}\,\delta(\boldsymbol{k}+\boldsymbol{q}-\boldsymbol{p}) c^{2\dagger}_{\boldsymbol{p}-\boldsymbol{q}} c^{1}_{\boldsymbol{p}} - \delta_{\alpha,1}\,\delta(\boldsymbol{k}-\boldsymbol{p}) c^{2\dagger}_{\boldsymbol{p}} c^{1}_{\boldsymbol{p}+\boldsymbol{q}} = -\left[n^{21}_{\boldsymbol{p}}, \mathcal{S}^{\alpha}_{\boldsymbol{k},\boldsymbol{q}}\right] \tag{C.15}$$

$$\left[n_{\boldsymbol{p}}^{21}, \mathcal{S}_{\boldsymbol{k},\boldsymbol{q}}^{\alpha\dagger}\right] = \left[c_{\boldsymbol{p}}^{2\dagger}c_{\boldsymbol{p}}^{1}, c_{\boldsymbol{k}+\boldsymbol{q}}^{\alpha\dagger}c_{\boldsymbol{k}}^{\alpha}\right] = \delta_{\alpha,1}\,\delta(\boldsymbol{k}+\boldsymbol{q}-\boldsymbol{p})c_{\boldsymbol{p}}^{2\dagger}c_{\boldsymbol{p}-\boldsymbol{q}}^{1} - \delta_{\alpha,2}\delta(\boldsymbol{k}-\boldsymbol{p})c_{\boldsymbol{p}+\boldsymbol{q}}^{2\dagger}c_{\boldsymbol{p}}^{1} = -\left[\mathcal{S}_{\boldsymbol{k},\boldsymbol{q}}^{\alpha\dagger}, n_{\boldsymbol{p}}^{21}\right] \tag{C.16}$$

Using Wick's theorem, we can simplify the terms obtained after the evaluation of the commutators. We first display the ones multiplied in Eq. (6.36) by $(1+n_B)$, i. e. the first line:

$$\langle c_{\boldsymbol{k}'}^{\beta\dagger}c_{\boldsymbol{k}'+\boldsymbol{q}}^{\beta}c_{\boldsymbol{p}}^{2\dagger}c_{\boldsymbol{p}-\boldsymbol{q}}^{1}\rangle = \delta(\boldsymbol{k}'-\boldsymbol{p}+\boldsymbol{q})\left[-\delta_{\beta,1}\langle n_{\boldsymbol{p}-\boldsymbol{q}}^{11}\rangle\langle n_{\boldsymbol{p}}^{21}\rangle + \delta_{\beta,2}\langle n_{\boldsymbol{p}-\boldsymbol{q}}^{21}\rangle\langle 1-n_{\boldsymbol{p}}^{22}\rangle\right] \tag{C.17}$$

$$\langle c_{\boldsymbol{k}'}^{\beta\dagger}c_{\boldsymbol{k}'+\boldsymbol{q}}^{\beta}c_{\boldsymbol{p}+\boldsymbol{q}}^{2\dagger}c_{\boldsymbol{p}}^{1}\rangle = \delta(\boldsymbol{k}'-\boldsymbol{p})\left[-\delta_{\beta,1}\langle n_{\boldsymbol{p}}^{11}\rangle\langle n_{\boldsymbol{p}+\boldsymbol{q}}^{21}\rangle + \delta_{\beta,2}\langle n_{\boldsymbol{p}}^{21}\rangle\langle 1-n_{\boldsymbol{p}+\boldsymbol{q}}^{22}\rangle\right] \tag{C.18}$$

$$\langle c_{\boldsymbol{p}-\boldsymbol{q}}^{2\dagger}c_{\boldsymbol{p}}^{1}c_{\boldsymbol{k}'+\boldsymbol{q}}^{\beta\dagger}c_{\boldsymbol{k}'}^{\beta}\rangle = \delta(\boldsymbol{k}'-\boldsymbol{p}+\boldsymbol{q})\left[\delta_{\beta,1}\langle n_{\boldsymbol{p}-\boldsymbol{q}}^{21}\rangle\langle 1-n_{\boldsymbol{p}}^{11}\rangle - \delta_{\beta,2}\langle n_{\boldsymbol{p}-\boldsymbol{q}}^{22}\rangle\langle n_{\boldsymbol{p}}^{21}\rangle\right] \tag{C.19}$$

$$\langle c_{\boldsymbol{p}}^{2\dagger}c_{\boldsymbol{p}+\boldsymbol{q}}^{1}c_{\boldsymbol{k}'+\boldsymbol{q}}^{\beta\dagger}c_{\boldsymbol{k}'}^{\beta}\rangle = \delta(\boldsymbol{k}'-\boldsymbol{p})\left[\delta_{\beta,1}\langle n_{\boldsymbol{p}}^{21}\rangle\langle 1-n_{\boldsymbol{p}+\boldsymbol{q}}^{11}\rangle - \delta_{\beta,2}\langle n_{\boldsymbol{p}}^{22}\rangle\langle n_{\boldsymbol{p}+\boldsymbol{q}}^{21}\rangle\right] \tag{C.20}$$

and now the ones multiplied in Eq. (6.36) by n_B, i. e. the second line:

$$\langle c_{\boldsymbol{k}'+\boldsymbol{q}}^{\beta\dagger}c_{\boldsymbol{k}'}^{\beta}c_{\boldsymbol{p}-\boldsymbol{q}}^{2\dagger}c_{\boldsymbol{p}}^{1}\rangle = \delta(\boldsymbol{k}'-\boldsymbol{p}+\boldsymbol{q})\left[-\delta_{\beta,1}\langle n_{\boldsymbol{p}}^{11}\rangle\langle n_{\boldsymbol{p}-\boldsymbol{q}}^{21}\rangle + \delta_{\beta,2}\langle n_{\boldsymbol{p}}^{21}\rangle\langle 1-n_{\boldsymbol{p}-\boldsymbol{q}}^{22}\rangle\right] \tag{C.21}$$

$$\langle c_{\boldsymbol{k}'+\boldsymbol{q}}^{\beta\dagger}c_{\boldsymbol{k}'}^{\beta}c_{\boldsymbol{p}}^{2\dagger}c_{\boldsymbol{p}+\boldsymbol{q}}^{1}\rangle = \delta(\boldsymbol{k}'-\boldsymbol{p})\left[-\delta_{\beta,1}\langle n_{\boldsymbol{p}+\boldsymbol{q}}^{11}\rangle\langle n_{\boldsymbol{p}}^{21}\rangle + \delta_{\beta,2}\langle n_{\boldsymbol{p}+\boldsymbol{q}}^{21}\rangle\langle 1-n_{\boldsymbol{p}}^{22}\rangle\right] \tag{C.22}$$

$$\langle c_{\boldsymbol{p}}^{2\dagger}c_{\boldsymbol{p}-\boldsymbol{q}}^{1}c_{\boldsymbol{k}'}^{\beta\dagger}c_{\boldsymbol{k}'+\boldsymbol{q}}^{\beta}\rangle = \delta(\boldsymbol{k}'-\boldsymbol{p}+\boldsymbol{q})\left[\delta_{\beta,1}\langle n_{\boldsymbol{p}}^{21}\rangle\langle 1-n_{\boldsymbol{p}-\boldsymbol{q}}^{11}\rangle - \delta_{\beta,2}\langle n_{\boldsymbol{p}}^{22}\rangle\langle n_{\boldsymbol{p}-\boldsymbol{q}}^{21}\rangle\right] \tag{C.23}$$

$$\langle c_{\boldsymbol{p}+\boldsymbol{q}}^{2\dagger}c_{\boldsymbol{p}}^{1}c_{\boldsymbol{k}'}^{\beta\dagger}c_{\boldsymbol{k}'+\boldsymbol{q}}^{\beta}\rangle = \delta(\boldsymbol{k}'-\boldsymbol{p})\left[\delta_{\beta,1}\langle n_{\boldsymbol{p}+\boldsymbol{q}}^{21}\rangle\langle 1-n_{\boldsymbol{p}}^{11}\rangle - \delta_{\beta,2}\langle n_{\boldsymbol{p}+\boldsymbol{q}}^{22}\rangle\langle n_{\boldsymbol{p}}^{21}\rangle\right] \tag{C.24}$$

Hence, the dissipative part of the time evolution of $\langle n_{\boldsymbol{p}}^{21}\rangle$ due to the acoustic phonons is given by

$$\begin{aligned}\frac{d}{dt}\langle n_{\boldsymbol{p}}^{21}\rangle^{\mathrm{ph}} = \sum_{\boldsymbol{q}}\Big\{ & n_B\left[\Gamma_{\boldsymbol{p},\boldsymbol{q}}^{1}\left(\langle n_{\boldsymbol{p}+\boldsymbol{q}}^{21}\rangle\langle 1-n_{\boldsymbol{p}}^{11}\rangle - \langle n_{\boldsymbol{p}+\boldsymbol{q}}^{11}\rangle\langle n_{\boldsymbol{p}}^{21}\rangle\right) + \Gamma_{\boldsymbol{p},\boldsymbol{q}}^{2}\left(\langle n_{\boldsymbol{p}+\boldsymbol{q}}^{21}\rangle\langle 1-n_{\boldsymbol{p}}^{22}\rangle - \langle n_{\boldsymbol{p}+\boldsymbol{q}}^{22}\rangle\langle n_{\boldsymbol{p}}^{21}\rangle\right)\right] + \\ & + [1+n_B]\left[\Gamma_{\boldsymbol{p},\boldsymbol{q}}^{1}\left(\langle n_{\boldsymbol{p}}^{11}\rangle\langle n_{\boldsymbol{p}+\boldsymbol{q}}^{21}\rangle - \langle n_{\boldsymbol{p}}^{21}\rangle\langle 1-n_{\boldsymbol{p}+\boldsymbol{q}}^{11}\rangle\right) + \Gamma_{\boldsymbol{p},\boldsymbol{q}}^{2}\left(\langle n_{\boldsymbol{p}}^{22}\rangle\langle n_{\boldsymbol{p}+\boldsymbol{q}}^{21}\rangle - \langle n_{\boldsymbol{p}}^{21}\rangle\langle 1-n_{\boldsymbol{p}+\boldsymbol{q}}^{22}\rangle\right)\right] + \\ & + n_B\left[\Gamma_{\boldsymbol{p}-\boldsymbol{q},\boldsymbol{q}}^{1}\left(\langle n_{\boldsymbol{p}}^{11}\rangle\langle n_{\boldsymbol{p}-\boldsymbol{q}}^{21}\rangle - \langle n_{\boldsymbol{p}}^{21}\rangle\langle 1-n_{\boldsymbol{p}-\boldsymbol{q}}^{11}\rangle\right) + \Gamma_{\boldsymbol{p}-\boldsymbol{q},\boldsymbol{q}}^{2}\left(\langle n_{\boldsymbol{p}}^{22}\rangle\langle n_{\boldsymbol{p}-\boldsymbol{q}}^{21}\rangle - \langle n_{\boldsymbol{p}}^{21}\rangle\langle 1-n_{\boldsymbol{p}-\boldsymbol{q}}^{22}\rangle\right)\right] + \\ & + [1+n_B]\left[\Gamma_{\boldsymbol{p}-\boldsymbol{q},\boldsymbol{q}}^{1}\left(\langle n_{\boldsymbol{p}-\boldsymbol{q}}^{21}\rangle\langle 1-n_{\boldsymbol{p}}^{11}\rangle - \langle n_{\boldsymbol{p}-\boldsymbol{q}}^{11}\rangle\langle n_{\boldsymbol{p}}^{21}\rangle\right) + \Gamma_{\boldsymbol{p}-\boldsymbol{q},\boldsymbol{q}}^{2}\left(\langle n_{\boldsymbol{p}-\boldsymbol{q}}^{21}\rangle\langle 1-n_{\boldsymbol{p}}^{22}\rangle - \langle n_{\boldsymbol{p}-\boldsymbol{q}}^{22}\rangle\langle n_{\boldsymbol{p}}^{21}\rangle\right)\right]\Big\}.\end{aligned} \tag{C.25}$$

Analogously, the dissipative part due to the radiative recombination reads ($\Gamma^{\mathrm{rr}} = \pi|w|^2$)

$$\frac{d}{dt}\langle n_{\boldsymbol{p}}^{21}\rangle^{\mathrm{rr}} = -\Gamma^{\mathrm{rr}}\langle n_{\boldsymbol{p}}^{21}\rangle\langle 1-n_{\boldsymbol{p}}^{11}+n_{\boldsymbol{p}}^{22}\rangle. \tag{C.26}$$

C.1.4 Anomalous interband correlations

Finally, we address the time evolution of the anomalous interband correlations $s_{\boldsymbol{p}}^{21} = c_{\boldsymbol{p}}^{2\dagger}c_{-\boldsymbol{p}}^{1\dagger}$. We start again evaluating the commutators of eq. (6.36)

$$\left[\mathcal{S}_{\boldsymbol{k},\boldsymbol{q}}^{\alpha}, s_{\boldsymbol{p}}^{21}\right] = \left[c_{\boldsymbol{k}}^{\alpha\dagger}c_{\boldsymbol{k}+\boldsymbol{q}}^{\alpha}, c_{\boldsymbol{p}}^{2\dagger}c_{-\boldsymbol{p}}^{1\dagger}\right] = \delta_{\alpha,2}\,\delta(\boldsymbol{k}+\boldsymbol{q}-\boldsymbol{p})c_{\boldsymbol{p}-\boldsymbol{q}}^{2\dagger}c_{-\boldsymbol{p}}^{1\dagger} - \delta_{\alpha,1}\delta(\boldsymbol{k}+\boldsymbol{p}+\boldsymbol{q})c_{-\boldsymbol{p}-\boldsymbol{q}}^{1\dagger}c_{\boldsymbol{p}}^{2\dagger} = -\left[s_{\boldsymbol{p}}^{21}, \mathcal{S}_{\boldsymbol{k},\boldsymbol{q}}^{\alpha}\right], \tag{C.27}$$

$$\left[s_{\boldsymbol{p}}^{21}, \mathcal{S}_{\boldsymbol{k},\boldsymbol{q}}^{\alpha\dagger}\right] = \left[c_{\boldsymbol{p}}^{2\dagger}c_{-\boldsymbol{p}}^{1\dagger}, c_{\boldsymbol{k}+\boldsymbol{q}}^{\alpha\dagger}c_{\boldsymbol{k}}^{\alpha}\right] = -\delta_{\alpha,1}\,\delta(\boldsymbol{k}+\boldsymbol{p})c_{\boldsymbol{p}}^{2\dagger}c_{-\boldsymbol{p}+\boldsymbol{q}}^{1\dagger} - \delta_{\alpha,2}\,\delta(\boldsymbol{k}-\boldsymbol{p})c_{\boldsymbol{p}+\boldsymbol{q}}^{2\dagger}c_{-\boldsymbol{p}}^{1\dagger} = -\left[\mathcal{S}_{\boldsymbol{k},\boldsymbol{q}}^{\alpha\dagger}, s_{\boldsymbol{p}}^{21}\right]. \tag{C.28}$$

Using Wick's theorem, we can simplify the terms obtained after the evaluation of the commutators. Here we show the ones multiplied in Eq. (6.36) by $(1+n_B)$, i. e. the first line:

$$\langle c^{\beta\dagger}_{\boldsymbol{k}'} c^{\beta}_{\boldsymbol{k}'+\boldsymbol{q}} c^{2\dagger}_{\boldsymbol{p}} c^{1\dagger}_{-\boldsymbol{p}+\boldsymbol{q}}\rangle = \delta_{\beta,1}\,\delta(\boldsymbol{k}'+\boldsymbol{p})\,\langle s^{21}_{\boldsymbol{p}}\rangle\,\langle 1-n^{11}_{-\boldsymbol{p}+\boldsymbol{q}}\rangle + \delta_{\beta,2}\,\delta(\boldsymbol{k}'-\boldsymbol{p}+\boldsymbol{q})\,\langle s^{21}_{\boldsymbol{p}-\boldsymbol{q}}\rangle\,\langle 1-n^{22}_{\boldsymbol{p}}\rangle \tag{C.29}$$

$$\langle c^{\beta\dagger}_{\boldsymbol{k}'} c^{\beta}_{\boldsymbol{k}'+\boldsymbol{q}} c^{2\dagger}_{\boldsymbol{p}+\boldsymbol{q}} c^{1\dagger}_{-\boldsymbol{p}}\rangle = \delta_{\beta,2}\,\delta(\boldsymbol{k}'-\boldsymbol{p})\,\langle s^{21}_{\boldsymbol{p}}\rangle\,\langle 1-n^{22}_{\boldsymbol{p}+\boldsymbol{q}}\rangle + \delta_{\beta,1}\,\delta(\boldsymbol{k}'+\boldsymbol{p}+\boldsymbol{q})\,\langle s^{21}_{\boldsymbol{p}+\boldsymbol{q}}\rangle\,\langle 1-n^{11}_{-\boldsymbol{p}}\rangle \tag{C.30}$$

$$\langle c^{2\dagger}_{\boldsymbol{p}-\boldsymbol{q}} c^{1\dagger}_{-\boldsymbol{p}} c^{\beta\dagger}_{\boldsymbol{k}'+\boldsymbol{q}} c^{\beta}_{\boldsymbol{k}'}\rangle = -\delta_{\beta,1}\,\delta(\boldsymbol{k}'+\boldsymbol{p})\,\langle s^{21}_{\boldsymbol{p}-\boldsymbol{q}}\rangle\,\langle n^{11}_{-\boldsymbol{p}}\rangle - \delta_{\beta,2}\,\delta(\boldsymbol{k}'-\boldsymbol{p}+\boldsymbol{q})\,\langle s^{21}_{\boldsymbol{p}}\rangle\,\langle n^{22}_{\boldsymbol{p}-\boldsymbol{q}}\rangle \tag{C.31}$$

$$\langle c^{1\dagger}_{-\boldsymbol{p}-\boldsymbol{q}} c^{2\dagger}_{\boldsymbol{p}} c^{\beta\dagger}_{\boldsymbol{k}'+\boldsymbol{q}} c^{\beta}_{\boldsymbol{k}'}\rangle = \delta_{\beta,2}\,\delta(\boldsymbol{k}'-\boldsymbol{p})\,\langle s^{21}_{\boldsymbol{p}+\boldsymbol{q}}\rangle\,\langle n^{22}_{\boldsymbol{p}}\rangle + \delta_{\beta,1}\,\delta(\boldsymbol{k}'+\boldsymbol{p}+\boldsymbol{q})\,\langle s^{21}_{\boldsymbol{p}}\rangle\,\langle n^{11}_{-\boldsymbol{p}-\boldsymbol{q}}\rangle \tag{C.32}$$

and here we show the ones multiplied in Eq. (6.36) by n_B, i. e. the second line:

$$\langle c^{\beta\dagger}_{\boldsymbol{k}'} c^{\beta}_{\boldsymbol{k}'+\boldsymbol{q}} c^{2\dagger}_{\boldsymbol{p}-\boldsymbol{q}} c^{1\dagger}_{-\boldsymbol{p}}\rangle = \delta_{\beta,1}\,\delta(\boldsymbol{k}'+\boldsymbol{p})\,\langle s^{21}_{\boldsymbol{p}-\boldsymbol{q}}\rangle\,\langle 1-n^{11}_{-\boldsymbol{p}}\rangle + \delta_{\beta,2}\,\delta(\boldsymbol{k}'-\boldsymbol{p}+\boldsymbol{q})\,\langle s^{21}_{\boldsymbol{p}}\rangle\,\langle 1-n^{22}_{\boldsymbol{p}-\boldsymbol{q}}\rangle \tag{C.33}$$

$$\langle c^{\beta\dagger}_{\boldsymbol{k}'} c^{\beta}_{\boldsymbol{k}'+\boldsymbol{q}} c^{1\dagger}_{-\boldsymbol{p}-\boldsymbol{q}} c^{2\dagger}_{\boldsymbol{p}}\rangle = -\delta_{\beta,2}\,\delta(\boldsymbol{k}'-\boldsymbol{p})\,\langle s^{21}_{\boldsymbol{p}+\boldsymbol{q}}\rangle\,\langle 1-n^{22}_{\boldsymbol{p}}\rangle - \delta_{\beta,1}\,\delta(\boldsymbol{k}'+\boldsymbol{p}+\boldsymbol{q})\,\langle s^{21}_{\boldsymbol{p}}\rangle\,\langle 1-n^{11}_{-\boldsymbol{p}-\boldsymbol{q}}\rangle \tag{C.34}$$

$$\langle c^{2\dagger}_{\boldsymbol{p}} c^{1\dagger}_{-\boldsymbol{p}+\boldsymbol{q}} c^{\beta\dagger}_{\boldsymbol{k}'} c^{\beta}_{\boldsymbol{k}'+\boldsymbol{q}}\rangle = -\delta_{\beta,1}\,\delta(\boldsymbol{k}'+\boldsymbol{p})\,\langle s^{21}_{\boldsymbol{p}}\rangle\,\langle n^{11}_{-\boldsymbol{p}+\boldsymbol{q}}\rangle - \delta_{\beta,2}\,\delta(\boldsymbol{k}'-\boldsymbol{p}+\boldsymbol{q})\,\langle s^{21}_{\boldsymbol{p}-\boldsymbol{q}}\rangle\,\langle n^{22}_{\boldsymbol{p}}\rangle \tag{C.35}$$

$$\langle c^{2\dagger}_{\boldsymbol{p}+\boldsymbol{q}} c^{1\dagger}_{-\boldsymbol{p}} c^{\beta\dagger}_{\boldsymbol{k}'} c^{\beta}_{\boldsymbol{k}'+\boldsymbol{q}}\rangle = -\delta_{\beta,2}\,\delta(\boldsymbol{k}'-\boldsymbol{p})\,\langle s^{21}_{\boldsymbol{p}}\rangle\,\langle n^{22}_{\boldsymbol{p}+\boldsymbol{q}}\rangle - \delta_{\beta,1}\,\delta(\boldsymbol{k}'+\boldsymbol{p}+\boldsymbol{q})\,\langle s^{21}_{\boldsymbol{p}+\boldsymbol{q}}\rangle\,\langle n^{11}_{-\boldsymbol{p}}\rangle \tag{C.36}$$

Hence, the dissipative part of the time evolution of $\langle s^{21}_{\boldsymbol{p}}\rangle$ due to the acoustic phonons is given by

$$\begin{aligned}\frac{d}{dt}\langle s^{21}_{\boldsymbol{p}}\rangle^{\mathrm{ph}} = -\sum_{\boldsymbol{q}}\Big\{ & n_B\left[\Gamma^{2}_{\boldsymbol{p},\boldsymbol{q}}\left(\langle s^{21}_{\boldsymbol{p}+\boldsymbol{q}}\rangle\,\langle 1-n^{22}_{\boldsymbol{p}}\rangle + \langle n^{22}_{\boldsymbol{p}+\boldsymbol{q}}\rangle\,\langle s^{21}_{\boldsymbol{p}}\rangle\right) + \Gamma^{1}_{-\boldsymbol{p}-\boldsymbol{q},\boldsymbol{q}}\left(\langle s^{21}_{\boldsymbol{p}+\boldsymbol{q}}\rangle\,\langle n^{11}_{-\boldsymbol{p}}\rangle + \langle 1-n^{11}_{-\boldsymbol{p}-\boldsymbol{q}}\rangle\,\langle s^{21}_{\boldsymbol{p}}\rangle\right)\right] + \\ & + [1+n_B]\left[\Gamma^{2}_{\boldsymbol{p},\boldsymbol{q}}\left(\langle n^{22}_{\boldsymbol{p}}\rangle\,\langle s^{21}_{\boldsymbol{p}+\boldsymbol{q}}\rangle + \langle s^{21}_{\boldsymbol{p}}\rangle\,\langle 1-n^{22}_{\boldsymbol{p}+\boldsymbol{q}}\rangle\right) + \Gamma^{1}_{-\boldsymbol{p}-\boldsymbol{q},\boldsymbol{q}}\left(\langle n^{11}_{-\boldsymbol{p}-\boldsymbol{q}}\rangle\,\langle s^{21}_{\boldsymbol{p}}\rangle + \langle s^{21}_{\boldsymbol{p}+\boldsymbol{q}}\rangle\,\langle 1-n^{11}_{-\boldsymbol{p}}\rangle\right)\right] + \\ & + n_B\left[\Gamma^{1}_{-\boldsymbol{p},\boldsymbol{q}}\left(\langle 1-n^{11}_{-\boldsymbol{p}}\rangle\,\langle s^{21}_{\boldsymbol{p}-\boldsymbol{q}}\rangle + \langle s^{21}_{\boldsymbol{p}}\rangle\,\langle n^{11}_{-\boldsymbol{p}+\boldsymbol{q}}\rangle\right) + \Gamma^{2}_{\boldsymbol{p}-\boldsymbol{q},\boldsymbol{q}}\left(\langle n^{22}_{\boldsymbol{p}}\rangle\,\langle s^{21}_{\boldsymbol{p}-\boldsymbol{q}}\rangle + \langle s^{21}_{\boldsymbol{p}}\rangle\,\langle 1-n^{22}_{\boldsymbol{p}-\boldsymbol{q}}\rangle\right)\right] + \\ & + [1+n_B]\left[\Gamma^{1}_{-\boldsymbol{p},\boldsymbol{q}}\left(\langle s^{21}_{\boldsymbol{p}}\rangle\,\langle 1-n^{11}_{-\boldsymbol{p}+\boldsymbol{q}}\rangle + \langle n^{11}_{-\boldsymbol{p}}\rangle\,\langle s^{21}_{\boldsymbol{p}-\boldsymbol{q}}\rangle\right) + \Gamma^{2}_{\boldsymbol{p}-\boldsymbol{q},\boldsymbol{q}}\left(\langle s^{21}_{\boldsymbol{p}-\boldsymbol{q}}\rangle\,\langle 1-n^{22}_{\boldsymbol{p}}\rangle + \langle n^{22}_{\boldsymbol{p}-\boldsymbol{q}}\rangle\,\langle s^{21}_{\boldsymbol{p}}\rangle\right)\right]\Big\}.\end{aligned} \tag{C.37}$$

Analogously, the dissipative part due to the radiative recombination reads

$$\frac{d}{dt}\langle s^{21}_{\boldsymbol{p}}\rangle^{\mathrm{rr}} = 0. \tag{C.38}$$

This feature ensures that radiative recombination is not detrimental for superconducting correlations.

C.1.5 Summary ($T = 0$)

We summarize the complete time evolution of the observables in the particular case of zero temperature, where $n_B = 0$.

$$\begin{aligned}\frac{d}{dt}\langle n_{\boldsymbol{p}}^{11}\rangle =& -\Omega\mathrm{Im}\left\{\langle n_{\boldsymbol{p}}^{21}\rangle\right\} - 2\mathrm{Im}\left\{\Delta\,\langle s_{\boldsymbol{p}}^{21}\rangle\right\} + \Gamma^{\mathrm{rr}}\langle n_{\boldsymbol{p}}^{22}\rangle\langle 1 - n_{\boldsymbol{p}}^{11}\rangle + \\ &+ 2\sum_{\boldsymbol{q}}\Big\{\Big[\Gamma^1_{\boldsymbol{p}-\boldsymbol{q},\boldsymbol{q}}\,\langle n_{\boldsymbol{p}-\boldsymbol{q}}^{11}\rangle\,\langle 1 - n_{\boldsymbol{p}}^{11}\rangle - \Gamma^2_{\boldsymbol{p}-\boldsymbol{q},\boldsymbol{q}}\mathrm{Re}\left\{\langle n_{\boldsymbol{p}-\boldsymbol{q}}^{21}\rangle\,\langle n_{\boldsymbol{p}}^{12}\rangle\right\} - \Gamma^2_{-\boldsymbol{p},\boldsymbol{q}}\mathrm{Re}\left\{\langle s_{-\boldsymbol{p}}^{21}\rangle\,\langle s_{-\boldsymbol{p}+\boldsymbol{q}}^{21\dagger}\rangle\right\}\Big] + \\ &- \Big[\Gamma^1_{\boldsymbol{p},\boldsymbol{q}}\,\langle n_{\boldsymbol{p}}^{11}\rangle\,\langle 1 - n_{\boldsymbol{p}+\boldsymbol{q}}^{11}\rangle - \Gamma^2_{\boldsymbol{p},\boldsymbol{q}}\mathrm{Re}\left\{\langle n_{\boldsymbol{p}}^{21}\rangle\,\langle n_{\boldsymbol{p}+\boldsymbol{q}}^{12}\rangle\right\} - \Gamma^2_{-\boldsymbol{p}-\boldsymbol{q},\boldsymbol{q}}\mathrm{Re}\left\{\langle s_{-\boldsymbol{p}-\boldsymbol{q}}^{21}\rangle\,\langle s_{-\boldsymbol{p}}^{21\dagger}\rangle\right\}\Big]\Big\}\end{aligned} \tag{C.39}$$

$$\begin{aligned}\frac{d}{dt}\langle n_{\boldsymbol{p}}^{22}\rangle =& +\Omega\mathrm{Im}\left\{\langle n_{\boldsymbol{p}}^{21}\rangle\right\} - 2\mathrm{Im}\left\{\Delta\,\langle s_{\boldsymbol{p}}^{21}\rangle\right\} - \Gamma^{\mathrm{rr}}\langle n_{\boldsymbol{p}}^{22}\rangle\langle 1 - n_{\boldsymbol{p}}^{11}\rangle + \\ &+ 2\sum_{\boldsymbol{q}}\Big\{\Big[\Gamma^2_{\boldsymbol{p}-\boldsymbol{q},\boldsymbol{q}}\,\langle n_{\boldsymbol{p}-\boldsymbol{q}}^{22}\rangle\,\langle 1 - n_{\boldsymbol{p}}^{22}\rangle - \Gamma^1_{\boldsymbol{p}-\boldsymbol{q},\boldsymbol{q}}\mathrm{Re}\left\{\langle n_{\boldsymbol{p}-\boldsymbol{q}}^{12}\rangle\,\langle n_{\boldsymbol{p}}^{21}\rangle\right\} - \Gamma^1_{-\boldsymbol{p},\boldsymbol{q}}\mathrm{Re}\left\{\langle s_{-\boldsymbol{p}}^{12}\rangle\,\langle s_{-\boldsymbol{p}+\boldsymbol{q}}^{12\dagger}\rangle\right\}\Big] + \\ &- \Big[\Gamma^2_{\boldsymbol{p},\boldsymbol{q}}\,\langle n_{\boldsymbol{p}}^{22}\rangle\,\langle 1 - n_{\boldsymbol{p}+\boldsymbol{q}}^{22}\rangle - \Gamma^1_{\boldsymbol{p},\boldsymbol{q}}\mathrm{Re}\left\{\langle n_{\boldsymbol{p}}^{12}\rangle\,\langle n_{\boldsymbol{p}+\boldsymbol{q}}^{21}\rangle\right\} - \Gamma^1_{-\boldsymbol{p}-\boldsymbol{q},\boldsymbol{q}}\mathrm{Re}\left\{\langle s_{-\boldsymbol{p}-\boldsymbol{q}}^{12}\rangle\,\langle s_{-\boldsymbol{p}}^{12\dagger}\rangle\right\}\Big]\Big\}\end{aligned} \tag{C.40}$$

$$\begin{aligned}\frac{d}{dt}\langle n_{\boldsymbol{p}}^{21}\rangle =& -\frac{i\Omega}{2}\,\langle n_{\boldsymbol{p}}^{22} - n_{\boldsymbol{p}}^{11}\rangle + i\epsilon(\boldsymbol{p})\,\langle n_{\boldsymbol{p}}^{21}\rangle - \Gamma^{\mathrm{rr}}\langle n_{\boldsymbol{p}}^{21}\rangle\langle 1 - n_{\boldsymbol{p}}^{11} + n_{\boldsymbol{p}}^{22}\rangle + \\ &+ \sum_{\boldsymbol{q}}\Big\{\Big[\Gamma^1_{\boldsymbol{p}-\boldsymbol{q},\boldsymbol{q}}\left(\langle n_{\boldsymbol{p}-\boldsymbol{q}}^{21}\rangle\,\langle 1 - n_{\boldsymbol{p}}^{11}\rangle - \langle n_{\boldsymbol{p}-\boldsymbol{q}}^{11}\rangle\,\langle n_{\boldsymbol{p}}^{21}\rangle\right) + \Gamma^2_{\boldsymbol{p}-\boldsymbol{q},\boldsymbol{q}}\left(\langle n_{\boldsymbol{p}-\boldsymbol{q}}^{21}\rangle\,\langle 1 - n_{\boldsymbol{p}}^{22}\rangle - \langle n_{\boldsymbol{p}-\boldsymbol{q}}^{22}\rangle\,\langle n_{\boldsymbol{p}}^{21}\rangle\right)\Big] + \\ &+ \Big[\Gamma^1_{\boldsymbol{p},\boldsymbol{q}}\left(\langle n_{\boldsymbol{p}}^{11}\rangle\,\langle n_{\boldsymbol{p}+\boldsymbol{q}}^{21}\rangle - \langle n_{\boldsymbol{p}}^{21}\rangle\,\langle 1 - n_{\boldsymbol{p}+\boldsymbol{q}}^{11}\rangle\right) + \Gamma^2_{\boldsymbol{p},\boldsymbol{q}}\left(\langle n_{\boldsymbol{p}}^{22}\rangle\,\langle n_{\boldsymbol{p}+\boldsymbol{q}}^{21}\rangle - \langle n_{\boldsymbol{p}}^{21}\rangle\,\langle 1 - n_{\boldsymbol{p}+\boldsymbol{q}}^{22}\rangle\right)\Big]\Big\}\end{aligned} \tag{C.41}$$

$$\begin{aligned}\frac{d}{dt}\langle s_{\boldsymbol{p}}^{21}\rangle =& +i\Delta^*\,\langle n_{\boldsymbol{p}}^{22} + n_{-\boldsymbol{p}}^{11} - 1\rangle + iE(\boldsymbol{p})\,\langle s_{\boldsymbol{p}}^{21}\rangle + \\ &- \sum_{\boldsymbol{q}}\Big\{\Big[\Gamma^1_{-\boldsymbol{p},\boldsymbol{q}}\left(\langle s_{\boldsymbol{p}}^{21}\rangle\,\langle 1 - n_{-\boldsymbol{p}+\boldsymbol{q}}^{11}\rangle + \langle n_{-\boldsymbol{p}}^{11}\rangle\,\langle s_{\boldsymbol{p}-\boldsymbol{q}}^{21}\rangle\right) + \Gamma^2_{\boldsymbol{p}-\boldsymbol{q},\boldsymbol{q}}\left(\langle s_{\boldsymbol{p}-\boldsymbol{q}}^{21}\rangle\,\langle 1 - n_{\boldsymbol{p}}^{22}\rangle + \langle n_{\boldsymbol{p}-\boldsymbol{q}}^{22}\rangle\,\langle s_{\boldsymbol{p}}^{21}\rangle\right)\Big] + \\ &+ \Big[\Gamma^2_{\boldsymbol{p},\boldsymbol{q}}\left(\langle n_{\boldsymbol{p}}^{22}\rangle\,\langle s_{\boldsymbol{p}+\boldsymbol{q}}^{21}\rangle + \langle s_{\boldsymbol{p}}^{21}\rangle\,\langle 1 - n_{\boldsymbol{p}+\boldsymbol{q}}^{22}\rangle\right) + \Gamma^1_{-\boldsymbol{p}-\boldsymbol{q},\boldsymbol{q}}\left(\langle n_{-\boldsymbol{p}-\boldsymbol{q}}^{11}\rangle\,\langle s_{\boldsymbol{p}}^{21}\rangle + \langle s_{\boldsymbol{p}+\boldsymbol{q}}^{21}\rangle\,\langle 1 - n_{-\boldsymbol{p}}^{11}\rangle\right)\Big]\Big\}\end{aligned} \tag{C.42}$$

where $\epsilon(\boldsymbol{p}) = E_2(\boldsymbol{p}) - E_1(\boldsymbol{p}) - \nu$ and $E(\boldsymbol{p}) = E_2(\boldsymbol{p}) + E_1(\boldsymbol{p})$.

From these equations, as we discuss in the main text, we observe that interband pairing $\langle s_{\boldsymbol{p}}^{21}\rangle$ is enhanced and can be brought out of the trivial vanishing solution by the condition $\langle n_{\boldsymbol{p}}^{22} + n_{-\boldsymbol{p}}^{11}\rangle \neq 1$. If the dynamics of the system is efficient, i.e. is such that populations of the conduction and valence bands satisfy this condition at shorter timescales with respect to the time necessary to achieve the steady state, such state can be characterized by a finite superconducting order parameter. The aforementioned condition is, hence, necessary but not sufficient to achieve superconductivity.

C.2 Solution for quadratic bands at $T = 0$

We now focus on a specific form of the semiconductor bands (assuming spherical symmetry, so that the d-dimensional model can be reduced to an equivalent one-dimensional model):

$$E_1(p) = A_1 p^2 - E_g/2 \qquad E_2(p) = A_2 p^2 + E_g/2 \tag{C.43}$$

where E_g represents the gap amplitude in $p = 0$. We are able to identify the allowed q selected by the different $\Gamma_{p,q}$ in the time evolution equations. Note that, as we discuss in the main text, since we are considering the zero temperature case phonons can only be emitted: the only possible transitions are the ones where the electron acquires a momentum $\pm q$ and loses an amount of energy equal to $v|q|$. According to this picture, if the band concavity is positive then the phonon transitions tend to move the electronic population to the center of the band, while, in the opposite case, the electrons tend to move to the edge of the momentum region considered.

The time evolution equations in Section C.1.5 can be solved numerically. In contrast to standard mean-field calculations, there is no need to solve it self-consistently together with an equation for the order parameter. Indeed the "self-consistency" is taken into account by the non-linearity of our master equation: Δ is a time-dependent quantity and there is no need for a self-consistency loop. In order to numerically solve Eqs. (C.39, C.40, C.41, C.42), we have to consider the momentum p as a discrete variable and we convert the energy conservation Dirac deltas into the momentum representation:

$$\begin{aligned}\delta\left[E_\beta(p-q) - E_\beta(p) - v|q|\right] =& \frac{1}{|2A_\beta p + v|}\delta\left[q - 2p - \frac{v}{A_\beta}\right]\Theta\left(p + \frac{v}{2A_\beta}\right) + \\ & \frac{1}{|2A_\beta p - v|}\delta\left[q - 2p + \frac{v}{A_\beta}\right]\Theta\left(-p + \frac{v}{2A_\beta}\right),\end{aligned} \tag{C.44}$$

$$\begin{aligned}\delta\left[E_\beta(p) - E_\beta(p+q) - v|q|\right] =& \frac{1}{|2A_\beta p + v|}\delta\left[q + 2p + \frac{v}{A_\beta}\right]\Theta\left(-p - \frac{v}{2A_\beta}\right) + \\ & \frac{1}{|2A_\beta p - v|}\delta\left[q + 2p - \frac{v}{A_\beta}\right]\Theta\left(p - \frac{v}{2A_\beta}\right),\end{aligned} \tag{C.45}$$

$$\begin{aligned}\delta\left[E_\beta(-p-q) - E_\beta(-p) - v|q|\right] =& \frac{1}{|2A_\beta p - v|}\delta\left[q + 2p - \frac{v}{A_\beta}\right]\Theta\left(-p + \frac{v}{2A_\beta}\right) + \\ & \frac{1}{|2A_\beta p + v|}\delta\left[q + 2p + \frac{v}{A_\beta}\right]\Theta\left(p + \frac{v}{2A_\beta}\right),\end{aligned} \tag{C.46}$$

$$\delta\left[E_\beta(-p)-E_\beta(-p+q)-v|q|\right]=\frac{1}{|2A_\beta p-v|}\delta\left[q-2p+\frac{v}{A_\beta}\right]\Theta\left(p-\frac{v}{2A_\beta}\right)+\frac{1}{|2A_\beta p+v|}\delta\left[q-2p-\frac{v}{A_\beta}\right]\Theta\left(-p-\frac{v}{2A_\beta}\right). \tag{C.47}$$

Note that every electronic state p is influenced by dissipation and phonons induce a constant momentum exchange given by their linear dispersion relation.
When we convert the energy conservation Dirac delta from energy to momentum space, we obtain the full k dependence of the scattering rate Γ^{ph}. Such dependence is due to both the density of states and the electron-phonon coupling strength $t_{k,q}$. In order to mimic realistic scenarios, which apply at low temperature for example to prototypical semiconductors like Silicon and Germanium [180], we set the coupling constants $t_{k,q}$ such that the corresponding scattering rate Γ^{ph} is approximately constant over the momentum window close to the resonance.
A problem which arises in this picture is the implementation of the particle number conservation in the system, which has to hold in the $\Delta = 0$ regime. To fulfill this condition, we ensure that our equations satisfy the principle of detailed balance. Furthermore, since we are considering a finite region in the momentum space near the laser resonance, where the rotating wave approximation works, states near the two edges of this box can only lose(receive) particles if the concavity of the band is positive(negative).
Note that all the energies are measured with respect to the gap amplitude E_g at $k = 0$, which is set to one for simplicity and is our unit of energy. We have performed all calculations with a standard 4-th order Runge-Kutta method.

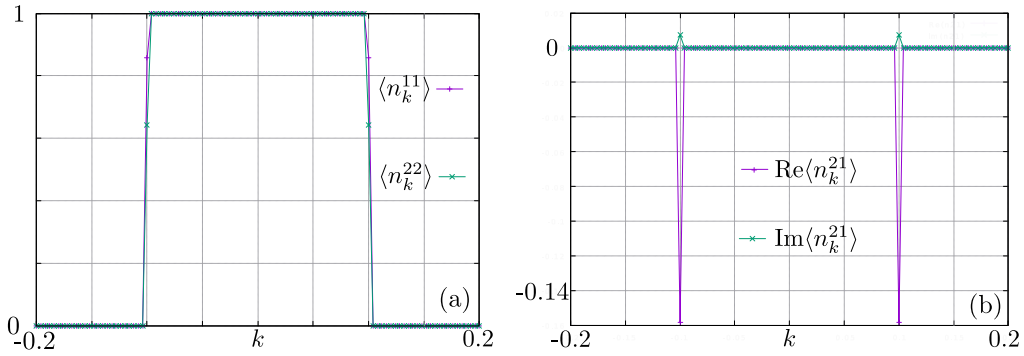

Figure C.1: a) Occupation number of valence $\langle n_k^{11}\rangle$ and conduction $\langle n_k^{22}\rangle$ bands in the stationary state. b) Real and imaginary part of the interband correlation $\langle n_k^{21}\rangle$ in the stationary state. Parameters: $A_1 = 8E_g$, $A_2 = 23E_g$, $k_c = 0.2$, $N_k = 100$, $\Gamma^{\text{ph}} = 0.01E_g$, $\Gamma^{\text{rr}} = \Gamma^{\text{ph}}$, and $\Omega = 0.25E_g$.

C.2.1 Numerical solution without superconductivity

In this section we show the numerical solution of the system in presence of dissipation and electric field. The latter is tuned at the resonant $k = 0$ point, where both bands have their minimum. In particular this condition amounts to fixing the

laser frequency to $\nu = E_g = 1$. We use the same parameters as in the previous section, the amplitude of the laser is set to $\Omega = 0.25E_g$, and the initial conditions coincide with the ground state of the system: $\langle n_k^{11}(t=0)\rangle = 1$, $\langle n_k^{22}(t=0)\rangle = 0$, and $\langle n_k^{21}(t=0)\rangle = 0$.
The resulting stationary state achieved starting from these initial conditions is shown in Figs. C.1 (a) and (b).
The stationary state is characterized by a very similarly populated conduction and valence bands and a vanishing interband correlation. Analogous results are obtained by $\Gamma^{\mathrm{rr}} = \Gamma^{\mathrm{ph}}/10$.

C.2.2 Complete numerical solution

In this section we focus on the full system of coupled equation described in Section C.1.5. The superconducting order parameter Δ, which derives from the mean field approximation performed in the density-density interaction Hamiltonian in Eq. (6.22), is given by:

$$\Delta^* = \frac{V}{N}\sum_k \langle s_k^{21}\rangle \xrightarrow{N\to\infty} \frac{V}{2\pi}\int_{-k_c}^{k_c} \langle s_k^{21}\rangle\, dk \tag{C.48}$$

Note that we do not need any correction to this formula to achieve a non-zero Δ in the stationary state reached by the system. Conversely, in Goldstein et al. derivation [168], this is a necessary condition.
We start with the initial conditions used in the previous sections and in addition we set $\langle s_k^{21}(t=0)\rangle = 10^{-20}(1+i)$. Note that the time evolution is strongly independent from this value: Δ, as a function of t, approaches always a value numerically compatible with zero before having a jump and stabilizing to its stationary value (see for example Figure C.3 (b), where the intensity of the repulsive interaction is set to $V = 5E_g$). We observe in Figure C.2 that in the stationary state the

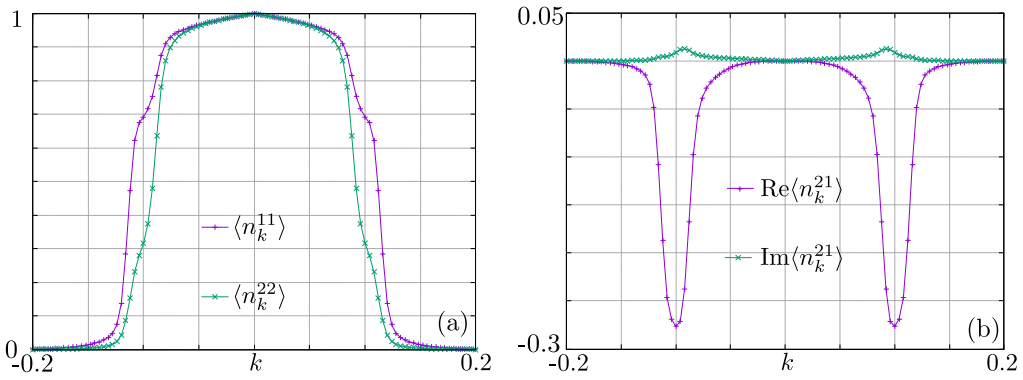

Figure C.2: (a) Occupation number of valence $\langle n_k^{11}\rangle$ and conduction $\langle n_k^{22}\rangle$ bands in the stationary state. (b) Real and imaginary part of the interband correlation $\langle n_k^{21}\rangle$ in the stationary state. Parameters: $A_1 = 8E_g$, $A_2 = 23E_g$, $k_c = 0.2$, $N_k = 100$, $\Gamma^{\mathrm{ph}} = 0.01E_g$, $\Omega = 0.25E_g$ and $V = 5E_g$. Here the interband dissipation is switched on and has the same intensity of the intraband one ($\Gamma^{\mathrm{rr}} = \Gamma^{\mathrm{ph}}$).

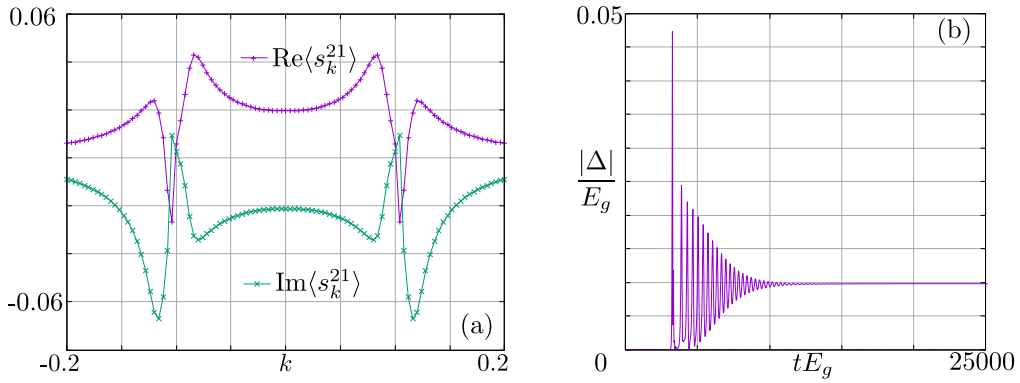

Figure C.3: (a) Real and imaginary part of the anomalous interband correlation $\langle s_k^{21} \rangle$ in the stationary state. (b) Modulus of the superconducting gap Δ as a function of time. Parameters: $A_1 = 8E_g$, $A_2 = 23E_g$, $k_c = 0.2$, $N_k = 100$, $\Gamma^{\rm ph} = 0.01E_g$, $\Omega = 0.25E_g$ and $V = 5E_g$. Here the interband dissipation is switched on and has the same intensity of the intraband one ($\Gamma^{\rm rr} = \Gamma^{\rm ph}$).

populations are smoothed and do not resemble a box function. Furthermore the interband correlations are not zero in the region where the populations of the valence and conduction bands become slightly different. In this region, where both the bands are partially filled, we find that $\langle n_k^{21} \rangle \neq 0$. Then, since the laser cancels out the energy difference between the valence and conduction bands, the electrons occupy with almost the same probability the two bands. This is also the region where the modulus of the anomalous interband correlator has its maxima (see Fig.C.3 (a)). Note that $\langle s_k^{21} \rangle \neq 0$ in the whole momentum region considered, but tends to zero near the boundaries of the momentum space region considered.

Bibliography

[1] D. P. DiVincenzo, "The physical implementation of quantum computation", Fortschritte der Physik: Progress of Physics **48**, 771–783 (2000).

[2] M. A. Nielsen and I. Chuang, *Quantum computation and quantum information* (AAPT, 2002).

[3] E. Knill, "Quantum computing with realistically noisy devices", Nature **434**, 39–44 (2005).

[4] T. D. Ladd, F. Jelezko, R. Laflamme, Y. Nakamura, C. Monroe, and J. L. O'Brien, "Quantum computers", Nature **464**, Review Article, 45 (2010).

[5] R. S. K. Mong, D. J. Clarke, J. Alicea, N. H. Lindner, P. Fendley, C. Nayak, Y. Oreg, A. Stern, E. Berg, K. Shtengel, and M. P. A. Fisher, "Universal topological quantum computation from a superconductor-abelian quantum hall heterostructure", Phys. Rev. X **4**, 011036 (2014).

[6] X. Zhang, H.-O. Li, G. Cao, M. Xiao, G.-C. Guo, and G.-P. Guo, "Semiconductor quantum computation", National Science Review **6**, 32–54 (2018).

[7] A. W. Harrow and A. Montanaro, "Quantum computational supremacy", Nature **549**, 203 (2017).

[8] S. Cong, Y. Zheng, B. Ji, and Y. Dai, "Overview of progress in quantum systems control", Frontiers of Electrical and Electronic Engineering in China **2**, 132 (2007).

[9] J. Eisert, M. Friesdorf, and C. Gogolin, "Quantum many-body systems out of equilibrium", Nature Physics **11**, Review Article, 124 (2015).

[10] G. Barontini, R. Labouvie, F. Stubenrauch, A. Vogler, V. Guarrera, and H. Ott, "Controlling the dynamics of an open many-body quantum system with localized dissipation", Phys. Rev. Lett. **110**, 035302 (2013).

[11] J. T. Barreiro, M. Müller, P. Schindler, D. Nigg, T. Monz, M. Chwalla, M. Hennrich, C. F. Roos, P. Zoller, and R. Blatt, "An open-system quantum simulator with trapped ions", Nature **470**, Article, 486 (2011).

[12]M. Rigol, V. Dunjko, V. Yurovsky, and M. Olshanii, "Relaxation in a completely integrable many-body quantum system: an ab initio study of the dynamics of the highly excited states of 1d lattice hard-core bosons", Phys. Rev. Lett. **98**, 050405 (2007).

[13]M. Heyl, "Dynamical quantum phase transitions: a review", Reports on Progress in Physics **81**, 054001 (2018).

[14]S. Porta, F. M. Gambetta, N. Traverso Ziani, D. M. Kennes, M. Sassetti, and F. Cavaliere, "Nonmonotonic response and light-cone freezing in fermionic systems under quantum quenches from gapless to gapped or partially gapped states", Phys. Rev. B **97**, 035433 (2018).

[15]S. Porta, N. T. Ziani, D. M. Kennes, F. M. Gambetta, M. Sassetti, and F. Cavaliere, "Effective metal-insulator nonequilibrium quantum phase transition in the su-schrieffer-heeger model", Phys. Rev. B **98**, 214306 (2018).

[16]S. Porta, F. Cavaliere, M. Sassetti, and N. T. Ziani, "Topological classification of dynamical quantum phase transitions in the xy chain", In preparation (2019).

[17]S. Porta, L. Privitera, N. T. Ziani, M. Sassetti, F. Cavaliere, and B. Trauzettel, "Feasible model for photoinduced interband pairing", Phys. Rev. B **100**, 024513 (2019).

[18]S. Porta, F. M. Gambetta, F. Cavaliere, N. Traverso Ziani, and M. Sassetti, "Out-of-equilibrium density dynamics of a quenched fermionic system", Phys. Rev. B **94**, 085122 (2016).

[19]M. F. Gambetta and S. Porta, "Out-of-equilibrium density dynamics of a spinful Luttinger liquid", Nuovo Cimento C **40**, 92 (2017).

[20]A. Cavalleri, "Photo-induced superconductivity", Contemporary Physics **59**, 31–46 (2018).

[21]M. Born and V. Fock, "Beweis des adiabatensatzes", Zeitschrift für Physik **51**, 165–180 (1928).

[22]T. Kato, "On the Adiabatic Theorem of Quantum Mechanics", Journal of the Physical Society of Japan **5**, 435 (1950).

[23]G Nenciu, "On the adiabatic theorem of quantum mechanics", Journal of Physics A: Mathematical and General **13**, L15–L18 (1980).

[24]A. Rahmani, B. Seradjeh, and M. Franz, "Optimal diabatic dynamics of majorana-based quantum gates", Phys. Rev. B **96**, 075158 (2017).

[25]X. Chen, A. Ruschhaupt, S. Schmidt, S. Ibáñez, and J. G. Muga, "Shortcut to adiabaticity in harmonic traps", Journal of Atomic and Molecular Sciences **1**, 1–17 (2010).

[26]J.-F. Schaff, P. Capuzzi, G. Labeyrie, and P. Vignolo, "Shortcuts to adiabaticity for trapped ultracold gases", New Journal of Physics **13**, 113017 (2011).

[27]X. Chen, A. Ruschhaupt, S. Schmidt, A. del Campo, D. Guéry-Odelin, and J. G. Muga, "Fast optimal frictionless atom cooling in harmonic traps: shortcut to adiabaticity", Phys. Rev. Lett. **104**, 063002 (2010).

[28]D. Sels, "Stochastic gradient ascent outperforms gamers in the quantum moves game", Phys. Rev. A **97**, 040302 (2018).

[29]P. Doria, T. Calarco, and S. Montangero, "Optimal control technique for many-body quantum dynamics", Phys. Rev. Lett. **106**, 190501 (2011).

[30]M. R. Kamsap, J. Pedregosa-Gutierrez, C. Champenois, D. Guyomarc'h, M. Houssin, and M. Knoop, "Fast and efficient transport of large ion clouds", Phys. Rev. A **92**, 043416 (2015).

[31]B. Damski, "The simplest quantum model supporting the kibble-zurek mechanism of topological defect production: landau-zener transitions from a new perspective", Phys. Rev. Lett. **95**, 035701 (2005).

[32]A. Del Campo and W. H. Zurek, "Universality of phase transition dynamics: Topological defects from symmetry breaking", International Journal of Modern Physics A **29**, 1430018 (2014).

[33]W. H. Zurek, "Cosmological experiments in superfluid helium?", Nature **317**, 505–508 (1985).

[34]M. Gong, X. Wen, G. Sun, D.-W. Zhang, D. Lan, Y. Zhou, Y. Fan, Y. Liu, X. Tan, H. Yu, Y. Yu, S.-L. Zhu, S. Han, and P. Wu, "Simulating the kibble-zurek mechanism of the ising model with a superconducting qubit system", Scientific Reports **6**, Article, 22667 (2016).

[35]P. Bocchieri and A. Loinger, "Quantum recurrence theorem", Phys. Rev. **107**, 337–338 (1957).

[36]M. Cramer, C. M. Dawson, J. Eisert, and T. J. Osborne, "Exact relaxation in a class of nonequilibrium quantum lattice systems", Phys. Rev. Lett. **100**, 030602 (2008).

[37]M. Rigol, V. Dunjko, and M. Olshanii, "Thermalization and its mechanism for generic isolated quantum systems", Nature **452**, 854 (2008).

[38]A. Polkovnikov, K. Sengupta, A. Silva, and M. Vengalattore, "Colloquium: nonequilibrium dynamics of closed interacting quantum systems", Rev. Mod. Phys. **83**, 863–883 (2011).

[39]P. Calabrese, F. H. L. Essler, and M. Fagotti, "Quantum quench in the transverse-field ising chain", Phys. Rev. Lett. **106**, 227203 (2011).

[40]J.-S. Caux and F. H. L. Essler, "Time evolution of local observables after quenching to an integrable model", Phys. Rev. Lett. **110**, 257203 (2013).

[41]M. Cheneau, P. Barmettler, D. Poletti, M. Endres, P. Schauß, T. Fukuhara, C. Gross, I. Bloch, C. Kollath, and S. Kuhr, "Light-cone-like spreading of correlations in a quantum many-body system", Nature **481**, 484 (2012).

[42]R Geiger, T Langen, I. E. Mazets, and J Schmiedmayer, "Local relaxation and light-cone-like propagation of correlations in a trapped one-dimensional bose gas", New Journal of Physics **16**, 053034 (2014).

[43]T. Kinoshita, T. Wenger, and D. S. Weiss, "A quantum newton's cradle", Nature **440**, 900–903 (2006).

[44]A. Iucci and M. A. Cazalilla, "Quantum quench dynamics of the luttinger model", Phys. Rev. A **80**, 063619 (2009).

[45]A. C. Cassidy, C. W. Clark, and M. Rigol, "Generalized thermalization in an integrable lattice system", Phys. Rev. Lett. **106**, 140405 (2011).

[46]E. Ilievski, J. De Nardis, B. Wouters, J.-S. Caux, F. H. L. Essler, and T. Prosen, "Complete generalized gibbs ensembles in an interacting theory", Phys. Rev. Lett. **115**, 157201 (2015).

[47]L. Vidmar and M. Rigol, "Generalized gibbs ensemble in integrable lattice models", Journal of Statistical Mechanics: Theory and Experiment **2016**, 064007 (2016).

[48]T. Langen, T. Gasenzer, and J. Schmiedmayer, "Prethermalization and universal dynamics in near-integrable quantum systems", Journal of Statistical Mechanics: Theory and Experiment **2016**, 064009 (2016).

[49]T. Langen, S. Erne, R. Geiger, B. Rauer, T. Schweigler, M. Kuhnert, W. Rohringer, I. E. Mazets, T. Gasenzer, and J. Schmiedmayer, "Experimental observation of a generalized gibbs ensemble", Science **348**, 207–211 (2015).

[50]B. Wouters, J. De Nardis, M. Brockmann, D. Fioretto, M. Rigol, and J.-S. Caux, "Quenching the anisotropic heisenberg chain: exact solution and generalized gibbs ensemble predictions", Phys. Rev. Lett. **113**, 117202 (2014).

[51]B. Pozsgay, M. Mestyán, M. A. Werner, M. Kormos, G. Zaránd, and G. Takács, "Correlations after quantum quenches in the xxz spin chain: failure of the generalized gibbs ensemble", Phys. Rev. Lett. **113**, 117203 (2014).

[52]C. Kollath, A. M. Läuchli, and E. Altman, "Quench dynamics and nonequilibrium phase diagram of the bose-hubbard model", Phys. Rev. Lett. **98**, 180601 (2007).

[53]M. Rigol and L. F. Santos, "Quantum chaos and thermalization in gapped systems", Phys. Rev. A **82**, 011604 (2010).

[54]J. M. Deutsch, "Quantum statistical mechanics in a closed system", Phys. Rev. A **43**, 2046–2049 (1991).

[55]M. Srednicki, "Chaos and quantum thermalization", Phys. Rev. E **50**, 888–901 (1994).

[56]M. Rigol and M. Srednicki, "Alternatives to eigenstate thermalization", Phys. Rev. Lett. **108**, 110601 (2012).

[57]T. Oka and S. Kitamura, "Floquet engineering of quantum materials", Annual Review of Condensed Matter Physics **10**, 387–408 (2019).

[58]M. Grifoni and P. Hänggi, "Driven quantum tunneling", Physics Reports **304**, 229 –354 (1998).

[59]A. Eckardt, "Colloquium: atomic quantum gases in periodically driven optical lattices", Rev. Mod. Phys. **89**, 011004 (2017).

[60]D. J. Thouless, "Quantization of particle transport", Phys. Rev. B **27**, 6083–6087 (1983).

[61]M. Bukov, L. D'Alessio, and A. Polkovnikov, "Universal high-frequency behavior of periodically driven systems: from dynamical stabilization to floquet engineering", Advances in Physics **64**, 139–226 (2015).

[62]A. Eckardt and E. Anisimovas, "High-frequency approximation for periodically driven quantum systems from a floquet-space perspective", New Journal of Physics **17**, 093039 (2015).

[63]J. Berges, S. Borsányi, and C. Wetterich, "Prethermalization", Phys. Rev. Lett. **93**, 142002 (2004).

[64]T. Mori, T. Kuwahara, and K. Saito, "Rigorous bound on energy absorption and generic relaxation in periodically driven quantum systems", Phys. Rev. Lett. **116**, 120401 (2016).

[65]D. Abanin, W. De Roeck, W. W. Ho, and F. Huveneers, "A rigorous theory of many-body prethermalization for periodically driven and closed quantum systems", Communications in Mathematical Physics **354**, 809–827 (2017).

[66]A. Lazarides, A. Das, and R. Moessner, "Periodic thermodynamics of isolated quantum systems", Phys. Rev. Lett. **112**, 150401 (2014).

[67]M. Vojta, "Quantum phase transitions", Reports on Progress in Physics **66**, 2069–2110 (2003).

[68]S. Sachdev, *Quantum phase transitions*, 2nd ed. (Cambridge University Press, 2011).

[69]G. Jaeger, "The ehrenfest classification of phase transitions: introduction and evolution", Archive for History of Exact Sciences **53**, 51–81 (1998).

[70]E. Schrödinger, "Are there quantum jumps? part ii", The British Journal for the Philosophy of Science **3**, 233–242 (1952).

[71]S. Bhattacharyya, S. Dasgupta, and A. Das, "Signature of a continuous quantum phase transition in non-equilibrium energy absorption: footprints of criticality on higher excited states", Scientific Reports **5**, Article, 16490 (2015).

[72]T. W. B. Kibble, "Topology of cosmic domains and strings", Journal of Physics A: Mathematical and General **9**, 1387–1398 (1976).

[73]M. Moeckel and S. Kehrein, "Interaction quench in the hubbard model", Phys. Rev. Lett. **100**, 175702 (2008).

[74]M. Eckstein, M. Kollar, and P. Werner, "Thermalization after an interaction quench in the hubbard model", Phys. Rev. Lett. **103**, 056403 (2009).

[75]N. Tsuji, M. Eckstein, and P. Werner, "Nonthermal antiferromagnetic order and nonequilibrium criticality in the hubbard model", Phys. Rev. Lett. **110**, 136404 (2013).

[76]S. Roy, R. Moessner, and A. Das, "Locating topological phase transitions using nonequilibrium signatures in local bulk observables", Phys. Rev. B **95**, 041105 (2017).

[77]J. C. Halimeh, V. Zauner-Stauber, I. P. McCulloch, I. de Vega, U. Schollwöck, and M. Kastner, "Prethermalization and persistent order in the absence of a thermal phase transition", Phys. Rev. B **95**, 024302 (2017).

[78]M. Heyl, A. Polkovnikov, and S. Kehrein, "Dynamical quantum phase transitions in the transverse-field ising model", Phys. Rev. Lett. **110**, 135704 (2013).

[79]M. Fisher, *The nature of critical points (lectures in theoretical physics vol 7c)*, 1964.

[80]C. N. Yang and T. D. Lee, "Statistical theory of equations of state and phase transitions. i. theory of condensation", Phys. Rev. **87**, 404–409 (1952).

[81]T. D. Lee and C. N. Yang, "Statistical theory of equations of state and phase transitions. ii. lattice gas and ising model", Phys. Rev. **87**, 410–419 (1952).

[82]A. Gambassi and A. Silva, "Large deviations and universality in quantum quenches", Phys. Rev. Lett. **109**, 250602 (2012).

[83]F. Pollmann, S. Mukerjee, A. G. Green, and J. E. Moore, "Dynamics after a sweep through a quantum critical point", Phys. Rev. E **81**, 020101 (2010).

[84]S. Vajna and B. Dóra, "Disentangling dynamical phase transitions from equilibrium phase transitions", Phys. Rev. B **89**, 161105 (2014).

[85]B. Zunkovic, M. Heyl, M. Knap, and A. Silva, "Dynamical quantum phase transitions in spin chains with long-range interactions: merging different concepts of nonequilibrium criticality", Phys. Rev. Lett. **120**, 130601 (2018).

[86]M. Heyl, "Dynamical quantum phase transitions in systems with broken-symmetry phases", Phys. Rev. Lett. **113**, 205701 (2014).

[87]P. Jurcevic, H. Shen, P. Hauke, C. Maier, T. Brydges, C. Hempel, B. P. Lanyon, M. Heyl, R. Blatt, and C. F. Roos, "Direct observation of dynamical quantum phase transitions in an interacting many-body system", Phys. Rev. Lett. **119**, 080501 (2017).

[88]J. Asbóth, L. Oroszlány, and A. Pályi, *A short course on topological insulators: band structure and edge states in one and two dimensions*, Lecture Notes in Physics (Springer International Publishing, 2016).

[89]W. P. Su, J. R. Schrieffer, and A. J. Heeger, "Solitons in polyacetylene", Phys. Rev. Lett. **42**, 1698–1701 (1979).

[90]C. Wu, B. A. Bernevig, and S.-C. Zhang, "Helical liquid and the edge of quantum spin hall systems", Phys. Rev. Lett. **96**, 106401 (2006).

[91], "Antisymmetric spin filtering in one-dimensional electron systems with uniform spin-orbit coupling", Phys. Rev. Lett. **90**, 256601 (2003).

[92]S. Heedt, N. Traverso Ziani, F. Crépin, W. Prost, S. Trellenkamp, J. Schubert, D. Grützmacher, B. Trauzettel, and T. Schäpers, "Signatures of interaction-induced helical gaps in nanowire quantum point contacts", Nature Physics **13**, 563 (2017).

[93]Y. A. Bychkov and E. I. Rashba, "Properties of a 2d electron gas with lifted spectral degeneracy", JETP lett **39**, 78 (1984).

[94]T. Meng and D. Loss, "Strongly anisotropic spin response as a signature of the helical regime in rashba nanowires", Phys. Rev. B **88**, 035437 (2013).

[95]L.-M. Duan, E. Demler, and M. D. Lukin, "Controlling spin exchange interactions of ultracold atoms in optical lattices", Phys. Rev. Lett. **91**, 090402 (2003).

[96]R. Schmied, T. Roscilde, V. Murg, D. Porras, and J. I. Cirac, "Quantum phases of trapped ions in an optical lattice", New Journal of Physics **10**, 045017 (2008).

[97]N. G. Berloff, M. Silva, K. Kalinin, A. Askitopoulos, J. D. Töpfer, P. Cilibrizzi, W. Langbein, and P. G. Lagoudakis, "Realizing the classical xy hamiltonian in polariton simulators", Nature materials **16**, 1120 (2017).

[98]S. Katsura, "Statistical mechanics of the anisotropic linear heisenberg model", Phys. Rev. **129**, 2835–2835 (1963).

[99]T. Niemeijer, "Some exact calculations on a chain of spins 1/2", Physica **36**, 377–419 (1967).

[100]T. Niemeijer, "Some exact calculations on a chain of spins 1/2 ii", Physica **39**, 313 –326 (1968).

[101]F. Franchini, *An introduction to integrable techniques for one-dimensional quantum systems*, Vol. 940 (Springer, 2017), p. 256601.

[102]G. F. Giuliani, G. Vignale, and E. Tosatti, "Quantum theory of the electron liquid", Physics Today **59**, 68 (2006).

[103]H. Haug and A.-P. Jauho, *Quantum kinetics in transport and optics of semiconductors*, Vol. 2 (Springer, 2008), p. 256601.

[104]G Grosso and G. P. Parravicini, *Solid state physics*, 2nd ed., Vol. 90 (Academic Press, 2013), p. 256601.

[105]U. Weiss, *Quantum dissipative systems*, Vol. 13 (World scientific, 2012), p. 256601.

[106]I. Bloch, "Quantum gases", Science **319**, 1202–1203 (2008).

[107]I. Bloch, J. Dalibard, and S. Nascimbène, "Quantum simulations with ultracold quantum gases", Nature Physics **8**, Review Article, 267 (2012).

[108]T. Kinoshita, T. Wenger, and D. S. Weiss, "Observation of a one-dimensional tonks-girardeau gas", Science **305**, 1125–1128 (2004).

[109]B. Sutherland, *Beautiful models*, Vol. 90 (WORLD SCIENTIFIC, 2004), p. 256601.

[110]M. A. Cazalilla, "Effect of suddenly turning on interactions in the luttinger model", Phys. Rev. Lett. **97**, 156403 (2006).

[111]D. Rossini, A. Silva, G. Mussardo, and G. E. Santoro, "Effective thermal dynamics following a quantum quench in a spin chain", Phys. Rev. Lett. **102**, 127204 (2009).

[112]D. Schuricht and F. H. L. Essler, "Dynamics in the ising field theory after a quantum quench", Journal of Statistical Mechanics: Theory and Experiment **2012**, P04017 (2012).

[113]M. D. Caio, N. R. Cooper, and M. J. Bhaseen, "Quantum quenches in chern insulators", Phys. Rev. Lett. **115**, 236403 (2015).

[114]D. Bercioux and P. Lucignano, "Quantum transport in rashba spin–orbit materials: a review", Reports on Progress in Physics **78**, 106001 (2015).

[115]R. Courant and D. Hilbert, *Methods of mathematical physics*, Vol. 90 (John Wiley & Sons, Ltd, 1953), p. 256601.

[116]T. Mishra, J. Carrasquilla, and M. Rigol, "Phase diagram of the half-filled one-dimensional t-V-V' model", Phys. Rev. B **84**, 115135 (2011).

[117]S. R. White, "Density matrix formulation for quantum renormalization groups", Phys. Rev. Lett. **69**, 2863–2866 (1992).

[118]U. Schollwöck, "The density-matrix renormalization group in the age of matrix product states", Annals of Physics **326**, January 2011 Special Issue, 96 –192 (2011).

[119]G. Vidal, "Classical simulation of infinite-size quantum lattice systems in one spatial dimension", Phys. Rev. Lett. **98**, 070201 (2007).

[120]R. Orús and G. Vidal, "Infinite time-evolving block decimation algorithm beyond unitary evolution", Phys. Rev. B **78**, 155117 (2008).

[121]D. Kennes and C. Karrasch, "Extending the range of real time density matrix renormalization group simulations", Computer Physics Communications **200**, 37 –43 (2016).

[122]B. Yan and C. Felser, "Topological materials: weyl semimetals", Annual Review of Condensed Matter Physics **8**, 337–354 (2017).

[123]B. Dóra, I. F. Herbut, and R. Moessner, "Coupling, merging, and splitting dirac points by electron-electron interaction", Phys. Rev. B **88**, 075126 (2013).

[124]G. Montambaux, F. Piéchon, J.-N. Fuchs, and M. O. Goerbig, "Merging of dirac points in a two-dimensional crystal", Phys. Rev. B **80**, 153412 (2009).

[125]J Voit, "One-dimensional fermi liquids", Reports on Progress in Physics **58**, 977–1116 (1995).

[126]T. Giamarchi and O. U. Press, *Quantum physics in one dimension*, Vol. 90, International Series of Monogr (Clarendon Press, 2004), p. 256601.

[127]D. Leibfried, R. Blatt, C. Monroe, and D. Wineland, "Quantum dynamics of single trapped ions", Rev. Mod. Phys. **75**, 281–324 (2003).

[128]J. Smith, A. Lee, P. Richerme, B. Neyenhuis, P. W. Hess, P. Hauke, M. Heyl, D. A. Huse, and C. Monroe, "Many-body localization in a quantum simulator with programmable random disorder", Nature Physics **12**, 907 (2016).

[129]E. Altman and R. Vosk, "Universal dynamics and renormalization in many-body-localized systems", Annual Review of Condensed Matter Physics **6**, 383–409 (2015).

[130]D. A. Abanin and Z. Papić, "Recent progress in many-body localization", Annalen der Physik **529**, 1700169 (2017).

[131]P. Calabrese and J. Cardy, "Quantum quenches in extended systems", Journal of Statistical Mechanics: Theory and Experiment **2007**, P06008–P06008 (2007).

[132]P. Fendley, "Parafermionic edge zero modes inZn-invariant spin chains", Journal of Statistical Mechanics: Theory and Experiment **2012**, P11020 (2012).

[133]S. Vajna and B. Dóra, "Topological classification of dynamical phase transitions", Phys. Rev. B **91**, 155127 (2015).

[134]G. D. Mahan, *Many-particle physics*, Vol. 90 (Springer Science & Business Media, 2013), p. 256601.

[135]N. H. Lindner, G. Refael, and V. Galitski, "Floquet topological insulator in semiconductor quantum wells", Nature Physics **7**, 490 (2011).

[136]G. Jotzu, M. Messer, R. Desbuquois, M. Lebrat, T. Uehlinger, D. Greif, and T. Esslinger, "Experimental realization of the topological haldane model with ultracold fermions", Nature **515**, 237 (2014).

[137]D. V. Else, B. Bauer, and C. Nayak, "Floquet time crystals", Phys. Rev. Lett. **117**, 090402 (2016).

[138]J. Zhang, P. W. Hess, A. Kyprianidis, P. Becker, A. Lee, J. Smith, G. Pagano, I.-D. Potirniche, A. C. Potter, A. Vishwanath, N. Y. Yao, and C. Monroe, "Observation of a discrete time crystal", Nature **543**, 217 (2017).

[139]S. Choi, J. Choi, R. Landig, G. Kucsko, H. Zhou, J. Isoya, F. Jelezko, S. Onoda, H. Sumiya, V. Khemani, C. von Keyserlingk, N. Y. Yao, E. Demler, and M. D. Lukin, "Observation of discrete time-crystalline order in a disordered dipolar many-body system", Nature **543**, 221 (2017).

[140]G. Kucsko, S. Choi, J. Choi, P. C. Maurer, H. Zhou, R. Landig, H. Sumiya, S. Onoda, J. Isoya, F. Jelezko, E. Demler, N. Y. Yao, and M. D. Lukin, "Critical thermalization of a disordered dipolar spin system in diamond", Phys. Rev. Lett. **121**, 023601 (2018).

[141]J. A. Sobota, S. Yang, J. G. Analytis, Y. L. Chen, I. R. Fisher, P. S. Kirchmann, and Z.-X. Shen, "Ultrafast optical excitation of a persistent surface-state population in the topological insulator Bi_2Se_3", Phys. Rev. Lett. **108**, 117403 (2012).

[142]P. W. Anderson, "Absence of diffusion in certain random lattices", Phys. Rev. **109**, 1492–1505 (1958).

[143]R. Nandkishore and D. A. Huse, "Many-body localization and thermalization in quantum statistical mechanics", Annual Review of Condensed Matter Physics **6**, 15–38 (2015).

[144]M. Marcuzzi, J. Marino, A. Gambassi, and A. Silva, "Prethermalization in a nonintegrable quantum spin chain after a quench", Phys. Rev. Lett. **111**, 197203 (2013).

[145]T. Puskarov and D. Schuricht, "Time evolution during and after finite-time quantum quenches in the transverse-field Ising chain", SciPost Phys. **1**, 003 (2016).

[146]U. Divakaran, S. Sharma, and A. Dutta, "Tuning the presence of dynamical phase transitions in a generalized xy spin chain", Phys. Rev. E **93**, 052133 (2016).

[147]C. Yang, L. Li, and S. Chen, "Dynamical topological invariant after a quantum quench", Phys. Rev. B **97**, 060304 (2018).

[148]M. König, S. Wiedmann, C. Brüne, A. Roth, H. Buhmann, L. W. Molenkamp, X.-L. Qi, and S.-C. Zhang, "Quantum spin hall insulator state in hgte quantum wells", Science **318**, 766–770 (2007).

[149]A. Roth, C. Brüne, H. Buhmann, L. W. Molenkamp, J. Maciejko, X.-L. Qi, and S.-C. Zhang, "Nonlocal transport in the quantum spin hall state", Science **325**, 294–297 (2009).

[150]Y. Xia, D. Qian, D. Hsieh, L. Wray, A. Pal, H. Lin, A. Bansil, D. Grauer, Y. S. Hor, R. J. Cava, and M. Z. Hasan, "Observation of a large-gap topological-insulator class with a single dirac cone on the surface", Nature Physics **5**, 398 (2009).

[151]S.-Y. Xu, I. Belopolski, N. Alidoust, M. Neupane, G. Bian, C. Zhang, R. Sankar, G. Chang, Z. Yuan, C.-C. Lee, S.-M. Huang, H. Zheng, J. Ma, D. S. Sanchez, B. Wang, A. Bansil, F. Chou, P. P. Shibayev, H. Lin, S. Jia, and M. Z. Hasan, "Discovery of a weyl fermion semimetal and topological fermi arcs", Science **349**, 613–617 (2015).

[152]B. Sacépé, J. B. Oostinga, J. Li, A. Ubaldini, N. J. G. Couto, E. Giannini, and A. F. Morpurgo, "Gate-tuned normal and superconducting transport at the surface of a topological insulator", Nature Communications **2**, 575 (2011).

[153]V. Mourik, K. Zuo, S. M. Frolov, S. R. Plissard, E. P. A. M. Bakkers, and L. P. Kouwenhoven, "Signatures of majorana fermions in hybrid superconductor-semiconductor nanowire devices", Science **336**, 1003–1007 (2012).

[154]C. H. L. Quay, T. L. Hughes, J. A. Sulpizio, L. N. Pfeiffer, K. W. Baldwin, K. W. West, D. Goldhaber-Gordon, and R. de Picciotto, "Observation of a one-dimensional spin–orbit gap in a quantum wire", Nature Physics **6**, 336 (2010).

[155]D. Pesin and A. H. MacDonald, "Spintronics and pseudospintronics in graphene and topological insulators", Nature Materials **11**, 409 (2012).

[156]J. Linder and J. W. A. Robinson, "Superconducting spintronics", Nature Physics **11**, 307 (2015).

[157]A. Kitaev, "Fault-tolerant quantum computation by anyons", Annals of Physics **303**, 2 –30 (2003).

[158]A. P. Drozdov, M. I. Eremets, I. A. Troyan, V. Ksenofontov, and S. I. Shylin, "Conventional superconductivity at 203 kelvin at high pressures in the sulfur hydride system", Nature **525**, 73 (2015).

[159]S. Gerber, H. Jang, H. Nojiri, S. Matsuzawa, H. Yasumura, D. A. Bonn, R. Liang, W. N. Hardy, Z. Islam, A. Mehta, S. Song, M. Sikorski, D. Stefanescu, Y. Feng, S. A. Kivelson, T. P. Devereaux, Z.-X. Shen, C.-C. Kao, W.-S. Lee, D. Zhu, and J.-S. Lee, "Three-dimensional charge density wave order in yba2cu3o6.67 at high magnetic fields", Science **350**, 949–952 (2015).

[160]D. Brida, A. Tomadin, C. Manzoni, Y. J. Kim, A. Lombardo, S. Milana, R. R. Nair, K. S. Novoselov, A. C. Ferrari, G. Cerullo, and M. Polini, "Ultrafast collinear scattering and carrier multiplication in graphene", Nature Communications **4**, 1987 (2013).

[161]M. Liu, H. Y. Hwang, H. Tao, A. C. Strikwerda, K. Fan, G. R. Keiser, A. J. Sternbach, K. G. West, S. Kittiwatanakul, J. Lu, S. A. Wolf, F. G. Omenetto, X. Zhang, K. A. Nelson, and R. D. Averitt, "Terahertz-field-induced insulator-to-metal transition in vanadium dioxide metamaterial", Nature **487**, 345 (2012).

[162]S. Ghimire and D. A. Reis, "High-harmonic generation from solids", Nature Physics **15**, 10–16 (2019).

[163]K. Sacha and J. Zakrzewski, "Time crystals: a review", Reports on Progress in Physics **81**, 016401 (2017).

[164]A. F. G. Wyatt, V. M. Dmitriev, W. S. Moore, and F. W. Sheard, "Microwave-enhanced critical supercurrents in constricted tin films", Phys. Rev. Lett. **16**, 1166–1169 (1966).

[165]A. H. Dayem and J. J. Wiegand, "Behavior of thin-film superconducting bridges in a microwave field", Phys. Rev. **155**, 419–428 (1967).

[166]G. M. Eliashberg, "Film superconductivity stimulated by a high-frequency field", JETP Lett. **11**, 114 (1970).

[167]A. Nava, C. Giannetti, A. Georges, E. Tosatti, and M. Fabrizio, "Cooling quasiparticles in a 3c 60 fullerides by excitonic mid-infrared absorption", Nature Physics **14**, 154 (2017).

[168]G. Goldstein, C. Aron, and C. Chamon, "Photoinduced superconductivity in semiconductors", Phys. Rev. B **91**, 054517 (2015).

[169]O. Hart, G. Goldstein, C. Chamon, and C. Castelnovo, "Steady-state superconductivity in electronic materials with repulsive interactions", arXiv preprint arXiv:1810.12309 **90**, 256601 (2018).

[170]A. Moreo, M. Daghofer, A. Nicholson, and E. Dagotto, "Interband pairing in multiorbital systems", Phys. Rev. B **80**, 104507 (2009).

[171]M. Tinkham, *Introduction to superconductivity*, Vol. 90 (Courier Corporation, 2004), p. 256601.

[172]J. Bardeen, L. N. Cooper, and J. R. Schrieffer, "Theory of superconductivity", Physical review **108**, 1175 (1957).

[173]H. Kramers, "Antisymmetric spin filtering in one-dimensional electron systems with uniform spin-orbit coupling", Proc. of Koninklijke Akademie van Wetenschappen **90**, 959–972 (1930).

[174]D H. Douglass, *Superconductivity in d- and f-band metals: second rochester conference*, Vol. 90 (American Physical Society, Jan. 1976), p. 256601.

[175]B. K. Ridley, *Quantum processes in semiconductors*, Vol. 90 (Oxford University Press, 2013), p. 256601.

[176]I. Esin, M. S. Rudner, G. Refael, and N. H. Lindner, "Quantized transport and steady states of floquet topological insulators", Phys. Rev. B **97**, 245401 (2018).

[177]N. Tandon, J. D. Albrecht, and L. R. Ram-Mohan, "Electron-phonon interaction and scattering in si and ge: implications for phonon engineering", Journal of Applied Physics **118**, 045713 (2015).

[178]M. I Dyakonov and A. Khaetskii, *Spin physics in semiconductors*, Vol. 157 (Springer, 2017), p. 256601.

[179]R. R. Puri, *Mathematical methods of quantum optics*, Vol. 79 (Springer Science & Business Media, 2001), p. 256601.

[180]N. Tandon, J. D. Albrecht, and L. R. Ram-Mohan, "Electron-phonon interaction and scattering in si and ge: implications for phonon engineering", Journal of Applied Physics **118**, 045713 (2015).

[181]L. A. Coldren, S. W. Corzine, and M. L. Mashanovitch, *Diode lasers and photonic integrated circuits*, Vol. 218 (John Wiley & Sons, 2012), p. 256601.

[182]B. Dóra, M. Haque, and G. Zaránd, "Crossover from adiabatic to sudden interaction quench in a luttinger liquid", Phys. Rev. Lett. **106**, 156406 (2011).

[183]M. J. Rice and E. J. Mele, "Elementary excitations of a linearly conjugated diatomic polymer", Phys. Rev. Lett. **49**, 1455–1459 (1982).

[184]R. Puebla, *Equilibrium and nonequilibrium aspects of phase transitions in quantum physics*, Vol. 90 (Springer, 2018), p. 256601.

[185]M. Kormos, L. Bucciantini, and P. Calabrese, "Stationary entropies after a quench from excited states in the ising chain", EPL (Europhysics Letters) **107**, 40002 (2014).

[186]K. S. Novoselov, A. K. Geim, S. V. Morozov, D. Jiang, M. I. Katsnelson, I. V. Grigorieva, S. V. Dubonos, and A. A. Firsov, "Two-dimensional gas of massless Dirac fermions in graphene", Nature **438**, 197 (2005).

[187]A. K. Geim and K. S. Novoselov, "The rise of graphene", Nature Materials **6**, 183 (2007).

[188]M. I. Katsnelson, "Graphene: carbon in two dimensions", Materials Today **10**, 20 –27 (2007).

[189]Y. Cao, V. Fatemi, S. Fang, K. Watanabe, T. Taniguchi, E. Kaxiras, and P. Jarillo-Herrero, "Unconventional superconductivity in magic-angle graphene superlattices", Nature **556**, 43 (2018).

[190]M. Yankowitz, S. Chen, H. Polshyn, Y. Zhang, K. Watanabe, T. Taniguchi, D. Graf, A. F Young, and C. R. Dean, "Tuning superconductivity in twisted bilayer graphene", Science **90**, 10.1126/science.aav1910 (2019).

[191]A. Shtyk, G. Goldstein, C. Aron, and C. Chamon, "Superfluid density of a photo-induced superconducting state", arXiv preprint arXiv:1802.02593 **90**, 256601 (2018).

[192]D. N. Basov, R. D. Averitt, and D. Hsieh, "Towards properties on demand in quantum materials", Nature Materials **16**, Review Article, 1077 (2017).